UNIVERSITY OF HAWAII
LIBRARY
OCT 21 '63

# NUCLEAR INSTRUMENTS & METHODS

A JOURNAL ON ACCELERATORS, INSTRUMENTATION
AND TECHNIQUES IN NUCLEAR PHYSICS

EDITOR: K. SIEGBAHN - UPPSALA

VOLUME 13

AUGUST — OCTOBER 1961

NORTH-HOLLAND PUBLISHING COMPANY — AMSTERDAM

L. 21 '83

PRINTED IN THE NETHERLANDS
DRUKKERIJ MEIJER N.V. - WORMERVEER AND AMSTERDAM

NUCLEAR INSTRUMENTS AND METHODS

EDITORIAL BOARD:

J. B. ADAMS (CERN)
F. A. ALSINA (Buenos Aires)
E. AMALDI (Rome)
H. L. ANDERSON (Chicago)
K. T. BAINBRIDGE (Cambridge, Mass.)
P. R. BELL (Oak Ridge)
R. E. BELL (Montreal)
A. BERTHELOT (Saclay)
H. BRINKMAN (Groningen)
E. H. COOKE–YARBOROUGH (Harwell)
S. DE BENEDETTI (Pittsburgh)
M. DE HEMPTINNE (Louvain)
A. DE-SHALIT (Rehovoth)
M DEUTSCH (Cambridge, Mass.)
S. DU TOIT (Pretoria)
B. S. DŽELEPOV (Leningrad)
W. GENTNER (Heidelberg)
P. C. GUGELOT (Amsterdam)
H. HALBAN (Paris)
O. HAXEL (Heidelberg)
P. HUBER (Basel)
S. KIKUCHI (Tokyo)
J. KOCH (Copenhagen)
M. S. KOZODAEV (Moscow)
S. LIVINGSTON (Cambridge, Mass.)
E. M. MCMILLAN (Berkeley)
M. G. MEŠČERJAKOV (Moscow)
P. B. MOON (Birmingham)
M. L. OLIPHANT (Canberra)
W. PAUL (Bonn)
A. S. RAO (Bombay)
G. SALVINI (Rome)
P. SAVIĆ (Belgrade)
P. SCHERRER (Zürich)
CH. SCHMELZER (CERN)
R. TANGEN (Oslo)
D. TAYLOR (Northampton)
V. I. VEKSLER (Moscow)
G. VON DARDEL (CERN)
O. WERNHOLM (Stockholm)
R. R. WILSON (Cornell)
S. D. WINTER (Saclay)

AUGUST 1961 VOLUME 13 (1961) No. 1

GREGG M. SINCLAIR LIBRARY
UNIVERSITY OF HAWAII
8-7-63

# NUCLEAR INSTRUMENTS & METHODS

A JOURNAL ON ACCELERATORS, INSTRUMENTATION AND TECHNIQUES IN NUCLEAR PHYSICS

EDITOR: K. SIEGBAHN - UPPSALA

CONTENTS

R. L. ZIMMERMAN, H. PALEVSKY, R. E. CHRIEN, W. C. OLSEN, P. P. SINGH and C. H. WESTCOTT, The U.S.-Canadian fast chopper installation at Chalk River . . . . . 1

WERNER SCHNEIDER and TORSTEN LINDQVIST, Automatic analysis of beta-ray spectra . . . 21

M. KONRAD and B. TURKO, Sorting of two coincident pulses according to their amplitudes . 29

TOYOJIRO FUKETA, Paired-chamber type pile oscillator . . . . . 35

EIICHI TANAKA, A low background beta-ray scintillation spectrometer using a coincidence method with a Geiger counter . . . . . 43

JEAN KERN, Détecteur G.M. pour un spectromètre bêta . . . . . 50

MARTIN REISER, Ioneneinfang und Anfangsbahnen im Isochron-Zyklotron Karlsruhe . . 55

R. BATCHELOR, W. B. GILBOY, J. B. PARKER and J. H. TOWLE, The response of organic scintillators to fast neutrons . . . . . 70

T. K. ALEXANDER and D. R. HEYWOOD, A twenty-Mc/s transistor decade scaler . . . . . 83

*Letters to the Editor*

RICHARD C. McCALL and E. INGEMAR LARSSON, A low priced automatic printout system for the Hutchinson-Scarrott analyser . . . . . 92

Y. HAZONI, A fast Flip-Flop circuit utilizing Tunnel-Diodes . . . . . 95

R. E. JENNINGS and R. E. RAND, Elimination of the dead space between channels in a Hutchinson-Scarrott pulse height analyser . . . 97

N. CINDRO, A possible method for distinguishing charged particles with semiconductor detectors . . . . . 99

NORTH-HOLLAND PUBLISHING COMPANY — AMSTERDAM

# NUCLEAR INSTRUMENTS AND METHODS

*A journal on accelerators, instrumentation and techniques in nuclear physics*

EDITOR: K. SIEGBAHN, UPPSALA



EDITORIAL BOARD:

J. B. ADAMS (CERN)
F. A. ALSINA (Buenos Aires)
E. AMALDI (Rome)
H. L. ANDERSON (Chicago)
K. T. BAINBRIDGE (Cambridge, Mass.)
P. R. BELL (Oak Ridge)
R. E. BELL (Montreal)
A. BERTHELOT (Saclay)
H. BRINKMAN (Groningen)
E. H. COOKE-YARBOROUGH (Harwell)
S. DE BENEDETTI (Pittsburgh)
M. DE HEMPTINNE (Louvain)
A. DE-SHALIT (Rehovoth)
M. DEUTSCH (Cambridge, Mass.)
S. DU TOIT (Pretoria)
B. S. DŽELEPOV (Leningrad)
W. GENTNER (Heidelberg)
P. C. GUGELOT (Amsterdam)
H. HALBAN (Paris)
O. HAXEL (Heidelberg)
P. HUBER (Basel)
S. KIKUCHI (Tokyo)
J. KOCH (Copenhagen)
M. S. KOZODAEV (Moscow)
S. LIVINGSTON (Cambridge, Mass.)
E. M. MCMILLAN (Berkeley)
M. G. MEŠČERJAKOW (Moscow)
P. B. MOON (Birmingham)
M. L. OLIPHANT (Canberra)
W. PAUL (Bonn)
A. S. RAO (Bombay)
G. SALVINI (Rome)
P. SAVIĆ (Belgrade)
P. SCHERRER (Zürich)
CH. SCHMELZER (CERN)
R. TANGEN (Oslo)
D. TAYLOR (Northampton)
V. I. VEKSLER (Moscow)
G. VON DARDEL (CERN)
O. WERNHOLM (Stockholm)
R. R. WILSON (Cornell)
S. D. WINTER (Saclay)


INSTRUCTIONS FOR CONTRIBUTORS

Contributions may be sent to the Editor, Professor K. Siegbahn, Institute of Physics, University of Uppsala, Sweden, either directly or through the intermediation of one of the members of the Editorial Board. Contributions may be written in English, French or German but should always, except for very short papers, be supplied with a brief abstract in English. Figures should be inked original drawings or glossy prints and they should be sufficiently large. Contributors should make sure that important details in drawings and photographs will show up clearly in the diminished copy used by the publisher.

Books for review should be sent to Professor Siegbahn.

Objective and descriptive material on endeavours and product developments from the industry for the section "Spotlight on Industry" should be sent directly to the publishers, North-Holland Publishing Company, P.O. Box 103, Amsterdam.


Nuclear Instruments and Methods is published monthly. The subscription price of a volume of about 360 pages is $ 17.00 (130 s), postage free.

Subscriptions should be sent to the publishers, North-Holland Publishing Company, P.O. Box 103, Amsterdam, or to any subscription-agent.



No part of this issue may be reproduced in any form, by print, photoprint, microfilm or any other means without written permission from the publisher.

# *What's good for nuclides in New Haven is good for those in New Zealand**

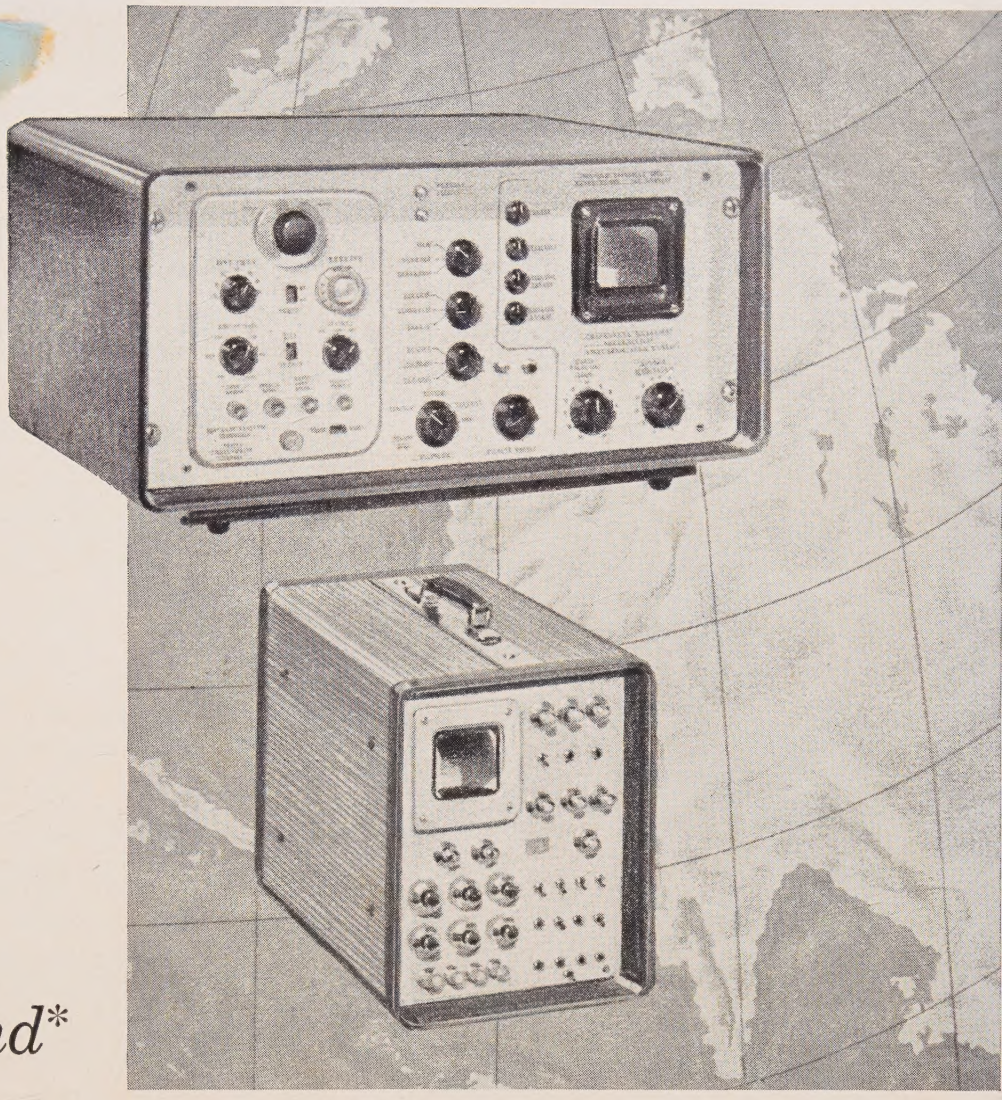

We think the reason people all over the world buy TMC pulse analyzers is pretty much the same reason they're widely purchased and used here: competently designed, bug-free circuits . . . straightforward operation with the same performance and stability today as yesterday . . . easy access to sub-assemblies and uncomplicated servicing if needed. Another way of putting it is the instruments give the user the information he wants in *his* work — with predictable behavior—regardless of where his site, lab or plant may be located. Here are two current examples:

The TMC CN-110 256 channel analyzer offers 7 interchangeable plug-in logics, including pulse height, time of flight, pulsed neutron, multiscaler, mass spectrometer, and coincidence pair. This widely used and thoroughly proven analyzer (over 100 units have been delivered) employs all-transistorized circuitry. Analog, binary, octal and decimal readout may be used. Data can be recorded on strip chart or X-Y recorders, printed paper tape, punched paper tape, or punched cards.

The Model 404 is a compact, 400-channel analyzer you can use anywhere there's a wall outlet and one square foot to put it down. It has a magnetic core memory that can be used in sub groups of two or four; four separate inputs and associated amplifiers; internal pulse routing circuity; pushbutton data transfer and display overlap; power requirement of *only 25 watts*, and many "system" advantages. While its versatility is a little less than the CN-110's, so are its size, price and purpose quite different from the 110's. Each does its *own* job well.

**Also wherever TMC Pulse Analyzers are used... in Canada, Brazil, Australia, Japan, Yugoslavia, France, Italy, Germany, Belgium, Sweden, Denmark, Switzerland, Israel, Formosa . . . as well as the United States.*

WRITE FOR LITERATURE.

TMC **TECHNICAL MEASUREMENT CORPORATION**

441 WASHINGTON AVE., NORTH HAVEN, CONN. • CE 9-2501

AEI INSTRUMENTATION INFORMATION SERVICE

# Transistorized....
# 4-5 litre ionization chamber
# AEI GAMMA MONITORS

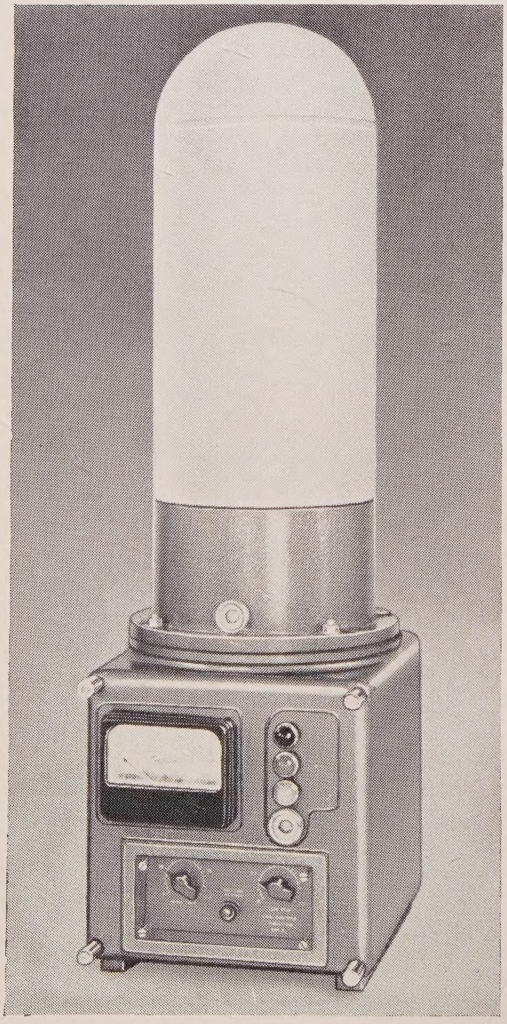

Designed for area radiation monitoring, the type GM2 logarithmic gamma monitor has a 5-decade scale with a maximum sensitivity of 100$\mu$ R/hr. The large and sensitive ionization chamber is filed with argon/air to ensure optimum flatness of gamma energy responce. Circuitry is transistorized apart from the electrometer input stage which is used as a cathode follower feeding directly into a negative feedback amplifier to obtain maximum stability. An instrument failure alarm is incorporated and over-rides the trips to prevent spurious radiation alarms. Also available as a linear monitor type GM1.

*Full details of types GM1 and GM2 monitors are given in Publication 2454-1 available from*
**AEI Instrumentation Division,**
**Process Control Department,**
**P.O. Box One, Harlow, Essex, England.**

◀ GM2 logarithmic gamma monitor with ion chamber mounted on the splash proof case ; it can also be mounted remotely.

AEI | **Instrumentation Division**
**Associated Electrical Industries Limited**

SC/136

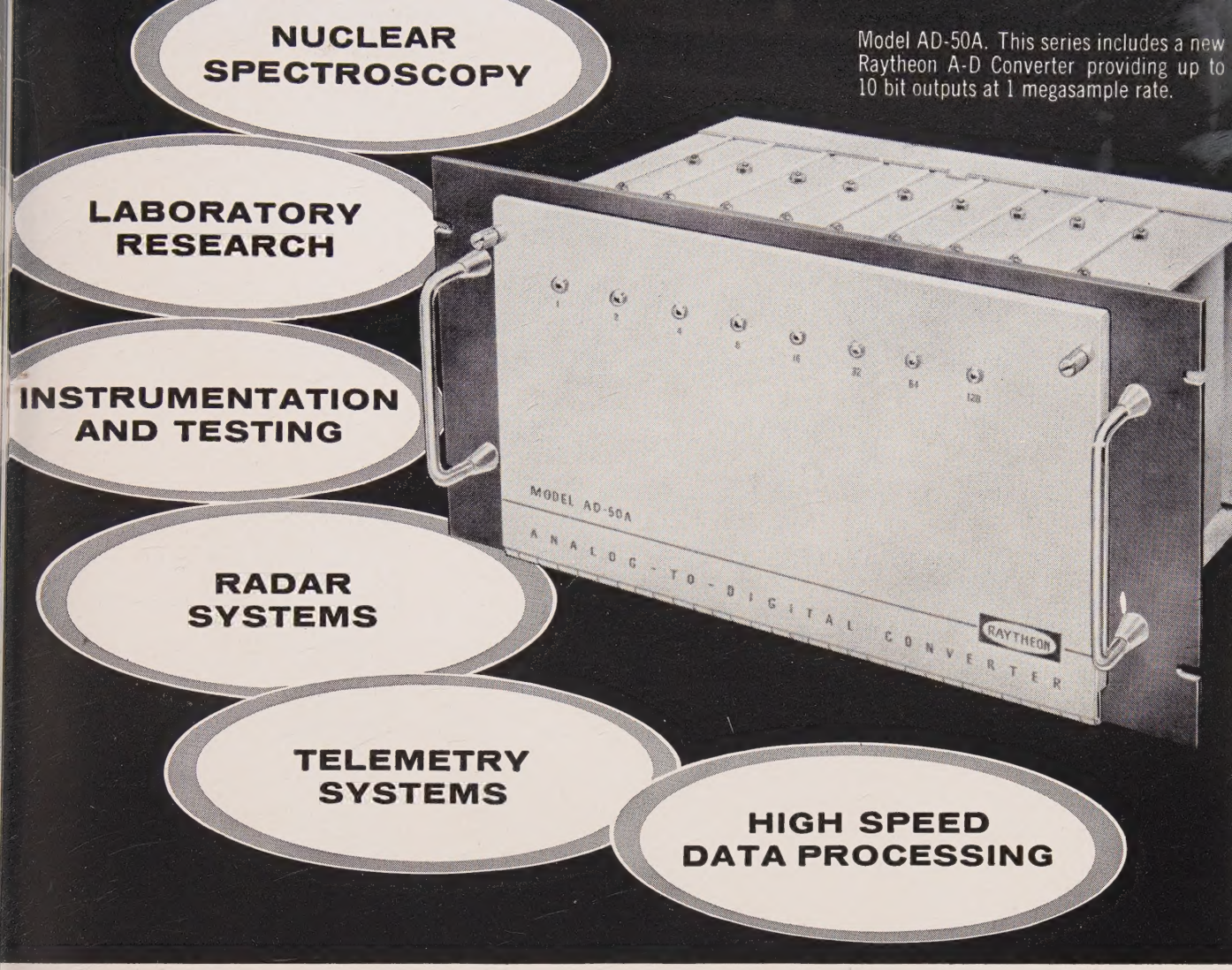
NUCLEAR SPECTROSCOPY
LABORATORY RESEARCH
INSTRUMENTATION AND TESTING
RADAR SYSTEMS
TELEMETRY SYSTEMS
HIGH SPEED DATA PROCESSING
Model AD-50A. This series includes a new Raytheon A-D Converter providing up to 10 bit outputs at 1 megasample rate.
MODEL AD-50A
ANALOG-TO-DIGITAL CONVERTER
RAYTHEON

# RAYTHEON'S NEW A-D CONVERTER: UP TO 5.0 x 10⁶ INDEPENDENT 8 BIT WORDS PER SECOND!

Faster than any other available, Raytheon Analog-Digital Converter's 25-nanosecond aperture time allows digitizing of pulses less than ½-microsecond in width. With multiplexed input, its applications encompass any product or process requiring digitized analog voltages in continuous or intermittent form.

About the size of an office typewriter, Model AD-50A is readily integrated with established systems: its flexible design allows acceptance of variable input as well as wide variations in output format and logic. Its almost unlimited systems applications offer industry, government and the military a basic, solid state tool that revolutionizes present state of the art.

All of its outputs are usable, every readout is valid, a can be operating in your system in less than 90 days

**MAIL COUPON TODAY FOR BROCHURE**

Raytheon Company, Dept. 31, Lexington 73, Massachusetts
Attention: M. B. Curran

Please mail me Specifications on:

☐ Model AD-50A 8 Bit Converter
☐ New 10 Bit, 1 megasample Converter

I'm interested in possible applications to the following type system(

_____

_____

_____

_____

*Name & Title* _____

*Company* _____

*Address* _____

*City & State* _____

RAYTHEON

RAYTHEON COMPANY

# Bendix TIME-OF-FLIGHT MASS SPECTROMETER

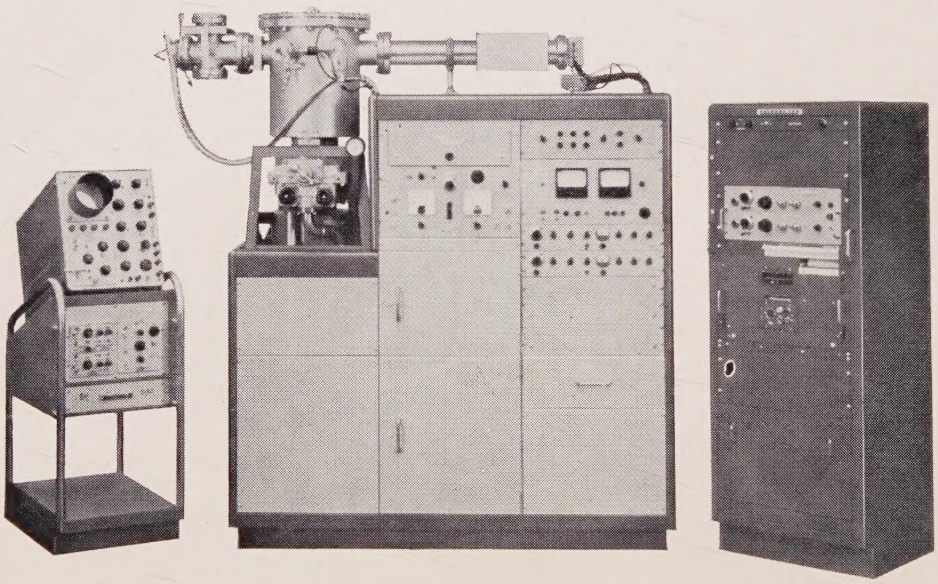

BENDIX MODEL 14-101 MASS SPECTROMETER SHOWN WITH AN OSCILLOSCOPE AND AN ANALOG RECORDER

The Bendix* Time-of-Flight Mass Spectrometer combines high speed and sensitivity with extreme versatility. 10,000 complete mass spectra are presented each second covering a mass range of m/e 1 to m/e 5000 with unit resolution to mass 200. The instrument exhibits the unique ability to handle a wide range of samples from the usual low boiling gases and liquids to solids with vapor pressure as low as $10^{-9}$ atmospheres at 2500°K. The versatility of the mass spectrometer coupled with a wide variety of Bendix engineered sample inlet systems make it particularly suited to such application as Monitoring chromatograph output, determinations of vapor pressures, heats of vaporization, free radical studies, solids' analyses, shock tube research, appearance potential measurements, photoionization, molecular structure studies, photochemical reaction studies, combustion analyses and plasma jet analyses.

*Registered Trademark

SPECIAL Bendix International FEATURES

• 10,000 complete mass spectra per second • Parts per million sensitivity • Wide mass range—1-5000 • High resolution • Multi-Channel recording • Modular plug-in electronics • Wide sample range • Analyzes liquids, solids, gases • Open source and detector geometry • Wiley electron multiplier • Stainless steel vacuum system • Getter-type pump (Optional) • Wide variety of sample inlet systems • No volume restricting magnets • Low noise level multiplier • Oscilloscope readout • Line of sight inlets • Variable electron energy

*Technical Sales and Service Representatives located in most major countries.*

Bendix International DIVISION THE Bendix CORPORATION

205 E. 42ND ST., NEW YORK 17, N.Y., U.S.A. CABLE ADDRESS: "BENDIXINT", N.Y.

*This new Tracerlab Gas Flow Counter with the Mono-Mol window (less than 125 micrograms/cm²) is the result of 15 years of continuous research and development in the field of nuclear instrumentation.*

*Only Tracerlab, the world's oldest and largest international supplier of nuclear instruments, can claim experience like this behind each of its products.*

Tracerlab

The new FD-1 and FD-2 Mono-Mol window gas flow counters function perfectly as Geiger counters and as proportional counters. ■ They display unsurpassed plateau-characteristics and highest efficiencies, even for the weakest emitters. ■ Their windows are so thin that they will replace windowless flow counters for most applications. ■ As proportional counters, they will function perfectly with pure methane, even with natural gas. ■ For a brochure with more complete information, contact the Tracerlab distributor in your country, or write to one of the addresses below.

**TRACERLAB, INC.**, 1601 Trapelo Rd., Waltham 54, Mass., U.S.A. ...or **TRACERLAB, S.A.**, Luchthaven Antwerpen, Antwerp, Belgium

# -how to sell your nuclear products internationally-

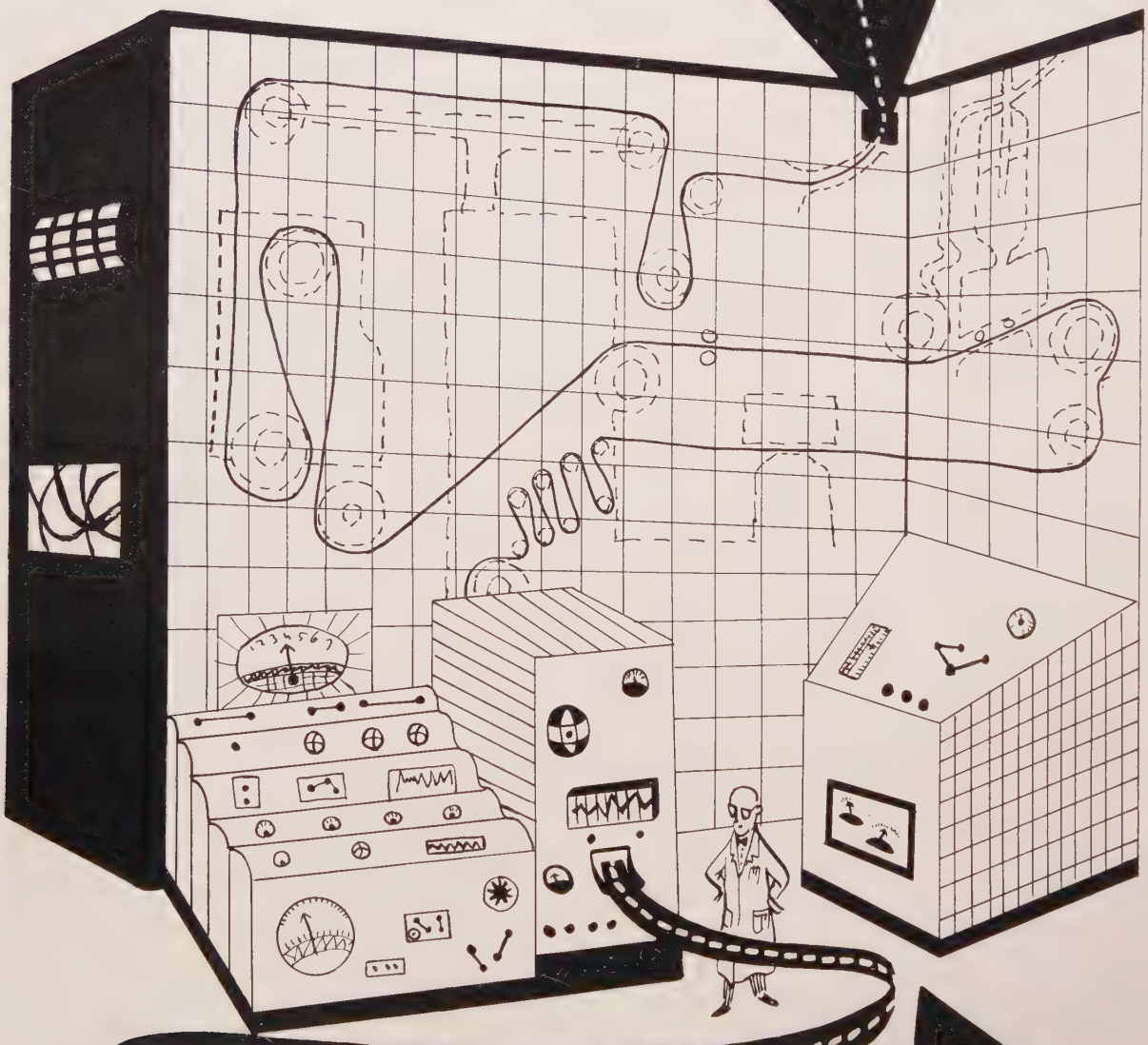

# -advertise in nuclear instruments & methods

Go International with your Sales Program today-Write

**William F. Baars-Advertising Manager, North-Holland Publishing Company**

**P.O. Box 103, Amsterdam, The Netherlands**

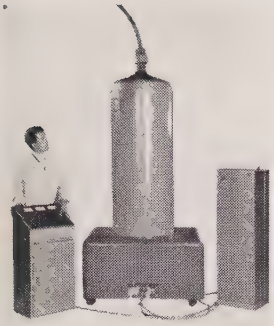

600 kV Generator

**Research Centres and Industry alike find the modern, polished solution to the problem of continued high voltage in the**

# SAMES ELECTROSTATIC GENERATOR

Electrostatic Painting with the STATRON

## HIGH VOLTAGE GENERATORS

* 50 kV to 600 kV
* 20 W to 3 kW
* Positive or negative polarity
* Medium or high stability for
* Electrostatic precipitation
* Electrical testing
* Electronic optics
* X-rays
* Nuclear Physis, etc.

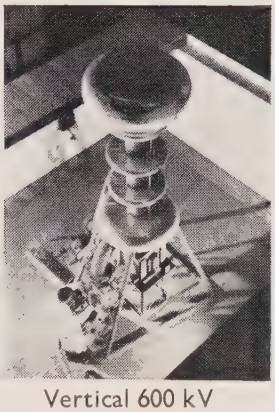

Vertical 600 kV
Accelerator at the Centre d'Etudes Nucléaires de Grenoble

## ELECTROSTATIC PAINTING

The STATRON is a portable equipment for electrostatic painting, featuring

* 90 kV voltage
* Complete safety, owing to use of electrostatic generator.
* Paint output: 15 litres/hour
* Supply: 110 or 220 V, single phase.
* Consumption: 110 Watts

## PARTICLE ACCELERATORS

| Type | Acceleration Voltage | Particles Accelerated | Application |
|---|---|---|---|
| J | 150 kV | ions | Neutron Generator by D/T or D/D reaction |
| L | 300 kV | ions | |
| S | 600 kV | ions or electrons | All applications |

SAMES

## SOCIETE ANONYME DE MACHINES ELECTROSTATIQUES

**21, RUE JEAN MACÉ, P.O. BOX 150, TEL: 44.77.64 GRENOBLE, FRANCE**

## REPRESENTATIVES

### GENERATORS AND ACCELERATORS

Austria: AUSTRONIK, Salzburg – Belgium: CENTRONICS, Brussels – Chinese People's Republic: Cie OLIVIER, Paris – Denmark: DANSK SCIENTA, Copenhagen – Great Britain: MILES HIVOLT LTD., Shoreham by Sea – Italy: SECI, Milan – Netherlands: PROJECTO, Amsterdam – Norway: LEHMKUHL, Oslo – Portugal: A.G.M.E., Lisbon – Spain: CRESA, Barcelona – Sweden: SCIENTA SCANDIA, Gothenburg – Switzerland: OMNIRAY, Zurich – Western Germany: DR. NAMUR, Darmstadt – Bulgaria, Czechoslovakia, Eastern Germany, Hungary, Poland, Rumania, U.S.S.R.: CIFAL, Paris.

### ELECTROSTATIC PAINTING EQUIPMENT

Algeria: FAMPA, Algiers – Austria: PETER PETERSEN, Vienna – Belgium: DURMECO, Brussels – Chinese People's Republic: Cie OLIVIER, Paris – Denmark: DANKS SCIENTA, Copenhagen – Eire: HODGES & SONS, Dublin – Great Britain: AEROSTYLE LDT., London – Italy: TRASMETAL, Milan – Netherlands: STUURMAN, Wormerveer – Norway: LEHMKUHL, Oslo – Portugal, RAMADA, Ovar – Spain: INSTITUTO ELECTROQUIMICO, Barcelona – Sweden: SCIENTA SCANDIA, Gothenburg – Switzerland: REGSA, Lausanne – Western Germany: A. WIRTH, Reutlingen – Bulgaria, Czechoslovakia, Eastern Germany, Hungary, Poland, Rumania, U.S.S.R.: CIFAL, Paris.

# "Charged Particles"

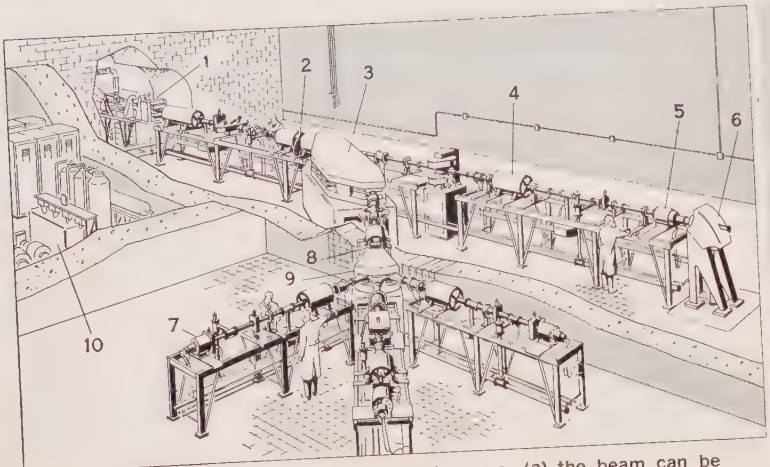


Typical high power electron beam analyzing and deflecting system for 10 to 80-Mev, 30 kw linac

1. Linac
2. Positron Target
3. Deflecting Magnet System and Energy-Defining Slits
4. Focusing Lens
5. Neutron Target
6. Terminating Magnet
7. Targets (3)
8. Monoenergetic Gamma Target
9. Switching Magnet
10. Equipment Room

The main features of this analyzing system are: (a) the beam can be delivered to any of three different experimental areas, focused to a small spot or spread out over a large area to facilitate target cooling; (b) net energy dispersion of the beam after deflection is negligible. This means that maximum beam of the desired energy is available because particles of varying energies move along the same center line into target regions; (c) in the deflecting magnet system there is a large energy dispersion at a collimator, which selects the required energy spectrum with a precision of 0.1 per cent or better; (d) the part of the electron beam discarded at this collimator or elsewhere in the system produces x-rays, the major portion of which are directed away from experimental areas; (e) the system can be converted to handle positrons produced in a shower target close to the entrance of the deflecting magnet system.

## High Power Linacs

In a recent discussion of *High Energy Linacs,* we indicated that the power of the new accelerators, plus better energy resolution opens up intriguing possibilities for the experimental physicist. One of these possibilities involves production of a monoenergetic gamma-ray beam, with adjustable energy, heretofore just a dream.

Positron annihilation in flight in a thin target produces such a gamma-ray beam. The linac electron beam is used to produce positrons in a wide energy spectrum in a shower target. These particles are energy-analyzed in a deflecting magnet before they impinge upon the annihilation target. Energy selection of the gamma rays is accomplished by varying the magnetic field of the deflecting magnet. The conversion factor is small, so it is essential to have an intense electron beam. It is not essential, however, to have a high degree of beam-energy homogeneity.

An experiment in which beam-energy homogeneity is important is the spectroscopic study of inelastically-scattered electrons from nuclei. Magnetic spectrometers for this kind of experiment can be built with a resolution of better than 0.1 per cent, and the electron beam must be analyzed to this accuracy before it impinges upon the scattering target.

## Hot Electron Beams

The high accuracy and power called for in these experiments requires considerable beam-handling ingenuity. The problems may be illustrated: A typical high-energy linac will put 45 kw of high-energy electrons on a one-half centimeter square — this equals 180 kw/cm², enough to vaporize any known material in a few seconds. To make such a system fail-safe requires precisely-protected beam slits and electron scattering devices, and specially cooled vacuum chambers, in addition to the analyzing and collimating equipment. The situation is complicated by an x-ray background which prohibits use of organic materials for coil insulation and vacuum gasketing.

The beam analyzing and deflecting system is an increasingly complex and important part of the linac experimental facility. An inadequate system will greatly reduce the accelerator's research utility. Fortunately, High Voltage Engineering has had years of experience designing and building extremely accurate, magnetic analyzing systems to guaranteed specifications.

---

**High Voltage Engineering Corporation**
Burlington, Massachusetts, U.S.A.
•
**Applied Radiation Corporation**
•
**High Voltage Engineering (Europa) N**

NUCLEAR INSTRUMENTS AND METHODS 13 (1961) 1–20; NORTH-HOLLAND PUBLISHING CO.

# THE U.S.-CANADIAN FAST CHOPPER INSTALLATION AT CHALK RIVER†

R. L. ZIMMERMAN††, H. PALEVSKY, and R. E. CHRIEN

*Brookhaven National Laboratory*

and

W. C. OLSEN†††, P. P. SINGH* and C. H. WESTCOTT

*Atomic Energy of Canada Limited, Chalk River, Ontario*

Received 2 May 1961

The physical arrangements and characteristics of the joint Brookhaven-AECL fast chopper installation at the NRU reactor in Chalk River are described. For flight paths similar to those previously used at Brookhaven the increase in intensity renders new classes of experiments feasible, while with an 88-metre flight path a resolution of 15 ns/m becomes possible for total cross section studies.

## 1. Introduction

In the past six years the bulk of the experimental data concerning the interaction of low-energy ($\lesssim$ 1 keV) neutrons and the nucleus has been obtained with fast choppers at various reactors[1–7]). The properties of the resonance levels in the compound nucleus have been derived mainly from measurements of neutron transmission as a function of energy. These measurements yield data on the spacing, $D$, of levels, the total width $\Gamma$, and the parameter $g\Gamma_n$ where $g$ is the statistical weight factor in the Breit-Wigner formula and $\Gamma_n$ is the neutron width. A good estimate of $\Gamma_n$ can be obtained in many cases with reasonable assumptions concerning the value of $g$, and, having determined $\Gamma$ and $\Gamma_n$, the radiation width may be inferred.

The major results of such fast chopper measurements are:

1) The radiation widths are rather constant from level to level in individual nuclides, and do not exhibit large variations from nuclide to neighbouring nuclide. 2) The neutron widths range over values differing by factors as large as several hundred in individual nuclides, and the average values for various nuclides also show wide variations. 3) The distribution of the spacing of levels, $D$, is nearly exponential but exhibits fewer smaller spacings than an exact exponential. 4) The experimentally determined strength function $\Gamma_n^0/D$, where $\Gamma_n^0 = \Gamma_n/\sqrt{E}$, is in good agreement with calculations based on the optical model of the nucleus, using a reasonable diffuse edge potential and known nuclear deformations, in the atomic weight region of $A = 140$–$240$. In the region of $A = 110$ the experimental results are an order of magnitude smaller than theory predicts.

It is clear that our knowledge of the properties of excited states of the nucleus near the neutron

† This work was partially supported by the U.S. Atomic Energy Commission.

†† Now at Case Institute of Technology, Cleveland, Ohio.

††† Now at the University of Alberta, Edmonton, Alberta.

* National Research Council (of Canada) Fellow.

1) F. G. P. Seidl, D. J. Hughes, H. Palevsky, J. S. Levin, W. Y. Kato and N. Sjöstrand, Phys. Rev. **95** (1954) 476.

2) L. M. Bollinger, R. E. Coté and G. E. Thomas, Proc. Sec. Int. Conf. on Peaceful Uses of Atomic Energy, Geneva 1958, P/688, Vol. 14 (United Nations, Geneva, 1958) 239.

3) R. G. Fluharty, F. B. Simpson and O. D. Simpson, Phys. Rev. **103** (1956) 1778.

4) R. C. Block, G. G. Slaughter and J. A. Harvey, Jour. Nuc. Sci. and Eng. **8** (1960) 112.

5) J. Julien, F. Netter, R. Martin, P. Rouge, R. Anditti and P. Chaffiotte, Proc. Int. Conf. on Peaceful Uses of Atomic Energy, Geneva 1958, P/1202, Vol. 14 (United Nations, Geneva, 1958) 252.

6) V. V. Vladimirsky and V. V. Sokolovsky, Proc. Sec. Int. Conf. on Peaceful Uses of Atomic Energy, Geneva 1958, P/2041, Vol. 14 (United Nations, Geneva, 1958) 283.

7) P. A. Egelstaff, Proc. on Pile Neutron Research in Physics (Vienna 1960) to be published.

binding energy (5–8 MeV) has been greatly increased by these transmission measurements. There remain, however, further details of the character of these excited states that are needed for a better understanding of the structure of the nucleus.

Two obvious experimental programs are:

1) The measurement of the spin $J = I \pm \frac{1}{2}$ for the s-wave resonances, (nearly all the observed levels at low energies are formed by neutrons having zero orbital momentum).

2) The measurement of details of the radiation process, for it is known that the total radiation width as determined from transmission measurements is 2–3 orders of magnitude smaller than theory would predict.

If measurements of the above nature could be carried out for the levels already investigated in transmission, a wealth of data would be available for investigating the spin dependence of level densities, fission widths and radiation widths.

The major experimental problem associated with the above classes of experiments is insufficient counting rate. For example, a preliminary experiment[8]) undertaken at Brookhaven to investigate the feasibility of determining the spin of levels in $W^{184}$ from the presence or absence of a ground state $\gamma$-ray transition[9]) had counting rates in the resonances of a few counts/h. Furthermore, the necessary equipment to perform such a partial cross section measurement is far more sophisticated than that used for transmission experiments. Since the time needed at Brookhaven for measurements of required statistical accuracy is in the order of 150 hours or one week, the problem of maintaining stable operating conditions during the period of the experiment becomes formidable.

It was at this point that, on the initiative of the late Dr. D. J. Hughes, a cooperative program was arranged with Atomic Energy of Canada Limited at Chalk River. When the NRU reactor reached high power early in 1959, a neutron flux some 50 times greater than that at Brookhaven became available. The same $W^{184}$ experiments were re peated early in 1959 at Chalk River and, in a fe hours, data superior to the results of a week running at Brookhaven were obtained[10]).

This paper is a report of the experimental fa chopper facility located at the NRU reactor a Chalk River. The installation and operation of thi apparatus is a joint undertaking of the Neutro Physics Group at Brookhaven and the Reacto Physics Group at Chalk River. Brookhaven sup plied the chopper and time-analyser and most o the related specialized equipment, while Chal River provided the collimator and other equipmen associated with the reactor, as well as a long fligh path and all local services.

## 2. Location of Chopper and Details of Collimatio

In the design of the NRU reactor, whose core i approximately a cylinder with axis vertical, 3.05 r high and 3.05 m in diameter, provision had bee

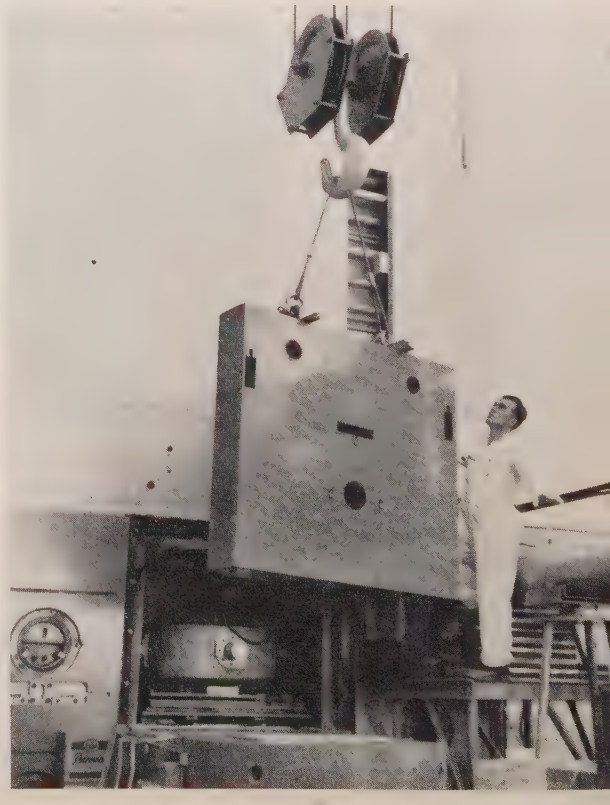

Fig. 1.
The chopper in position at the south face of NRU. The shieldin door is being fitted into position with the overhead cran

[8]) J. D. Fox, R. L. Zimmerman, D. J. Hughes, H. Palevsky, M. K. Brussel and R. E. Chrien, Phys. Rev. **110** (1958) 1472.

[9]) H. H. Landon and E. R. Rae, Phys. Rev. **107** (1957) 1333.

[10]) D. J. Hughes, M. K. Brussel, J. D. Fox and R. L. Zimmerman, Phys. Rev. Lett. **2** (1959) 505.

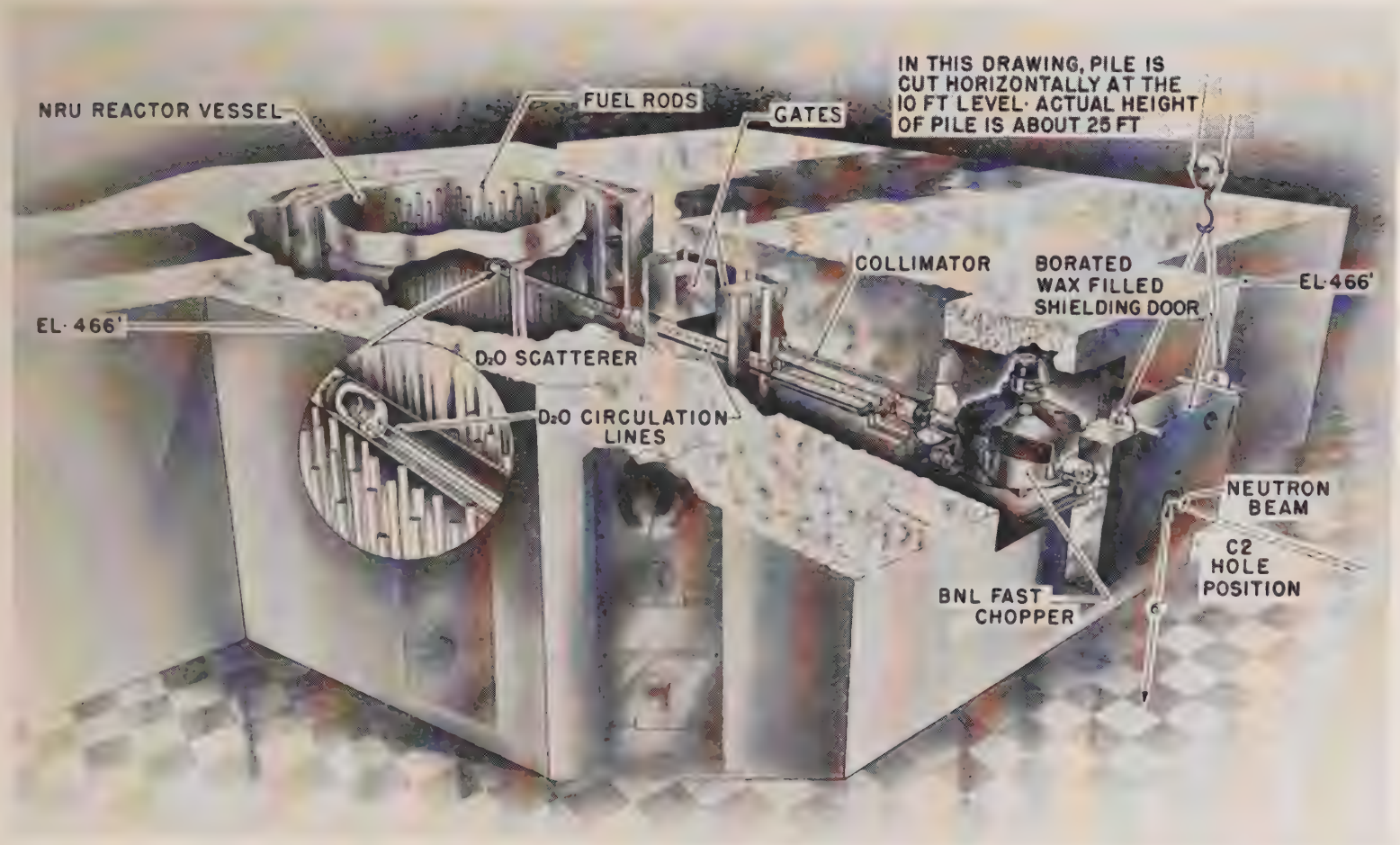


Fig. 2. The general arrangement of the fast chopper installation at NRU, showing the $D_2O$ scatterer.

made for two horizontal through-tubes passing within 76 cm of the axis of the reactor, respectively 46 cm above and below the median plane. The cross section of these tubes is rather small (elliptical with major axis vertical, internal dimensions about 10.8 cm × 7.5 cm), but the neutron flux at their centre is ≈ 80% of the maximum anywhere in the reactor, so that within a narrow angle a very high intensity is available. The upper of these tubes, C.2., was used for the fast chopper installation. In order to scatter the neutrons along the tube a short section of scatterer was necessary, and for this purpose an aluminum can filled with $D_2O$ was used. A collimator located within the reactor shielding yielded two parallel beams of neutrons 2.54 cm apart having half-angles of divergence of $\frac{1}{75}$ radian in the vertical and $\frac{1}{175}$ radian in the horizontal plane, and the scatterer formed a "source" having a thermal flux of some $1.6 \times 10^{14}$ n·cm$^{-2}$·sec$^{-1}$. Its area was sufficient to "fill" the beams completely except that at the extreme angular limits a few neutrons came from the walls of the through-tubes. In order to accommodate the through-tubes, the normal lattice pitch had been increased slightly at the position of the tubes by a slight additional separation transverse to them. This made it relatively easy to satisfy the conditions that essentially none of the vertical natural-uranium fuel rods was seen by the beam and that only scattered $\gamma$-rays could reach the detector. Thus a high flux of thermal neutrons, accompanied by a $1/E$ spectrum of epithermal neutrons, was available under conditions which were favourable in respect of $\gamma$-ray background in the beam.

The beam emerging from the south end of the through-tube was chosen, because at this end of the hole a cubical piece (side 1.2 m) of the reactor shielding was removable. The external flight-path is at places some 7 m above terrain and passes near some buried tanks containing active waste, but these disadvantages could be accepted. It was possible to make some slight modifications to the Brookhaven chopper to enable it to be fitted within the cubical space. A shielding door outside the reactor face was provided which, with some other inserted material, gave adequate overall shielding. The door, 30 cm thick, is of 1.27 cm steel plate construction, filled with a $H_3BO_3$-parawa mixture. The location of the chopper itself provide shielding for neutrons scattered at the choppin point. With the NRU reactor operating at a powe level of 200 megawatts, the following radiation fi ures are obtained at the outer surface of th shielding door: $\gamma$-rays, 80 to 120 mr/h; slo neutrons, 1.5 to 2.0 mrem/h, and fast neutrons, to 35 mrem/h. The levels at the joint between th door and the reactor shield can be significantl higher, especially for fast neutrons (up to 15 mrem/h).

The assembly of the chopper and its positionin plates is mounted on rails, and can easily be rolle into or out of the cavity when necessary. Fig. shows the chopper assembly in its operating positio while fig. 2 shows the general arrangement. Th collimator itself, located between the main gate the experimental hole and the chopper, is 91 c long and extends inwards from the inner face of th 1.2 m cubical space. At this face the two beam (2.54 cm apart) are each 0.424 cm × 3.472 cm i size. The distance between the centre of th through-tube and the chopping point is 455 cm Fig. 3 is a schematic drawing of the collimato which, for most of its length, is filled with a lea loaded borated resin mixture (77.2% PbO, 17.7 resin, 5–6% $B_2O_3$ by weight), into which slits ca be readily cast; over part of the length this is l cated within a wooden cylinder of 8.89 cm I.D the whole being within a steel tube. At the reacto end is a 6.35 cm long lead cylinder beyond which 7.6 cm long graphite cylinder is bolted to the end the collimator, to protect the resin from ove heating by scattering away most of the neutron which otherwise would impinge directly on the res material. Accurate positioning of the collimator the hole is effected by rails in the hole and groov in the collimator. The rails also permit easy remov or installation of the collimator.

At the outermost end of the collimator, mounte eccentrically, is a 13.2 cm diameter hollow mi steel cylinder which forms a second "gate", a ditional to the main gate built permanently in the reactor shield. This cylinder, of 0.635 cm thic steel walls, is filled with lead except for a 4.47 c square resin section through which the slits a

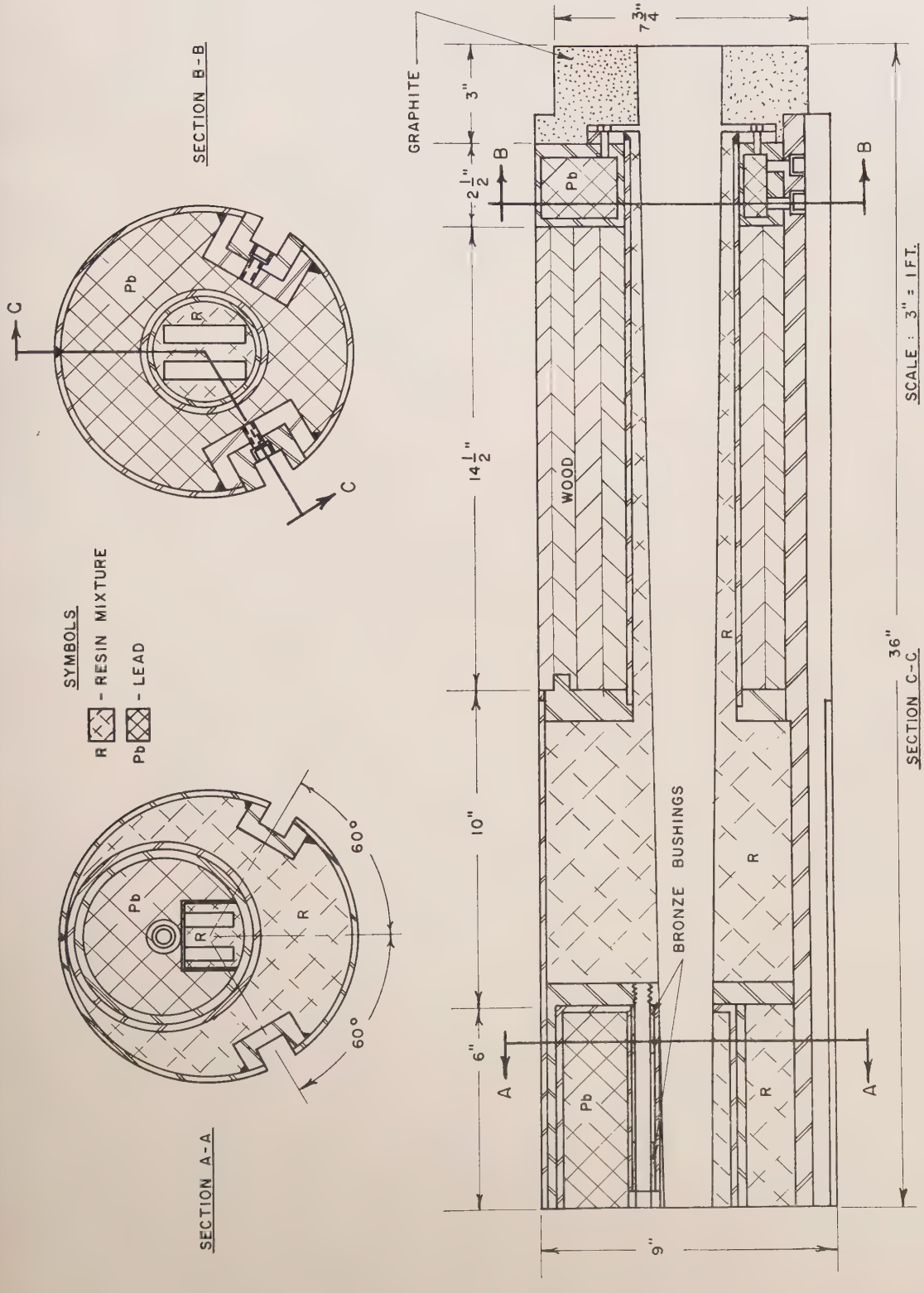


Fig. 3. The collimator for the chopper beam. This collimator is located just in front of the chopper entrance stator.

cast; when the cylinder is rotated about its own axis the slits in the collimator are closed and 15 cm of lead inserted.

### 3. The Scatterer and its Cooling Arrangements

The scatterer required at the centre of the through-tube could in principle be of any material having a low neutron absorption but since graphite might change shape in the high neutron flux, only beryllium and heavy water were considered. Natural water would have been undesirable in that its sudden accidental expulsion would have given rise to a positive reactivity transient, but perhaps more important was a desire to exclude $H_2O$ from a region where normally only $D_2O$ was present. Heavy water canned in Al was therefore chosen because of fabrication and cooling difficulties with beryllium. With a $D_2O$ volume of about 750 ml the heat produced in the scatterer and associated canning is about 2 kW (mainly $\gamma$-ray heating) at full reactor power; forced-circulation cooling with an external $D_2O$–$H_2O$ heat exchanger was therefore adopted, the $D_2O$ being pressurized to 20.7 p.s.i.a. It was found that an empty Al can left uncooled would attain 275°C with the reactor at full power, so that should be $D_2O$ coolant be accidentally expelled, the can could not be refilled while the reactor was at power; fortunately such occasions have been rare. Automatic controls were provided to "dump" the heavy water into a "catch tank" in the event of either high temperature ($> 93.3$°C) or excessive pressure ($> 30$ p.s.i.a.) in the loop. High and low pressure alarms (25 and 15 p.s.i.a. respectively) and a low-flow rate alarm are also provided with a temperature alarm at 82°C.

A centrifugal canned pump produces a $D_2O$ flow rate of about 2.5 litres/min. An ion exchange purifier carries some 5% of the main $D_2O$ flow-rate; this tends to reduce radiolysis of the $D_2O$. The heat exchanger consists of two concentric pipes 180 cm in length, with the $D_2O$ flowing in the inner (0.635 cm nominal) tube. The $D_2O$ is enclosed under a helium atmosphere, and the pipes to and from the scatterer pass along the through-tube of the reactor and through the lower part of the collimator. The tube by which the $D_2O$ leaves the scatterer is bent upwards to touch the inside of the top of the scattering can so that any gases from radiolysis or ex- pelled from solution are rapidly removed from the can (see inset in fig. 2). The ends of the can are made spheroidal for maximum strength combined with minimum Al in the beam (wall thickness 0.9 mm over this surface).

### 4. Fast Neutron Chopper

Basically, the fast neutron chopper is similar to the one which has been in continuous use at Brookhaven National Laboratory[1]). An aluminum rotor 76 cm in diameter, which contains the neutron defining slits, spins on a vertical axis at speeds up to a maximum of 10000 rpm. The spinning rotor is housed in a vacuum chamber so that the power required to maintain this speed is only about 320 watts. The rotor is supported and driven by a flexible steel shaft extending vertically through a vacuum seal to a direct-current motor; the shaft stiffness is such that the rotor is self-balancing and non-resonant at all operating speeds.

The rotor is fabricated from two shallow conical aluminum forgings held together with steel through-bolts. The system of neutron defining slits made of cloth-reinforced phenolic resin is held between the forgings by the pressure of these through-bolts and by intermeshing grooves in the aluminum and the phenolic pieces. A cruder slit system of steel is placed inside a 7.6 cm radius to stop fast neutrons and $\gamma$-rays which penetrate the phenolic plastic[11]).

The slit system in the rotor is so arranged that the neutron beam is open eight times per revolution. In a single open position of the rotor, two beams each defined by an entrance stator slit $0.0115 \pm 0.0005$ by 1.00 inches high pass through the slightly divergent slits in the rotor. The paths through the rotor are displaced laterally so that it is impossible for neutrons to pass through this same pair of slits one-half revolution later.

The divergence of the pair of beams is also determined by the entrance stator slits. The duration of the neutron burst at a given rotor speed is determined by the width of the stationary slits plus the width of the rotor slits. Each dimension is

[11]) F. G. P. Seidl, H. Palevsky, D. J. Hughes and R. L. Zimmerman, Nucl. Instr. **1** (1957) 92.

0.0115 ± 0.0005 in., giving a neutron burst duration of about one microsecond at 10000 rpm.

To establish an accurate time reference a light beam is allowed to pass through one of the rotor slits to a phototube near the exit port. At Brookhaven this light beam was made to pass through a slit simultaneously with the neutrons using an optical system of mirrors, lenses, and vacuum windows. At Chalk River, such a system is impractical because the radiation level would cause a blackening of the quartz windows. Consequently, in the Chalk River chopper the light was made to pass through the slit system at 90° from the one transmitting the burst of neutrons. The accuracy of machining of the rotor was sufficient that negligible loss in timing accuracy results from this modification. The optical elements show no signs of radiation damage after two years of operation.

The speed of the chopper is changed and controlled by conventional means. The armature of the direct current drive motor is fed by a bank of silicon rectifiers, and an electronic supply provides the field excitation. For deceleration, resistors are connected across the armature. The speed is measured and controlled by integrating the pulses from a magnetic pick-up coil close to an appropriately shaped iron nut on the motor shaft. A difference amplifier compares the output of the integrator with the voltage across a calibrated helipot. The resulting correction signal controls a motor-driven Variac feeding the rectifiers which provide the armature voltage. The speed is held constant to about 0.1%.

Although the chopper as installed at Brookhaven had relatively little space limitation the overall design worked well at Chalk River where there were severe space limitations. The cubical cavity in the NRU reactor shielding fortunately was able to receive the complete chopper assembly after the size of the vacuum system and the drive motor assembly had been reduced. Except for this and the modifications to the light pulse system, no essential change was made; the rotor was, in fact, one which had on occasion been used interchangeably in the Brookhaven installation.

Minor maintenance operations requiring no more than a few minutes can be done with the chopper in position and without requiring experimenters on adjacent reactor ports to interrupt their experiments. The general inaccessibility and the high radiation fields within the cavity made it necessary to operate the chopper somewhat differently from what is ususal at Brookhaven. Since the chopper cannot easily be visually inspected, remote instrumentation is provided to check operating conditions, and thereby increase reliability. For example, a thermocouple gives the temperature of the main bearing in the direct current motor which bears the weight of the rotor. A vibration-sensitive device is fastened to the motor to detect troubles arising from deterioration of the bearings. Both of these devices, as well as others sensitive to the rotor speed, vacuum, motor torque, and armature current are all connected to an inter-locking system to prevent damage to the chopper during the long periods between visual inspections.

When major maintenance is required two adjacent experimental beam ports must be closed. The shielding door is removed from the cavity and the chopper, which is mounted on its own wheels, is rolled out on tracks provided for the purpose and then removed by the overhead crane to a separate carriage on them in a floor of the reactor building.The time required for the chopper removal and the replacement of the shielding door is less than two hours.

When the chopper is replaced after servicing, some realignment is necessary. Motor driven positioning screws provide horizontal translation transverse to the beam, as well as rotation of the chopper about a vertical axis through the chopping point. This alignment can be accomplished in a few minutes by maximizing the total counting rate in the $BF_3$ counter bank at 88 metres. The vertical alignment, being relatively non-critical, was set visually when the apparatus was first installed and does not need readjustment.

### 5. Detectors

For transmission measurements using a flight path of 18 m or less (inside the reactor building), $BF_3$ counters of conventional type and $ZnS$-$B_2O_3$ scintillation detectors[12]) have been used. For partial

[12]) H. R. Muether, H. Palevsky and R. L. Zimmerman, Bull. Am. Phys. Soc. Ser II, 2, No. 4 (1957) 217.

cross section measurements appropriate detectors must be placed outside the beam and the target placed in the beam near the detector. For a study of neutron-capture $\gamma$-rays such a detector consisting of six 7.6 cm × 7.6 cm NaI scintillation detectors has been constructed and used at 15.6 metres. Further details of this system will be included in a future publication describing the results of this investigation. For neutron scattering investigations, an annular assembly of $BF_3$ counters has been constructed and will also be described in a later publication.

For the transmission measurements using an 88-m flight path a neutron detector is required which is fast enough to preserve the inherent time resolution of the chopper, discriminates against the $\gamma$-rays in the beam and is as efficient as possible.

A bank of $BF_3$ detectors of the type in use at the chopper at Brookhaven was built for the long flight path at Chalk River. This bank is 36 × 102 cm in area and 18 cm deep and is made from 384 separate proportional counter tubes all operating in parallel in a common atmosphere of $BF_3$ gas enriched to 96% $B^{10}$. The outer tubes are mild steel (2.22 cm internal diameter) selected for low natural radioactivity, the centre wire is 0.015 cm tungsten and, with a pressure of 120 cm Hg of $BF_3$, the counters operate at about 6200 volts. The size of the beam passed by the chopper, including penumbra, is approximately 1 × 2.5 m at 88 m (see fig. 7). To obtain a higher counting rate, additional banks of $BF_3$ proportional counters are under construction.

The efficiency of the present detector is about 2% for 1000 eV neutrons. Operating with the highest possible resolution, the counting rate at 88 metres with this detector is about 45–50 counts per hour in a one microsecond time-of-flight channel. This is approximately half the rate obtained with the same chopper at Brookhaven with the detector at only 20 metres. The background at Chalk River is about 15% of this rate, about half due to natural radioactivity within the counters; most of the rest arises from fast neutrons from other experimental ports. Leakage through the reactor shielding is normally undetectable.

**6. Flight Paths**

Within the reactor hall the beam passes through a helium atmosphere contained in a polythene balloon 45 cm in diameter, with 0.05 mm thick Mylar windows fastened on the ends by means of aluminum flanges; the balloon usually used is about 14 m long. For convenience, a second similar balloon 3.6 m long is added when the long flight path is in use, being replaced by the detector system for the measurements with a 16–17 m flight path. When this balloon section is not in use, a small shielding wall of lead 15 cm thick is placed at the end of the 14 m balloon and in front of the detector system; this wall is 45 cm wide and 10.5 m high and contains a beam-collimating hole 10 cm wide × 20 cm high. Another, larger, wall is permanently in position about 5 m from the reactor face; this serves to reduce the background levels in all detectors used from various sources of leakage neutrons. It is 2.7 m high × 3 m wide and has a slit about 20 cm × 60 cm through which the beam passes. In parts the wall consists of a 15 cm layer of a parawax-$H_3BO_3$ mixture contained between two 6 mm steel plates, and in other parts is 30 cm thick, consisting of dry $H_3BO_3$ powder between wooden walls.

The flight path continues for a distance of about 67 metres from the outside face of the reactor building, giving an overall length of 88.2 metres from the chopping point to the neutron detectors. This external portion consists of an elevated waterproof wooden tunnel, built in two sections, in which are suspended continuous (polyvinyl chloride) balloons filled with argon, through which the neutrons pass.

A 6 metre gap at present exists at a reactor service roadway but plans are in hand to insert a removable section containing an argon-filled balloon at this point. This should result in a 30% increase in counting rate. The cross section of the tunnel is rectangular, increasing in size in steps as shown from 0.6 × 1.2 metres to a final transverse section (over the last 22.8 m of length) of 1.1 m wide by 3.25 m high. The first section of the tunnel is simply supported, but the later sections (shown in fig. 4) are at places ≈ 6 m above ground level and are carried by two steel arches fabricated from

Fig. 4. Far end of the flight path enclosure. The counting hut is at the extreme left and the reactor roadway is out of view on the right.

20 cm dia. pipe mounted on reinforced concrete bases.

The balloons are of polyvinyl chloride 0.25 mm thick except at their ends, which are only about 0.1 mm thick. The longer one has a "step" in its cross section to fit the wooden tunnel. The balloons are suspended at frequent intervals from longitudinal cables within the tunnel, but care is necessary that diurnal volume changes of the contained argon do not cause the balloons to contract and obscure the beam. At Chalk River the temperature changes can be severe, perhaps as much as 40 centigrade degrees in 24 hours, and the temperature may dip as low as −40° C. While a change of volume of perhaps 10% can be tolerated, removal of excess gas is provided for and the gas is replenished by hand as necessary. Ten 9.35 $m^3$ cylinders of argon were required to fill the 44.2 m balloon, and two to fill the 13.7 m one. In the fourteen months that the long flight path has been in operation 23 cylinders of argon have been required for replenishment.

The counting hut is attached to the end of the third box in the flight path. It is 2.7 m by 2.7 m in plan and is 4.2 m high. Rectangular openings, of dimensions 1.27 m by 3.38 m, at the front and back of the hut are provided for the beam. The opening in the back wall is covered with two 3 mm thick sheets of 1S aluminum separated by 8.9 cm of air to insulate the interior of the hut from the outside atmosphere, and to provide minimum backscattering of the beam neutrons into the detector. The other opening is usually uncovered, but if necessary thin sheets of aluminum could be stretched across this window to complete the thermal insulation of the hut.

### 7. 1024-Channel Time-of-Flight Analyzer

Timing circuits and a memory device are needed to measure and store the flight times of the neutrons producing the effects under investigation. Such an analyzer should have timing channels smaller than the neutron burst duration, and a memory capacity large enough to permit efficient data collection. The analyzer already in use at Brookhaven was copied for Chalk River and satisfies these requirements, since it stores up to 10000 counts in each of 1024 channels whose width may be either $\frac{1}{4}$, $\frac{1}{2}$, 1 or 2 $\mu$sec. Delays of up to 5.6 msec duration may be introduced between the chopper burst and the first time channel to make it possible to investigate in greater detail interesting regions of the time-of-flight spectrum.

The timing is done by a 4-Mc/s oscillator which runs continuously except for a brief interval at time zero when it is stopped long enough to reset its scaler. Time zero is determined by a light beam passing through the neutron defining slits. The time of flight of the neutron is determined by the state of the 4-Mc/sec scaler when the neutron pulse (or other event) occurs. One count is then added at an appropriate address in the memory. Since neither the oscillator nor its scaler is interrupted by the neutron pulse, more than one pulse may be analyzed and stored during the interval between consecutive chopper bursts. The time required to analyze and store one count is 24 $\mu$sec, and the counting rate loss of the analyzer is calculated from this number.

An electrostatic memory consisting of 16 cathode ray tubes (RCA type 6571) stores the analyzed counts as four digit decimal (binary-coded) numbers; each tube contains 1024 channels in a 32 × 32 matrix of focused points. A common deflection system in all 16 tubes is controlled by the time of flight of the neutron as determined by the 4-Mc/sec scaler.

All the data stored in the 16 tubes are systematically read and rewritten sequentially by channels 60 times per second, the process being interrupted only for 24 $\mu$sec each time a counting event is to be analyzed and stored. This regeneration action makes up for the inherently short memory of an electrostatic system. An analogue display of the data is available during a run to monitor both the operation of the analyzer as well as the progress of the experiment. The memory may be read, without disturbing it, at the rate of 10 channels per second in binary coded decimal format on punched paper tape. A typewritten record and an automatic plot are made later with accessory machines from the punched paper tape. Either one of two codes, one suitable for the Royal McBee LGP-30 or one suitable for the Burroughs Datatron 205 Computer at Chalk River, may be punched as desired.

For the study of capture $\gamma$-rays originating from

individual resonances in the compound nucleus, it is desirable not only to determine the energy of the neutron which gives rise to the $\gamma$-rays, but also to determine the energy of the $\gamma$-rays. The pulse-height distribution from the NaI scintillation detector already described is related to the $\gamma$-ray energy, and the timing of the $\gamma$-ray pulse gives the neutron time of flight, and consequently the neutron energy. For these experiments the 1024-channel analyzer was supplemented by a pulse-height selector attachment called the "splitting circuit" which modifies the addresses of the 1024 channels so that a portion of the address is controlled by $\gamma$-ray pulse height while the remainder is controlled by the neutron time of flight as usual. In this way a $\gamma$-ray energy distribution can be measured at the same time as the time of flight analysis is performed.

In the splitting circuit the neutron time-of-flight spectrum is still determined relative to the states of the 4-Mc/s scaler. The pulse height is determined relative to the state of a scaler after an appropriate pulse-height-to-time conversion. This scaler is driven by a separate 2-Mc/s oscillator.

A considerable measure of flexibility in the selection of the number of channels allotted to time analysis and to pulse-height analysis, as well as in time and pulse-height channel widths and positions, is provided and enables the 1024 memory channels to be used in a variety of ways according to the experiment being performed. Up to 8 separate groups of time channels may be located as desired within the inter-burst period to investigate specific neutron energies. Each group must contain an equal number ($2^n$, where $n$ is an integer) of channels and any two groups must be spaced a minimum of 8 $\mu$sec apart. The width of the time channels in each group is normally the same, but provision is made so that after group 2 or group 4 the width of all following channels may be doubled.

All time groups are also pulse-height analyzed, but since the number of locations in the memory is limited to 1024, the total number of time channels and the number of pulse-height channels must multiply together to give 1024. The threshold of pulse-height analysis is continuously variable and the channel-width in pulseheight units may be varied by factors of two; a change of scale by a factor of five is also provided to allow closer examination of any desired portion of the spectrum. Pulses whose sizes exceed the predetermined maximum are counted but not time analyzed. In order to minimize dead-time effects, only pulses occurring in the selected time regions are analyzed, and those below the variable pulse-height threshold do not give rise to any dead time. A coincidence gate is included in the circuit and may be used when experiments warrant this refinement. The great flexibility that the splitting circuit gives to the 1024 channel analyzer has made possible capture $\gamma$-ray experiments not otherwise practicable with the Brookhaven 1024 channel analyzer.

### 8. Beam Intensity and Characteristics

The thermal flux at the scatterer in NRU is confirmed by calculations from chopper counting rate as near the value ($1.6 \times 10^{14}$ n·cm$^{-2}$·sec$^{-1}$) expected, the cadmium ratio of the unchopped beam being about 41 for a $1/v$ detector. The 88-metre station counting rate after background subtraction is about 1 count per minute per 1-$\mu$sec channel, which may be compared to a rate of 1 count per minute per 0.5-$\mu$sec channel obtained with the 20 metre flight path at Brookhaven.

Transverse scans of the beam have been measured at both the 16-m and the 88-m stations. Fig. 5 shows the results for 10000 rpm at 15.6 metres. Measurements have been made with both directions of spin of the rotor and, for reasons explained in the next paragraph, a lower counting rate is expected for clockwise rotation, as is in fact found. However fig. 5 shows that the two profiles have a similar form, being both roughly triangular in shape with full width of 7.9 cm at half maximum. A slight asymmetry in this profile is mainly due to the left-hand slit, as is seen from the dotted curves in the figure.

The chopper as designed (counterclockwise direction of rotation) cuts off neutrons at an energy of about 8 eV at 10000 rpm; correspondingly for a flight path of about 30 m, the slowest neutrons will fall behind one full burst-interval, so that for longer flight paths "overlap" will occur (this effect occurs at the same path-length for all chopper speeds). However, by rotating the chopper clockwise, a more

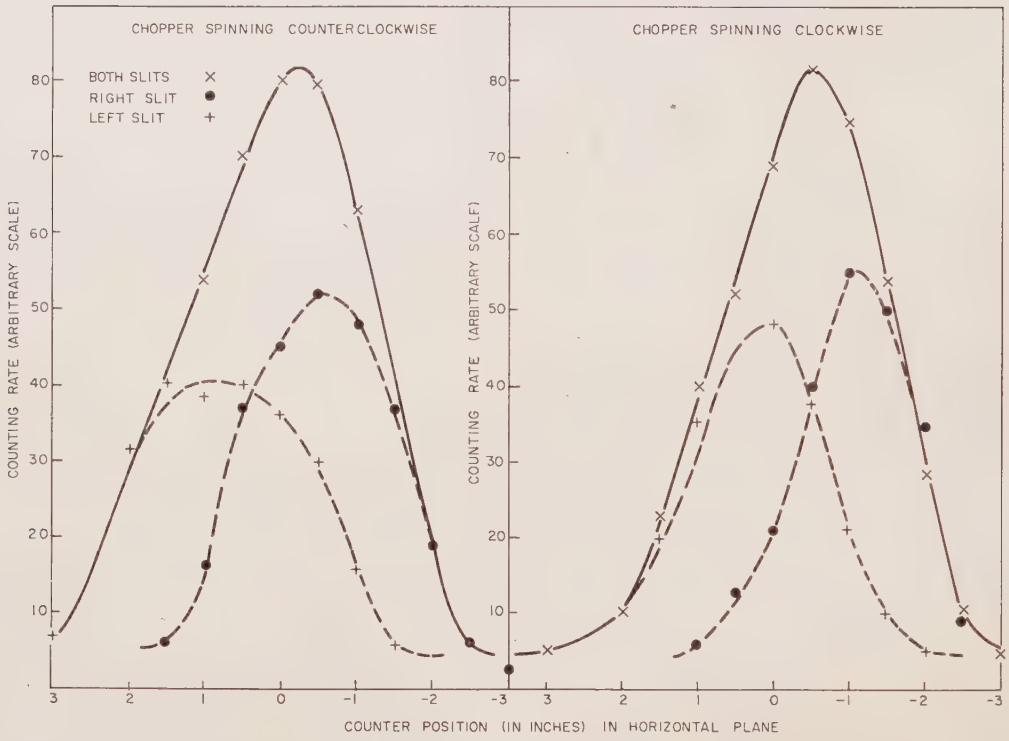


Fig. 5. Beam profiles at 15.6 metres, taken with a 2.22 cm diameter $B^{10}F_3$ counter filled to 40 cm. The rates for the two directions of rotation have been normalized to equality; actually, the clockwise rate is some 29% lower.

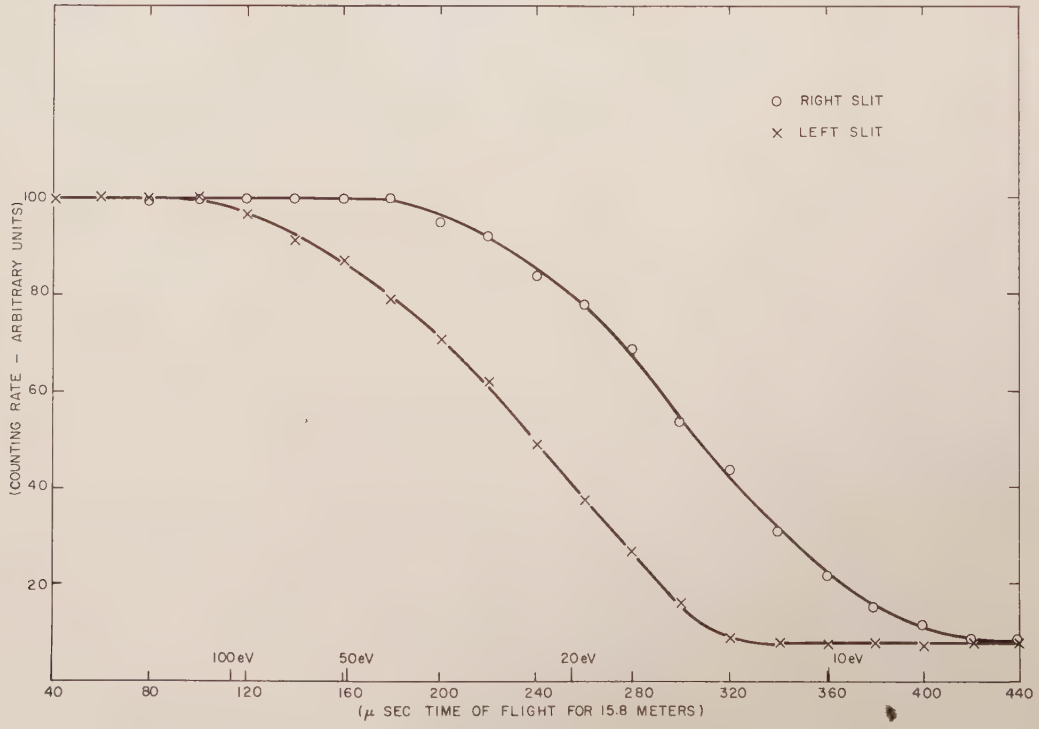


Fig. 6. The open beam counting rate curves at 15.6 metres with the chopper spinning clockwise at 9100 rpm. Different low energy cutoffs are obtained with each slit due to the rotor construction. The data were taken with a 6.35 cm $B^{10}F_3$ detector filled to 120 cm of Hg.

severe low-neutron-speed cut-off characteristic is imposed and overlap only begins at about 44 m flight path. This characteristic is used with the 88-m path and then ensures that only one overlap "frame" of neutrons occurs, or if "third-frame" neutrons occur at all they are confined to a very few channels. This effect could have been eliminated altogether by changing (with the same slit design) to a four-arm rotor, but not only are the eight arms desirable for the 16-m station work, their use for 88-m work also doubles signal-to-background ratios and for these reasons the 8-arm rotor system has been retained for all work to date. The problem of dealing with overlap will be further discussed below.

Fig. 6 shows the neutron counting rate vs. time of flight for clockwise rotation at 9100 rpm, measured at 15.8 metres for each slit separately. The cut-off characteristics of the two slits are seen to be different. This difference is expected because the rotor was designed for counterclockwise rotation, and in this design certain differences exist in the leading edges of each member of a slit pair. With clockwise rotation the leading and trailing edges of a slit become interchanged, leading to differences in cut-off characteristics.

It is clear that the left slit has the more favourable cut-off characteristic for 88 metre operation since it will help lessen the fraction of overlap neutrons. For this reason when only limited quantities of sample material are available (as in the case of many separated isotopes) the left slit only is used. The data of fig. 6 are obtained with a 6.35 cm $BF_3$ counter filled to 120 cm of $BF_3$ enriched to 96% $B^{10}$. This counter was chosen to subtend approximately the same solid angle as the counter bank at 88 metres. The counts shown occurring at a time later than the cut-off are due to a constant room background. The $\gamma$-ray flux at this 15.8 metre station, in the beam, is 4 mr/h.

At 88.2 metres the beam profile was scanned, both horizontally and vertically, as shown in fig. 7, using a scintillation detector composed of three 5 cm photomultiplier tubes with $ZnS\text{-}B_2O_3$ caps[12]). For this experiment the chopper was spun clockwise at 10000 rpm. The outline of the main $BF_3$ bank is also shown and, as is evident, it covers most of the beam in the horizontal plane but does not cover the beam completely vertically. With the installation of additional new detectors use will be made of practically all the beam.

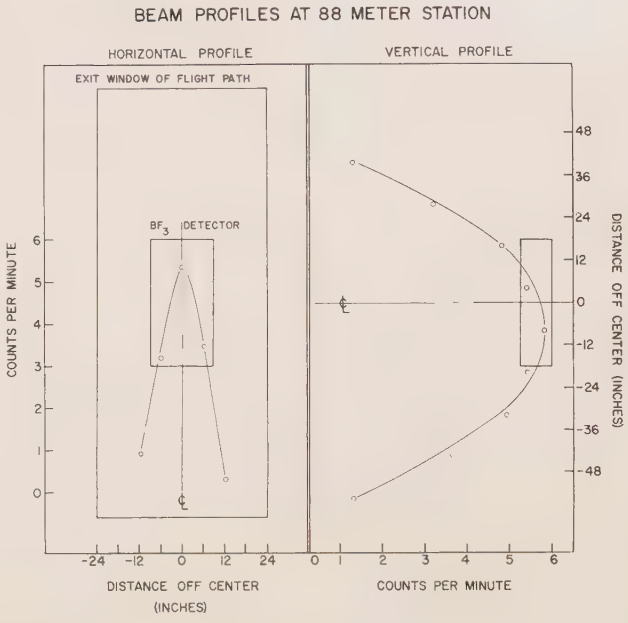
BEAM PROFILES AT 88 METER STATION
HORIZONTAL PROFILE
VERTICAL PROFILE
EXIT WINDOW OF FLIGHT PATH
BF3 DETECTOR
COUNTS PER MINUTE
DISTANCE OFF CENTER (INCHES)
-24 -12 0 12 24
DISTANCE OFF CENTER (INCHES)
0 1 2 3 4 5 6
COUNTS PER MINUTE
48 36 24 12 0 -12 -24 -36 -48

Fig. 7. Beam profiles at 88 metres taken with a 5 cm diameter $ZnS\text{-}B_2O_3$ detector. The rectangle represents the $BF_3$ detector.

At the 88-m station the nature of the counting rate curve obtained is quite complex, on account of the overlap just mentioned; the measured curve of counting rate vs. channel number (without sample) is given in fig. 8. It will be noted that the aluminum resonances at 84 and 36.2 keV are quite prominently seen in this curve, but it is not feasible to remove all the aluminum from the beam.

In addition to the overlap neutrons and the constant room background, the curve at the high energy end contains a time-dependent background. This arises from the multiple scattering of the high energy ($> 100$ keV) neutrons in the materials around the beam, such as the plywood walls of the flight path. These scattered neutrons arrive at the detector at a time which is not uniquely related to their initial energy. This component is called "spurious" background to distinguish it from the room background.

Various components of the neutron spectrum are experimentally determined in the following way.

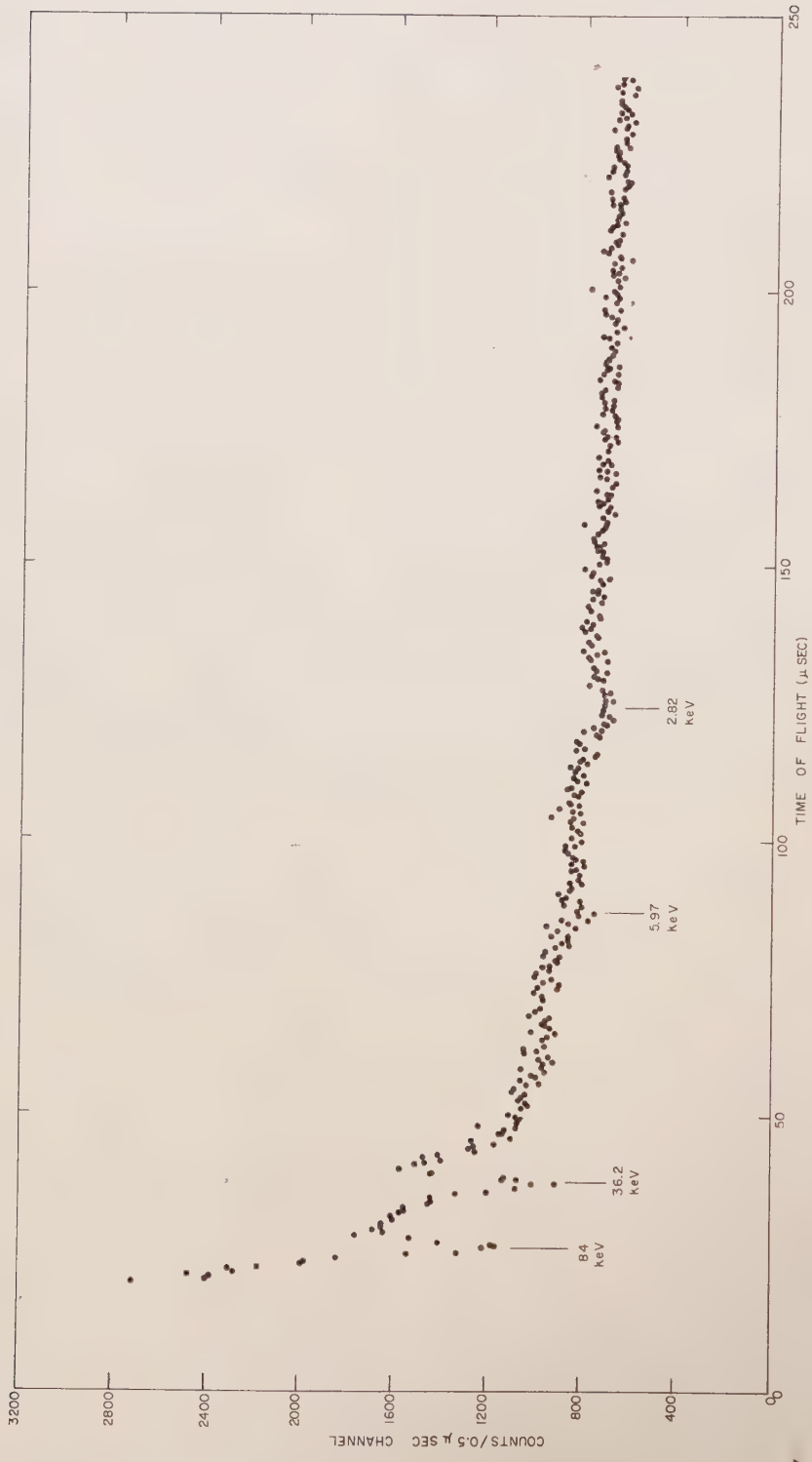


Fig. 8. A portion of the open beam counting rate curve at 88 metres from 20 to 240 $\mu$sec, obtained in a 30 hour run. Structure in the beam attributed to Al resonances is shown, including the weak resonance at 5.9 keV. The resonance at 2.8 keV is believed to be due to sodium.

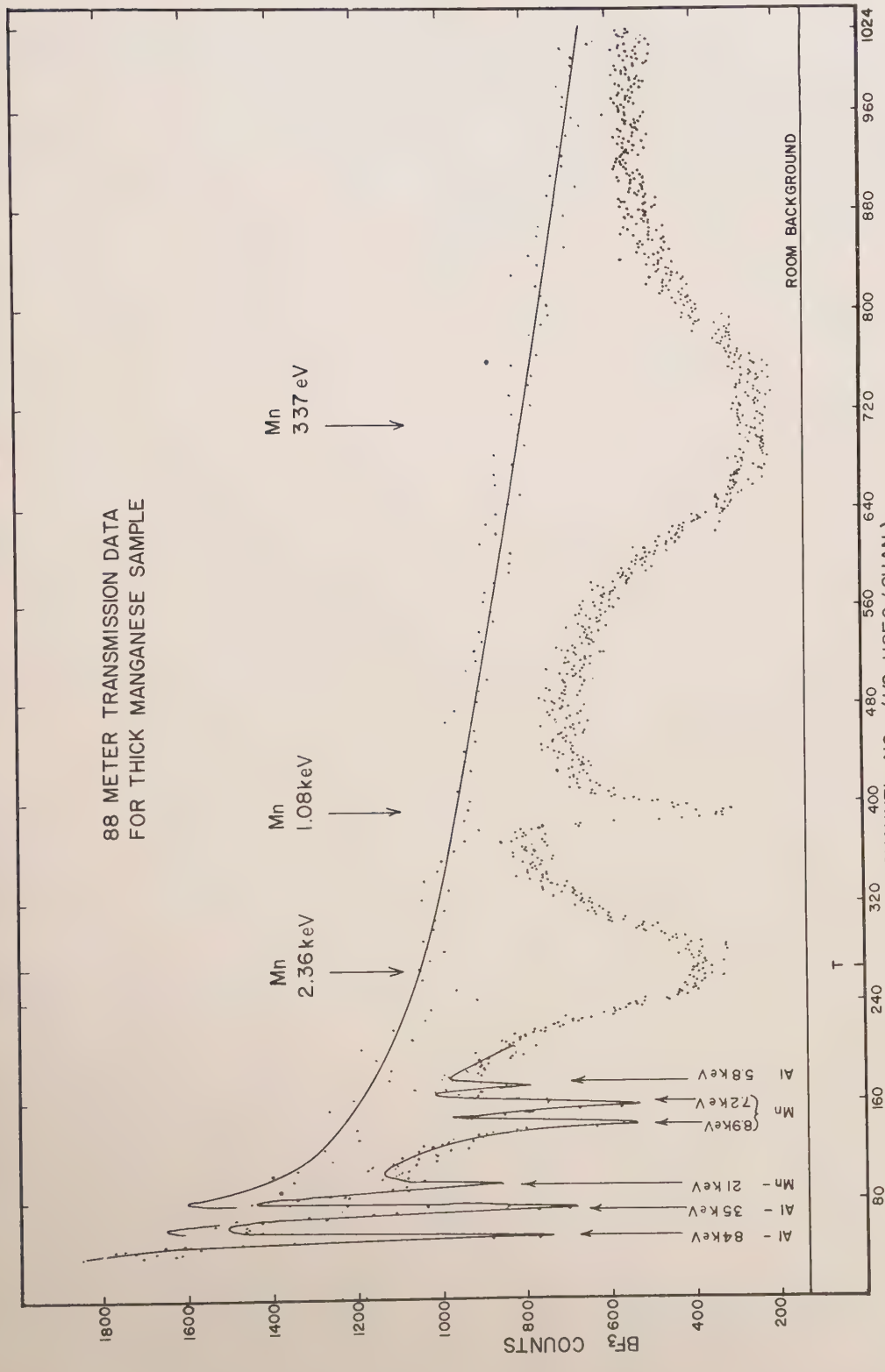


Fig. 9. A transmission measurement on manganese of thickness $0.01 \times 10^{24}$ atoms/cm$^2$.

(a) ROOM BACKGROUND

Room background is determined by placing a 6.35 cm thick lucite block in front of the exit stator. This thickness was empirically determined to be such as to remove all resonance neutrons from the beam. The remaining neutrons are time analyzed and the high energy neutrons occurring in the burst are gated out.

(b) OVERLAP AND SPURIOUS NEUTRONS

In principle one way of determining the time-dependent backgrounds is to introduce a sample in the beam which removes completely, over a small energy range, all the neutrons belonging to the primary part. The counts in these time channels, less room background and corrected for their attenuation by the sample, would be the overlap plus the spurious counts. Fortunately the presence of neutron resonances in many elements gives us a good choice of materials for using this method.

Fig. 9 shows a typical curve obtained with a manganese sample in the beam; manganese is known to have three large and quite wide resonances at 2.36 keV, 1.08 keV and 337 eV. The thickness was chosen so that the sample removed neutrons of a fairly wide energy range around each resonance. One can thus determine the "blacked-out" level quite accurately. Other points in the spectrum were obtained from measurements of "blacked-out" resonances in vanadium (11, 7, 4.2 keV), $U^{238}$ (191 and 36 eV) and cobalt (132 eV). The amount of the secondary neutrons (overlap + spurious) so determined was then expressed as a fraction of the total neutrons at that point in the open spectrum. These fractions $F(t)$ are plotted in fig. 10.

The distinction between overlap and spurious background is important only if it is desired to investigate the transmission of the overlap neutrons —a practice which is generally to be avoided. Nevertheless an estimate of the spurious neutron component at the 88 metre detector station has been made by comparing the counting rate curve obtained at 16 metres, where no spurious background is expected to be present. One thus obtains the fraction of the total neutron beam current that is due to overlap neutrons as shown by the dotted curve in fig. 10. It is evident that there is no appreciable spurious background after 240 $\mu$sec flight time. From the probable origin of this component, it is reasonable that it should be appreciable only for rather short flight times.

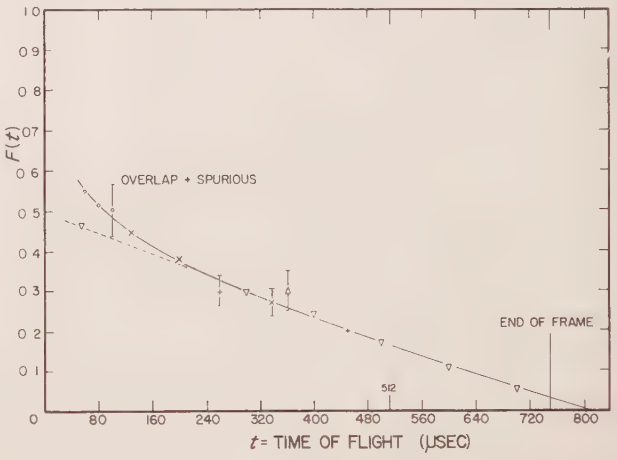


Fig. 10. The fraction of the total neutron beam current that is due to overlap + spurious neutrons. The curve has been determined by the use of "blacked-out" levels in V(○), Mn (×), $U^{338}$(+), and the extrapolation of the spectrum measured at 16 metres to 88 metres (△). Below 250 $\mu$sec a significant portion of the total background is attributed to kilovolt neutrons (spurious neutron) scattered by the walls of the flight path enclosure. The dotted curve is based on the spectrum obtained at 15.6 metres.

A third method of separating first and second frame neutrons is also available, but has not so far been carried out. This consists in measuring with and without a $1/v$-law absorber, using techniques similar to those used in crystal spectrometry for estimating order corrections.

A summary of these beam studies is shown on fig. 11. This is a typical open-beam run of 24 hours duration with the chopper spinning at 10000 rpm. The various curves indicate separately the three components of the beam. For typical operating conditions at a time of flight corresponding to a neutron energy of 500 eV, the overlap plus spurious background, and the room background each contribute about 20% to the total counting rate.

The $\gamma$-ray background level in the beam at the 88-m station is 1 mr/h. To reduce background from thermal neutrons at this point to a small quantity the counter bank is surrounded on all sides by 6-mm thick boral sheets. With this covering the total background rate, taken with a 6.35 cm lucite plug

blocking the neutron beam, is 140 counts/min. A large number of these counts are due to high energy neutrons which pass through the lucite plug. The background count taken with 32 $\mu$sec delay inserted in the analyzer, so as to eliminate the burst of high energy neutrons, is 91 counts/min. For comparison the background with the gate at the experimental

One unfortunate effect occurs from time to time, due to the proximity of the $D_2O$ scattering can to the control rod no. 13 of the NRU reactor; we observe a change in the shape of the open spectrum at 16 metres (with a corresponding change at 88 metre station) as this rod is lowered and raised. Fortunately during the steady running of the reactor this

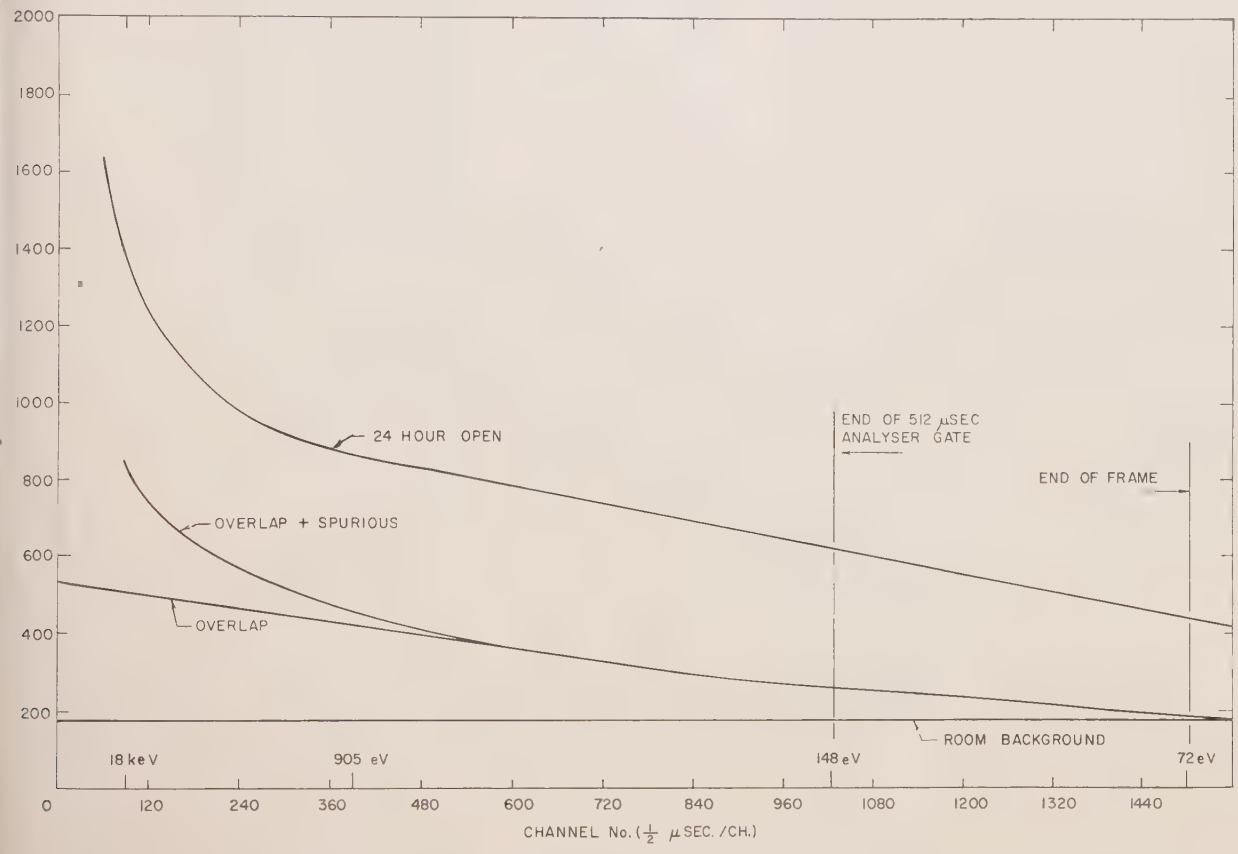


Fig. 11. An idealized open beam run showing the various beam components. The counting rates are those obtained for a 24 hour run. The resonant structure in the open spectrum is not shown.

hole in the pile shielding closed is 72 counts/min and the pile-down background, mostly due to $\alpha$-activity in counter walls, is 50 counts/min. The removal of the boral sheet from the front of the counter bank increases the room background to 600 counts/min, indicating the high counter sensitivity to thermal neutrons.

The fluctuations in the beam intensity are monitored by a $BF_3$ counter placed inside the chopper cavity, and the various runs are normalized to each other by the monitor counts.

rod is not used; it is only needed during reactor start-ups. For this period (sometimes approaching 24 hours) satisfactory measurements are not possible, although rough tests can still be made. Fortunately, shut-downs of NRU of appreciable duration are rather rare.

### 9. Resolution

The uncertainty in the time of arrival of the neutrons at the detector consists of four components: the one microsecond burst width (at 10000 rpm),

Fig. 12. The curve of total neutron cross section vs. energy for As, compiled from various sample thicknesses. The symbols are ●●● — 41.61 × $10^{-3}$ atoms/barn; □ □ □ — 10.979 × $10^{3}$ atoms/barn; ▲▲▲ — 2.996 × $10^{-3}$ atoms/barn; ○ ○ ○ 0.626 × $10^{-3}$ atoms/barn; but all points, represented by ○ ○ ○, above 800 eV corresponds to a thickness of 33.053 × $10^{-3}$ atoms/barn. This is an illustration of the quality of transmission work with the 88 metre flight path.

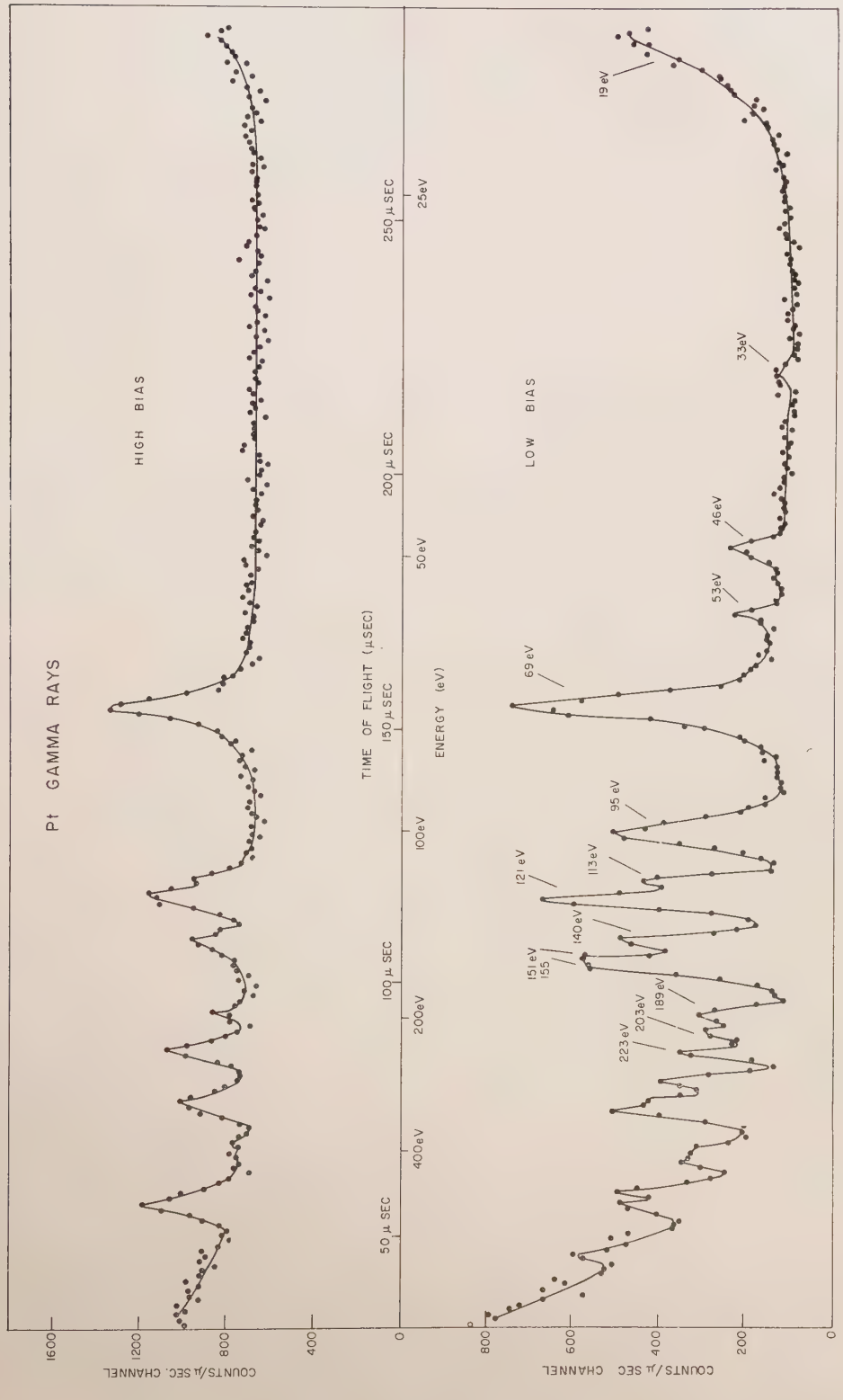


Fig. 13. Gamma rays from Pt observed at 16 metres, chopper spinning at 7000 rpm with 1 $\mu$sec time channels. High energy (above 7 MeV) and low energy (above 2.8 MeV) gamma rays are shown recorded with an integral discriminator.

the flight time (0.4 $\mu$sec for 500 eV neutrons) of neutrons in the detector, the 0.5 $\mu$sec pulse collection time in the counter element and the 0.5 $\mu$sec time channels. For 500 eV neutrons, the overall uncertainty in arrival time is 1.3 $\mu$sec. This corresponds to a resolution of 0.015 $\mu$sec/m. This value was experimentally confirmed by examining a few resonances, e.g. the 239 eV level in $U^{238}$.

### 10. Typical Data

For the first two years of operation, work has been divided between transmission measurements using the 88 metre flight path and resonance capture $\gamma$-ray experiments at 16 metres. Fig. 12 shows some typical cross section data on arsenic derived from transmission measurements at 88 metres. For some of these data boron filters were used to reduce the contribution of overlap neutrons. The different markings of the experimental points correspond to the several sample thicknesses used. The triangles below the curve are provided to show how the overall resolution varies with neutron energy. In the present data, the two levels near 320 eV are well resolved, although earlier published transmission data on arsenic show only one level[13]). From these data it seems plausible that in arsenic substantially all the levels up to several kilovolts are resolved.

Fig. 13 shows some of the early data obtained in the resonance capture $\gamma$-ray program. The target in this case is a thick (1.27 cm) piece of platinum. Two time-of-flight plots are shown corresponding to two integral discriminator settings. The upper curve, a run of 1857 minutes duration represents $\gamma$-rays above 7 MeV, and the lower curve, a run of 42 minutes duration, shows the radiation above 2.8 MeV. These simple plots indicate some of the interesting aspects of the capture $\gamma$-ray experiments. The absence of high energy $\gamma$-rays from some levels, the 33 eV, 46 eV, 53 eV, and 95 eV levels, can be ascribed to the lower neutron binding energy of the even Pt isotopes relative to the $Pt^{195}$ isotope. The absence of $\gamma$-rays above 7 MeV for the 203 eV level is ascribed to a $0^-$ spin assignment for that level. Thus capture $\gamma$-rays can be used for isotope identifications and for spin assignments. A logical exploration of the feasibility of assigning level spins on the basis of the strength of the high energy transitions has led to a study of the fluctuation of electric dipole transition probabilities from the capturing state to the ground state, or states near ground of the compound nucleus. This study is now in progress.

The use of neutron time-of-flight techniques for sorting out $\gamma$-rays from individual resonances provides a significant advantage over thermal capture $\gamma$-ray studies, in which the capturing "state" is usually a mixture of several states of the compound nucleus.

### Acknowledgements

We desire to acknowledge our indebtedness to many members of the staff of the Brookhaven National Laboratory and Atomic Energy of Canada Limited, who have contributed to the installation and operation of this equipment, and in particular to Messrs. Borge Espensen and Clive Reed who were responsible respectively for assembly and design modifications at Brookhaven. At Chalk River the Engineering Design Division was responsible for the in-pile scatterer, collimator and 88-metre flight path, and Mr. J. P. Inglis was responsible for reactor operations aspects of the work. The help of the reactor operating staff and of H. Jackson, B. Pringle, and R. Roth for technical assistance in maintenance and in connection with data processing is also acknowledged.

[13]) R. E. Coté, L. M. Bollinger and James M. LeBlanc, Phys. Rev. **111** (1958) 288.

NUCLEAR INSTRUMENTS AND METHODS 13 (1961) 21–28; NORTH-HOLLAND PUBLISHING CO.

# AUTOMATIC ANALYSIS OF BETA-RAY SPECTRA

WERNER SCHNEIDER† and TORSTEN LINDQVIST

*Institute of Physics, University of Uppsala, Uppsala*

Received 29 June 1961

The analysis of beta-ray spectra has been programmed for an electronic computer. As an application the analysis of the line spectra obtained in a magnetic semicircular beta spectrograph is described, as well as the Kurie-analysis of a continuous beta-spectrum.

## 1. Introduction

At present, there is a trend in experimental physics to automatize as much as possible the routine work connected with the various experimental procedures. However, so far mainly the recording of the primary data has been automatized. The computing parts of the experiments are in general still performed with the help of desk calculators. For the physicist this method is more time- and effort-consuming than necessary. The reasons for this situation (lack of training in the use of electronic computers, no computer easily accessible, no funds for paying a commercial computing centre etc.) are well known. However, it seems that physicists become more and more computer-minded and that the number of physics departments having a computer available is growing rapidly.

Along these lines our institute has started to adapt for computer programming the most time consuming treatments of primary data in connection with the experimental work††.

The following three problems are presented in this article:

a. The calculation of the energies and the classifying analysis of conversion electron lines recorded by a precision semicircular beta-ray spectrograph. The primary data are the relative positions of the electron lines on the photographic plate.

b. The calculation of the energies and the classifying analysis of conversion electron lines recorded by a double focusing beta-spectrometer with an iron yoke. The primary data are the readings of a potentiometer or a current measuring bridge.

c. The Kurie analysis of a continuous beta spectrum recorded by any magnetic beta spectrometer. The primary data are quantities proportional to the momentum of the electrons, e.g. an ampère meter reading or a potentiometer reading, and the corresponding electron intensities.

The computer programs have been written for physicists, i.e. simplicity and clearness in programming and in application has been one of the most important goals.

The explicit form of the programs is at present made for the FACIT computer of the Swedish Board of Computing Machinery, Stockholm. However, all programs discussed in this paper will be translated to FORTRAN in the near future. Detailed information about the computer programs presented here can be obtained upon request.

## 2. Analysis of $\pi$-Spectrograph Data

### 2.1. GENERAL PROCEDURE

The semicircular spectrograph used was constructed by Karlsson and Siegbahn[1]).

The instrument is provided with special

† On leave from Swiss Federal Institute of Technology (E.T.H.) Zürich.

†† After completion of this article it was announced in Phys. Rev. Letters 6, nr 11 (1961), that Helmer and Burson at the Argonne National Laboratory have used a computer for the analysis of their $\pi$-spectrometer data (R.G. Helmer and S. B. Burson, Decay of $Tm^{172}$, Phys. Rev. to be published.)

[1]) E. Karlsson and K. Siegbahn, Nucl. Instr. and Meth. 7 (1960) 113.

arrangements for careful relative measurements. The focusing field is obtained from an electromagnet, the current of which is stabilized with a transistor circuit.

The instrument has been used extensively and it is most useful for relatively shortlived isotopes ($T_{\frac{1}{2}} < 20$ h) which have a great number of transitions. Recently an investigation of neutron deficient Au isotopes was carried out[2]), where more than 300 electron lines were found.

The most accurate method of determining the energies of the recorded electron lines described by Karlsson and Siegbahn, involves the determination of three parameters (see fig. 1), namely two

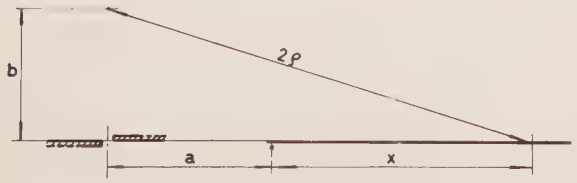


Fig. 1. Explanation of the quantities $a$, $b$, $x$ and $\rho$ used in the calibration calculations. (Figure taken from ref. [1]).)

distances $a$ and $b$ related to the radius $\rho$ of the electron path and the magnetic field $B$. The variable quantity, $x$, is the distance between an arbitrarily chosen point on the photographic plate and the recorded electron line, and is measured with a precision comparator. The determination of the parameters $a$, $b$ and $B$ requires three calibration lines and the solution of the following system of equations:

$$\begin{aligned}(x_1 + a)^2 + b^2 &= \frac{4(B\cdot\rho_1)^2}{B^2}\\ (x_2 + a)^2 + b^2 &= \frac{4(B\cdot\rho_2)^2}{B^2}\\ (x_3 + a)^2 + b^2 &= \frac{4(B\cdot\rho_3)^2}{B^2},\end{aligned} \qquad (1)$$

where $x_{1,2,3}$ and $\rho_{1,2,3}$ are respectively the positions of the electron lines and radii of electron paths for the three calibration lines. When the calibration parameters are calculated, the momenta $(B\cdot\rho_i)$ of each individual electron line can be obtained from the equation

$$B\rho_i = \tfrac{1}{2}B\sqrt{(x_i + a)^2 + b^2} \qquad (2)$$

and the energies $E_i$ from the well-known relation

$$E_i = E_0\left\{\sqrt{\left(\frac{e}{m_0}\frac{B\rho_i}{c}\right)^2 + 1} - 1\right\}, \qquad (3)$$

or when (2) is inserted in (3)

$$E_i = E_0\left\{\left[\left(\frac{e}{m_0 c}\right)^2\frac{B^2}{4}((x_i + a)^2 + b^2) + 1\right]^{\frac{1}{2}} - 1\right\}, \qquad (4)$$

where the values of the fundamental constants can be taken from the article by Du Mond and Cohen[3]).

The final step in a complete analysis of the data from the $\pi$-spectrograph involves a classification of the electron lines with respect to the originating nuclear transition and electron shell.

From the above-mentioned description it is obvious that the complete analysis is a very tedious work to be done by hand with the help of a desk calculator. A striking example of this is the analysis of the Au isotopes[2]), which should have taken several weeks to complete. The extensive investigation of the Au isotopes, which gave more than 100 electron lines on each photographic plate, actually initiated our interest for applying electronic computer methods to the analysis.

### 2.2. COMPUTER PROGRAM

In fig. 2 and fig. 3 the flow chart of the computer program is presented in an abbreviated form. The easiest way to discuss the program is to follow the flow chart box by box.

Box 1. In most cases the complete electron line spectrum can not be recorded on one photographic plate because of the limited energy range of the $\pi$-spectrograph. Therefore the program provides the possibility to make the classification analysis of a collection of electron lines which have been obtained from two or more plates. In this case the electron energies are of course already calculated when the program is started. In Box 1 the decision is made, whether it is planned to analyze *one* plate or a combination of two or more plates.

Box 2. Input data are the coordinates $x_i$ and

[2]) I. Marklund and E. Karlsson, to be published in Nuclear Physics.

[3]) J. W. M. Du Mond and E. R. Cohen, Rev. Mod. Phys. 25 (1953) 691.

$B\rho_i$-values of the three calibration lines, the coordinates of the lines to be analyzed and some indicators and constants.

Box 3. In this part of the program the constants $a$, $b$ and $B$ (see fig. 1) are calculated from the system of equations given in (1).

Box 4. Calculation of the electron energies. The programmed formulas have the simplest form possible.

Box 5. Here it is decided whether only the calculated electron energies are required or also the classification analysis is requested.

Box 6. A table of the electron energies is printed. After this printout the run is finished.

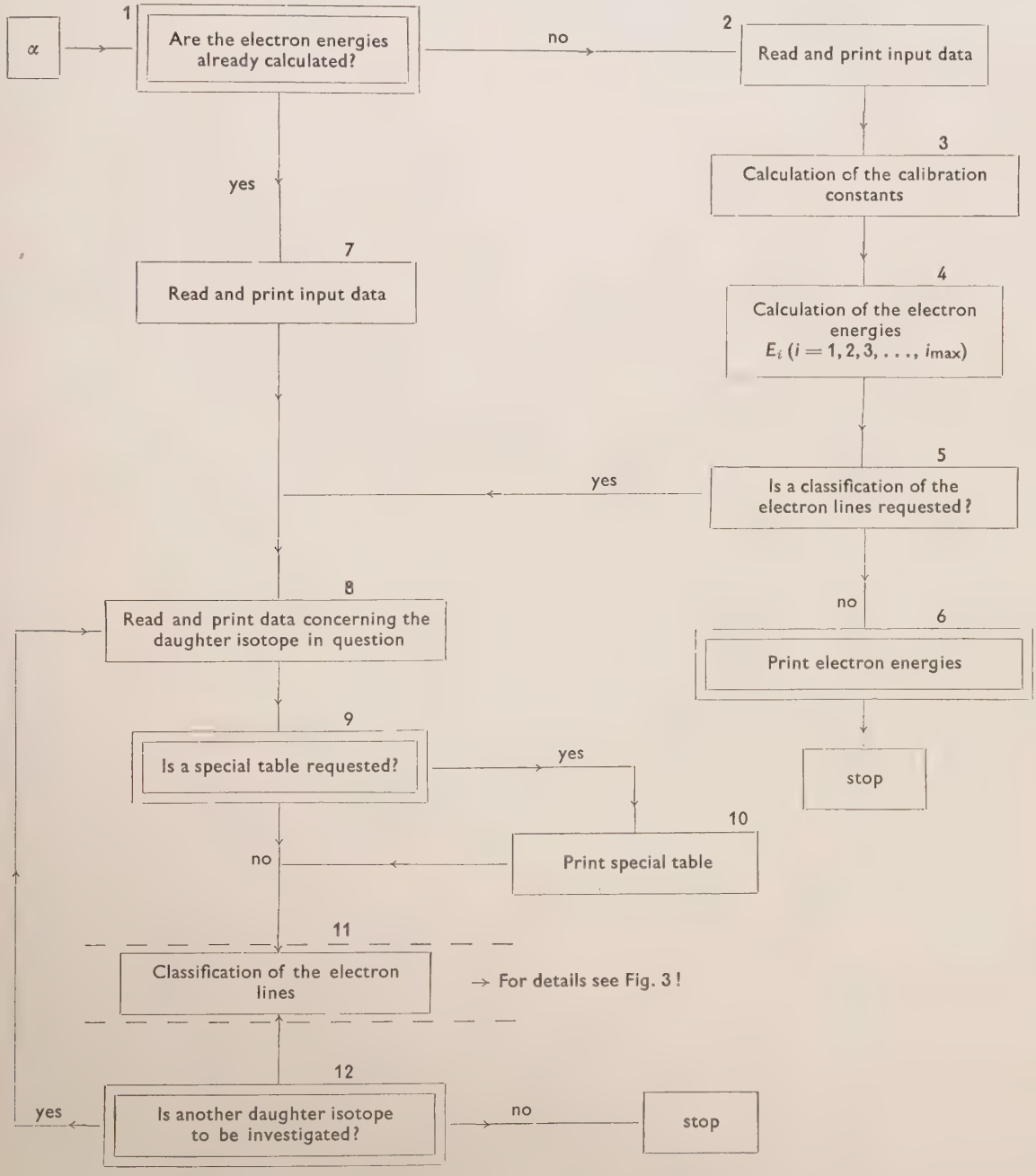


Fig. 2. Program for the analysis of $\pi$-spectrograph data. Flow chart.

Box 7. If in Box 1 it has been indicated that a combination of plates is to be analyzed, the electron energies are read in here. As in Box 2 also indicators and constants are read in and printed.

Box 8. If a classification of the electron lines is requested, the computer has to be informed in detail about some properties of the daughter isotope in question: X-ray absorption data etc. In addition the different conditions of accuracy which are valid for the classification of the electron lines must be specified.

Box 9, 10. As a test of the classification analysis carried out by the computer it is useful to have a special table, in which the energy of each electron line is printed and also the corresponding "trial" gamma energies under the assumption that the electron line is a K-line, $L_I$-line, $L_{II}$-line etc. up to any conversion line. The analysis made by the computer is usually limited to a series of 2 or 3 main electron shells.

Box 11. (see also fig. 3).

Box 110. The first set of conditions of accuracy is taken.

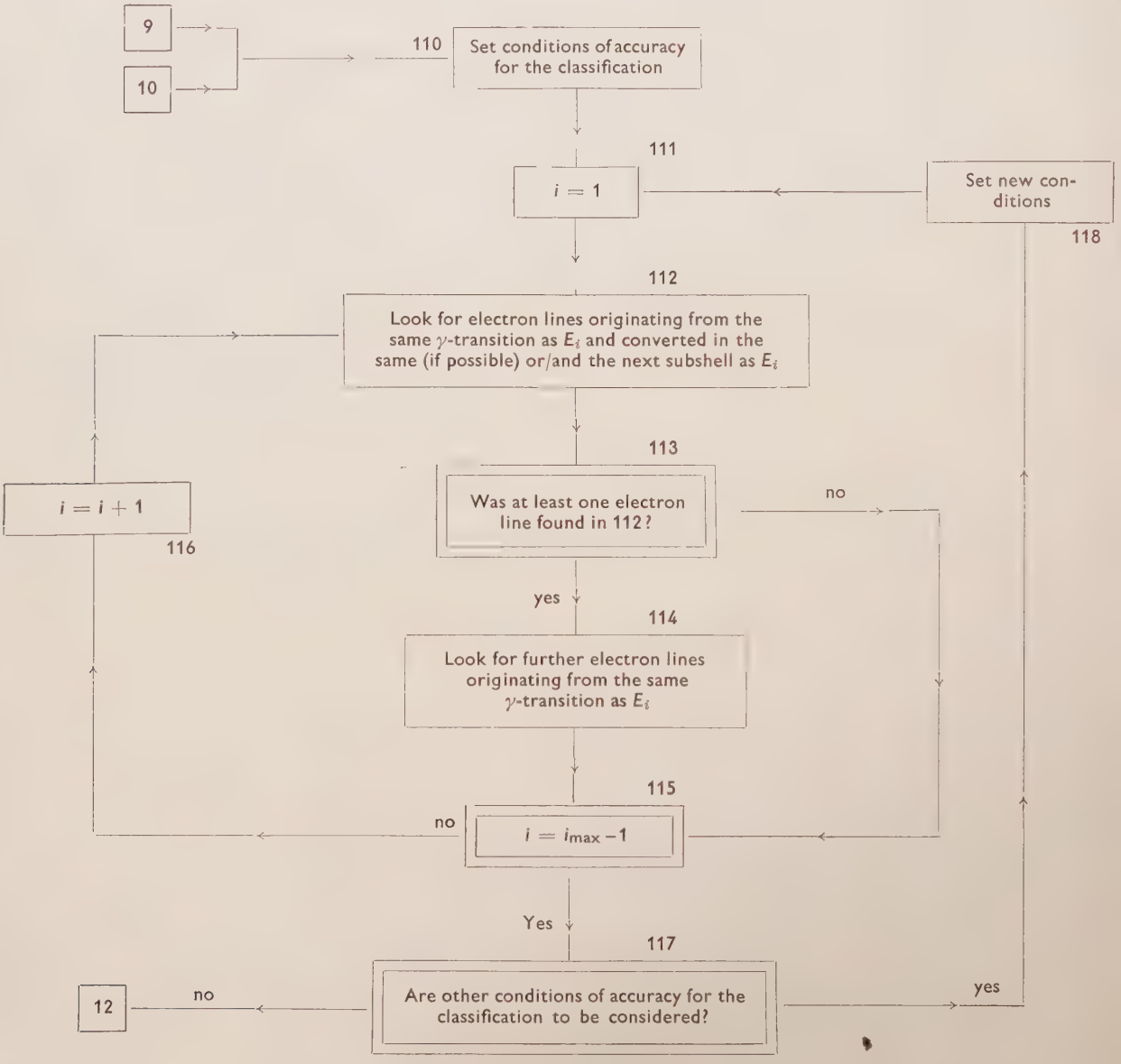


Fig. 3. Detailed presentation of Box 11 in flow chart of Fig. 2.

Box 111. The index, $i$, of the electron line is set equal to 1.

Box 112, 113, 114. The classification procedure programmed in our routine, tests the collection of electron lines, to find a series of electron lines originating from the same gamma transition and converted in one or several electron shells specified through the input in Box 8. In most cases the computer looks for a K-$L_I$-$L_{II}$-$L_{III}$-$M_I$ . . . series. However, particularly in the low energy region, one sometimes looks also for a $L_I$-$L_{II}$-$L_{III}$-$M_I$ . . . series or a $L_{II}$-$L_{III}$-$M_I$ . . . series. The length and character of the series are arbitrarily chosen depending on the experimental data, and the resolution of the spectrograph etc. and is specified through Box 8. If none of the second, third or fourth members of a series can be found, the analysis for that series is generally stopped. E.g., if $E_i$ is assumed to be a K-line from a gamma-transition $E_k^\gamma$ and if no L-lines of the same gamma-transition $E_k^\gamma$ are found, no further analysis with respect to M-lines is carried out.

It should be noted that in our program no special provisions are made for avoiding accidental series to be printed. In general, accidental series can easily be picked out by the experimentalist. In this way complicated and time-consuming consistency checks have been omitted.

Box 115. The last electron line cannot be classified as the first line of a series through the program. Therefore the classification routine stops when $i = i_{max} - 1$.

Box 117. If the classification has to be made for other conditions of accuracy these are set in Box 118. Otherwise the next box will be Box 12.

Box 12. If another daughter-isotope is to be investigated the program restarts at Box 8. Otherwise the machine stops.

As mentioned before the program is now in use for some time and a great number of photographic plates have been analyzed. The time gain with this procedure is considerable, and, in addition, one has a higher accuracy and greater possibilities for tests than with the deskcalculator method.

## 2.3. RESULTS

In order to demonstrate the formal presentation of the results from the computer we have measured the well-known ThB decay in the $\pi$-spectrograph. We selected 10 strong electron lines including the well-known calibration lines, F, I, and J. The formal presentation of both input and output data can be seen in table 1. "PISA" stands for "$\pi$-spectrum analysis". It should be noted that the notations in the computer language do not agree completely with the notations of the equations (1), (2) and (3). In addition, the printout in the Fortran version will be more sophisticated.

Table 1

Example of the printout from a run of program PISA on the FACIT computer.

```
PISA                                                    18.04.61

    C1  5.1561          C2  8.8493          C3  9.4106
    P1  1388.440        P2  1753.890        P3  1811.130
    E0  510.984         F1  0.089876
    PK  7.00 E = — 4

    5.1561    7.2902    8.2648    8.8493    8.8799
    9.4106    9.5489    9.5822   11.5200   11.5490

          A   5.570
          H 222.406     H2 4.946459 E = 4
          B   6.392     B2 4.085129 E = 1

Z 83
        KL1  74.154     KL2  74.831     KL3  77.123
        KM1  86.540     KM2  86.845     KM3  87.363
        KM4  87.852     KM5  87.962

XRA
          90.540    16.386    15.709    13.417
           4.000     3.695     3.177     2.688
           2.578     0.938     0.805     0.676
           0.464     0.440     0.162     0.156
           0.157     0.119     0.092     0.024

ISO 0

GAMMA ENERGIES KEV
        148.08    238.62    164.47    163.79    161.50
        152.08    151.77    .......
          :
          :

EEI  148.08  I  1  EGI  238.62
EEJ  222.21  J  4  XRD   74.154  MU 1  ERR  0.259
EEJ  222.28  J  5  XRD   74.831  MU 2  ERR  0.260
EEJ  234.61  J  6  XRD   86.540  MU 4  ERR  0.268

EEI  209.59  I  3  EGI  300.13
EEJ  283.43  J  9  XRD   74.154  MU 1  ERR  0.345
EEJ  284.13  J 10  XRD   74.831  MU 2  ERR  0.346
```

In the last part of table 1 it can be seen that the K, $L_I$, $L_{II}$, and $M_I$ conversion lines of the 238 keV transition and the K, $L_I$ and $L_{II}$ conversion lines of the 300 keV transition were found.

The computer program was in this case set to test only up to M-lines. However, from the special table of "trial" gamma energies two more electron lines were classified, namely two N lines of the 238 keV transition, which demonstrates the usefulness of the special table.

The computer analysis of the Au-spectra really showed the capacity of the computer method. The complete analysis, comprising several plates with more than 100 electron lines, was performed in some hours. The time required for the computer analysis was orders of magnitude shorter compared to the desk calculator analysis.

### 3. Other Precision Spectrometers

In the case of other precision beta spectrometers, e.g. double focusing spectrometers with or without iron, the calculation of the electron energies is somewhat more simple than for a $\pi$-spectrograph. The primary data are usually an ampère meter reading $J_i$ or potentiometer reading $R_i$, both proportional to the electron momentum $B\rho_i$. The proportionality factor can be obtained from one or more calibration lines or from a complete calibration curve.

Once the electron energies are calculated the classification analysis will be exactly the same as in the case of the $\pi$-spectrograph. The general flow charts of fig. 2 and fig. 3 are still valid. Box 1 then implies the possibility of combining the results from various energy regions, where various calibration constants have been used. Box 3 receives input data through Box 2, e.g. a calibration curve, or a calibration factor valid for the energy region in question (in the case of iron free spectrometer this is only a constant).

### 4. Kurie Analysis

#### 4.1. GENERAL PROCEDURE

The theory of beta-decay gives the well-known expression for the probability per unit time that a beta particle is emitted with a momentum between $p$ and $p + \mathrm{d}p$:

$$N(p)\mathrm{d}p = CF(Z,p)p^2 \mid M \mid^2 (W_0 - W)^2 \mathrm{d}p\,, \qquad (5)$$

where

$C$ is the normalization factor

$F(Z,p)$ is the Fermi function tabulated e.g. in ref.[4])

$W$ is the energy in $m_0c^2$-units

$W_0$ the endpoint energy

$p$ the momentum in $m_0c$-units

$M$ the nuclear matrix element.

The standard procedure of analysis of continuous beta-ray spectra is to plot

$$Y = \sqrt{\frac{N(p)}{p^2F(Z,p)}}$$

against $W$ (Kurie plot). In the case of allowed and some first forbidden decays, $|M|^2$ is independent of $W$ which implies that $Y(W)$ will result in a straight line intersecting the $W$-axis at $W_0$, the maximum energy of the beta transition, which is to be determined.

In forbidden decays $|M|^2$ is, in general, dependent of the electron energy and $Y(W)$ will not be a straight line. Thus a shape factor $S(W)$ has to be introduced in such a way that the function $Y^*(W) = Y(W)/\sqrt{S(W)}$ gives a straight line. The computer program presented below is constructed in such a way that the correction factor $S(W)$ can easily be introduced in the calculations.

In general case when more than one beta component are present one has to make an intermediate stop. The plotting of the data may of course be done by an analogue plotter connected to the computer. However, a completely automatized Kurie analysis without any intermediate judgement of the physicist seems to be very difficult to realize at present.

#### 4.2. COMPUTER PROGRAM

As in chapter 2 the program is discussed following the flow chart presented in fig. 4.

Box 1. See comments to Box 9.

Box 2. The principal input data are:

1. The measured beta-ray spectrum.

In general one measures the number $N'$ of the electrons recorded per unit time as a function of a variable which is proportional to the momentum of the electrons, e.g. the current $J$ or the resistance $R$ of a precision bridge.

[4]) A. H. Wapstra *et al.*, Nuclear spectroscopy tables (North Holland Publ. Co., Amsterdam).

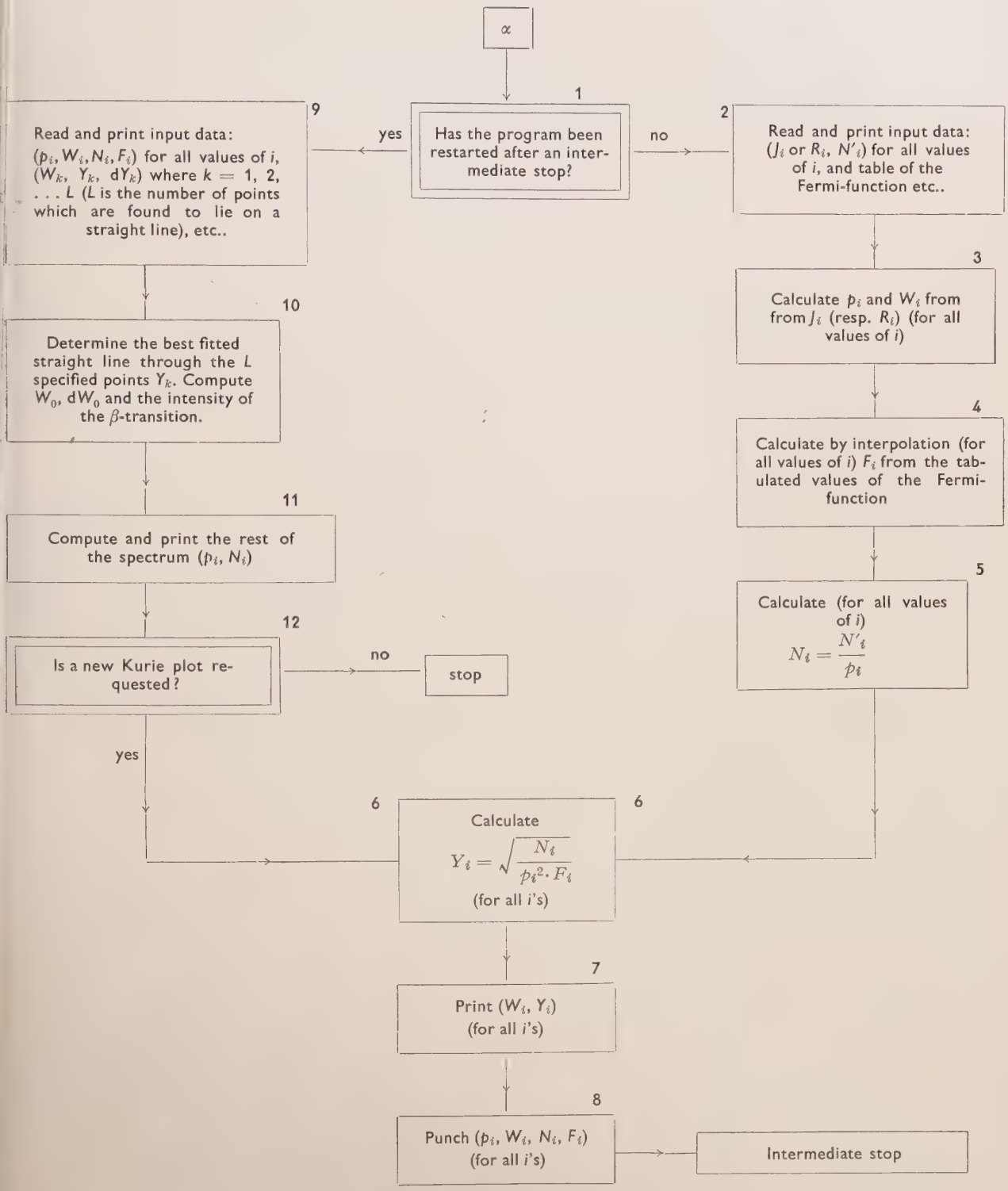
α
1
Has the program been restarted after an intermediate stop?
yes
no
9
Read and print input data: ($p_i, W_i, N_i, F_i$) for all values of $i$, ($W_k$, $Y_k$, $dY_k$) where $k = 1, 2, \ldots L$ ($L$ is the number of points which are found to lie on a straight line), etc..
2
Read and print input data: ($J_i$ or $R_i$, $N'_i$) for all values of $i$, and table of the Fermi-function etc..
3
Calculate $p_i$ and $W_i$ from from $J_i$ (resp. $R_i$) (for all values of $i$)
4
Calculate by interpolation (for all values of $i$) $F_i$ from the tabulated values of the Fermi-function
5
Calculate (for all values of $i$) $N_i = \frac{N'_i}{p_i}$
10
Determine the best fitted straight line through the $L$ specified points $Y_k$. Compute $W_0$, $dW_0$ and the intensity of the $\beta$-transition.
11
Compute and print the rest of the spectrum ($p_i$, $N_i$)
12
Is a new Kurie plot requested?
no
stop
yes
6
Calculate $Y_i = \sqrt{\frac{N_i}{p_i^2 \cdot F_i}}$ (for all $i$'s)
6
7
Print ($W_i$, $Y_i$) (for all $i$'s)
8
Punch ($p_i$, $W_i$, $N_i$, $F_i$) (for all $i$'s)
Intermediate stop

Fig. 4. Program for the Kurie plot analysis. Flow chart.

2. The tabulated values of the Fermi function.
3. Calibration data.
4. Constants and indicators.

Box 3. From the measured values of $J_i$ (resp. $R_i$) the corresponding values of momentum and energy are computed.

Here

$$p = \frac{B\rho}{m_0 c} W - \frac{E}{m_0 c^2} .$$

Box 4. The values $F(W_i)$ are computed by quadratic interpolation from the stored table of the Fermi function.

Box 5. No comments.

Box 6. No comments.

Box 7, 8. The values $Y(W_i)$ are printed out. If the computer is provided with an analogue curve plotter the Kurie plot may be presented directly. At this moment an intermediate stop of the program is required to allow a study of the results. For further analysis, however, the values $p_i$, $W_i$, $N_i$, $F_i$ (for all $i$'s) must be preserved. This is done by punching them on a paper tape (cards or magnetic tape).

Box 9. If further analysis is required after Box 8, the flow is linked to Box 9 through Box 1 when the program is restarted. The data punched in Box 8 have to be read in again together with necessar indicators and constants. In addition, all poin $Y_k$, lying on a straight line, are read in togeth with the corresponding energy values $W_k$ and th errors of $Y_k$, $\mathrm{d}Y_k$.

Box 10. By means of the least square method th best fitted straight line through the L points ($W$ $Y_k$) is determined, taking the errors $\mathrm{d}Y_k$ int account. From the straight line $W_0$ and $\mathrm{d}W_0$ a obtained and finally the intensity of the actual be component is calculated.

Box 11. No comments.

Box 12. If further beta components in th continuous spectrum are to be determined, a ne Kurie plot is computed (Box 6 ff). Otherwise th program is finally stopped.

**Acknowledgements**

The authors are indebted to Professor Kai Sieg bahn and Fil.lic. Erik Karlsson for important di cussion about the technique of the measuremen with the $\pi$-spectrograph. Further thanks are due t the Swedish Board of Computer Machinery fo putting free computer time on the FACIT comput to our disposal, and particularly to Mrs. M. An dersson for running the programs. One of us (W.S likes to thank the Schweizerische Kommission fü Atomwissenschaft for financial support.

NUCLEAR INSTRUMENTS AND METHODS **13** (1961) 29–34; NORTH-HOLLAND PUBLISHING CO.

# SORTING OF TWO COINCIDENT PULSES ACCORDING TO THEIR AMPLITUDES

M. KONRAD and B. TURKO

*Institute "Rudjer Bošković", Zagreb, Yugoslavia*

Received 22 April 1961

Systems are described for sorting coincidences of two pulses according to their amplitudes into channels of an analyzer. The amplitude of pulse A is divided into $N$ amplitude channels and of pulse B into $M$ channels. If the amplitude $a$ of pulse A is in the amplitude channel $n$ and of pulse $B$ in channel $m$, the event is placed into the $T = nM + m$ channel. The comparator of an amplitude analyzer is replaced by another one, consisting of two amplitude to time converters, which are connected so that either the total time of conversion is proportional to $T$ (with circulating memory), or the number of output pulses equals to $T$ (with ferrite memory). Block diagrams of these comparators are given, and a comparator is described which has been used at the Institute "Rudjer Bošković" with a modified Hutchinson type analyzer.

## 1. Introduction

In some nuclear physics experiments it is necessary to establish how many pulses of a detector A have an amplitude $a$ when a detector B gives a coincident pulse of an amplitude $b$, i.e. to count coincident events satisfying amplitude criteria. In such experiments it is mostly required to find the number of coincidences as a function of the amplitudes $a$ and $b$. This can be made by dividing the pulse amplitudes of the detector A into $N$ channels and those of the detector B into $M$ channels so that coincidences are divided into $NM$ coincidence channels according to a code, which determines the number of the coincidence channel $T$ as a function of the amplitude channels $n$ and $m$ of the pulses A and B ($n = 0, 1, 2, \ldots N-1$, $m = 0, 1, 2, \ldots M-1$). The required function is then obtained from the number of counts as a function of $T$. To determine the latter, it is convenient to use the memory system of a multichannel analyzer with a sorter to which the pulses from the detector A and B are applied and which sorts the coincident events into the channels of the memory. A simple and convenient code according to which the coincident events are divided into channels is the equation

$$T = nM + m$$

on which the sorters described here are based.

It may seem to be most convenient to build a sorter which after the performed sorting operation gives an output pulse of an amplitude proportional to $T$, as then a multichannel amplitude analyzer could be used for counting without making any changes to it. Such a system would lead to serious errors, as it does not ensure that all pulses corresponding to the $T$-th coincidence channel will be placed only in this channel of the amplitude analyzer and not into adjacent channels $T-1$ and $T+1$. Coincidences with $m = M-1$ and $m = 0$ could then be placed also into channels corresponding to $n+1$, $m = 0$ and $n-1$, $m = M-1$, which cannot be tolerated, as they are not adjacent channels with respect to $m$. To avoid such an error, the sorting system has to be designed so that it supplies the data directly into the memory. If the memory system of an amplitude analyzer is used, the sorter which replaces the amplitude converter should be based on such a principle that as few changes as possible on the memory system are required.

In this paper some coincidence pulse amplitude sorting systems are described, which were built or are under development at the Institute "Rudjer Bošković" for use of the existing multichannel amplitude analyzers with ferrite or magnetostrictive wire memories. From the functional point of view these coincidence pulse amplitude sorters have a coincidence unit with temporary pulse storage which

applies to the sorting unit only coincident pulses to be sorted, so that no time is wasted for the amplitude to time conversion of incoming pulses which are not coincident. This is particularly important if a circulating memory is used. This unit makes also possible a simpler design of the amplitude to time converters used for sorting.

## 2. Coincidence Unit

The block diagram of this unit is given in fig. 1. PLA and PLB are two pulse lengtheners based on charging condensers to the peak amplitude of the incoming pulses. The output voltages of the pulse

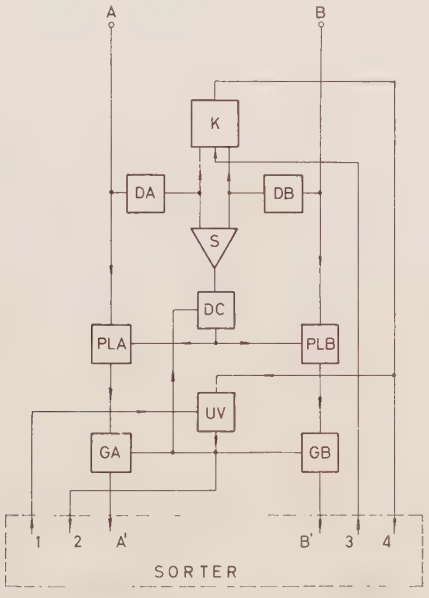


Fig. 1. Coincidence unit.

DA, DB integral discriminators
K coincidence
PLA, PLB pulse lengtheners
S or circuit
DC pulse lengthener discharge circuit
UV gate opening univibrator
GA, GB gates.

lengtheners are converted into pulses by opening the gates GA and GB for a short time. The opening and closing of these gates is controlled by the univibrator UV, which opens both gates simultaneously, and closes them a few $\mu$sec later. The closing of these gates can be synchronized with clock pulses applied to input 1 of the unit. DC is the pulse lengthener discharge circuit, which discharges the condenser when triggered after a interval somewhat longer than the resolution of th coincidence, or the length of the incoming pulses This circuit is triggered by pulses from the integra discriminators DA and DB, which are also applie to the coincidence K. When the univibrator UV i triggered, i.e. the incoming pulses are coincident the discharge circuit is made inactive until thi univibrator returns into its normal state, i.e. th gates are closed. During the sorting process, th coincidence K can be blocked with a voltage ap plied to input 3.

## 3. Sorters for Ferrite Memory

Fig. 2 is the block diagram of a fast sortin circuit which requires the memory address counte to be divided into two parts AC I and AC II havin a capacity of $M$ and $N$ pulses. With this divisior the address counter is placed into the position cor responding to $T = nM + m$ by applying $m$ pulse to AC I and $n$ pulses to AC II instead by applyin $T$ pulses to the input of the counter as a whole. Thi makes the sorting operation not only simple bu also fast, as the number of pulses which have to b applied is much smaller than $T$.

The $n$ and $m$ pulses are applied to AC II and AC from the clock pulse generator CO through the gat G1 and the gates G2 and G3, which are controlle by the output voltages of the amplitude to tim converters ATA and ATB. The gate G1 is close during the time the pulses A and B are applied t the converters, and opened after the clock puls which synchronized the trailing edge of pulses and B and started in this way the amplitude to tim conversion in both converters. This ensures that respectively $m$ pulses corresponding to the ampl tude channel pass through the gates G2 and G3.

After the address counter is placed into the $T$-t position the memory cycle start pulse has to b applied, to perform the read out, add 1 and writ operation. This pulse is obtained from the trailin edge of the output voltage of the OR and trailin edge delay circuit SD by differentiation, and applied to the memory through the gate AG1. Th gate is closed to prevent the memory cycle sta pulse if more than $M - 1$ or $N - 1$ pulses ar applied to the address counter parts AC I and AC I

In such a case a pulse is applied from the address counter parts through the circuit S2 to the bistabile BS which closes the gate AG 1. This bistabile is returned into its normal position and the gate is opened again at the beginning of the following sorting operation, with the coincidence pulse from the coincidence unit output 4 which resets the address counter.

SD and UV give the coincidence blocking voltage during the sorting operation and the memory cycle. SD gives the blocking voltage as long as either of the amplitude to time converters gives an

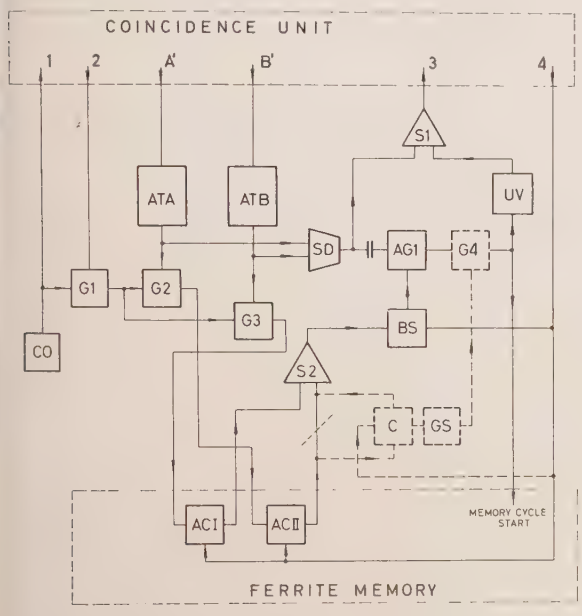


Fig. 2. Fast sorter circuit for ferrite memory.

ATA, ATB amplitude to time converters
G1 to G4 gates
AG1 anticoincident gate
CO clock pulse generator
ACI and ACII address counter parts
S1 S2 or circuits
SD or and trailing edge delay circuit
UV univibrator
C group counter
GS group selector
BS bistabile circuit.

output voltage. If the disappearance of this voltage results with a memory cycle start pulse, this pulse triggers UV which applies a blocking voltage somewhat longer than the time of the memory cycle.

This sorter was designed for the use with a 256 channel memory for $N = M = 16$. With a rather low clock pulse frequency of 0.5 Mc/s which ensures reliable operation and simple design the sorting time is given approximately by the expression

$$t \leq 2a + 24 < 54\ \mu\text{sec}$$

where $a$ is $n$ or $m$ whichever is larger. The additional time of 24 $\mu$sec includes the memory cycle time, the coincidence unit operational time of 2 $\mu$sec, and the maximum conversion waiting time of 2 $\mu$sec.

The described system with a 256 channel memory is not limited to a 16 $\times$ 16 channel division but can also be applied for 32 $\times$ 8, 64 $\times$ 4 etc. channel divisions.

The additional circuit in fig. 2 makes it possible to obtain a 32 $\times$ 32 channel sorting which is divided into four 8 $\times$ 32 sorting operations. In this case both amplitude to time converters are designed for 32 channel operation. AC I has a capacity of 32 and AC II of 8. To the output of AC II an additional counter C is connected having a capacity of 4 which through the selection unit opens the gate G4 through which the memory start pulse is applied only if the number of pulses applied during the sorting process from AC II has a predetermined value $l = 0, 1, 2,$ or 3 which correspond to values of $n = 0$–7, 8–15, 16–23 or 24–31.

The described method of pulse sorting is fast but has the disadvantage that not only the amplitude to time converter has to be replaced with the sorter, but also some changes have to be made on the address counter of the memory, if the ferrite memory of an amplitude multichannel analyzer is used. This however is not important if the memory is used only in connection with a sorter, so that in such cases this method is the best and simplest way of sorting.

When no changes are allowed to be made on the memory system of an amplitude multichannel analyzer where the sorter replaces the amplitude comparator, the sorter has to be designed so that it applies $T$ pulses to the address counter. These $T$ pulses consist of $n$ groups of $M$ pulses plus $m$ pulses. Fig. 3 shows a block diagram of such a sorter which performs 16 $\times$ 16 sorting operations. CO is the clock pulse generator. The right-hand output of this generator gives groups of 16 pulses which are separated one from another by one

missing pulse. This missing pulse appears on the upper output of the clock pulse generator as a group pulse, which is used for the same purpose as the clock pulse in the previously described sorter. Thus $n$ respectively $m$ group pulses appear on the output of the gates G2 and G3 during the sorting operation. These pulses from the gate G2 control through the bistabile circuit BS1 the gate G4 so that this gate passes $n$ groups of 16 pulses. The first of these pulses which are applied to BS1 triggers this bistabile which opens the gate G4. At the arrival of the $n + 1$-th pulse the gate G2 is closed and the gate AG1

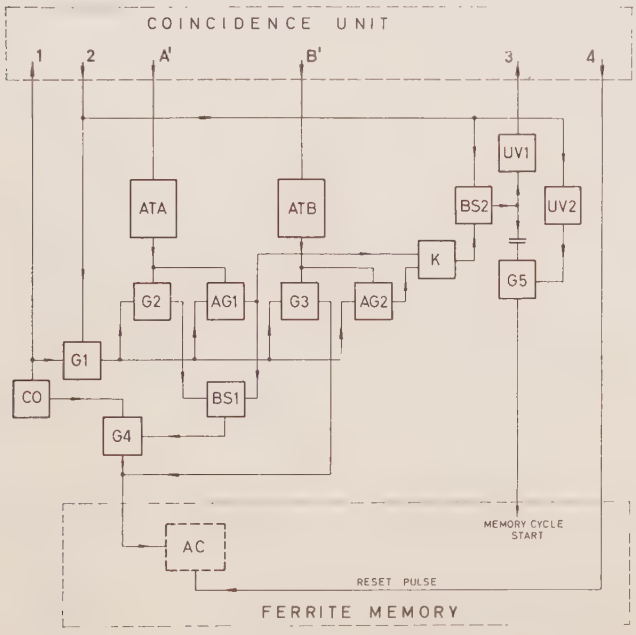


Fig. 3. Sorter circuit for ferrite memory which replaces the amplitude comparator.

ATA, ATB amplitude to time converters
G1 to G5 gates
AG1, AG2 anticoincident gates
CO clock pulse generator
BS1, BS2 bistabile circuits
K coincidence
UV1, UV2 univibrators
AC memory address counters.

is open so that this pulse returns the bistabile BS1 into its normal position and closes the gate G4. Through this gate thus $n$ groups of 16 pulses passed. Into the empty space between these groups $m$ pulses from the gate G3 are inserted, so that the total number of pulses applied to AC equals to $T$. The memory cycle start pulse is obtained by differentiation of the trailing edge of the outpu voltage of the bistabile BS2 on its return into it normal position and is applied through the gate G to the memory. At the beginning of the sorting th bistabile is triggered with the pulse from 2, an returns into its normal position with the first coi cidence pulse from K, i.e. at the first group puls when both gates AG1 and AG2 are open. Thes gates are closed only during the amplitude to tim conversion. The trailing edge of the pulse from triggers the univibrator UV2 which opens the gat G5 for a time somewhat longer than required tha 15–16 group pulses pass the gates G2 or G3, so tha if $n$ or $m$ is larger than $N - 1 = M - 1 = 15$ n memory cycle start pulse can be applied.

The coincidence blocking voltage is the outpu voltage from the trailing edge delay univibrato UV1, which starts with the triggering of th bistabile BS2 with the leading edge of pulse 2, an ends about 18 $\mu$sec later after this bistabile returned into its normal position. This delay is re quired for blocking the coincidence during th memory cycle.

With a clock pulse frequency of 2 Mc/s th sorting time is equal to

$$t \leq 8a + 36 \leq 156\ \mu\text{sec}$$

where $a$ is $n$ or $m$ whichever is larger. The addition time of 36 $\mu$sec includes the minimum coincidenc operational time of 2 $\mu$sec and the maximum re quired conversion waiting time of 8 $\mu$sec.

## 4. Sorter for a Circulating Memory

When a circulating memory is used the sorter ha to be designed so that it gives a memory puls which is delayed with respect to the start puls according to $T$. The output of the memory require for the operation of the sorter are the chann pulses, which are grouped within a memory cyc and follow in regular intervals. These groups a separated by a time interval at the end of the cycl The first pulse of the group is the sorter start puls If a pulse is applied to the memory in the interv between the $n$ — 1-th and $n$-th channel pulse, th pulse is placed into the $T_n$-th channel and th content of this channel is increased by 1.

The block diagram of a sorter for such a memo

is shown in fig. 4. The univibrator UV1 which controls the gate AG1 selects the start pulse. This univibrator is triggered by the channel pulses so that it remains triggered during the whole group of pulses, but returns into its normal state in the interval between the groups. In this latter interval the gate AG1 is opened so that the first pulse of the group passes through it. The division circuit DIV is designed so that only every $M$-th channel pulse starting with the first channel pulse appears on its output. The start of division is synchronized with the output voltage from UV1, i.e. with the first pulse. The first start pulse after the application of

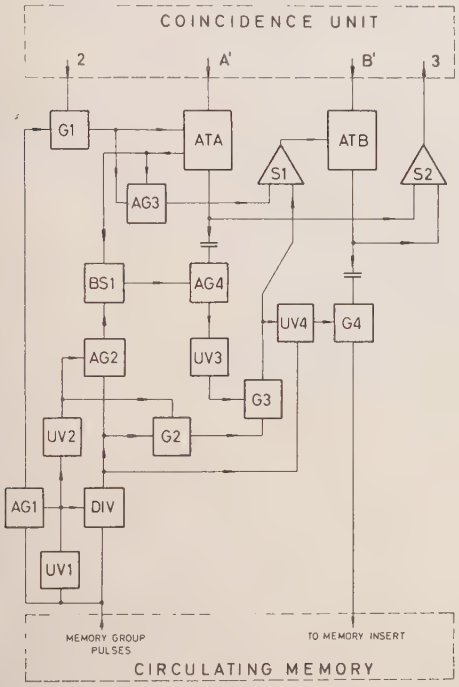


Fig. 4. Sorter circuit for circulating memory.
ATA, ATB amplitude to time converters
G1 to G4 gates
AG1 to AG4 anticoincident gates
UV1 to UV4 univibrators
S1, S2 or circuits
DIV division circuit.

the A and B pulse starts the amplitude to time conversion in ATA. The disappearance of the output voltage of ATA triggers through AG4 the univibrator UV3, which opens the gate G3 for a time interval longer than the interval between the $N-2$-th and 0 group pulses. The following group pulse starts then through the gate G2 and G3 the amplitude to time conversion in ATB. The start of conversion is thus coincident with the $n+1$-th group pulse, except for $n = N-1$ when it is coincident with the 0 group pulse as for the $N-1$-th and the following group pulses the gate G2 is closed. G2 which is controlled by the univibrator UV2 is opened by the pulse from UV1 which triggers UV2 in the interval between channel pulse groups, and closes with the return of UV2 in its normal position after the $N-2$-th group pulse. The pulse from G3 triggers also the univibrator UV4, which opens the gate G4 for an interval equal to the interval between two group pulses. At the end of conversion, the disappearance of the output voltage of ATB gives a pulse to G4, which applies it, if open, to the memory as the memory insert pulse. UV4 and the gate G4 prevent the application of this pulse for $m > M-1$. The return of UV2 to its normal position not only closes the gate G2 but also opens the gate AG2. The $N-1$-th group pulse is thus applied to the bistabile BS1 which closes the gate AG4, so that no pulse is applied to UV3 if the amplitude to time conversion lasts more than N — 1 group pulse intervals. To discharge ATB in such cases the start pulse is applied through the anticoincidence AG3. This pulse does not trigger UV4 so that at the end of conversion no memory insert pulse is applied. This start pulse is applied to every cycle except when conversion in ATA is started, as then the pulse from G1 is coincident with the pulse from ATA. The gate AG4 is opened again with the conversion start pulse from ATA.

With this system the coincident event is placed into the $T$-th channel of the memory according to the relation

$$T = nM + m + M + 1$$

when $n \leqq N-2$ and

$$T = m + 1$$

when $n = N-1$. From these expressions follows that no event is placed into the first channel of the memory $T = 0$ so that the capacity of the memory must be for 1 channel larger. From the first expression it can also be seen that without the system which inserts the events into the first channels for $n = N-1$, the capacity of the memory would have to be increased for additional $M$ channels.

The maximum sorting time is somewhat greater

than the memory cycle, not taking into account the maximum waiting time for the start of the sorting, which can be also one memory cycle. In the worst case thus a time of more than two memory cycles may be required from the arrival of the pulses to the end of the sorting operation, which indicates that a sorter with a circulating memory is much slower than with a ferrite memory.

According to fig. 4 a sorter was built for use with a 101 channel magnetostrictive wire memory, with $N = 5$ and $M = 20$. As ATA the standard amplitude to time converter of the multichannel analyzer is used, with reduced rundown velocity to cover only the voltage range of 20 V. This makes it possible to shift the threshold of the five channels ($N$) from 0 to 80 V in order to work in the region of A pulse amplitudes which is of interest in the experiment. The A and B pulse rate was in the experiments, for which this sorter was built about 1000 pulses per second with less than 1 coincidence per second. From these data the importance of the temporary pulse storage in the coincidence unit can be seen. The low sorting speed of this circuit of about 800 events/sec is of no importance in this case.

## 5. Conclusions

The sorting systems described in this paper ar only one of the possible solutions, which may b useful for the future design of such systems. Onl block diagrams are given, as the actual circuit which were used followed the usual design practice Till now, only the last mentioned sorting syste has been used in practice for several months at ou Institute as it was adequate to meet the present re quirements. This sorter was used with the counte telescope[1]) for the discrimination of protons fro deuterons where it replaced the pulse multiplier t give a better resolution, more reliable operation an easier setup in the experiment to obtain evidenc about the existance of the dineutron[2]).

The two other sorting systems are intended fo similar future experiments where the coincidenc rate is too fast for the previously mentioned sorte and a larger number and capacity of channels i required.

[1]) L. G. Kuo, M. Petravić and B. Turko, Nuclear Instr. an Meth. **10**, No. 1 (1961) 35.

[2]) K. Ilakovac, L. G. Kuo, M. Petravić, I. Šlaus and P Tomaš, Phys. Rev. Letters **6** (1961) 356.

NUCLEAR INSTRUMENTS AND METHODS **13** (1961) 35–42; NORTH-HOLLAND PUBLISHING CO.

# PAIRED-CHAMBER TYPE PILE OSCILLATOR

TOYOJIRO FUKETA

*Nuclear Physics Laboratory, Japan Atomic Energy Research Institute, Tokai-mura, Naka-gun, Ibaraki-ken, Japan*

Received 29 April 1961

pile oscillator, which has been improved from a conventional e with the intention of eliminating the effect from the ctuation of the reactor power by using a method of compen- tion, is reported. The signal-to-noise ratio was increased by a ctor of about 100. The maximum sample size in this os- cillator is 17 mm in diameter and about 100 mm in length. The attainable standard deviation of the measured value is less than $0.5 \times 10^{-3}$ cm² in the whole macroscopic cross section $\Sigma_a V$ of the sample.

## Introduction

The so-called pile oscillation method which is sed for the purpose of neutron absorption cross- ection measurement has been developed since the iddle of 1940's, and has achieved a sensitivity of bout $10^{-3}$ cm² in $\Sigma_a V$ of a sample, where $\Sigma_a$ enotes the absorption cross-section per unit volu- ne and $V$ the volume of the sample. This figure neans that one can measure the absorption cross ction of a sample as little as 80 mg provided that has an absorption cross section of 1 barn and tomic mass of 50; in other words, it needs an mount of about 8 g of such material to measure ne cross section with an accuracy of one per cent.

Today, the thermal neutron absorption cross- ction data for natural elements have become early complete. As regards the isotopic cross ections, however, the nuclides whose cross sections an not be looked up in BNL-325[1]) exceed one undred in number. In general, separated or en- ched isotopes are available only in small amounts nd their enrichments are not always sufficiently igh, so it is desired that sensitivity of the cross- ction measurement is improved. This paper resents one of the approaches towards such an aim.

The pile oscillator is classified in general into ver-all signal type and local signal type. The former neasures the over-all response of neutron flux in a reactor whose reactivity is modulated by the motion of the sample in it, while the latter detects the local depression of neutron flux around the sample which moves back and forth in the reflector of a reactor. By the way, an intermediate type was developed in Châtillon[2]).

The fluctuation of the reactor power disturbs the measurement directly. For the purpose of elimination of this disturbance, narrow-band amplification, which emphasizes the signal due to the sample oscillation, has been a common technique†. This method was also applied to a conventional pile oscillator of local-signal type[3]) which was installed at JRR-1, a Water-Boiler type reactor of 50 kW, but it was not sufficient to eliminate the effect of fluctuation caused by the motion of the control rod. Hence, the measurements had to be made with the automatic power control devices stopped. Moreover, in those cases where accurate data were required, it was necessitated to run the reactor at a low power level††, say 500 W, at which the fluctuation was relatively small.

But now, an improvement has been made to eliminate the influence of the fluctuation of the reactor power by using the method of compensation, and measurements can be made with refined sensitivity.

† For the reference, see ref.[3]).

†† In this oscillator, the frequency of the sample oscillation as about 1 cycle/sec. It has recently turned out that this was ccidentally just the frequency at which distribution of reactor oise takes a minimum, when the power level exceeds 500 watt[4]).

[1]) D. J. Hughes and R. B. Schwartz, Neutron Cross Sections, BNL-325, 2nd edition, (1958).

[2]) D. Breton, Geneva Conference, Paper No. 356 (1955).

[3]) T. Fuketa and S. Otomo, Japan Atomic Energy Research Institute Report 1009 (1960).

[4]) K. Sumita and S. Yamada, private communication.

## 2. Method

The principle of the method is simple as illustrated by fig. 1. In fig. 1, "A" and "B" are neutron detectors having an identical construction, e.g., two boron-coated ionization chambers of the same design.

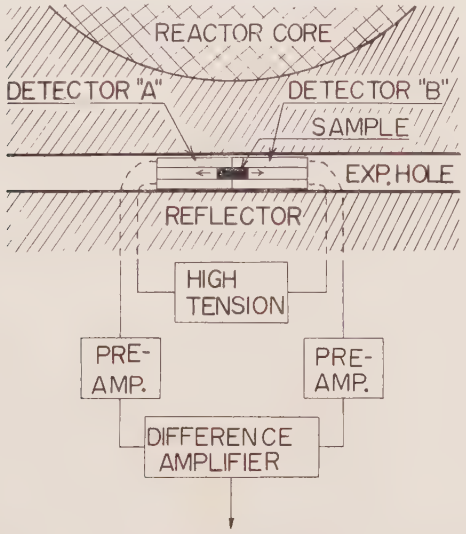


Fig. 1. Principle of the paired-chamber type pile oscillator.

The output current $I(t)$ of the detector, which is operated at a saturation voltage, can be written as follows:

$$I(t) = E(\phi_0 + \Delta\phi(t))\,(1 + p(t))\,(1 + s(t))\,, \qquad (1)$$

where,

$t$ = a variable of time,

$E$ = a constant, relating to the efficiency of the detector,

$\phi_0$ = the neutron flux at the detector corresponding to the mean value of the reactor power during a course of measurement,

$\Delta\phi(t)$ = the variation of the flux corresponding to the fluctuation of the power,

$p(t)$ = a term which represents the modulation of the flux by the oscillation of the sample,

$s(t)$ = a term corresponding to statistical fluctuation in the local flux and the detector efficiency.

Under a high flux, say more than $10^{10}$ n/cm$^2$ sec, the current of an ionization chamber approaches saturation very gradually according as the voltage is increased. When the current is not saturated perfectly, a factor which contains a term depending the variation of the applied voltage has to be cluded in the above formula. But, under the act condition of the experiment this term was negligi small as compared with $p(t)$ and $s(t)$. Moreover current, which is induced by the fluctuation of high tension through the capacity of the detec is omitted in the above formula because of minor importance. However, even if they are tak into account, the argument similar to the follow holds good.

Practically, $\Delta\phi$ is a few percent of $\phi_0$ at most, $p$ is ordinarily less than $10^{-3}$ which corresponds to oscillation of a sample having a $\Sigma_a V$ of about 1 c and $s(t)$ is of an order of $3 \times 10^{-4}$† when the reac is operated at 40 kW, the flux at the detector be $2.8 \times 10^{11}$ n/cm$^2$ sec. Therefore, by neglecting cross terms, eq. (1) is written as follows:

$$I(t) = E\{\phi_0\,(1 + p(t) - s(t)) + \Delta\phi(t)\}\,.$$

If one uses suffixes A and B to classify quantities relating to either of the detectors " and "B",

$$\frac{\Delta\phi^{\mathrm{A}}(t)}{\phi_0{}^{\mathrm{A}}} = \frac{\Delta\phi^{\mathrm{B}}(t)}{\phi_0{}^{\mathrm{B}}}\,.$$

A component of the output current, $I_{\mathrm{p0}}$, wh is due to the oscillation of the sample (referred as pile-oscillator signal or P.O. signal in the lowing) is given by

$$I_{\mathrm{p0}}{}^{\mathrm{A}} = E^{\mathrm{A}}\phi_0{}^{\mathrm{A}}p^{\mathrm{A}}(t) = E^{\mathrm{A}}\phi_0{}^{\mathrm{A}}\sum_1^{\infty}\alpha_n \sin(n\omega t + \varepsilon_n)\,,$$

and

$$I_{\mathrm{p0}}{}^{\mathrm{B}} = E^{\mathrm{B}}\phi_0{}^{\mathrm{B}}p^{\mathrm{B}}(t) = E^{\mathrm{B}}\phi_0{}^{\mathrm{B}}\sum_1^{\infty}\beta_n \sin(n\omega t + \delta_n)\,,$$

providing the sample is a pure absorber, where and $\beta_n$ are constants proportional to the absorpt cross section of the sample, and $\omega/2\pi$ the freque of the oscillation. When the sample is oscilla between the centers of the two detectors, then fundamental ($n = 1$) is predominant, and, mo over, if the flux distribution is symmetric about middle point of the two detectors,

$$\alpha_n = \beta_n, \quad \varepsilon_n = \delta_n - \pi, \quad \text{and} \quad \phi_0{}^{\mathrm{A}} = \phi_0{}^{\mathrm{B}}\,.$$

† This value is a fractional standard deviation in a t range which is equal to the time constant of the cham $\approx 10^{-5}$ sec.

By taking difference of the output voltages of the two detectors, which have the output resistances of the same magnitude, $\Delta\phi$ is cancelled and the resultant voltage signal $S$ is given by

$$S = CE^{A}\phi_0^{A}\{2\sum_{1}^{\infty}\alpha_n \sin(n\omega t + \varepsilon_n) + (s^{A}(t) - s^{B}(t))\}, \quad (3)$$

where $C$ is a constant. Since $s(t)$ is statistical in nature, the following approximation can be made:

$$s^{A}(t) - s^{B}(t) \approx s^{A}(t) + s^{B}(t),$$

and

$$\overline{(s^{A}(t))^2} \approx \overline{(s^{B}(t))^2}.$$

Consequently,

$$S \approx 2CE^{A}\phi_0^{A}\{\sum_{1}^{\infty}\alpha_n \sin(n\omega t + \varepsilon_n) + s^{A}(t)\}. \quad (4)$$

During a course of measurement, as described in the next section, the signal $S$ is integrated for a portion of its positive or negative half-cycles. For example, if such an integration is done over 1 minute, the integrated value of $s(t)$ is decreased down to about $2 \times 10^{-7}$ at the reactor power of 40 kW, whereas that of $p(t)$ amounts to about $6 \times 10^{-5}$ for a sample having a $\Sigma_a V$ of $10^{-3}$ cm$^2$.

If $\phi_0^{A} \neq \phi_0^{B}$ and the center of the sample oscillation is set at an arbitrary point, relations (2), (3), and (4) do not hold. However, anyway, $\Delta\phi$ can be cancelled by using an output resistance of "B" which is $E^{A}\phi_0^{A}/E^{B}\phi_0^{B}$ times larger than that of "A". The expression of the output of the difference amplifier becomes intricate, but, it remains to be linear in regard to $\alpha_n$ and $\beta_n$ and hence proportional to the absorption cross section of the sample.

When the effect of scattering of neutrons by the sample is to be taken into account, $p(t)$ needs to include another Fourier series which is similar to one expressing the absorption effect of the sample. Then, the pile-oscillator signal is expressed by a linear combination of two series of terms which are proportional to the absorption and scattering cross sections of the sample, respectively. Hoover *et al.*[5]) introduced a method which has been used successfully to eliminate the effect of scattering in the conventional pile oscillator of local signal type. In this method, the center of the oscillation is adjusted relative to the annular-type ionization chamber so that an appropriate phase or waveform difference may be made between the component of the signal due to absorption and that due to scattering. Then, the output signal is integrated over a certain phase interval of the oscillation, in which the integrated value of the scattering component vanishes. It is obvious that Hoover's method is applicable in our case also.

In order to measure the absorption cross section of a sample, it is necessary to monitor $\phi_0$; but, when the reactor is controlled automatically, the flux is so steady that it is a minor factor in the correction.

### 3. Equipment

The equipment is common to the conventional pile oscillator of local-signal type[3]), with the exception of the neutron detector and the difference amplifier. Fig. 2 represents the schematic diagram of the detector arrangement and the driving mechanism. The rotational speed of the driving motor is regulated by means of a magnetic amplifier system. The sample is set in an accurate simple-harmonic motion along the axis of the "paired" annular ionization chambers by a rotation-to-sinusoidal motion converter with a constancy of the period less than 2%. The sample-oscillation frequency and its amplitude are variable, but, in the present investigation, they are fixed at 1 cycle/sec and $\pm$ 10 cm, respectively. The rotating shutter produces photo-signals which indicate the phase of sample oscillation.

Two types of the plug, in which the paired chambers and the sample supporting mechanism are mounted, were prepared. One, type A, which is suitable for the measurement of a sample having a small $\Sigma_a$ or requiring a large space, is illustrated schematically in fig. 2. A part of the other, type B, which is prepared for the measurement of plate- or foil-shaped sample, is shown in fig. 3. In the type-A plug, the sample is suspended in an aluminium pipe having an inside diameter of 18 mm by a string from its top, and the pipe is oscillated up and down. In the type-B plug, a sample holder made of thin zirconium sheet is mounted on an endless stainless-steel tape stretched between pulleys at the two

[5]) J. I. Hoover, W. H. Jordan, C. D. Moak, L. Pardue, H. Pomerance, J. D. Strong and E. O. Wollan, Phys. Rev. **74** (1948) 864.

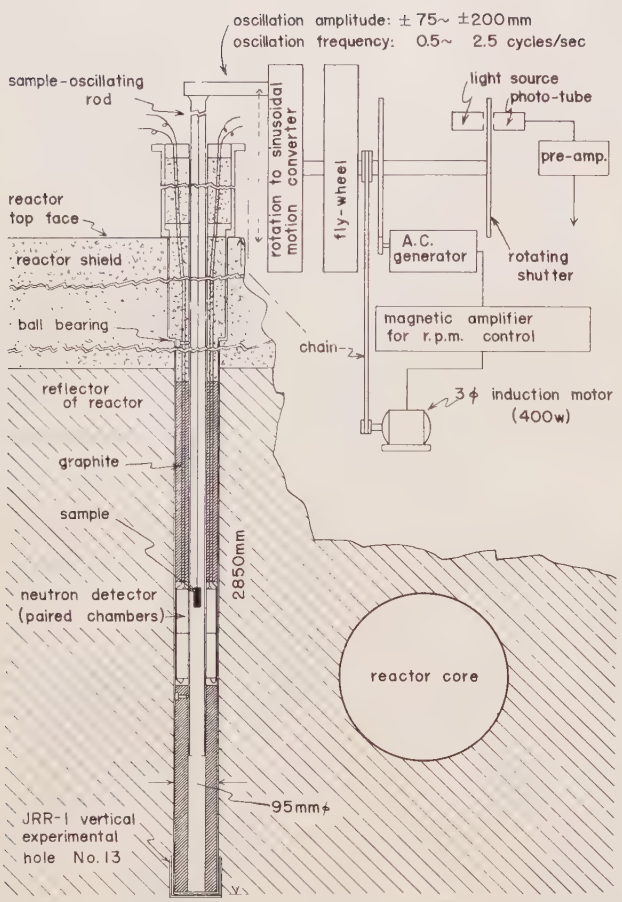


Fig. 2. Schematic diagram of the detector arrangement and the driving mechanism.

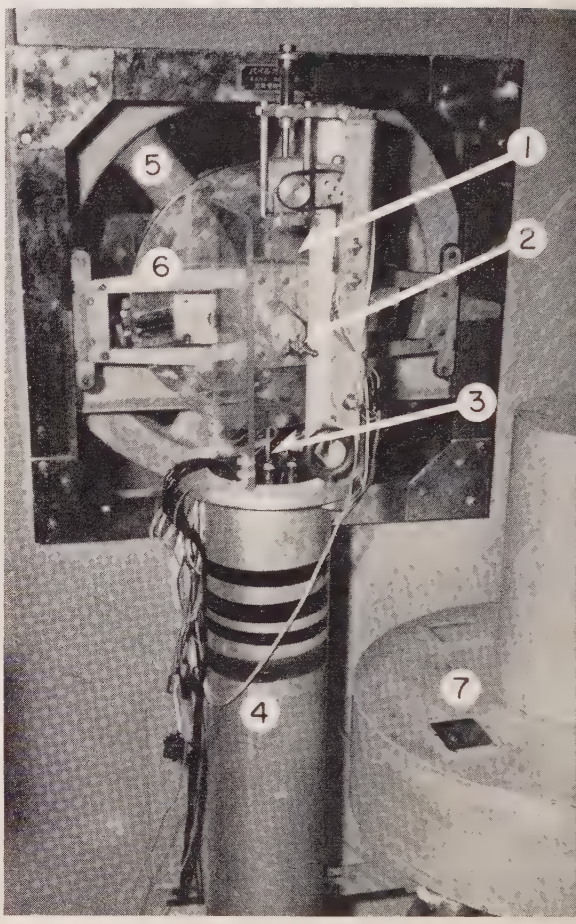


Fig. 3. Front of the sample driving mechanism and the upp part of the type-B plug.

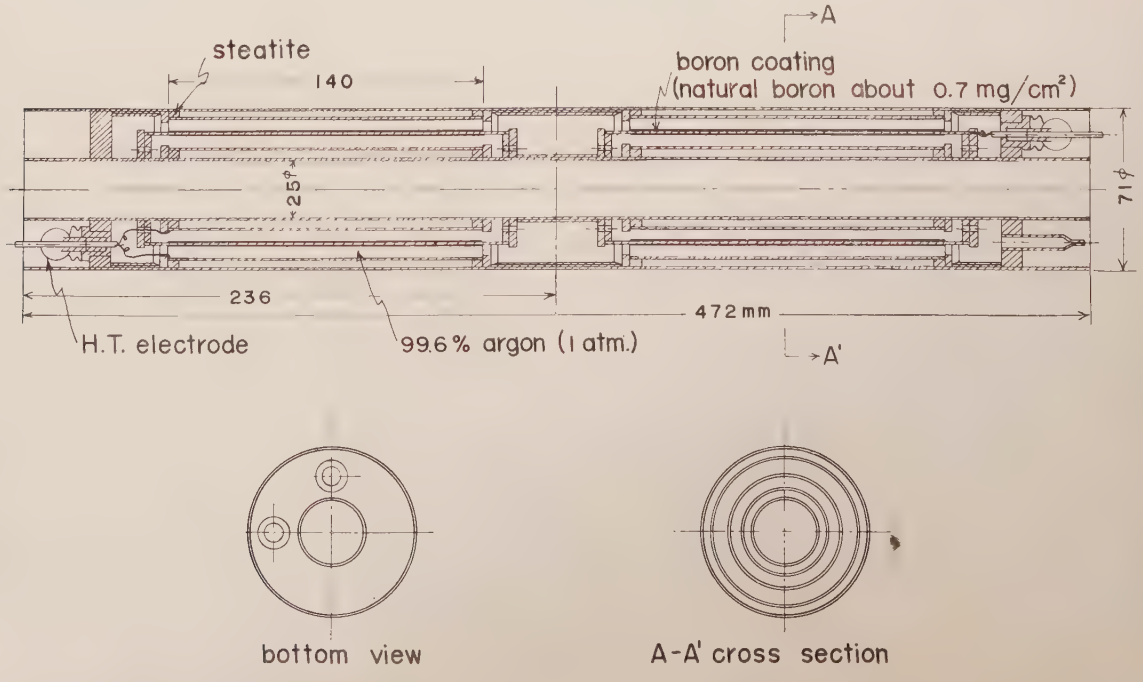


Fig. 4. "Paired" annular ionization chambers.

Fig. 3.
① : endless stainless-steel tape,
② : clutch,
③ : sample holder made of thin zirconium sheet,
④ : type-B plug,
⑤ : fly-wheel,
⑥ : rotation-to-sinusoidal motion converter,
⑦ : control-rod mechanism of the JRR-1.

ends of the plug, and the tape is driven by the arm of the rotation-to-sinusoidal motion converter.

The center of the detector had better be set at the center level of the reactor core, because the flux is maximum and its gradient is minimum at that place; this latter condition is favorable to decrease the scattering effect of the sample. The center of the paired chambers in the type-B plug is set at the core center level, whereas in the type-A plug it is shifted upwards to reduce the end-effect of the oscillating aluminium pipe.

The structure of the paired chambers is shown in fig. 4. At a flux of $3 \times 10^{10}$ neutrons/cm$^2$ sec, the ion current is nearly saturated at a collecting voltage of 600 volts and amounts to about 100 microamperes.

The block diagram of the circuit is shown in fig. 5. The signals from the paired chambers are fed to the difference amplifier, which is a conventional one with a 12AX7 tube having a constant current circuit at its cathode. The output of the difference amplifier is then amplified by the main amplifier, whose frequency response is approximately flat from 0.6 to 10 cycles/sec. After the signal being amplified to a range up to one hundred volts in peak-to-peak value, it is sent to the integrator. The input circuit of the integrator is gated for a proper phase interval for the purpose of cancelling the neutron scattering signal. The gating circuit is triggered by the signals from the rotating shutter. The output of the integrator is recorded continuously by an electronic recorder, and the cross-sectional value to be measured is obtained from the gradient of the recorded line—strictly speaking, a step function. Meanwhile, the d.c. output of the one part of the paired chambers is also recorded in another electronic recorder to monitor the power level of the reactor.

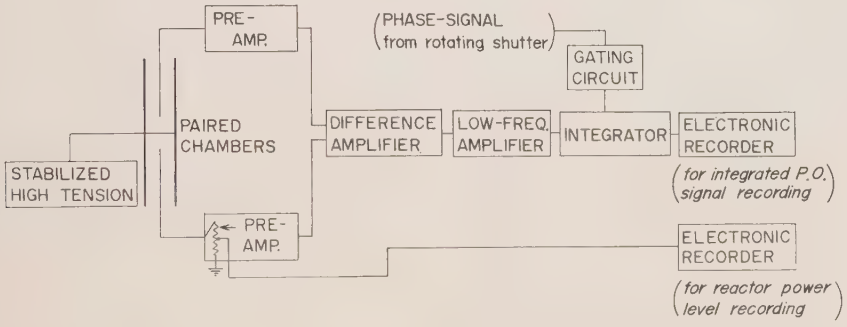


Fig. 5. Block diagram of the circuit.

## 4. Performance

### 4.1. ELIMINATION OF THE INFLUENCE OF THE REACTOR POWER FLUCTUATION

How the effects of the reactor power fluctuation induced in the two chambers cancel each other is illustrated in fig. 6. In Fig. 6(a), the two lower traces represent the signals from each of the two chambers, and the upper one the output of the difference amplifier. While the pile-oscillator signal is hardly recognized in the output from the individual chamber, it is predominant resolutely in the output of the difference amplifier. From this figure, it is estimated that the ratio of the pile-oscillator signal to the power-fluctuation signal is improved by a factor of about 100. Fig. 6(b) and (c) are the records of the integrated pile-oscillator signal and the reactor power level, respectively. The latter shows a power fluctuation of about 3.4%

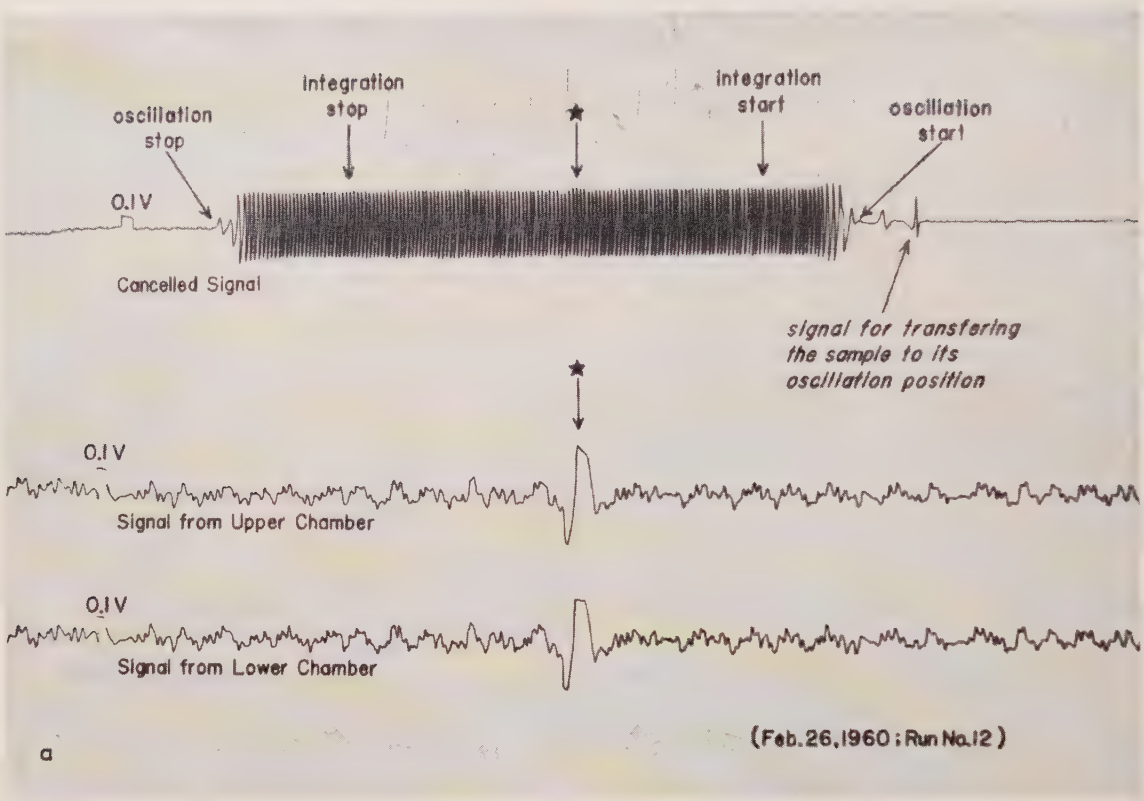


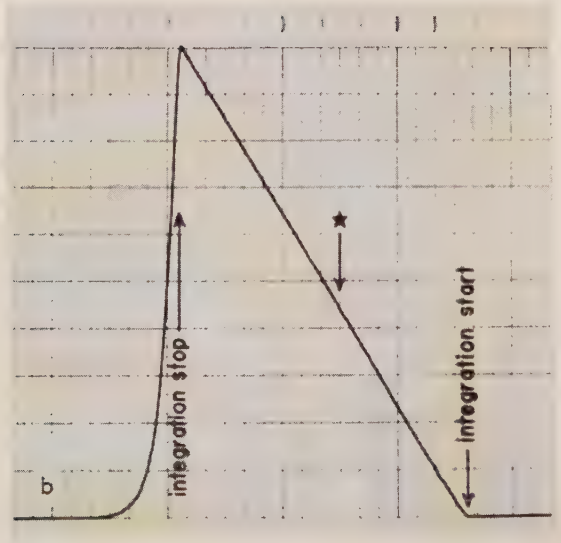


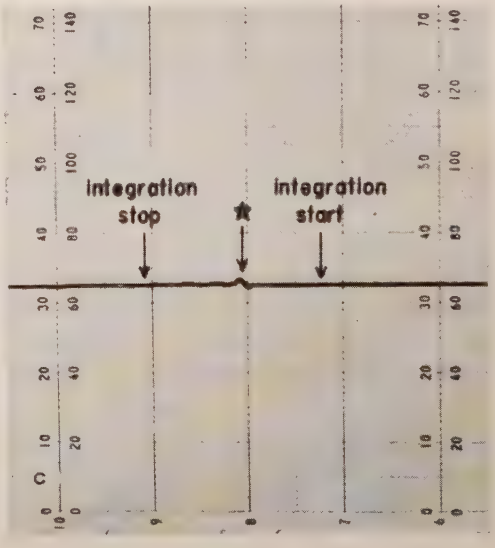


Fig. 6. Illustration of elimination of the influence of the reactor power fluctuation.

(a) shows the oscillograms of the output signal of the difference amplifier and the signals from the paired chamber
(b) is a record of the integrated pile-oscillator singal, and (c) that of the d.c. component of one of the chambers. A samp
having a $\Sigma_a V$ of about 0.55 cm² is used with the type-A plug.

n peak-to-peak value at the mark of star which indicates the moment of action of the control rod, but the outputs of the difference amplifier and the integrated pile-oscillator signal are not affected by it, as seen in (a) and (b).

The reactor noise depends on the power level, the fuel condition and so on; and, moreover, the response of the control rod changes according to the characteristics of the control circuit, e.g., the time constant. Therefore, the elimination of the influence of the power fluctuation depends somewhat upon the operating condition of the reactor. The above-quoted factor of 100 is presented as an example. It is always easy to make this factor larger than 25.

### 4.2. RESPONSE OF THE PILE-OSCILLATOR SIGNAL

The waveform of the output of the difference amplifier depends on the position of the sample-oscillation center relative to the chambers, the amplitude of oscillation, the size, and the ratio of absorption to scattering cross section of the sample. To check this dependence, it is convenient to use cadmium and graphite samples which can be regarded as a pure absorber and scatterer, respectively. The recorded waveforms for various positions of the oscillation center are shown in fig. 7. The ordinates which linearly depend on the cross sections of the samples are shown in a scale common to both scattering and absorption cross sections. The variation of the waveforms or the phases with the positions of the sample oscillation are clearly different in the two cases. Besides the phase relation, it is worthy of notice that the minima of the amplitudes of the scattering signals occur at about + 24 cm and — 21 cm of the sample position, whereas the absorption signals are not so small thereabout.

In order to find a proper phase interval, in which the output signal was to be integrated, a series of measurements were done, in which the phase interval of integration was shifted as a variable, while the magnitude of the interval being fixed at a constant value of 90 degrees and the position of the sample varied as a parameter. The result is shown in fig. 8. The abscissa represents the phase angle of the center of integration interval, and the ordinates

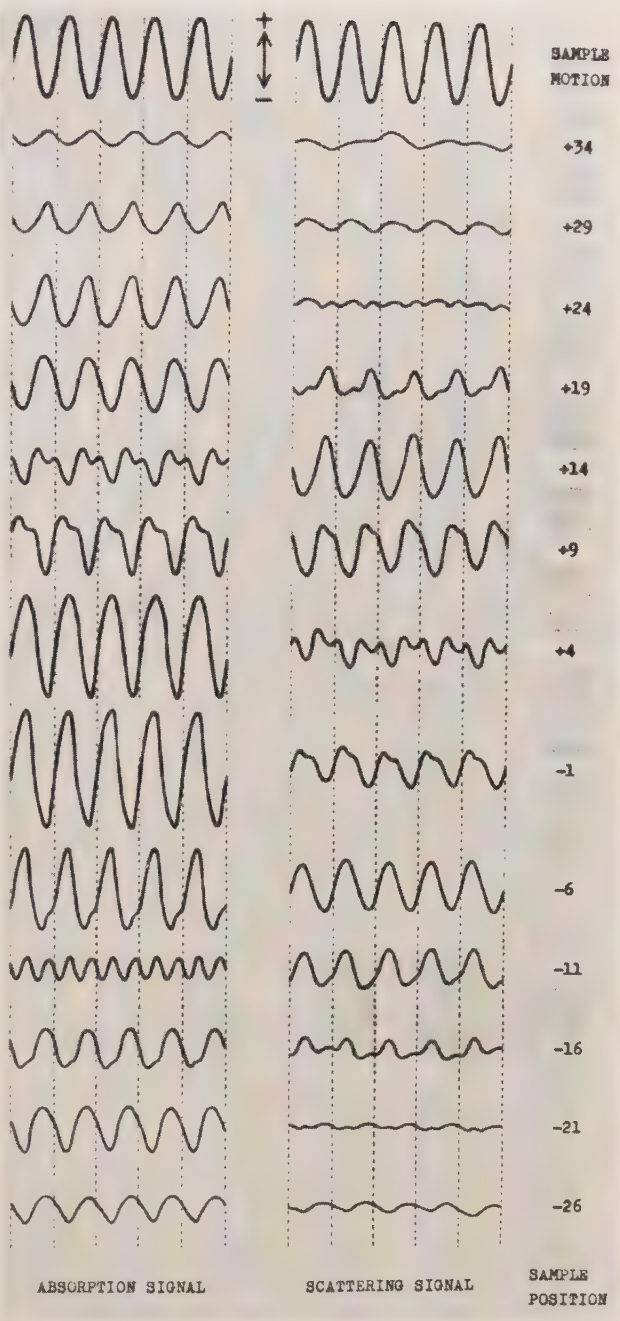


Fig. 7. Waveforms of the pile-oscillator signals, that is, outputs of the difference amplifier.

the integrated pile-oscillator signals of a cadmium and graphite sample, both of which have cross sections of the same magnitude. The hatched portion is the most favorable to eliminate the effect of scattering, here the ratio (the signal of a scatterer of unit scattering cross section)/(the signal of an

absorber of unit absorption c.s.) being less than 0.002.

The linearity of the measurement, that is the linear relationship between the integrated output and the $\Sigma_a V$ of the sample, is affected by the accuracy of correction for the power-level drift, the linearity, and the stability of the measuring circuit.

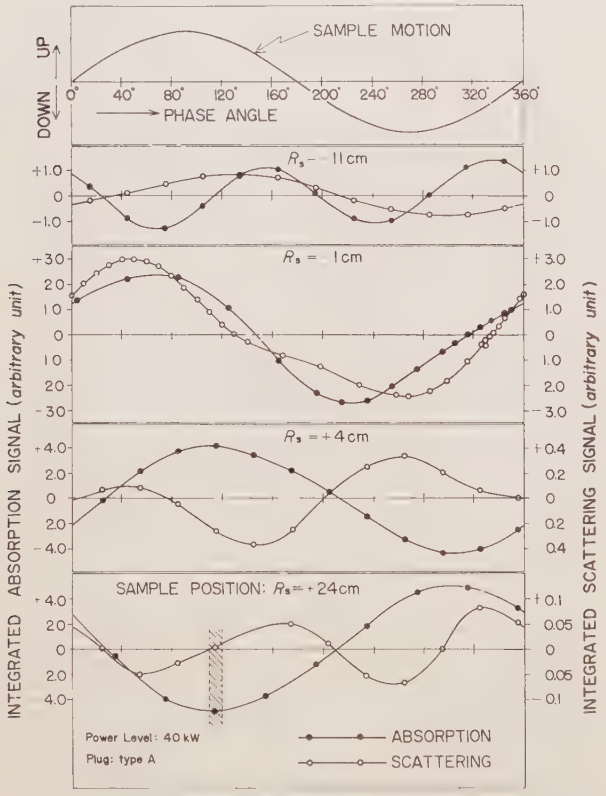


Fig. 8. Dependences of the integrated pile-oscillator signals upon the phase of the integration interval. The position of the sample oscillation is taken as a parameter. The interval of the integration is fixed at 90 degrees and the abscissa represents the phase angle of its center.

The linearity is checked by changing the mass of the sample under the condition that no correction for self-shielding is required. The linearity is illustrated in fig. 9. Each plot corresponds to a measurement of 2 ~ 3 minutes. The straight line in this figure is fitted by means of the least-squares method, and the quoted error is the standard deviation. Such a line is determined in each series of measurements by using several standard samples (for example: gold foils or boric-acid solutions), and is used as a calibration line by which the integrated P.O. signal is converted to the $\Sigma_a V$ value. Generally, the measurement is made either with thin or diluted samples in order to minimize the correction for the self-shielding effect, or with standard samples having $\Sigma_a d$ nearly equal to that of the sample to be measured, where $d$ represents the thickness of sample.

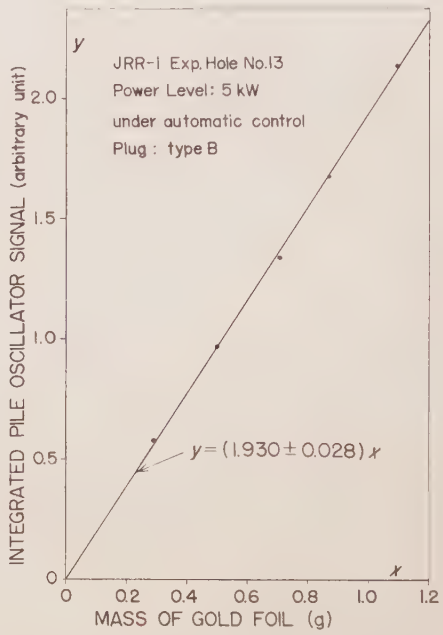
JRR-1 Exp. Hole No.13
Power Level: 5 kW
under automatic control
Plug : type B
$y = (1.930 \pm 0.028)\,x$
INTEGRATED PILE OSCILLATOR SIGNAL (arbitrary unit)
MASS OF GOLD FOIL (g)

Fig. 9. An example of the calibration curve.

### 4.3 ACCURACY OF THE CROSS-SECTION MEASUREMENT

In order to check the accuracy and the stability of the measurement, we measured a sample having a $\Sigma_a V$ of 0.2 cm² seven times at intervals of four minutes, time of each measurement being four minutes. The standard deviation of the mean value was 0.28%, i.e., $0.57 \times 10^{-3}$ cm².

It will not be difficult to compare two samples with an accuracy less than $0.5 \times 10^{-3}$ cm² by a measurement of less than two hours.

**Acknowledgements**

The author wishes to thank Dr. T. Momota for his constant encouragement, advices, and critical reading of the manuscript, and Mr. S. Otomo and Mr. M. Ishii for their assistance and cooperation during the experiments.

NUCLEAR INSTRUMENTS AND METHODS 13 (1961) 43–49; NORTH-HOLLAND PUBLISHING CO.

# A LOW BACKGROUND BETA-RAY SCINTILLATION SPECTROMETER USING A COINCIDENCE METHOD WITH A GEIGER COUNTER

EIICHI TANAKA

*Physics Division, National Institute of Radiological Sciences, 250, Kurosuna-cho, Chiba-shi, Japan*

Received 15 May 1961

The design and performance of a new type of $\beta$-ray scintillation spectrometer suitable for measuring very low $\beta$-ray activities of solids are described. The spectrometer consists of a scintillation counter using a plastic scintillator and a gas flow G-M counter located in a hollow of the scintillator, and the coincidence operation between these two counters is applied. Cosmic ray counts are rejected by pulse height analysis. Inside the 10 cm lead shield the background counting rate is less than that of conventional low background counters using anti-coincidence shields, and a typical background counting rate of 0.15 cpm for the energy range from 0.5 to 2.5 MeV was obtained.

This system can also be used as a low background counting device in a limited energy range. For relatively high energy $\beta$-ray emitters, the coincidence countings are used between scintillation pulses and G-M pulses. In this case, the background is reduced by rejecting cosmic ray counts, high and low energy components of the $\gamma$-ray background and noise or spurious counts of the detectors. For low energy $\beta$-ray emitters, on the other hand, the anti-coincidence countings are suitable, then the cosmic ray counts and high energy components of the $\gamma$-ray background can be rejected.

## 1. Introduction

In the field of a low level counting of $\beta$-ray activities, it is often desired to get information about their energy spectra. Beta-ray energy analyses by absorption methods, for instance Feather's analysis[1]) or Harley's method[2]), using conventional low background $\beta$-ray counters are not only very troublesome but also time-consuming for measurements and they are practically impossible in the case of extremely low level counting, because of the reduction of counting rate due to the $\beta$-ray absorption.

Other methods of $\beta$-ray spectrometry are those using scintillation counters[3]) but these detectors have relatively high backgrounds because of their high efficiencies for environmental $\gamma$-radiations, so they cannot be used in low level countings.

The method described here offers combined advantages of the high efficiency of a scintillation type spectrometer and the low background of a G-M counter. The detector consists of a scintillation counter using a hollow type plastic scintillator, and a gas flow G-M counter which is located in the hollow of the scintillator (fig. 1), and scintillation pulses coincident with G-M pulses are analyzed or counted. The $\beta$-particles emitted from a sample trigger both counters and give coincidence outputs, but most of the background counts of the scintillation counter do not coincide with the G-M counter signals, so that the background of the system is restricted by that of the G-M counter. Cosmic ray $\mu$ mesons may give coincidence outputs, but these pulses can be discriminated by the pulse height selection.

## 2. Description of Apparatus

The detection system used here is shown schematically in fig. 1. A plastic scintillator has a hollow in its lower face, of 26 mm diameter and 10 mm depth. The inner surface of the hollow, coated with Al and then Au by vacuum evaporation, acts as a cathode of a Q-gas flow G-M counter. The window of the counter is a gold plated Mylar film of a total thickness of about 1.3 mg/cm$^2$. The anode of the G-M counter is a horizontal loop of stainless steel wire of 0.05 mm in diameter. The anode output terminal and the inlet and outlet tubes for the

[1]) N. Feather, Proc. Cambridge Phil. Soc. **34** (1938) 599; E. Bleuler and W. Zunti, Helv. Phys. Acta **19** (1946) 137.
[2]) J. H. Harley and N. Hallden, Nucleonics **13**, 1 (1955) 32.
[3]) P. R. Bell, in K. Siegbahn (ed.), Beta- and Gamma-ray. Spectroscopy (North-Holland Publishing Co., Amsterdam, 1955).

counting gas are located in another Lucite plate, making possible the easy light shielding of the scintillator as shown in the figure.

The scintillator is coupled to a 2″ photomultiplier tube, EMI 6097B, through a Lucite light pipe. The sides of the scintillator and the light pipe are surrounded by MgO powder light reflector. The size and shape of the plastic scintillator are chosen to give sufficiently large scintillation signals for cosmic ray $\mu$ mesons which pass through the G-M counter, so that the $\mu$ mesons are discriminated from $\beta$-rays emitted from commonly used isotopes. The minimum path length which the $\mu$ meson must traverse in the scintillator to trigger the G-M counter, is about 17 mm except a small part near the anode supporter. This path length corresponds to an energy loss of about 3.5 MeV, for the $\mu$ mesons.

The associated electronic circuitry is shown schematically in fig. 2. The amplifier used in the scintillation system is a non-overloading amplifier using an delay line shaping whose rise time is 0.2 $\mu$sec and clipping time is 1 $\mu$sec, but the output

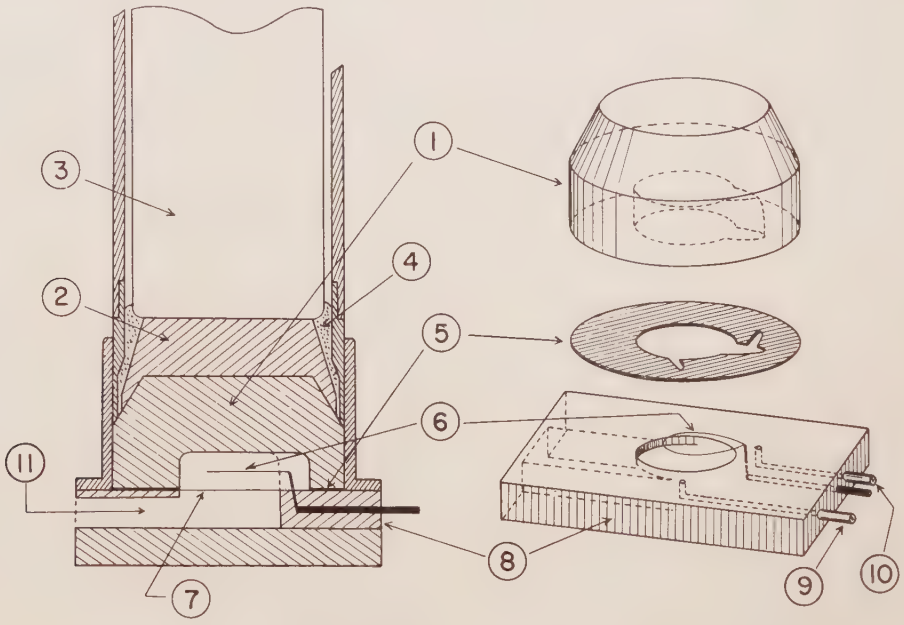


Fig. 1. Cross-section and exploded view showing the detector assembly.

(1) Plastic scintillator;
(2) Lucite light pipe;
(3) Photo-multiplier tube (EMI 6097B);
(4) MgO powder light reflector;
(5) Vinyl packing;
(6) Anode wire of the G-M counter;
(7) Window of the G-M counter (Gold plated Mylar film of 1.3 mg/cm² thick);
(8) Lucite plate;
(9) Counting gas inlet tube;
(10) Counting gas outlet tube;
(11) Sample inlet.

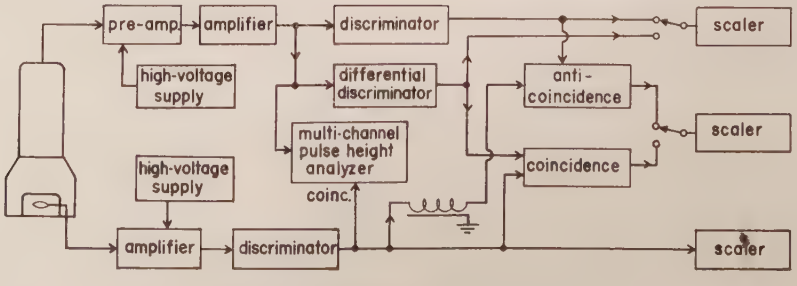


Fig. 2. Block diagram of the electronic circuitry.

stage coupled to the multi-channel pulse height analyzer was somewhat modified to be matched with it. The preceding pre-amplifier is of a White cathode follower type. The amplifier and the discriminator used in the G-M counter system have an over-all input sensitivity of about 0.3 V.

Various operational modes can be used according to the measuring purposes. In the $\beta$-ray spectrometry, the scintillation pulses are sorted by the multi-channel pulse height analyzer (RCL 256 channel analyzer). To obtain coincidence spectra, signals from the G-M counter are used to gate the analyzer. The G-M pulses are shaped to 4.5 $\mu$sec square pulses and are fed into the "Delayed Coincidence" terminal of the analyzer, while the gating pulses of the analyzer are delayed 1 $\mu$sec and have 1 $\mu$sec widths, then the total resolving time of the coincidence would be about 5.5 $\mu$sec.

In the coincidence or anti-coincidence counting, the resultant counting rates are recorded in a scaler, while the counting rates of the both detectors are monitored by the other two scalers. The total resolving time of the coincidence was chosen to be about 11 $\mu$sec. In the anti-coincidence arrangement, 4.5 $\mu$sec G-M signals which are delayed 1.5 $\mu$sec in a delay line and the inhibit signals of about 8 $\mu$sec widths from the scintillation counter are fed to the anti-coincidence circuit.

The counting characteristics of the G-M counter are as follows: the plateau of the counter lies 1100 to 1300 V, and has a slope of less than 3% per 100V. The counting efficiency of the G-M counter was checked by counting a natural potassium sample (KCl 15 mg) deposited uniformly on a Lucite holder. When the sample was located about 5 mm from the window, the counting efficiency at the middle of the plateau was 39%. (The $\beta$-particle emission rate was taken to be 0.91 $\beta$/min/mg KCl.)

The energy resolution of the scintillation counter defined by the full width at half maximum is about 20% for the internal conversion electrons emitted from a collimated $Cs^{137}$ source. This resolution is not so good as expected; this may be due to the poor scintillation efficiency of the plastic scintillator used. (It is about 35% of that of an anthracene crystal.)

The detector assembly is shielded with lead bricks 10 cm thick, and all the data reported here have been taken in this shield.

### 3. Spectra of the Background

The pulse height spectra of the background of the scintillation counter obtained with and without the coincidence operation are shown in fig. 3. The peak at about 4 MeV is caused by cosmic rays. In the coincidence spectrum, the pulse height distribution of the cosmic rays has a sharply defined edge on its lower energy side, and it will be seen that the rejection of cosmic ray counts by pulse size discrimination is easily obtainable. On the other hand, in the spectrum obtained without the coincidence operation, it spreads to the low energy region due to the short cut paths of the cosmic ray particles through the edge of the scintillator.

The background in the low energy region is mainly caused by the environmental $\gamma$-rays. The reduction in the background count in this region by the coincidence operation is quite effective. For example, in the energy range of 0.5–2.5 MeV, the background count was reduced by the factor of

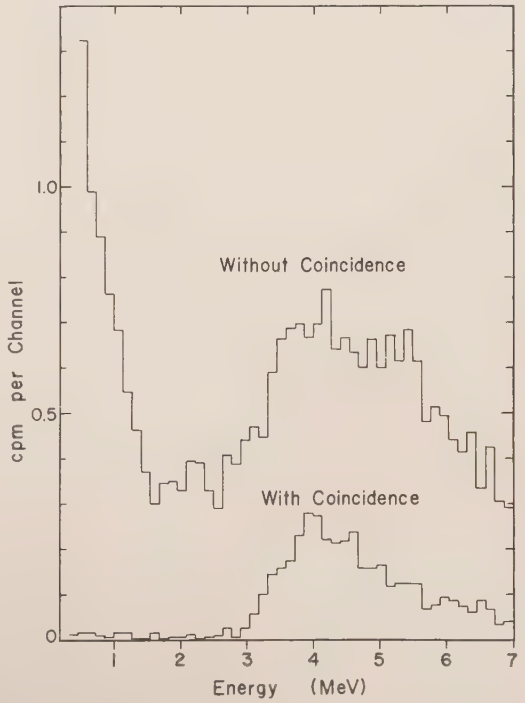


Fig. 3. Pulse height distribution of the background of the scintillation counter obtained with and without the coincidence operation.

more than 50, and a typical value of 0.15 cpm was obtained.

The total background counting rate of the G-M counter is 5.3 cpm, and is stable for long periods. The composition of this background was examined by the various operations. These results are expressed as the counting rates of the G-M pulses which coincide with the scintillation pulses in a certain energy range, and summarized in table 1.

TABLE 1
Composition of the background of the G-M counter in a 10 cm lead shield

| Energy range (MeV) | Coincidence (cpm) | Remark |
|---|---|---|
| $> 2.5$ | 5.0 | including cosmic ray counts |
| 2.0 –2.5 | $\approx 0.04$ | 0.25 cpm |
| 1.5 –2.0 | $\approx 0.03$ | |
| 1.0 –1.5 | $\approx 0.03$ | |
| 0.5 –1.0 | $\approx 0.05$ | |
| 0.025–0.5 | $\approx 0.10$ | |
| $< 0.025$ or not coincide | $\approx 0.08$ | including spurious counts |
| Total | 5.3 | |

Most of the coincidence counts in energy ranges higher than 2.5 MeV are due to cosmic rays.

There were a few counts which do not coincide with the scintillation pulses greater than 25 keV. These counts seem to be caused by the electrons which are stopped or back-scattered before they enter the scintillator deeply, or the electrons emitted from the boundary layer between the both detectors, or the spurious counts of the G-M counter.

## 4. Performance as a $\beta$-ray Spectrometer

To use this system as a low background $\beta$-ray spectrometer, the scintillation pulses which coincide with the G-M pulses are sorted by the 256 channel analyzer.

### 4.1. SPECTRUM OF PURE $\beta$-RAY EMITTER

Fig. 4 shows the pulse height spectra of $Sr^{90}$-$Y^{90}$ obtained with and without the coincidence operation. In this case, as the source is a pure $\beta$-ray emitter ($E_\beta = 0.54$; 2.26 MeV), these two spectra have nearly the same shape, and it can be seen that the coincidence operation does not cause a serious distortion in the spectrum. However, a little decrease in counting rate is observed. The reason for this reduction is perhaps that the intrinsic efficiency of the G-M counter is not exactly 100%.

In order to examine this in more detail, the ratio

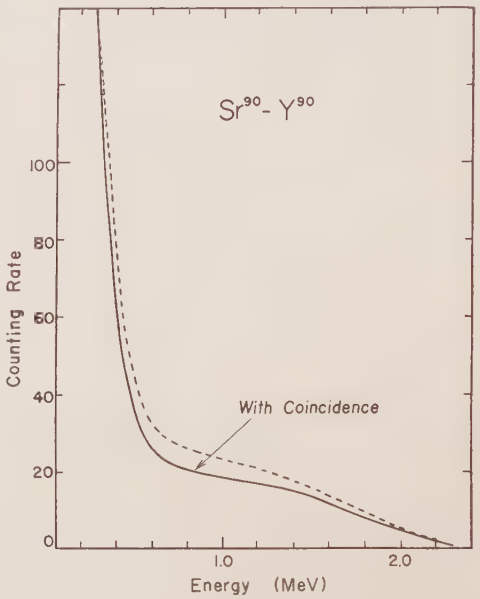


Fig. 4. Pulse height spectra of $Sr^{90}$-$Y^{90}$. Solid curve: obtained with coincidence operation. Dashed curve: obtained without coincidence operation.

of the coincidence counting rate to the scintillation counting rate was checked by using the differential discriminator at the various level settings. The intrinsic efficiency at the middle of the plateau was found to be about 80% for high energy electrons ($> 0.5$ MeV) and to reach about 90% as the electron energy decreases. The reason for this seems to be that the specific ionization of an electron in the counting gas increases with the decrease of the electron energy.

### 4.2. EFFECTS OF $\gamma$-RAYS

In the case of a $\beta$–$\gamma$ emitter whose $\beta$-disintegration is accompanied by the emission of $\gamma$-rays, the $\beta$-ray spectrum obtained with a simple scintillation counter is often distorted by the $\gamma$-rays, and this

effect is serious when the scintillator is large. The distortion of the spectrum is due to two phenomena; i.e. the detections of $\gamma$-rays which are not simultaneous with $\beta$-ray detections, and the simultaneous detections of $\beta$- and $\gamma$-rays. When the coincidence method is used, it is evident that only the latter case occurs, and the former distortion is effectively eliminated.

Let us now consider a sample which emits one $\beta$-particle and one $\gamma$-ray quantum per disintegration. The $\gamma$-ray counting rates recorded with and without the coincidence operation are given by $\varepsilon_\beta \varepsilon_\gamma N$ and $\varepsilon_\gamma N$ respectively, where $N$ is the disintegration rate of the source, $\varepsilon_\beta$ is the counting efficiency of the G-M counter for $\beta$-rays, and $\varepsilon_\gamma$ is the counting efficiency of the scintillation counter for $\gamma$-rays.

Thus, if the type of distortion is not concerned, it may be described that the coincidence operation improves the distortion by the factor of

$$K = \frac{\varepsilon_\gamma N}{\varepsilon_\beta \varepsilon_\gamma N} = \frac{1}{\varepsilon_\beta}.$$

For this reason, the spectrum distortion is fairly improved, although a relatively large size scintillator must be used in our coincidence spectrometer.

Figs. 5(a) and (b) show the spectra of $Co^{60}$ ($E_\beta = 0.31$ MeV, $E_\gamma = 1.17$; 1.33 MeV) obtained in the different geometries. The sample is mounted on a Lucite holder, and is located about 7 mm and 3 mm from the window respectively. $\varepsilon_\beta$'s obtained from the sample activity and the counting rates measured with the G-M counter are 0.33 at 3 mm and 0.24 at 7 mm. It will be seen that the coincidence operation decreases the $\gamma$-ray counts by the factor of about $1/\varepsilon_\beta$.

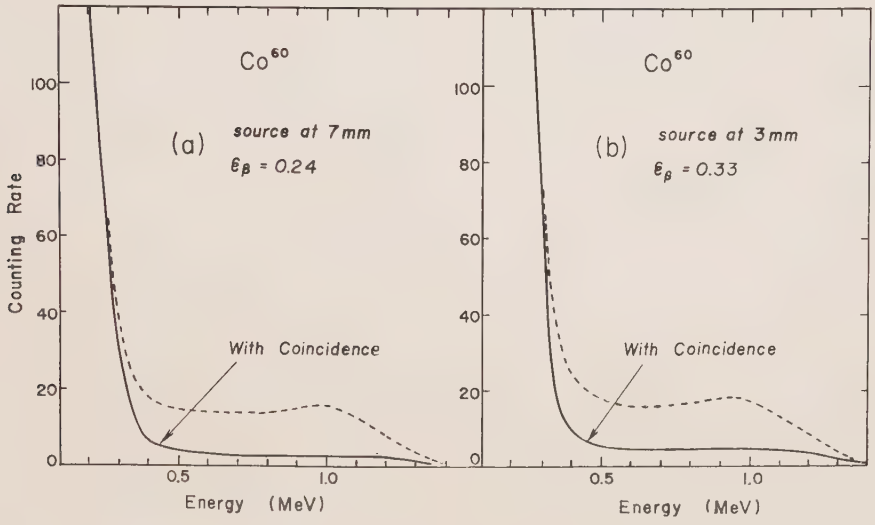


Fig. 5. Pulse height spectra of $Co^{60}$. Solid curve: obtained with coincidence operation. Dashed curve: obtained without coincidence operation.

In the case where $\gamma$-rays are emitted not simultaneously with $\beta$-rays, the disturbance of the $\gamma$-rays is effectively eliminated by the coincidence operation, and no consideration is necessary. As an example, the spectra of $Cs^{137}$ ($E_\beta = 0.51$ MeV (92%); 1.17 MeV (8%), $E_\gamma = 0.662$ MeV) obtained with and without the coincidence operation are shown in fig. 6. The main difference between these spectra is caused by the Compton scattering of $\gamma$-rays. The peak at about 0.63 MeV is an internal conversion line of $Ba^{137m}$.

### 4.3. EXAMPLES OF LOW LEVEL SAMPLES

A few examples of $\beta$-ray spectra obtained with low activity samples are shown in figs. 7–9, and the backgrounds obtained in the same measuring conditions are also shown as the shadowed area in the figures. Fig. 7 is a spectrum of $K^{40}$ ($E_\beta = 1.32$ MeV) in 15 mg of natural KCl deposited on a Lucite

holder. The net counting rate of the sample determined with the G-M counter was about 5.7 cpm.

Fig. 8 shows a spectrum of $Cs^{137}$ in soil. The sample was extracted chemically from 10 g of dried soil, and deposited as $Cs(PtCl_6)$ on a filter paper. The amount of the solid obtained was 50 mg, and the sample counting rate was about 2.0 cpm. The dashed curve in the figure is the spectrum shape obtained with a strong $Cs^{137}$ source.

Fig. 9 is a spectrum of $Sr^{90}$-$Y^{90}$ sample extracted from 4.0 g of human bone ash. The sample was 74 mg of $SrCO_3$ deposited on a filter paper, and its activity was about 0.8 cpm. The dashed curve also shows the spectrum shape of a strong $Sr^{90}$-$Y^{90}$ source.

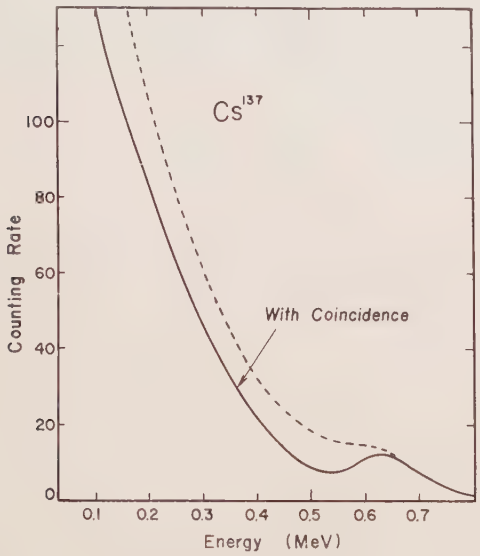


Fig. 6. Pulse height spectra of $Cs^{137}$. Solid curve: obtained with coincidence operation. Dashed curve: obtained without coincidence operation.

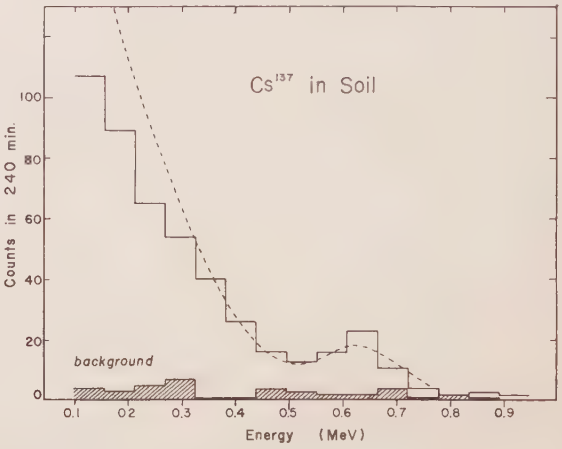


Fig. 8. Spectrum of $Cs^{137}$ in soil. Net counting rate is 2.0 cpm. (dashed curve shows the spectrum shape of a strong $Cs^{137}$ source).

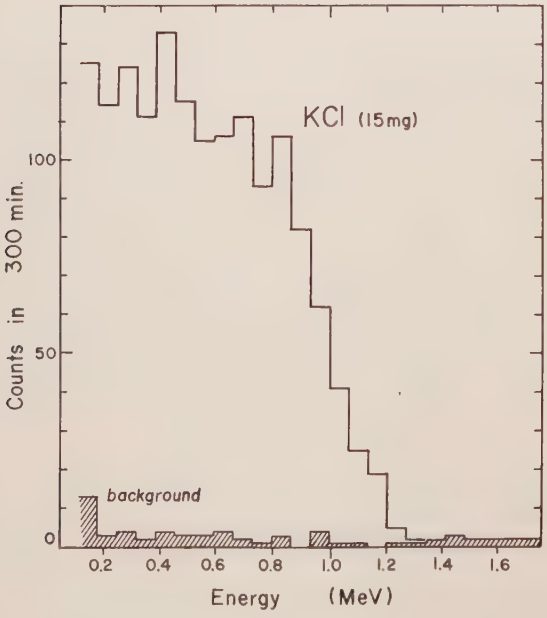


Fig. 7.
Spectrum of $K^{40}$ in natural KCl. Net counting rate is 5.7 cpm.

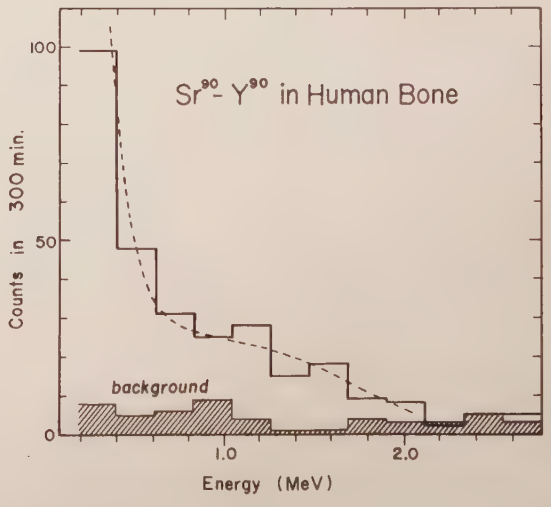


Fig. 9. Spectrum of $Sr^{90}$-$Y^{90}$ in human bone. Net counting rate is 0.8 cpm (dashed curve shows the spectrum shape of a strong $Sr^{90}$-$Y^{90}$ source).

## 5. Performance as a Low Background Counter

### 5.1. COINCIDENCE METHOD

This system can be used as a low level counting device when the coincident pulses between both the detectors are counted. A differential discriminator is used in the scintillation counter system, to reject large pulses caused by cosmic rays or high energy $\gamma$-rays and undesirable small pulses including detector noises.

This method offers several advantages, especially in measuring the medium or high energy $\beta$-ray emitters. First, the background is extremely low. The background counting rate is, of course, a function of the level setting of the differential discriminator, and it is estimated from table 1. Second, noise or spurious counts of the detectors are not counted. This effect is of great advantage, since the true counting rate of the G-M counter is often far larger than the source counting rate due to the cosmic ray counts, and so a little probability of the spontaneous or multiple discharge of the G-M counter may cause a large error in the case of an anti-coincidence type low background counter. Finally, when a sample consists of two or more different energy $\beta$-ray emitters, the selective counting of the high energy component is possible. For example, it can be determined whether a $Cs^{137}$ sample is contaminated by $K^{40}$ or not.

For the measurements of $K^{40}$ ($E_\beta = 1.32$ MeV), for instance, when the energy range was adjusted to 0.2–1.2 MeV, the background counting rate was only about 0.11 cpm. In this condition, the counting efficiency for $\beta$-ray of a natural KCl sample deposited on a Lucite sample holder, which is located about 5 mm from the window, was about 33%. (The counting efficiency of the G-M counter itself in the same condition was 39% as described before.)

### 5.2. ANTI-COINCIDENCE METHOD

This system may be used in the anti-coincidence operation just as conventional low background counters. In this case, the discriminator outputs of scintillation pulses are fed into the anti-coincidence circuit as the inhibit signals.

The use of a plastic or liquid scintillator as an anti-coincidence shield has been tried by several workers[4,5]), and its advantages over an orthodox G-M tube shield have been pointed out. These are high detection efficiency for cosmic ray particles, complete screening of the sample counter, easy maintenance, and long life, etc. Our system, however, has another important feature.

If the discriminator is adjusted to pass only cosmic ray pulses, the background will be equivalent to that of the conventional low background counters, but by lowering the level of the discriminator the high energy component of the $\gamma$-ray background can be rejected too. Therefore, this method is suitable for measuring low energy $\beta$-ray emitters. The counting efficiency is exactly the same as that of the G-M counter, so far as the discrimination energy is higher than the maximum energy of the sample's $\beta$-ray, but noise or spurious counts of the G-M counter cannot be rejected in this method.

**Acknowledgements**

The author would like to thank Mr. T. Hiramoto for giving invaluable aid with the equipment and the measurements. The author also wishes to thank Mr. G. Ito, Chief of the Physics Division, and Mr. M. Izawa, Chief of the Chemistry Division, for their excellent guidance and encouragement. Finally, he wishes to thank Mr. T. Koyanagi for offering valuable samples.

[4]) J. R. Gat (Gutmann) and J. Gilat, Nucl. Instr. and Meth. 8 (1960) 233.

[5]) R. P. Parker, Nucl. Instr. and Meth. 8 (1960) 339.

NUCLEAR INSTRUMENTS AND METHODS **13** (1961) 50–54; NORTH-HOLLAND PUBLISHING CO.

# DETECTEUR G. M. POUR UN SPECTROMETRE BETA

JEAN KERN

*Institut de Physique de l'Université, Fribourg (Suisse)*

Reçu le 12 mai 1961

The dependence of the slope of the plateau of a G.M. counter upon counting rate is measured with two modes of irradiation. Also a twin Geiger-Müller counter is described. Its operational caracteristics are given. The slope of the plateau of the two counters in coincidence is less than 1 %/100 V when the counting rate is 120 counts/sec in each tube. The plateau length exceeds 300 V. The background is reduced by a factor of approx. 5 compared with single counting. Peak counting rate up to 1500 coincidences/sec were used without any difficulty.

## 1. Introduction

Dans un travail précédent[1]) nous avons cherché à ajuster les paramètres de construction d'un compteur G.M. de diamètre de cathode donné, de façon à obtenir une pente du plateau minimum et si possible nulle. Nous avons montré qu'en utilisant comme gaz de remplissage un mélange de $\approx 90\%$ d'argon et 10–12% d'alcool à la pression totale de 100 Torr, on pouvait obtenir une pente relative du plateau $(\Delta N/N)_{\Delta V = 100\,\mathrm{V}}$ de l'ordre de 0.5% et une longueur du plateau de 150 à 200 V, caractéristiques mesurées avec un taux de comptage d'environ 40 c/sec et une irradiation homogène du compteur. Pour obtenir ce résultat il faut choisir convenablement le $\phi$ de l'anode et supprimer les effets de bord en construisant des électrodes de protection. Pour une irradiation concentrée on peut utiliser des électrodes simples, pour une irradiation homogène il est préférable d'employer des électrodes doubles, telles qu'elles sont représentées dans la fig. 1. Avec de telles électrodes, on obtient avec une irradiation concentrée sur le milieu de l'anode et pour un taux de comptage de 35 c/sec une pente de $0.24 \pm 0.14\%$ (pour $\Delta V = 100\,\mathrm{V}$) sur 160 V due exclusivement à la diminution du temps mort qui se produit lorsqu'on accroit la surtension.

La détermination précise de l'intensité d'une transition pose au détecteur d'un spectromètre bêta deux conditions: admettre un taux de comptage élevé et avoir un faible mouvement propre. La première condition résulte de la nécessité de pouvoir comparer des intensités très différentes avec une même géométrie, ou de mesurer une ligne sur un fonds continu important avec une bonne statistique. La seconde est nécessaire pour mesurer une ligne sur un fonds faible, comme c'est le cas à haute énergie.

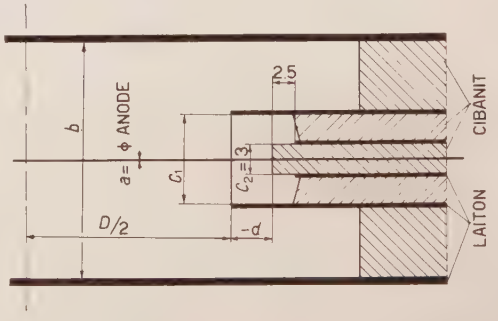


Fig. 1. Compteur avec électrode double.

Dans ce travail nous étudions le plateau pour des taux de comptage plus élevés et décrivons un compteur double fonctionnant en coïncidence construit pour obtenir un faible fonds continu.

## 2. Pente du plateau en fonction du taux de comptage

Nous avons étudié sous ce respect les compteurs désignés par V/2 et V/3 dans la réf.[1]). Ces compteurs ont des électrodes de garde doubles. Ils se différencient par le diamètre $c_1$ de l'électrode extérieure qui est de 10 mm dans le compteur V/2 et de 16 mm dans le compteur V/3. En utilisant les notations de

[1]) J. Kern et O. Huber, Helv. Phys. Acta **33** (1960) 27.

la fig. 1, les autres paramètres de construction sont: $D = 104$ mm (106 pour V/3); $a = 0.18$ mm; $c_2 = 3$ mm; $d = -5$ mm ($-6$ pour V/3); $b = 30$ mm.

Soit $R$ le rapport entre la tension $V_g$ des électrodes de garde et la tension d'anode $V$. On désigne par $R_{th}$ la valeur de $R$ qui donne aux électrodes de garde le potentiel correspondant à celui de leur rayon dans la distribution cylindrique non perturbée. On a respectivement $R^1_{th} = 0.214$ et $R^2_{th} = 0.450$ pour les électrodes externes et internes du compteur V/2 et $R^1_{th} = 0{,}123$ et $R^2_{th} = 0.450$ pour les électrodes du compteur V/3. Pour les mesures on a fixé $R_1 = 0.210$ et $R_2 = 0.430$ pour le compteur V/2 et $R_1 = 0.120$ et $R_2 = 0.430$ pour le compteur V/3.

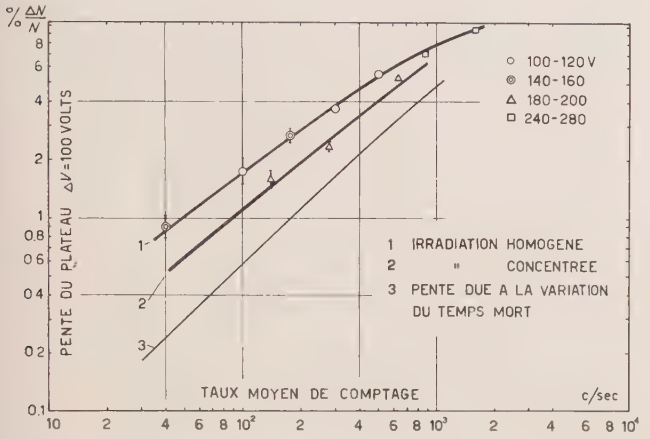


Fig. 2a. Compteur V/2. Pente du plateau en fonction du taux de comptage, mesurée avec irradiation homogène et concentrée.

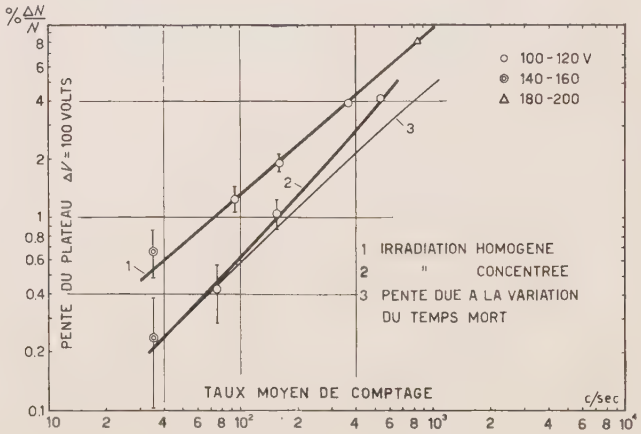


Fig. 2b. Compteur V/3. Pente du plateau en fonction du taux de comptage, mesurée avec irradiation homogène et concentrée.

Les résultats des mesures effectuées avec irradiation homogène et concentrée sont représentées dans les figs. 2a et 2b sur une échelle double logarithmique. Les différents signes, ○, ◎, □ ... indiquent la différence des tensions entre lesquelles la pente du plateau a été mesurée avec précision.

On a un accroissement marqué de la pente lorsqu'on passe à des taux de comptage élevés. Cet accroissement est plus considérable que celui qui est dû à la diminution des pertes statistiques calculées d'après le temps mort mesuré, sauf pour les taux de comptage supérieurs à 1000 c/sec. On sait que pour des taux de cet ordre il y a une diminution marquée du temps mort[2]). Nous avons mesuré le temps mort qui a servi de base au calcul avec un taux de comptage d'environ 100 c/sec. On remarque un allongement de plateau lorsqu'on augmente le taux des impulsions.

L'ouverture du faisceau nous oblige à donner au compteur du spectromètre[3]) une longueur d'au moins 60 mm et le mouvement propre est relativement grand. Dans le spectromètre il est d'environ 40 c/min.

### 3. Compteur double

L'idée de construire un compteur double permettant de n'enregistrer que des électrons pénétrant depuis une direction donnée n'est pas nouvelle[4]). En incorporant des électrodes de garde simples on obtient cependant des caractéristiques intéressantes.

Le compteur est présenté en coupe simplifiée dans les figs. 3 et 4. Le compteur I a un diamètre de cathode de 20 mm, le compteur II de 25 mm. La longueur de l'anode est de 68 mm dans les deux cas et son diamètre est de 0.15 mm. Les électrodes de garde ont un diamètre de 3 mm. L'isolation intérieure est en retrait de 2 mm par rapport à l'extrémité. La fenêtre d'entrée a $13 \times 24$ mm, et la fenêtre intermédiaire $17 \times 37$ mm. Cette dernière est montée sur un cadre métallique qui peut être glissé dans les rainures A (cf. fig. 3). Les fenêtres

[2]) E. Picard, Rapport C.E.A. No. 482 (1955).
[3]) H. Wild und O. Huber, Helv. Phys. Acta **30** (1957) 3.
[4]) Bradt, Heine und Scherrer, Helv. Phys. Acta **16** (1943) 455.

sont en Mylar de 0.9 mg/cm² légèrement aluminisé. Celle d'entrée est collée sur la paroi extérieure. Un second compteur à fenêtre amovible est en construction.

La fermeture du compteur vers le haut et le bas est assurée par deux flasques (non dessinées) sur lesquelles sont soudées des traversées en verre Philips. Un joint torique en Neoprene assure l'étanchéité.

La caractéristique de la longueur $L$ du domaine de Geiger (ou palier) en fonction de $R$ présente une

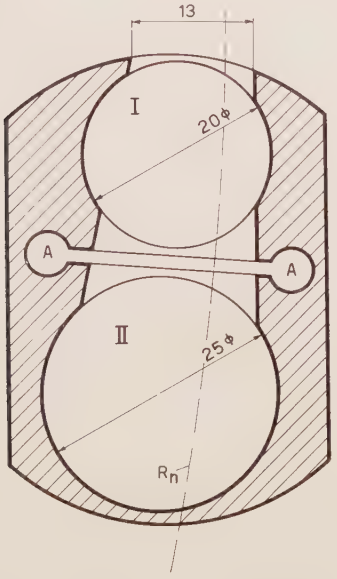


Fig. 3. Compteur double. Coupe transversale. $R_n$ = rayon normal du spectromètre.

cassure pour $R = K$ (cf. réf.[1]), fig. 3): pour les valeurs $R > K$, $L$ est indépendant de $R$, tandis que cette longeur diminue rapidement lorsqu'on abaisse $R$ au dessous de $K$. Pour les compteurs I et II on a mesuré respectivement $K = 0.55$ et $K = 0.600$ tandis que les valeurs $R_{th}$ sont de 0.39 et 0.415.

La tension de seuil est désignée par $V_s$. Elle correspond à une discrimination de 0.5 V.

Le schéma des connexions électriques est représenté dans la fig. 5. La tension d'anode du compteur I est diminuée à l'aide d'un potentiomètre d'environ 4% par rapport à celle du compteur II, pour compenser le diamètre de cathode plus petit. Les deux compteurs ont ainsi des tensions de travail identiques. Les tensions indiquées ci-dessous pour le compteur I ne sont pas corrigées pour cette différence. Les électrodes de garde ont été directement connectées. Le rapport $R$ a été fixé à 0.615 pour le compteur II, ce qui correspond à 0.640 pour le compteur I.

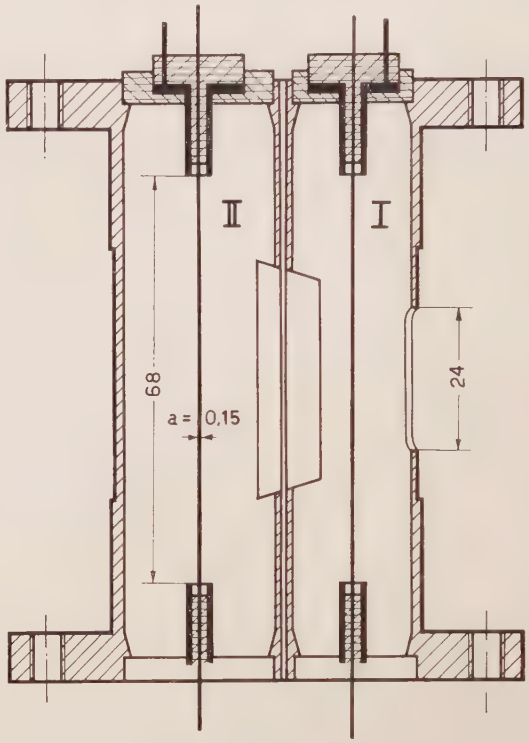


Fig. 4. Compteur double. Coupe longitudinale.

La résolution de l'étage de coïncidences est: $2\tau = 10$ $\mu$sec. Cette valeur relativement élevée nous assure contre la perte de coïncidences vraies. Le taux des coïncidence fortuites est donné par $2\tau X_I X_{II}$; $X_J$ est la somme des taux des impulsions parasites plus du mouvement propre dans le compteur $J$. En supposant que ces taux aient la valeur énorme de 100 imp./sec dans le spectromètre, le taux des coïncidences fortuites ne serait que de 0.2/sec, soit 0.2% de $X_I$ ou $X_{II}$, taux eux-mêmes beaucoup plus petits que celui des coïncidences vraies.

Les mesures de test ont été effectuées en dehors du spectromètre avec irradiation homogène latérale (c. à d. depuis une direction perpendiculaire au plan

des axes des compteurs) due à une source de $Co^{60}$. Les valeurs suivantes ont été mesurées:

Compteur I seul: $V_{sI} = 1200$ V; Pente = 1.70 $\pm$ 0.15% sur 200 V, entre 1380 et 1580 V; Taux de comptage 125 c/sec.

Compteur II seul: $V_{sII} = 1160$ V; Pente = 1.48 $\pm$ 0.15% sur 240 V, entre 1380 et 1620 V; Taux de comptage 135 c/sec.

I et II en coïncidence: $V_{sI} = 1150$ V, $V_{sII} = 1110$ V; Pente = 0.98 $\pm$ 0.2% sur 240 V entre 1220 et 1460 V; Longueur du plateau supérieure à 360 V.

Les taux de comptage étaient de: Compteur I 119/sec; Compteur II 125/sec; Coïncidences 25/sec.

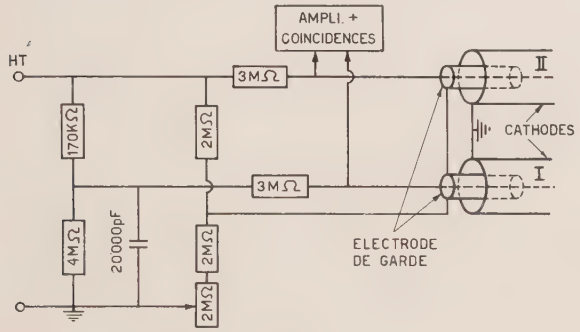


Fig. 5. Compteur double. Connexions électriques.

Le mouvement propre dans le spectromètre est d'environ 7 coïncidences/min. L'amélioration par rapport au comptage simple avec le compteur I est d'environ un facteur 5.

La longueur et la pente du plateau en coïncidence sont satisfaisants. La correction statistique du taux de comptage due au temps mort est donnée par:

$$K_0 = \frac{K_x}{1 - T_m^I N_I - T_m^{II} N_{II} + T_m^x K_{xv} + (N_I - K_{xv})(N_{II} - K_{xv})\, T_m^I T_m^{II}}$$

où $T_m^x$ représente le plus petit des deux temps morts $T_m^I$ ou $T_m^{II}$ des compteurs respectifs I et II. $K_m^I$ est la fréquence des coïncidences que l'on mesure et $K_0$ est la fréquence que l'on aurait observée si les temps morts étaient nuls. $K_{XV}$ est le taux des coïncidences vraies, c. à d. des coïncidences mesurées moins les coïncidences fortuites. Ces dernières ne représentent dans notre cas que 0.2 c/sec et peuvent être négligées. Le dernier terme du dénominateur de la formule représente la contribution des superpositions de temps mort (y compris les coïncidences fortuites) et peut aussi être négligé.

Les temps morts ont été mesurés par la méthode oscillographique et leurs valeurs sont reportées dans la fig. 6. Pour une tension donnée on a toujours que $T_m^{II} > T_m^I = T_m^x$. La correction statistique devient:

$$K_0 = \frac{K_x}{1 - T_m^I (N_I - K_x) - T_m^{II} N_{II}}.$$

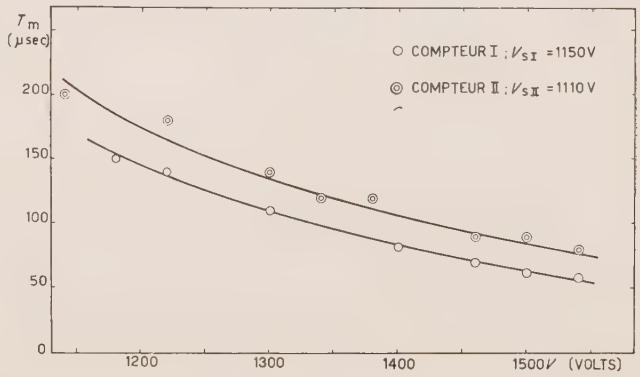


Fig. 6. Compteurs I et II. Temps mort en fonction de la surtension.

Les pertes statistiques sont de 3.38% à 1220 V et de 1.81% à 1460 V, ce qui donne lieu à une pente du plateau de 0.65%. La pente mesurée, 0.98 $\pm$ 0.2% n'est que de peu supérieure à cette valeur. Ce bon résultat s'explique par les deux raisons suivantes: D'une part il y a une plus grande probabilité pour que l'ionisation primaire provoquée par une particule qui traverse les deux compteurs soit près du centre que des extrémités de l'anode, car cette particule passe plus facilement (exclusivement pour les électrons) à travers la fenêtre intermédiaire qu'à travers la paroi intermédiaire qui sépare les extrémités des compteurs; au milieu de l'anode il n'y a pas de perturbation du champ électrique. D'autre part, si l'on désigne par $P$ la probabilité pour qu'une impulsion "vraie" soit suivie par une impulsion parasite, la probabilité que des décharges parasites aient lieu simultanément dans les

deux compteurs est égale à $P^2$. Dans le domaine de tension correspondant au plateau P est certainement petit et $P^2$ l'est à fortiori. Cette dernière propriété est responsable de la longueur du plateau vers les hautes tensions; il est cependant défavorable pour la vie du compteur de travailler avec des tensions telles que l'un des compteurs soit dans une région où se déclanchent de nombreuses décharges multiples.

Telles qu'elles se présentent dans le spectromètre[3]) les circonstances seront beaucoup plus favorables que lors du test indiqué: Le faisceau sera centré par la fenêtre d'entrée et pour des taux de comptage élevés, c. à d. beaucoup plus grands que l'effet zéro, on aura que $K_x \cong N_{II}$; la correction de temps mort sera donc moins importante.

Signalons encore que nous avons mesuré avec ce compteur des taux de coïncidences jusqu'à 1500/sec sur le sommet de lignes, dans le spectromètre, sans qu'aucune difficulté ne soit apparue. Le compteur supporte certainement encore des taux plus élevés, mais la correction statistique due au temps mort devient prohibitive.

**4. Conclusion**

On peut être frappé dans l'examen des caractéristiques du compteur double de la faible pente et de la longueur satisfaisante du plateau des compteurs I et surtout II en comptage simple, comparées avec les valeurs correspondantes quant au taux de comptage et mode d'irradiation des compteurs V/2 et V/3.

Avant de discuter ce point, rappelons brièvement les causes probables de l'augmentation du taux de comptage à tension croissante dans la région du plateau:

1) augmentation du volume sensible.

2) impuretés dans le gaz de remplissage.

3) Impulsions parasites provenant de la désexcitation d'états métastables des atomes d'argon, selon un processus décrit par Orient[5]). Le taux de ces impulsions est d'autant plus grand que le temps mort est plus court.

4) diminution des pertes statistiques avec la réduction du temps mort.

5) impulsions parasites ayant leur origine dans les phénomènes de neutralisation à la cathode. Le taux de ces impulsions augmente avec la charge neutralisée et le champ électrique à la surface de la cathode.

Pour réaliser un bon plateau à faible taux de comptage, c'est l'effet 3 qui est dominant et il faut choisir un fil d'anode relativement épais (0.18 — 0.20 mm de diamètre) et une cathode d'une diamètre relativement grand pour obtenir un long temps mort.

A des taux de comptage élevés, ce sont les effets 4) et 5) qui deviennent importants et il faut diminuer le diamètre de l'anode. Dans le compteur double nous avons mis un fil de 0.15 mm de diamètre.

Comme nous l'avons vu, ce compteur satisfait à la double exigence d'un petit fonds continu et d'un plateau de pente faible.

Nous remercions le Prof. O. Huber de l'intérêt qu'il a porté à notre travail et le Fonds National de la Recherche Scientifique de son aide financière. Nous remercions également Monsieur Ch. Seilaz qui a exécuté les constructions mécaniques.

[5]) O. J. Orient, Nucl. Instr. and Meth. **6** (1960) 309.

NUCLEAR INSTRUMENTS AND METHODS **13** (1961) 55–69; NORTH-HOLLAND PUBLISHING CO.

# IONENEINFANG UND ANFANGSBAHNEN IM ISOCHRON-ZYKLOTRON KARLSRUHE

MARTIN REISER

*AEG-Forschungsinstitut Frankfurt am Main-Niederrad*

Eingegangen am 4. Mai 1961

Theoretical and experimental studies have been carried out on the problem of ion capture, initial orbits and optimum field configuration in the center of the Isochronous Cyclotron Karlsruhe (50 MeV deuterons). The theoretical studies including calculations on vertical focusing and ion paths on the first turns proved that excellent beam quality could be expected for special geometrical conditions. A group of ions starting in the phase interval before the peak dee voltage is reached is strongly bunched in radius, energy and orbit centers and is also vertically well focused by electric and magnetic forces. For experimental investigation a full scale 45 cm proton model cyclotron of the center of the big machine has been constructed. The results obtained in the experiments are in good agreement with the theory.

## 1. Einführung

Im Rahmen der theoretischen und experimentellen Voruntersuchungen für das Isochron-Zyklotron Karlsruhe, welches 100 $\mu$A Deuteronen auf 50 MeV beschleunigen soll, wurde ein Protonenmodell von der Mitte gebaut, um den Ioneneinfang zu studieren. Ziel der Arbeit war, durch optimale Gestaltung der elektrischen und magnetischen Feldverhältnisse im Bereich der ersten Teilchenumläufe einen ionenoptisch sauberen Strahlverlauf zu erhalten.

Das zur Zeit im Bau befindliche Karlsruher Zyklotron ist eine AVF-Maschine mit 60° Radialsektoren[1]). In der Tabelle sind die wichtigsten Daten zusammengestellt, Abb. 1 zeigt den Aufbau in 3 Schnitten. Das Beschleunigungssystem besteht aus 3 sektorförmigen Elektroden, die in den "Tälern" der Polschuhe untergebracht sind; die Ionenquelle wird durch eine Polschuhbohrung von unten in die Vakuumkammer eingeführt. Dieser Aufbau ermöglicht es, den Magnetspalt verhältnismässig klein zu halten, wodurch die magnetische Feldgestaltung, bei der es darauf ankommt, bereits bei kleinen Radien einen hohen "Flutter" und damit gute Axialfokussierung zu erreichen, wesentlich erleichtert wird. Die 3 HF-Sektoren schwingen gleichphasig mit einer Scheitelspannung von 40 kV und der dreifachen Teilchenumlaufsfrequenz. Sie sind im Mittelpunkt über eine Transformationsleitung durch den Polkern an den auf dem Magneten stehenden HF-Generator angekoppelt.

[1]) K. Steimel und A. Lerbs, Atomwirtschaft **4** (1959) 273.

TABELLE
Daten des Relativistischen Isochron-Zyklotrons Karslruhe

| | |
|---|---|
| Deuteronen-Endenergie | 50 MeV |
| $\beta = v/c$ | 0.226 |
| Stromstärke (geplant) | 100 $\mu$A interner Strahl<br>10$\mu$A ausgelenkter Str. |
| Polschuhdurchmesser | 225 cm |
| Endradius | 104.5 cm |
| Luftspalthöhe | 8 cm kleiner Spalt<br>16 cm grosser Spalt |
| Magnetgewicht | 280.5 t |
| Mittlere magnetische Induktion | 14.4 bis 14.7 kG |
| Maximale Induktion | 19.5 kG |
| Flutterfaktor $f_{eff}$ | 0 bis 0.4 |
| Teilchenumlaufsfrequenz | 11 MHz |
| Frequenz der Beschleunigungsspannung | 33 MHz |
| HF-Scheitelspannung | 40 kV |
| Ausgangsleistung des HF-Generators | 30 kW |
| Hochvakuumpumpe | 8000 l/s |

Bei der vom konventionellen Aufbau fundamental abweichenden Form des Beschleunigungssystems entsteht im Zentrum des Karlsruher Zyklotrons infolge des Durchgriffs an den schmalen Sektorspitzen eine räumlich komplizierte elektrische

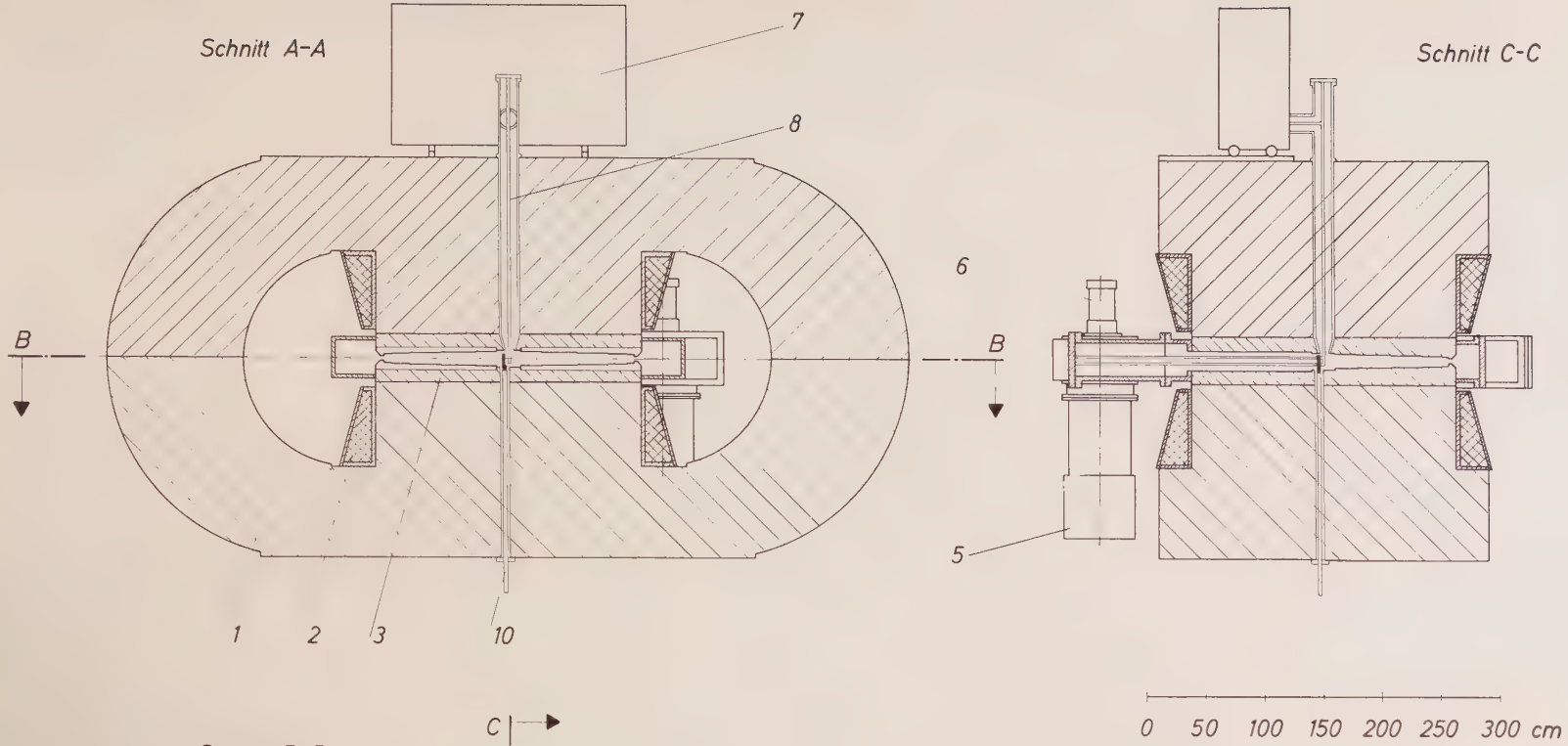


Abb. 1. Aufbau des Isochron-Zyklotrons Karlsruhe.

Feldkonfiguration, die mit einem Absinken der Feldstärke zum Mittelpunkt hin verbunden ist. Hinzu kommt, dass die HF-Schwingungsdauer nur ein Drittel der Teilchenumlaufszeit beträgt, was in der Nähe der Ionenquelle den Beschleunigungsprozess erschweren kann. Während aussen die Breite der Beschleunigungsspalte noch hinreichend klein ist gegen den Bahnumfang, kann in der Mitte die Laufzeit der Teilchen im elektrischen Feld unter Umständen in die Grössenordnung einer halben Schwingungsperiode kommen, so dass sich das Feld noch während der Spaltdurchquerung umpolt und die Ionen wieder abbremst. Es war daher zu untersuchen, inwieweit überhaupt eine Beschleunigung der Teilchen aus der Mitte heraus möglich ist bzw. ob die Teilchen auf ihrem ersten Umlauf genügend Energie gewinnen, um an der Ionenquelle vorbeizukommen.

Neben diesem durch den speziellen Aufbau des Karlsruher Zyklotrons bedingten Problem hat ein anderer Gesichtspunkt von allgemeiner Bedeutung die Aufgabenstellung bestimmt. In einem AVF-Zyklotron ist der Stabilitätsbereich für den Verlauf der Teilchenbahnen durch die kritischen Resonanzen und Koppelschwingungen eng begrenzt. Das gilt in besonderem Masse für die Radialbewegung, wo unter Umständen schon relativ geringe Abweichungen von der Sollbahn zur Instabilität führen. Es ist daher eine ausserordentlich wichtige Aufgabe, dass man durch kontrollierten Ioneneinfang im Zentrum des Zyklotrons definierte Anfangsbedingungen und günstige Voraussetzungen für den weiteren Beschleunigungsprozess schafft. Mit den folgenden theoretischen und experimentellen Untersuchungen der physikalischen Vorgänge im Bereich der Ionenquelle und der ersten Teilchenumläufe wurde eine Lösung angestrebt, bei der ein grosser Teil des startenden Ionenpaketes als gut gebündelter, elektrisch und magnetisch fokussierter Strahl auf zentrierten, sauber getrennten Bahnen nach aussen läuft, während alle Teilchen mit ungünstigen Startbedingungen noch in unmittelbarer Nähe der Ionenquelle abgefangen werden.

## 2. Theoretische Untersuchungen

### 2.1. ALLGEMEINE UEBERLEGUNGEN

Der schlechte Wirkungsgrad beim Ioneneinfang und der Strahlextraktion ist eines der schwierigsten Probleme des Zyklotrons. In den meisten der zur Zeit existierenden Maschinen erreicht nur ein geringer Teil der aus der Ionenquelle kommenden Teilchen den Endradius; davon gehen wiederum bis zu 90% und mehr bei der Auslenkung aus dem Magnetfeld verloren. Hinzu kommt die für präzise kernphysikalische Untersuchungen unzureichende Energiehomogenität des ausgelenkten Strahls, welche eine Filterung im Analysiermagneten notwendig macht und die nutzbare Intensität um einen weiteren Faktor verringert. Die ausscheidenden Ionen verbrauchen oft den grössten Teil der in die Beschleunigung gesteckten Hochfrequenzleistung, bilden eine starke thermische Belastung für die Dee's und das Auslenksystem und verursachen vor allem die unerwünschte Radioaktivität der Maschine.

Für die stromstarken AVF-Zyklotrons hoher Endenergie wird wegen der grossen Schwierigkeiten und hohen Kosten der Abschirmung eine wesentliche Verbesserung der Strahlqualität und der Extraktionsrate zu einer Lebensfrage. Da aber die Strahlqualität und mit ihr das Gelingen der Extraktion wesentlich von den Startbedingungen der Teilchen abhängt, muss jede Arbeit in dieser Richtung mit dem Ioneneinfang beginnen.

Obwohl man die Bedeutung der Vorgänge im Zentralbereich des Zyklotrons schon früh erkannt hat, ging die Entwicklung nur langsam voran und brachte erst in den Jahren nach dem letzten Krieg gewisse Fortschritte. Durch schrittweise Verbesserung der Ionenquelle und Einbau von "feelers" erreichte man zunächst eine bemerkenswerte Erhöhung des in Umlauf gelangenden Ionenstroms, ohne indessen den Wirkungsgrad des Einfangsprozesses merklich zu vergrössern. Bei Beginn dieser Arbeit im Frühjahr 1958 waren auch schon eine Reihe von Beiträgen veröffentlich, die sich mit Teilfragen des Ioneneinfangs selbst, wie z.B. mit der Verringerung der elektrischen Defokussierung durch fokussierende Blenden, befassten[2–6]). Es

[2]) R. J. Jones, Phys. Rev. **91** (1953) 223.
[3]) W. F. Stubbins, UCRL-2078 (1953).
[4]) H. G. Blosser, F. Irwin, Bull. Amer. Phys. Soc., Series II, **3** (1958) 180.
[5]) N. D. Fedorov, Kernenergie **1** (1958) 140.
[6]) V. S. Panasjuk, Kernenergie **1** (1958) 652.

fehlte aber eine eingehende theoretische und experimentelle Untersuchung, die alle Aspekte dieses komplexen Problems berücksichtigt. Inzwischen wird, wie einige Vorträge auf der Konferenz über "Sector-Focused Cyclotrons" in Sea Island, USA[7]), vor allem aber die interessante Arbeit von Morton und Smith[8,9]), zeigen, vielerorts an einer Verbesserung des Ioneneinfangs gearbeitet. Morton und Smith sind in ihren grundsätzlichen Ueberlegungen ähnlich vorgegangen wie wir, wenn auch die Geometrie und die Feldverhältnisse in ihrem konventionellen 7.7 MeV Protonenzyklotron mit einem Dee anders liegen als in unserem Fall. Ueber Vertikalfokussierung und Phasenschlupf im Zentrum eines AVF-Zyklotrons hat Randle in Harwell theoretische Untersuchungen angestellt, die in die gleiche Richtung gehen[10]).

Die hohen Teilchenverluste in der Mitte des Zyklotrons sind im wesentlichen auf schlechte Bahnzentrierung, ungenügende Energieaufnahme und elektrische Defokussierung zurückzuführen. Während die Bahnzentrierung in erster Linie von der Lage der Ionenquelle und der Symmetrie des Magnetfeldes abhängt (einseitige Feldfehler führen zum Aufschaukeln instabiler Radialschwingungen), spielt bei den anderen Effekten die Phase und Laufzeit der Ionen im Hochfrequenzfeld des Beschleunigungsspaltes die entscheidende Rolle.

Um ein Bild von den Vorgängen beim Start der Teilchen zu erhalten, sei der Fall betrachtet, dass die Ionenquelle einer am Dee befestigten Absaugelektrode gegenübersteht. In jeder negativen Halbperiode der Hochfrequenzspannung, also während eines Phasenintervalls von 180°, werden positive Ionen aus dem Bogenplasma extrahiert. Die Ionenstromdichte wächst dabei, sofern man nicht in die Sättigung kommt, mit dem Momentanwert der Spannung $U = U_0 \cos \omega_e t$, im einfachen reinen Raumladungsbetrieb zum Beispiel mit $U^{\frac{3}{2}}$. Im ersten Beschleunigungsspalt, wo die Ionenlaufzeit noch besonders gross ist, passiert nun folgendes: Teilchen mit negativer Startphase zur Hochfrequenz, z.B. $-60°$ verweilen lange genug im ansteigenden elektrischen Feld, um einen hohen Energiebetrag aufzunehmen. Sehr spät, etwa mit einer Phase von $+ 60°$, startende Teilchen dagegen gewinnen praktisch keine Energie mehr, sondern werden unterwegs durch das sich umpolende Feld zur Umkehr gezwungen und scheiden aus. Sofort nach dem Start entsteht so eine starke radiale und energetische Auffächerung des Ionenbündels. Brauchbar für die Weiterbeschleunigung ist nur eine Gruppe von Ionen negativer Startphase mit guter radialer Bündelung, einheitlicher Energie und gleichen Bahnmittelpunkten. Alle anderen Teilchen gehen direkt an der Ionenquelle oder nach einer Reihe von Umläufen verloren.

Für die Vertikalbewegung liegen die Verhältnisse gerade umgekehrt. Hier erfahren die Ionen mit negativer Phase zur Hochfrequenz eine elektrische

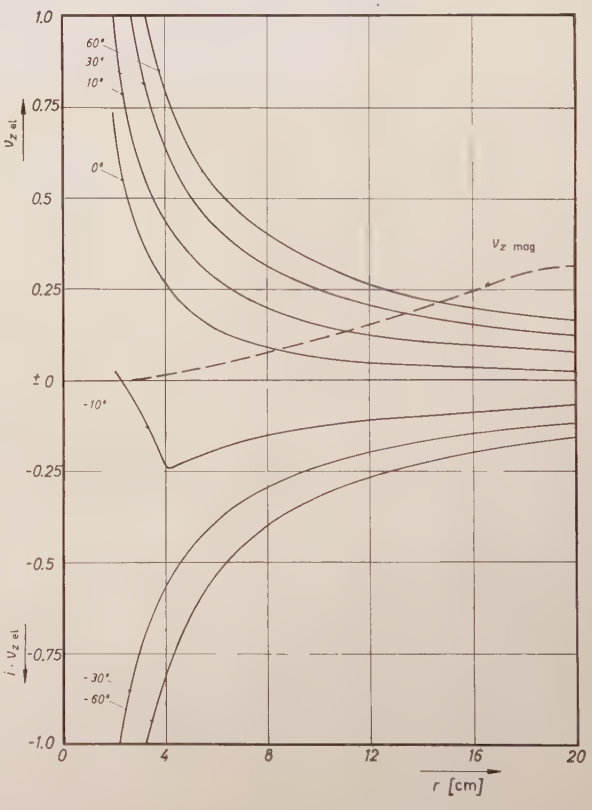


Abb. 2. Schwingungszahl $\nu_{z\,el}$ der elektrischen Axialfokussierung für Teilchen verschiedener Phase zur Hochfrequenz als Funktion des Radius. Gestrichelte Kurve: Frequenz der magnetischen Axialschwingungen.

[7]) F. T. Howard, Sector-Focused Cyclotrons, National Academy of Sciences – National Research Council, Publication 656 (1959).

[8]) A. H. Morton, W.I.B. Smith, Nucl. Instr. and Meth. **4** (1959) 36.

[9]) W. I. B. Smith, Nucl. Instr. and Meth. **9** (1960) 49.

[10]) T. C. Randle, AERE-R 3479 (1960).

Defokussierung, solche mit positiver Phase dagegen werden fokussiert. Bei der Gruppe von Teilchen, die für die Horizontalbewegung günstige Startbedingungen hat, würden also durch axiale Defokussierung hohe Intensitätsverluste entstehen. Man kann nun aber durch geeignete Anordnung von Ionenquelle und Absaugelektrode die Laufzeit der Teilchen zwischen dem ersten und zweiten Beschleunigungsspalt verlängern und damit die Phase nach positiven Werten verschieben.

Diese allgemeinen Ueberlegungen wurden zunächst theoretisch durch Rechnungen über die Axialfokussierung und den Verlauf der Anfangsbahnen genauer untersucht, wodurch die notwendige quantitative Klarheit über die physikalischen Zusammenhänge und konkrete Richtlinien für die Experimente im Versuchszyklotron gewonnen wurden. Die ersten Versuche wurden mit ebenen Polplatten durchgeführt, um im homogenen Magnetfeld den Einfluss des elektrischen Linseneffektes auf die Vertikalbewegung zu studieren. Anschliessend wurde mit profilierten Polschuhen gearbeitet, die in der Mitte ein ebenes Plateau haben.

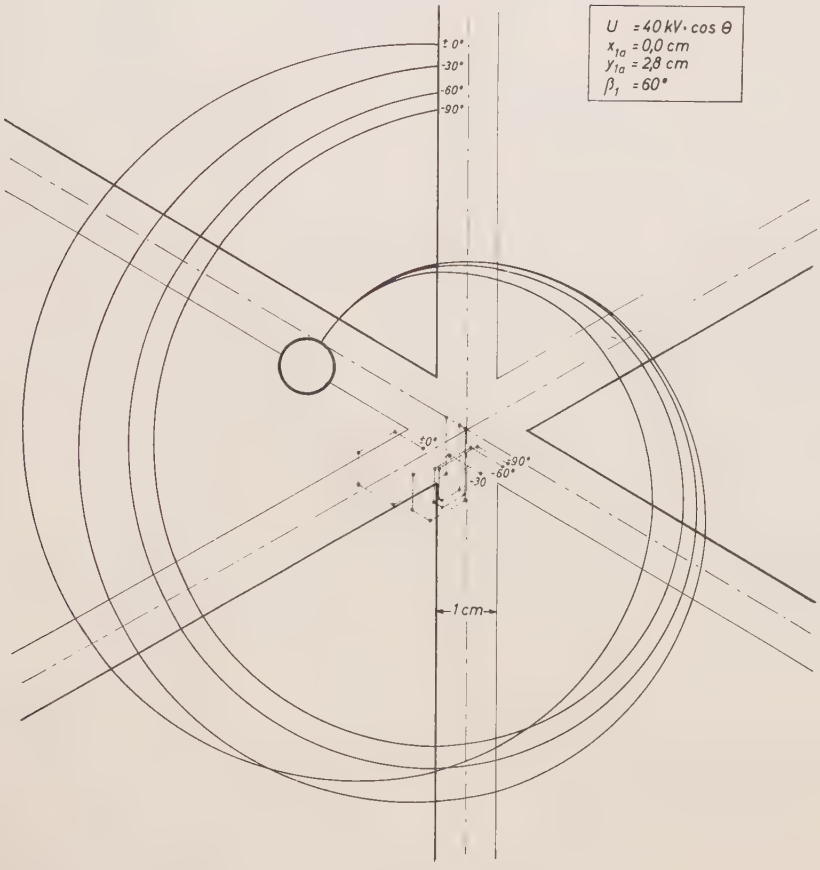


Abb. 3. Berechnete Anfangsbahnen von Deuteronen verschiedener Startphase mit den zugehörigen Mittelpunkten in den elektrisch feldfreien Sektoren (1. Fall).

## 2.2. AXIALFOKUSSIERUNG IM ZENTRUM

Der Einfluss des elektrischen Beschleunigungsfeldes auf die Vertikalbewegung der Teilchen wirkt sich nur auf den ersten Umläufen aus. Ausserhalb des Zentrums wird die Bahn durch magnetische Kräfte stabilisiert, speziell im Thomas-Zyklotron durch Fokussierung an den Sektorkanten. Ein Mass für die Stabilität sind die Frequenzen $\nu_r$ und $\nu_z$ der radialen und axialen Betatronschwingungen um die Sollbahn. In einem Radialsektorfeld $N$-facher azimutaler Periodizität

$$B(r,\vartheta) = \overline{B}(r)\,(1 + \sum_{\nu=1}^{\infty} f_\nu \cos \nu N\vartheta) \qquad (1)$$

gilt näherungsweise[11])

$$\nu_r = (1 + \bar{k})^{\frac{1}{2}} \qquad (2)$$

$$\nu_z = \left(-k + \frac{N^2}{N^2 - 1}\,\frac{f^2_{\text{eff}}}{2}\right)^{\frac{1}{2}}. \qquad (3)$$

Funktionen des Radius $r$, die in der Mitte ($r \to 0$) auf Null absinken. Nach Formel (3) wird daher in diesem Bereich $\nu_z$ verschwindend klein, d.h. es ist keine ausreichende magnetische Axialfokussierung mehr vorhanden. Für die Polschuhgestaltung ergibt sich daraus die Forderung, in der Mitte mög-

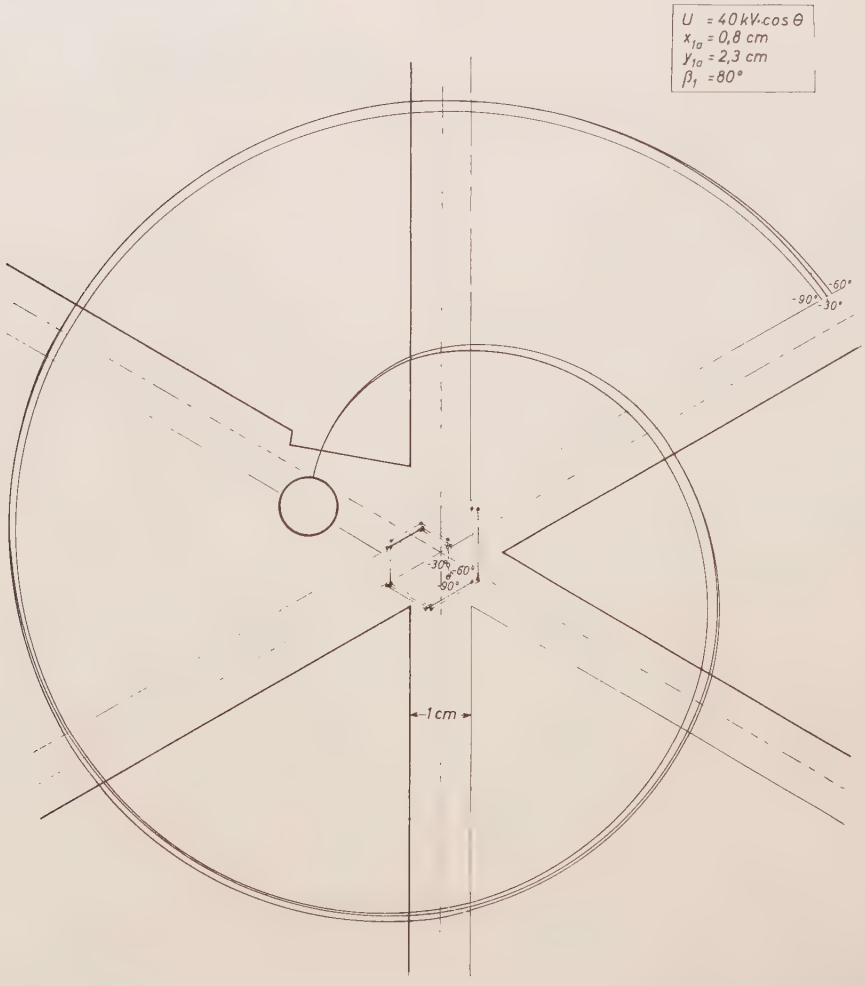


Abb. 4. Anfangsbahnen (2. Fall).

Darin ist

$$\bar{k} = \frac{r}{\overline{B}}\,\frac{\mathrm{d}\overline{B}}{\mathrm{d}r},$$

der auf das mittlere Feld

$$\overline{B}(r) = \frac{1}{2\pi}\int_0^{2\pi} B(r,\vartheta)\,\mathrm{d}\vartheta$$

bezogene Feldindex und $f^2_{\text{eff}} = \Sigma_{\nu=1}^{\infty} f_\nu^2$ der effektive "Flutterfaktor". Beide Grössen sind ebenfalls

lichst schnell einen grossen Flutterfaktor zu erreichen. Dies ist um so leichter, je kleiner der Luftspalt und je geringer die Zahl der Sektoren ist. Beim Karlsruher Zyklotron sind diese Bedingungen durch die besondere Konstruktion des Beschleunigungssystems sehr gut erfüllt, worauf bereits einleitend hingewissen wurde.

[11]) P. Staehelin, Technical Report No. 1, University of Illinois.

Mit dem elektrischen Linseneffekt, dem wegen der geringen magnetischen Fokussierung im Zentralbereich grosse Bedeutung zukommt, haben sich etwa gleichzeitig Rose[12]) und Wilson[13]) befasst. Später hat Cohen die Rechnungen von Rose durch Berücksichtigung weiterer Korrekturglieder noch verbessert[14]). Er erhält für die Richtungsänderung eines Teilchens bei der $n$-ten Durchquerung des Beschleunigungsspaltes

$$\Delta \frac{\mathrm{d}z}{\mathrm{d}n} = \pi z \left[ -\frac{eU_0 \sin\theta_\mathrm{m}}{2E_\mathrm{k}} \frac{\omega_\mathrm{e} r}{v} - \frac{1}{2}\left(\frac{eU_0}{2E_\mathrm{k}}\right)^{\frac{3}{2}} \cos^2\theta_\mathrm{m} + \right.$$

$$\left. + \left(\frac{eU_0}{4m\omega^2 d^2}\right)^{\frac{1}{3}} \left(\frac{eU_0}{2E_\mathrm{k}}\right)^{\frac{3}{2}} \sin^2\theta_\mathrm{m} \right] . \qquad (4)$$

Darin ist $U_0$ der Scheitelwert und $\omega_\mathrm{e}$ die Kreisfrequenz der beschleunigenden HF-Spannung, $d$ die Spaltbreite, $E_k$ die kinetische Energie, $v$ die Geschwindigkeit, $\omega$ die Winkelgeschwindigkeit und $\theta_\mathrm{m}$ die Phase der HF, wenn die Ionen die Spaltmitte passieren.

Um diese Formel auf das Karlsruher Zyklotron zu übertragen und einen groben quantitativen Vergleich mit der magnetischen Fokussierung durchführen zu können, soll nun (4) unter Vernachlässigung des kleinen Gliedes mit $\sin^2\theta_\mathrm{m}$ auf die Form einer einfachen Schwingungsgleichung gebracht werden. Führt man den Winkel $\vartheta = n\pi/N$ ein, so kann man wegen $\Delta n = 1$ statt (4) näherungsweise schreiben

$$\frac{\mathrm{d}^2 z}{\mathrm{d}\vartheta^2} + \nu^2_{z\,\mathrm{el}}\, z = 0 . \qquad (5)$$

Mit $\omega_\mathrm{e} = N\omega = N\, v/r$ und $E_k = \frac{1}{2} m\, \omega^2 r^2$ ergibt sich für die elektrische Schwingungszahl $\nu_{z\,\mathrm{el}}$ der Ausdruck

$$\nu_{z\,\mathrm{el}} = \left[\frac{N}{2\pi}\left(\frac{eU_0}{m\omega^2}\right)^{\frac{2}{3}} \frac{\cos^2\theta_\mathrm{m}}{r^3} + \frac{N^2}{\pi}\frac{eU_0}{m\omega^2}\frac{\sin\theta_\mathrm{m}}{r^2}\right]^{\frac{1}{2}} . \qquad (6)$$

Das erste Glied mit $\cos^2\theta_\mathrm{m}$ ist immer positiv, sinkt aber mit $1/r^3$ schnell ab und kann daher bald gegenüber dem zweiten Summanden vernachlässigt werden. Fokussierung tritt also praktisch nur bei positiver Phase $\theta_\mathrm{m}$ ein, wo $\nu_{z\,\mathrm{el}}$ reell ist. Ferner ist $\nu_{z\,\mathrm{el}}$ etwa proportional $N$, d.h. der elektrische Linseneffekt ist bei gleicher HF-Scheitelspannung im Karlsruher Zyklotron mit 6 Beschleunigungsspalten stärker als in einem 2 Dee-System. In Abb. 2 ist $\nu_{z\,\mathrm{el}}$ für verschiedene Phasen $\theta_\mathrm{m}$ der Teilchen zur Hochfrequenz in Abhängigkeit vom Radius aufgetragen. Zugrunde gelegt sind die Werte $N = 3$,

$$\left(\frac{e}{m}\right)_d = 4.7922 \times 10^7 \ \mathrm{As/kg}, \qquad \omega = 6.9 \times 10^7 \ \mathrm{s^{-1}}$$

und $U_0 = 40000$ V. Bei negativer Phase $\theta_\mathrm{m}$ wird der Ausdruck (6) imaginär, so dass Defokussierung entsteht (untere Hälfte des Diagramms). Zum Vergleich wurde auch der ungefähre Verlauf von $\nu_{z\,\mathrm{mag}}$ eingezeichnet, wie er sich nach Formel (3) mit in unserem Modellmagneten gemessenen Werten für $\bar{k}$ und $f_\mathrm{eff}$ ergibt. Man sieht nun auch quantitativ, wie stark am Anfang, je nach Phasenlage der Teilchen, der elektrische Einfluss auf die Axialbewegung überwiegt. Erst bei Radien oberhalb von etwa 10 bis 15 cm kommt die magnetische Fokussierung voll zur Geltung.

### 2.3. BERECHNUNG VON ANFANGSBAHNEN

Für die näherungsweise Berechnung der ersten Teilchenbahnen in der Mittelebene sei das Magnetfeld als homogen vorausgesetzt, was für Versuche mit ebenen Polplatten und innerhalb des Plateaus bei den profilierten Platten gut erfüllt ist. Das elektrische Feld in den Beschleunigungsspalten sei ebenfalls homogen; diese grob vereinfachende Annahme reicht für unsere Zwecke völlig aus. Eine Teilchenbahn setzt sich dann zusammen aus den Kurvenstücken in den Spalten und den Kreisbögen im elektrisch feldfreien Raum innerhalb der Beschleunigungssektoren.

Für die Rechnung seien kartesische Koordinaten eingeführt mit dem Ursprung im Mittelpunkt der Maschine. Die $z$-Achse liegt in Richtung der magnetischen Feldlinien, die $y$-Achse verlaufe parallel zu den Sektorkanten, die $x$-Achse quer zum Spalt wie die elektrischen Feldlinien.

Die Bewegungsgleichungen lauten dann

$$\ddot{x} = \frac{e}{m} E \cos\omega_\mathrm{e} t + \frac{eB}{m} y \qquad (7)$$

$$\ddot{y} = -\frac{eB}{m}\dot{x} . \qquad (8)$$

[12]) M. E. Rose, Phys. Rev. **53** (1938) 392
[13]) R. R. Wilson, Phys. Rev. **53** (1938) 408.
[14]) B. L. Cohen, Rev. Sci. Instr. **24** (1953) 589.

Mit den Anfangsbedingungen $x = x_a$, $y = y_a$, $\dot{x} = \dot{x}_a$, $\dot{y} = \dot{y}_a$ für $t = t_a$ und mit $eB/m = \omega = (\omega_e/N)$, $\omega_e t = \theta$, $\omega_e t_a = \theta_a$ ergeben sich folgende Lösungen

$$x = \frac{E}{B\omega_e}\left[\frac{N}{N^2-1}\left(\cos\theta_a \cos\frac{\theta-\theta_a}{N} - \right.\right.$$

$$\left. - N \sin\theta_a \sin\frac{\theta-\theta_a}{N} - \cos\theta\right)\Big] + \tag{9}$$

$$+ \frac{N}{\omega_e}\left[\dot{x}_a \sin\frac{\theta-\theta_a}{N} + \dot{y}_a\left(1 - \cos\frac{\theta-\theta_a}{N}\right)\right] + x_a$$

$$y = \frac{E}{B\omega_e}\left[\frac{N}{N^2-1}\left(\frac{\sin\theta}{N} - \cos\theta_a \sin\frac{\theta-\theta_a}{N} - \right.\right.$$

$$\left. - N \sin\theta_a \cos\frac{\theta-\theta_a}{N}\right) + \sin\theta_a\Big] - \tag{10}$$

$$- \frac{N}{\omega_e}\left[\dot{x}_a\left(1 - \cos\frac{\theta-\theta_a}{N}\right) - \dot{y}_a \sin\frac{\theta-\theta_a}{N}\right] + y_a$$

$$\dot{x} = \frac{E}{B}\frac{\sin\theta - \sin\theta_a}{N} + \frac{\omega_e}{N}(y - y_a) + \dot{x}_a \tag{11}$$

$$\dot{y} = -\frac{\omega_e}{N}(x - x_a) + \dot{y}_a\,. \tag{12}$$

Mit diesen Formeln, die auch die Kreisbögen in den elektrisch feldfreien Sektoren enthalten ($E = 0$), wurden die Teilchenbahnen über mehrere Umläufe durch Drehung des Koordinatensystems von Spalt zu Spalt auf einer IBM 650 sukzessive berechnet.

Für die festen Parameter wurden folgende Werte angenommen:

$$B = 14\,400\ G, \quad N = 3, \quad \omega_e = 2.07 \times 10^8\ s^{-1},$$

$$U = 40000\ V \cdot \cos\theta\,.$$

Spaltbreite $d$ an der Ionenquelle 0.5 cm, sonst überall 1 cm, elektrische Feldstärke $E = U_0/d =$ 80000 V/cm auf der 1. Beschleunigungsstrecke und 40000 V/cm sonst; Startgeschwindigkeit der Deuteronen $x_{1a} = y_{1a} = 0$, Dreh- bzw. Sektorwinkel $\beta = 60°$, ausser beim 1. Schritt, wo auch andere Winkel ($\beta_1 > 60°$) in Betracht gezogen wurden. Die Lage des Austrittsschlitzes der Ionenquelle ($x_{1a}$, $y_{1a}$) wurde vorgegeben und der Bahnverlauf für verschiedene Startphasen $\theta_{1a}$ berechnet.

Im ersten gerechneten Fall wurde $\beta_1 = 60°$ gewählt und die Ionenquelle so gelegt, dass die Mittelpunkte der Kreisbögen im ersten feldfreien Sektor möglichst in den Nullpunkt fallen, womit sich die Anfangswerte $x_{1a} = 0$, $y_{1a} = 2.8$ cm ergaben. Abb. 3 zeigt den ermittelten Bahnverlauf für Deuteronen mit negativer Startphase; später startende Teilchen ($\theta_{1a} > 0°$) gewinnen erwartungsgemäss nicht genügend Energie und scheiden für die Weiterbeschleunigung aus. Das Ergebnis dieser ersten Berechnung ist insofern noch unbefriedigend, als die radiale Bündelung und die Bahnzentrierung nicht besonders gut sind; überdies ist die Phase beim Passieren der Spaltmitten für alle Teilchen durchweg negativ, sodass elektrische Defokussierung eintritt.

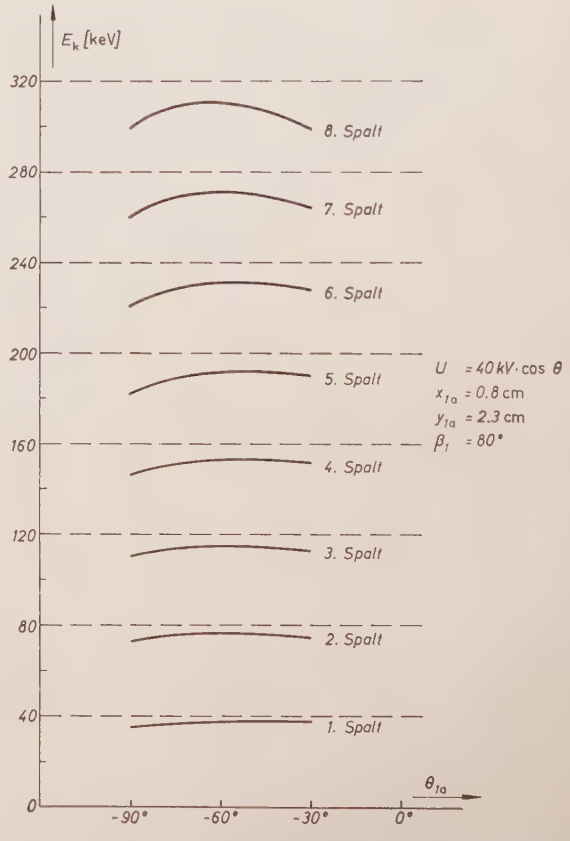


Abb. 5. Kinetische Energie der Deuteronen nach dem Durchlaufen der einzelnen Beschleunigungsspalte in Abhängigkeit von der Startphase (2. Fall).

In den weiteren Rechnungen wurde angestrebt, zwei Ziele gleichzeitig zu realisieren: bessere Bahnzentrierung durch Verschieben der Ionenquelle nach der Mitte hin und Verlängerung des Weges bzw. der Laufzeit im ersten Sektor, damit die Phase

in den folgenden Spalten positiv wird. Letzteres erreicht man z.B. durch Vergrösserung des Winkels $\beta_1$. Das beste Ergebnis wurde mit $x_{1a} = 0.8$ cm, $y_{1a} = 2.3$ cm und $\beta_1 = 80°$ erzielt. Wie man in Abb. 4 sieht, ist hier für eine Gruppe von Deuteronen negativer Startphase eine ausgezeichnete Bündelung und Bahnzentrierung erreicht, die mit einer Startphasenintervall umso grösser, je geringer die Breite $d_1$ der ersten Beschleunigungsstrecke ist. Da überdies bei Raumladungsbetrieb mit kleinerem $d_1$ auch der extrahierbare Ionenstrom wächst, sollte die Ionenquelle so nahe an die Absaugelektrode gebracht werden, wie es die Ueberschlagsfestigkeit erlaubt.

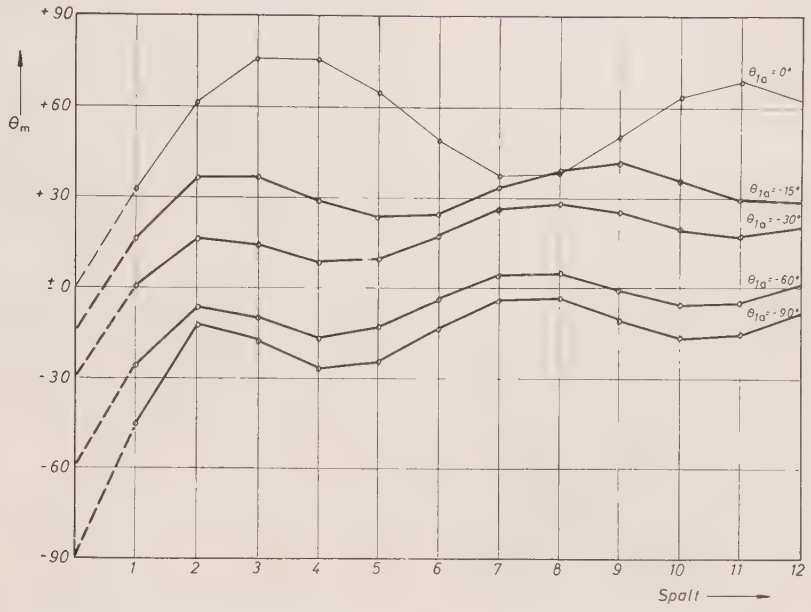


Abb. 6. Verlauf der mittleren Phase zur Hochfrequenz in den ersten Beschleunigungsspalten (2. Fall).

gleichmässigen Energieaufnahme in den aufeinanderfolgenden Spalten verbunden ist (Abb. 5). Die Zentrierung ist in unserem Beschleunigungssystem besser als in einem 180° Dee-System, wo die Mittelpunkte immer nur auf einer Linie parallel zur Dee-Kante verschoben werden. Nach der Rechnung erstreckt sich der günstige Startphasenbereich von — 90° bis etwa — 10°, also über rund 80°; später kommende Ionen sind infolge zunehmend starker Aufspreizung und Exzentrizität der Bahnen nicht mehr brauchbar. Durch den vergrösserten Sektorwinkel $\beta_1$ wird die mittlere Phase zwischen dem 1. und 2. Spalt im gewünschten Sinne verschoben (Abb. 6), sodass der grösste Teil des Deuteronenpaketes elektrisch fokussiert wird. Darüber hinaus ist trotz der guten radialen Bündelung auch eine gewisse Phasenbündelung vorhanden (von 75° Startbreite auf 37° im 12. Spalt, d.h. nach 2 Umläufen). Wie die Rechnung zeigt, ist das günstige

## 3. Experimentelle Ergebnisse

### 3.1. MODELLZYKLOTRON UND MESSANORDNUNG

In dem für die experimentellen Untersuchungen gebauten Versuchszyklotron wurde ein zentraler Ausschnitt der grossen Maschine mit einem Durchmesser von 40 cm im Modellmasstab 1:1 nachgebildet. Durch die Verwendung von Protonen statt Deuteronen wurde der Aufwand erheblich verringert, da bei gleicher Bahngeometrie und gleicher Umlaufsfrequenz nur die halbe Magnetfeldstärke und die halbe Beschleunigungsspannung benötigt werden. Der gewählte Ausschnitt war gross genug, um alle Probleme des Ioneneinfangs, wie Bahnverlauf, Strahlqualität und besonders den Effekt der elektrischen Fokussierung zu studieren.

Der konstruktive Aufbau des Modellzyklotrons ist wesentlich einfacher als der der grossen Maschine. Im Unterschied zu dieser wurde die Ionenquelle von oben eingeführt, während der HF-Generator

unter dem Magneten sitzt. Als frequenzbestimmender Schwingkreis des selbsterregten HF-Generators dient ein in der Polkernachse liegender $\frac{1}{4}\lambda$-Resonanztopf, an dessen Innenleiter die Beschleunigungselektroden freitragend befestigt sind. Als Gegenelektroden dienen zwei dem Polschuhprofil angepasste Kupferdeckel (Abb. 7). Die Ionenquelle ist nach dem in Oak Ridge entwickelten Typ[15]) mit geschlossener Brennkammer und Reflektor gebaut und hat eine Ionenaustrittsöffnung von $1 \times 16\ mm^2$. Ihre Eigenschaften und die Besonderheiten der geometrischen Anordnung in der Polschuhbohrung wurden unter statischen Bedingungen in der entsprechend umgebauten Versuchsanlage studiert[16]). Im statischen Betrieb liefert die Quelle einen Gesamtionenstrom von maximal 15 mA, bei grösserer Austrittsöffnung bis zu 100 mA, wobei der Protonenanteil im günstigsten Fall 95% beträgt.

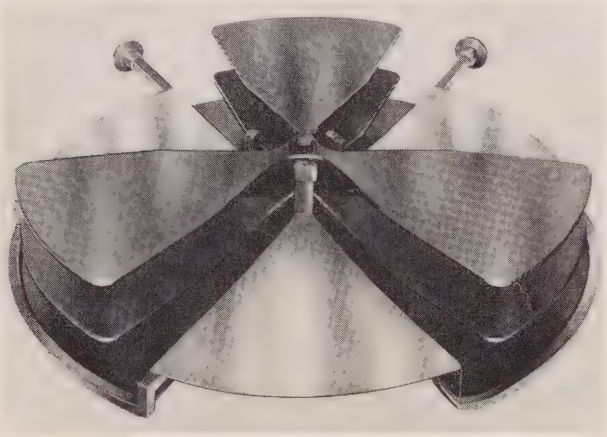

Abb. 7. Beschleunigungssystem des Versuchszyklotrons. (Innenleiter und untere Hälfte des Aussenleiters.)

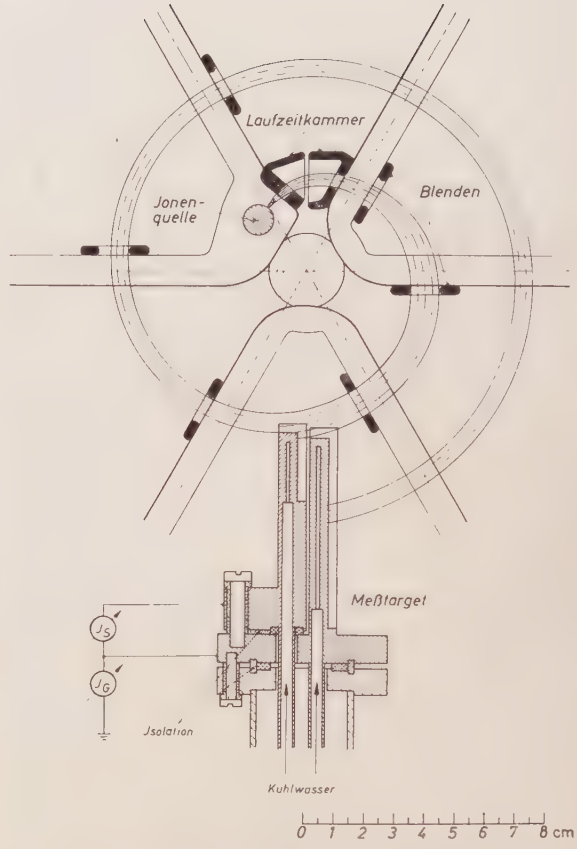


Abb. 8. Experimentelle Anordnung von Ionenquelle, Laufzeitkammer, Blenden und Messtarget im Versuchszyklotron.

Durch die eindeutigen Ergebnisse der Rechnung war der Weg für die experimentelle Untersuchung des Ioneneinfangs klar vorgezeichnet. Allerdings war es nicht angebracht, durch Einbau von Blenden die theoretisch vorausgesetzte Homogenität des elektrischen Feldes anzustreben, weil im homogenen Feld keine Axialfokussierung zustande kommt. Hier wurde ein Kompromiss geschlossen und Blenden nur an die Strahlaustrittsseite der Spalte gesetzt, was einerseits die Feldstärke erhöht und andererseits noch eine zusätzliche Fokussierung bringt, die sich auch auf Teilchen mit negativer Phasenlage erstreckt. Diese Methode der "focusing grids" wird vor allem bei Linearbeschleunigern angewandt. Ihre Verwendung im Zyklotron setzt einen definierten Strahlverlauf auf getrennten Bahnen voraus. Wo das nicht der Fall ist, geht durch falsches Ausblenden unter Umständen wesentlich mehr Ionenstrom verloren als man durch die zusätzliche Axialfokussierung gewinnt.

In unserem Falle war es nach den Bahnberechnungen einfach, Abmessungen und Sitz der Blenden festzulegen. Im wichtigen ersten Sektor an der Ionenquelle wurde eine Laufzeitkammer eingebaut, um einen echten feldfreien Raum zu schaffen und unerwünschte Teilchen sofort nach dem Start

[15]) R. S. Livingston und R. J. Jones, Rev. Sci. Instr. **25** (1954) 552.

[16]) M. Reiser, Ionenquelle und Anfangsbahnen des Relativistischen Isochron-Zyklotrons Karlsruhe, Dissertation, Mainz (1960).

abzufangen. Die experimentelle Anordnung ist in Abb. 8 dargestellt. Die Ionenquelle sitzt an der durch die Rechnung ermittelten günstigen Stelle, ausser der Laufzeitkammer sind sechs Blenden

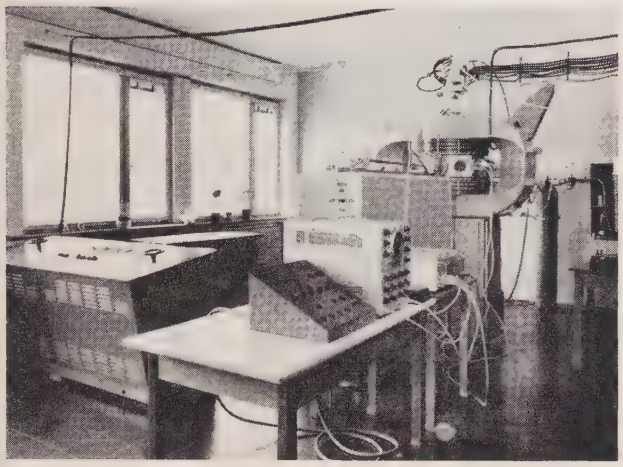

Abb. 9. Gesamtansicht der Versuchsanlage.

längs des ersten Umlaufs eingebaut. Ein Doppeltarget aus zwei wassergekühlten Kupferplatten, von denen die hintere durch die vordere bis auf einen überstehenden Rand von 1 mm Breite abgedeckt wird, gestattet eine gleichzeitige differentielle und integrale Messung des radialen Intensitätsverlaufes. Abb. 9 zeigt eine Gesamtansicht des Modellzyklotrons mit verschiedenenen elektrischen Versorgungsgeräten und Steuerpulten sowie der pneumatischen Targeteinfahrvorrichtung.

### 3.2. VERSUCHE MIT EBENEN POLPLATTEN

Das Modellzyklotron hat einen Polschuhdurchmesser von 45 cm. Bei den ebenen Polplatten für den ersten Versuchsabschnitt betrug die Luftspalthöhe 10 cm. Das Magnetfeld war bis zu einem Radius von 13 cm genügend homogen, so dass keine Randshims zur Vergrösserung des nutzbaren Bereichs verwendet wurden. Die Feldschwächung in der Mittelebene durch die Polschuhbohrungen wurde mit Shimringen bis auf 1 Promille korrigiert.

In den Versuchen wurden Magnetfeld und Beschleunigungsspannung jeweils nach der gemessenen Frequenz des HF-Systems eingestellt, und zwar ersteres so, dass es im homogenen Bereich nahe der Ionenquelle dem theoretischen Sollwert entsprach. Die HF-Scheitelspannung wurde mit einem Diodenvoltmeter gemessen.

Der mit dem Doppeltarget gemessene radiale Intensitätsverlauf (Abb. 10) entsprach den theoretischen Erwartungen. Der Gesamtstrom bleibt nach einem geringen Abfall von der ersten auf die zweite Bahn innerhalb des nutzbaren Magnetfeldbereichs praktisch konstant, woraus man auf die Wirksamkeit der elektrischen Fokussierung schliessen kann. Die differentielle Intensitätsmessung zeigt, dass der Strahl radial sehr gut gebündelt ist und die einzelnen Umlaufbahnen sauber voneinander getrennt sind.

In einem weiteren Versuch wurde anstelle des Messtargets ein Bronze-Drahtgewebe in den Strahlengang gebracht. Die Durchstosslöcher zeigen anschaulich, wie gut die räumliche Bündelung des Ionenpaketes ist (Abb. 11) und geben im übrigen auch ein Bild von den Teilchenschwingungen; auf der dritten Bahn zum Beispiel hat der Strahl einen fast kreisrunden Querschnitt mit einem Durchmesser von ca 5 mm.

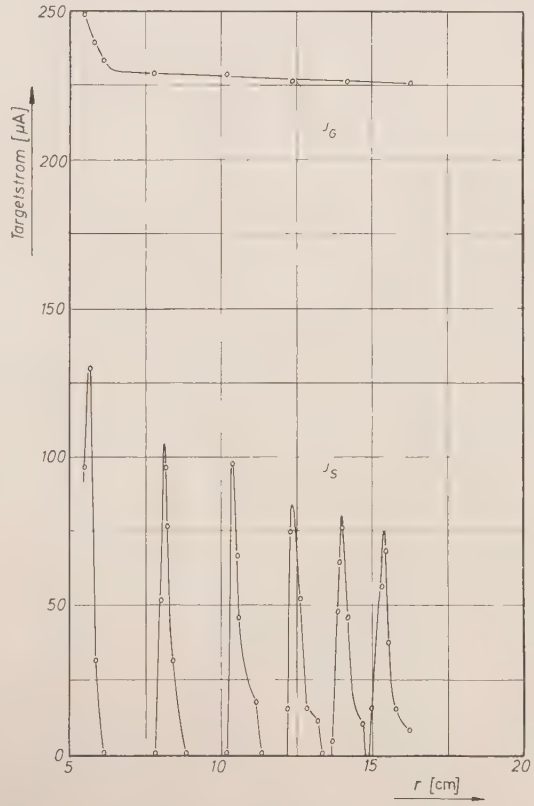


Abb. 10. Radialer Verlauf von Stromdichte $J_S$ und Gesamtstrom $J_G$ (ebene Polplatten).

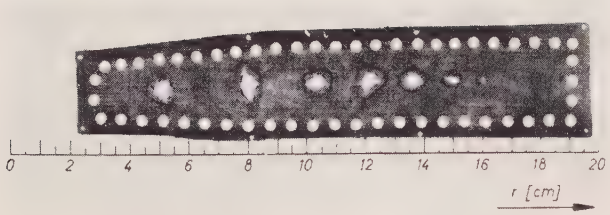


Abb. 11. Vom Ionenstrahl durchlöchertes Drahtnetz.

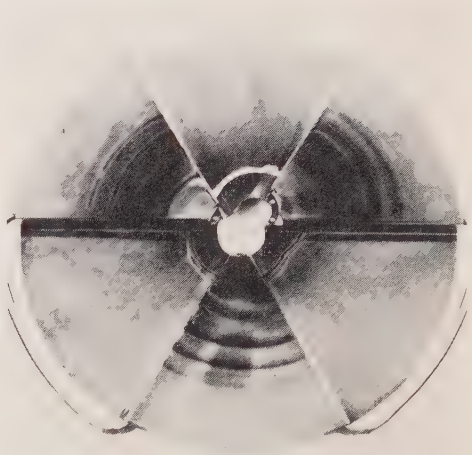

Abb. 12. Bahnspuren auf dem oberen Aussenleiter des Beschleunigungssystems.

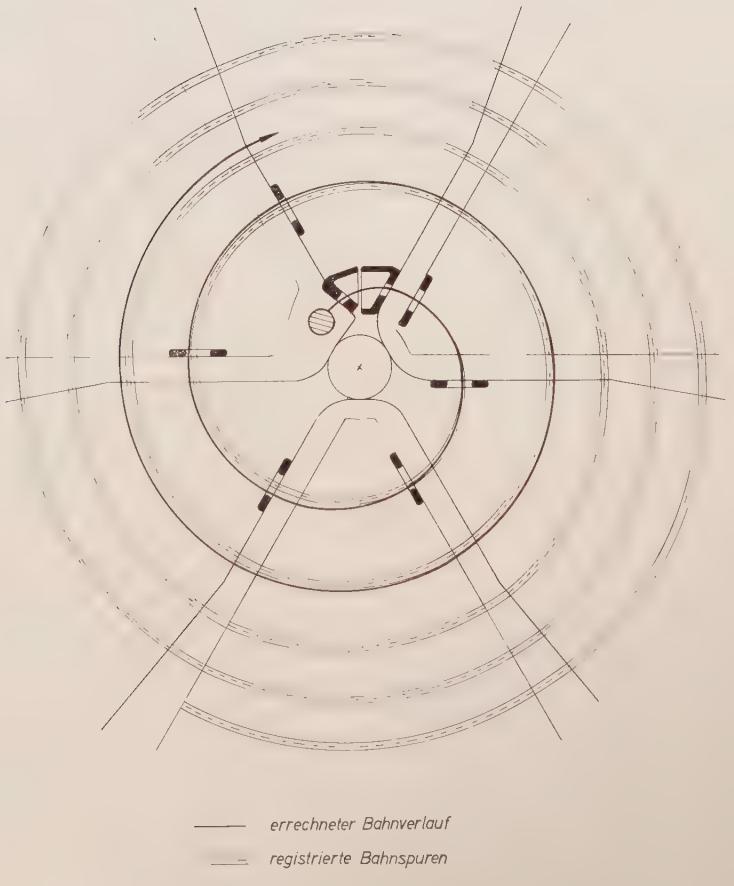


Abb. 13. Vergleich der Bahnspuren mit dem berechneten Verlauf

Bei den Experimenten stellte sich heraus, dass der Ionenstrahl bzw. die wenigen defokussierten Protonen auf dem Beschleunigungssystem durch Schwärzung Spuren hinterlassen (Abb. 12). Dadurch konnte man nun direkt bis ins Detail den wirklichen Bahnverlauf mit der Rechnung vergleichen und zum Beispiel auch die wichtige Frage der Bahnzentrierung klären, wozu man sonst drei Targets benötigt hätte. Abb. 13 zeigt die sehr gute Uebereinstimmung zwischen gerechnetem und experimentell registriertem Bahnverlauf. Die Abweichung des elektrischen Feldes von der theoretischen Annahme ist offenbar so gering, dass sie keinen grossen Einfluss auf die Teilchenbewegung ausübt.

Sehr aufschlussreich waren auch Versuche, bei denen keine oder nur die 3 ersten Blenden eingebaut waren. In diesen Fällen wurden einerseits die Bahnen exzentrisch und die elektrische Axialfokussierung war geringer, was sich in stärkerer Schwärzung auf dem Beschleunigungssytem auswirkte; andererseits kamen auch Teilchen mit in Umlauf, die sonst ausgeblendet wurden. Bei der Analyse der Schwärzungsspuren wurden auch Bahnen entdeckt, die nicht von Protonen herrührten. Die Rechnung ergab, dass es sich hier um $H_2^+$-Ionen handelte, die wider Erwarten auf stark exzentrischer Bahn ebenfalls beschleunigt werden und viele Umläufe machen können. Diese immer in einem gewissen Prozentsatz vorhandenen Molekülionen können die Targetmessungen leicht verfälschen. Mit Hilfe genauer Bahnberechnungen konnten die Laufzeitkammer und die erste Blende so dimensioniert werden, dass alle $H_2^+$-Ionen abgefangen wurden.

### 3.3. VERSUCHE MIT PROFILIERTEN POLPLATTEN

Nachdem die Versuche mit ebenen Polplatten gezeigt hatten, dass auf den ersten Umläufen eine ausreichende elektrische Fokussierung vorhanden ist, konnte ohne Bedenken für die endgültige Polschuhform ein ebenes Zentralplateau von 20 cm Durchmesser mit anschliessendem Uebergang in die Sektoren vorgesehen werden (Abb. 14). Zur Vergrösserung des nutzbaren Feldbereichs wurden Randshims aufgesetzt. Der relative radiale Feldverlauf im starken und schwachen Sektor sowie der Verlauf des mittleren Feldes $\bar{B}$ sind in Abb. 15 aufgetragen. Wie man sieht, beginnt der "Flutter"-Bereich schon innerhalb des Plateaus; im übrigen konnte das theoretisch geforderte Isochronfeld bis zu einem Radius von ca. 18 cm realisiert werden.

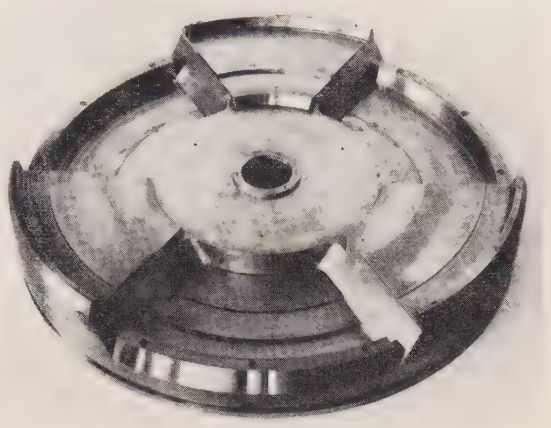

Abb. 14. Untere profilierte Polplatte des Versuchszyklotrons.

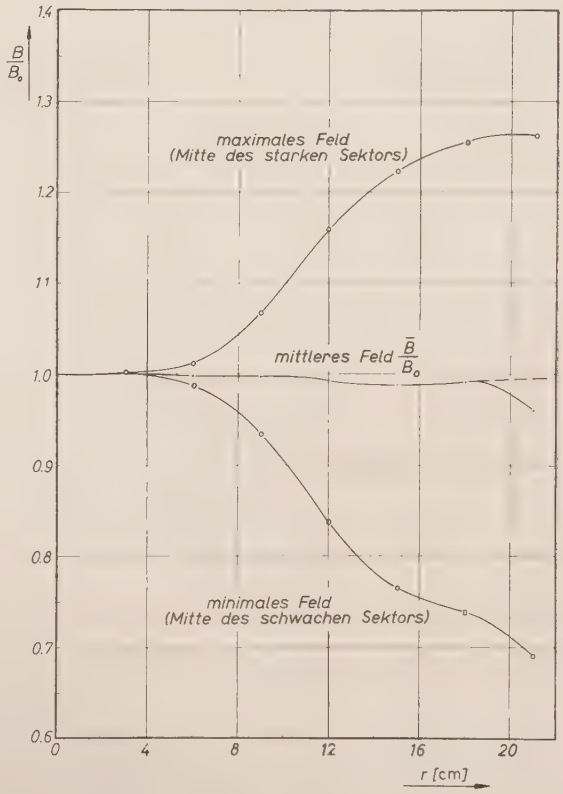


Abb. 15. Relativer Verlauf des Magnetfeldes im starken und schwachen Sektor sowie des mittleren Feldes $\bar{B}$ als Funktion des Radius. Gestrichelte Kurve: Isochronfeld in der grossen Maschine.

Die mit der vollständigen Blendenanordnung durchgeführten Experimente zeigten zunächst, dass der Strahl infolge der früh einsetzenden azimutalen Feldschwankung schon auf dem ersten Umlauf seine Bahn gegenüber dem Verlauf im homogen Feld etwas geändert hat und teilweise auf die

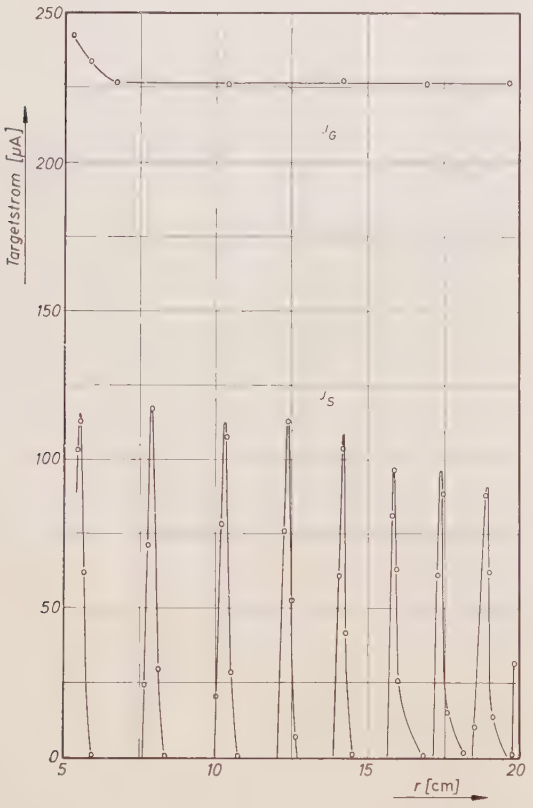


Abb. 16. Targetströne $J_s$ und $J_G$ bei profilierten Polplatten.

Blenden traf. Die fünfte und sechste Blende wurden deswegen um 1.5 mm bzw. 2 mm weiter nach innen versetzt. Im übrigen ergaben die Targetmessungen in den Versuchen mit profilierten Polplatten einen ganz analogen Intensitätsverlauf wie in Abb. 10, mit dem Unterschied, dass der Strahl noch etwas besser radial gebündelt ist und wegen des grösseren nutzbaren Magnetfeldbereichs eine grössere Zahl von Umläufen macht (Abb. 16).

Bahnspuren waren auf dem Beschleunigungssystem wegen der zusätzlichen Thomas-Fokussierung nur noch an einzelnen Stellen und dort auch nur äusserst schwach festzustellen. Der trotzdem noch rekonstruierbare Strahlverlauf liess deutlich die unterschiedliche Krümmung in den Sektoren mit starkem und schwachem Magnetfeld erkennen und ergab ausserdem, dass die gute Zentrierung der ersten Umläufe durchweg erhalten bleibt.

Mit einer für die Feineinstellung des Magnetfeldes in der grossen Maschine entwickelten Phasenmessapparatur[17]), die nach der Sampling-Methode arbeitet, wurde schliesslich noch der Ionenpulk auf den einzelnen Bahnen oszillographiert. Eine aus dem Beschleunigungssystem ausgekoppelte HF-Bezugsspannung wird hierbei auf dem Oszillographenschirm als Kreis geschrieben. Der mit einem in den Strahl geschobenen Diskriminator-Target aufgefangene Ionenimpuls erscheint als radiale Ausbuchtung dieses Kreises. Mit Hilfe eines Polarkoordinaten-Rasters können Breite und

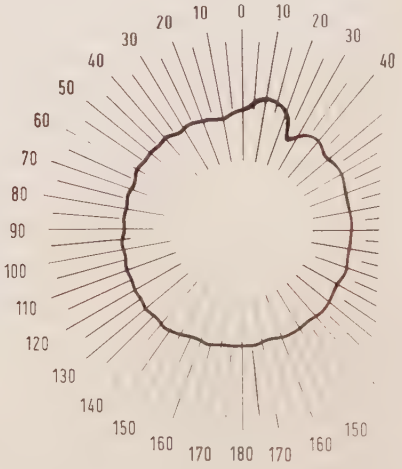


Abb. 17. Oszillogramm des Ionenpaketes auf der 2. Bahn.

Phasenlage des Pakets zur Hochfrequenz abgelesen werden. Abb. 17 zeigt ein auf der zweiten Bahn aufgenommenes Oszillogramm. In guter Uebereinstimmung mit der Rechnung hat das Ionenpaket hier eine Breite von ca. 30°, bei einer Phasenlage des Intensitätsmaximums von + 10°. Im Verlauf der weiteren Umläufe erfolgt eine Bündelung des Pakets auf etwa 20°, wobei die Lage des Maximums erhalten bleibt.

Wir dürfen aus diesen Ergebnissen den Schluss ziehen, dass das gesteckte Ziel für den Ioneneinfang

[17]) Diese Apparatur wurde von Herrn H. H. Feldmann, AEG-Forschungsinstitut Berlin-Reinickendorf, gebaut, der an anderer Stelle darüber berichten wird.

im Karlsruher Zyklotron, eine auf getrennten Bahnen erfolgende Strahlführung bei guter Zentrierung und Bündelung, auch im Uebergang vom homogenen Bereich in das Sektorfeld erreicht wurde. Ein störender Einfluss der gefürchteten $\nu_r = 1$ Resonanz auf die Radialbewegung war infolge der günstigen Anfangsbedingungen und des schnellen Uebergangs in das "Flutter"-Gebiet nicht zu beobachten. Wenn in der grossen Maschine die gute Strahlqualität der ersten Umläufe bis zum Endradius erhalten bleibt, so sind von dieser Seite her für eine saubere Extraktion gute Voraussetzungen gegeben. Im Modellzyklotron, wo der Bahnabstand am Polschuhrand etwa 1 cm beträgt, konnte der Strahl praktisch vollständig ausgelenkt werden, ohne dass sich sein Querschnitt von etwa $5 \times 5$ mm² im Streufeld viel änderte. Die Auslenkung bei höheren Energien dürfte natürlich wegen der engeren Bahnabstände und der Gefahr von Koppelresonanzen wesentlich schwieriger sein.

Zum Schluss möchte ich Herrn Direktor Dr. K. Steimel für wertvolle Anregungen und Diskussionen bestens danken. Ebenso danke ich allen seinen Mitarbeitern am Projekt des Karlsruher Zyklotrons, die mir bei der Durchführung dieser Arbeit geholfen haben, insbesondere Herrn H. H. Feldmann, der den HF-Generator und die Phasenmessapparatur gebaut hat, sowie Herrn W. Wolff für die Herstellung des magnetischen Sektorfeldes.

NUCLEAR INSTRUMENTS AND METHODS 13 (1961) 70–82; NORTH-HOLLAND PUBLISHING CO.

# THE RESPONSE OF ORGANIC SCINTILLATORS TO FAST NEUTRONS

R. BATCHELOR, W. B. GILBOY, J. B. PARKER and J. H. TOWLE

*Atomic Weapons Research Establishment, Aldermaston, Berks.*

Received 29 April 1961

The pulse height distributions for organic liquid scintillation counters irradiated with fast neutrons have been calculated using a Monte Carlo computer programme. The results obtained at 1, 4 and 14 MeV neutron energies for a cylindrical scintillator 2″ diameter × 2½″ long have been compared with experimental measurements and good agreement is obtained. In the experiments, the pulse shape discrimination and time of flight techniques have been used independently to eliminate the effect of $\gamma$-rays. The neutron detection efficiency has also been measured in the energy range 0.4 to 3.5 MeV and the results compared qualitatively with those obtained by the Monte Carlo calculation. In addition the pulse height response of the liquid scintillator type NE213 for protons and electrons is obtained and this is similar to that of the plastic phosphor type NE102.

## 1. Introduction

Since the discovery that pulses due to protons and electrons from counters employing certain organic scintillators can be distinguished from their shapes[1,2]), the utility of these scintillators has increased considerably. Thus a scintillator with linear dimensions of a few inches can be used as an efficient monitor of fast neutrons in the presence of a fairly intense $\gamma$-ray flux. Several methods have previously been used to reduce the relative efficiency to $\gamma$-rays[3]). For example this can be achieved by restricting the size of the scintillator such that the recoil protons are retained within the material whereas most of the lightly ionising electrons escape[4]). However, this invariably leads to a much reduced efficiency for neutron detection.

Litherland *et al.*[5]) have shown that a cylindrical liquid scintillator of dimensions 1½″ diameter, 1½″ long can also be used as a crude neutron spectrometer in certain cases. They were able to distinguish the neutron groups emitted in the reactions $Be^9(He^4, n)C^{12}$ and $Be^9(He^3, n)C^{11}$. These authors also pointed out the usefulness of the detector, when used in conjunction with a NaI detector, for coincidence measurements between neutrons and $\gamma$-rays emitted in nuclear reactions. Subsequently the idea was demonstrated in a study of (d,n) stripping reactions on $B^{10}$ and $B^{11}$ (ref. [6])).

In view of these developments it is therefore of considerable interest to know the pulse height distributions from these counters when placed in fluxes of monoenergetic neutrons. Such distributions could be used to deduce a neutron spectrum from an observed pulse distribution. Also if the area under each distribution is related theoretically to the incident neutron flux, then unknown neutron intensities can be measured.

This paper reports the results of some Monte Carlo calculations carried out for two cylindrical liquid scintillators, type NE213† 2″ diameter, 2½″ long and 3″ diameter, 4″ long, using the Aldermaston I.B.M. 7090 computer. These calculations, which have been made for incident neutrons of energies 0.7, 1, 2, 4, 8 and 14 MeV, and also for a fission spectrum, take into account all the known important effects which influence output pulse height. Thus, each neutron is tracked through the scintillator until it either escapes or is absorbed by the material. The type of each interaction it makes is catalogued and also the energies imparted to the

† Supplied by Nuclear Enterprises (G.B.) Ltd., Edingburgh.

[1]) F. D. Brooks, Nucl. Instr. and Meth. 4 (1959) 151.

[2]) R. B. Owen, Trans. I.R.E. on Nuclear Sci. NS-5 (1958) 198.

[3]) C. D. Swartz and G. E. Owen, Fast Neutron Physics, Part I (1960) 215.

[4]) J. R. Beyster, R. L. Henkel, R. A. Nobles and J. M. Kister, Phys. Rev. 98 (1955) 1216.

[5]) A. E. Litherland, E. Almqvist, R. Batchelor and H. E. Gove, Phys. Rev. Letters 2, No. 3 (1959) 511.

[6]) A. J. Ferguson, H. E. Gove, A. E. Litherland and R. Batchelor, Bull. Am. Phys. Soc. Series II, 5 (1960) 45.

emitted charged particles. The energy of each charged particle is then converted into a light output using a reasonable law relating the two quantities and the total light output for each incident neutron is obtained by simple addition. To calculate the pulse height distribution this procedure is repeated for about $10^5$ neutrons.

Some experimental measurements with incident neutrons of 0.96, 3.99 and 13.95 MeV have been made to compare with the results of these calculations. Two different methods have been used to ensure that electron pulses from $\gamma$-ray interactions were not observed. First pulse shape discrimination was applied to the output pulse using a circuit previously described by Batchelor *et al.*[7]). Secondly, the scintillator was set up as the detector in a time of flight spectrometer and the incident neutrons and $\gamma$-rays distinguished by their different flight times from a pulsed source.

As a further check on the calculations, the efficiency of the scintillator has been measured relative to a calibrated long counter in the region up to 4 MeV.

Some previous work of this nature has been reported by Hardy[8]), Swartz and Owen[3]) and Broek and Anderson[9]). However, it has been usual to consider only two neutron collisions within the scintillator and hence the calculations are applicable only to scintillators of small dimensions. Hardy[8]) considered the case of a scintillator of thickness 2″, but he encountered difficulty in explaining the observed pulse height distribution. He noted that the calculations did not reproduce a rise at low proton energy in the experimental distribution. Broek and Anderson give details of a method of obtaining a neutron spectrum from an observed pulse height distribution.

In the present work, full details of the neutron interactions are taken into account. As expected this procedure leads to good agreement between theory and experiment.

## 2. Monte Carlo Calculations

The calculations to be described have been made for the geometrical arrangement shown in fig. 1, in which a uniform parallel beam of neutrons is incident on the curved surface of the cylindrical detector. The scintillating liquid has a density of 0.88 g/cc and can be considered to consist of a mixture of hydrogen and carbon atoms in the ratio 1.21 : 1. The liquid is contained in a cylindrical glass

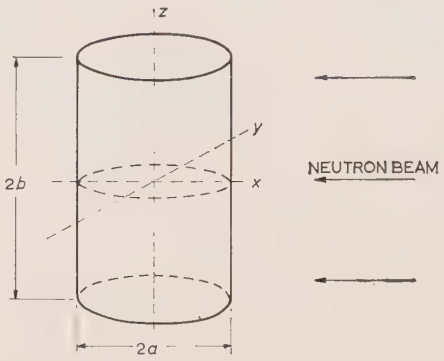


Fig. 1. Geometry of scintillator.

container, the presence of which is ignored in these calculations. The starting co-ordinates of a neutron are defined as

$$x = a\sqrt{1-\xi_1^2} \tag{1}$$

$$y = a\xi_1 \tag{2}$$

$$z = b\xi_2 \tag{3}$$

where $a$ is the radius and b the half height of the cylinder and $\xi_1$, $\xi_2$ are random numbers uniformly distributed in the range 0, 1). Because of symmetry this representation reproduces a uniform beam of neutrons, with each neutron having direction cosines $(-1, 0, 0)$. The probability distribution of neutron path length, $\rho$, within the scintillator is given in terms of the neutron mean free path, $\lambda$, in the scintillator material by the equation

$$P(\rho)\,\mathrm{d}\rho = \frac{1}{\lambda}\exp\left(-\frac{\rho}{\lambda}\right)\mathrm{d}\rho \quad (0 \leqslant \rho < \infty)\,. \tag{4}$$

It can be easily shown that $\rho = -\lambda \log \xi_3$ is a random deviate from this distribution, $\xi_3$ being a third random number uniform in (0, 1).

By comparing $\rho$ with the thickness of scintillator as seen by the neutron $(2a\sqrt{1-\xi^2_1})$, a decision is

[7]) R. Batchelor, W. B. Gilboy, A. D. Purnell and J. H. Towle, Nucl. Instr. and Meth. **8** (1960) 146.

[8]) J. E. Hardy, Rev. Sci. Instr. **29** (1958) 705.

[9]) H. W. Broek and C. E. Anderson, Rev. Sci. Instr. **31** (1960) 1063.

[10]) E. D. Pendlebury, to be published.

made as to whether this particular neutron escaped without collision, thereby making no contribution to the output, or whether an interaction took place. If a collision occurs, i.e. $\rho < 2a\sqrt{1-\xi^2_1}$, the nuclear data, pertinent to neutron collisions with hydrogen and carbon, are consulted and the energy and direction of the emergent neutron (if any), together with the energy deposited, $E_d$, are computed. The track is then continued, as before, and the process repeated until the neutron escapes or is absorbed or is moderated to thermal energy.

The nuclear data are stored in the machine in a suitable form for consultation by a special subroutine which has generalised inbuilt collision routines and is independent of the main Monte Carlo tracking and analysis programme.

Details of the nuclear data for many elements, including hydrogen and carbon, used at A.W.R.E. will shortly be published[10]), Published experimental cross-sections are used, where available, otherwise the values are based on nuclear theory, or interpolation and extrapolation of the experimental points. The data are converted into punched card form and processed in a special manner[11]) to yield partial cross-sections in each of 128 energy groups extending from 0.025 eV up to 14 MeV. For inelastic events, scattering is assumed to be isotropic in the laboratory system. Elastic scattering by hydrogen is taken to be isotropic in the centre of mass system, but use is made of the measured angular distributions for carbon[12]). Each distribution is assumed to be valid over a certain range of incident neutron energy and is simulated by 32 discrete scatter angle cosines, previously determined in such a manner that random sampling from these 32 members is a correct $\delta$-function representation of the angular distribution in the laboratory system. The corresponding energy reduction factor is precomputed for each of the 32 discrete cosines, thus eliminating the need for extra calculation during the Monte Carlo tracking at the expense of extra storage space.

Table 1 shows a list of all the neutron interactions with hydrogen and carbon which have been introduced into the calculations. Into the third column of this table are entered the charged particles, emitted in these reactions, which have been taken into account in computing the final light output. To simplify the calculations, the light outputs due to reactions with carbon leading to the emission of three $\alpha$-particles have been neglected. Similarly no account has been taken of any $\gamma$-rays emitted in the nuclear reactions. These assumptions are justified in view of the low probabilities of the processes involved.

TABLE 1
Neutron interactions in the scintillator considered in the Monte Carlo calculations

| Material | Type of reaction introduced into the Monte Carlo calculations | Charged particle considered in computing light output |
|---|---|---|
| H | Elastic scatter | Proton |
| | (n, $\gamma$) | — |
| C | Elastic scatter | Carbon recoil |
| | $C^{12}(n,\alpha)Be^{9}$ | $\alpha$-particle |
| | $C^{12}(n,n')C^{12*}(3\alpha)$ | — |
| | $C^{12}(n,n')C^{12*}$ | — |
| | $C^{12}(n,\alpha)Be^{9*}(n)Be^{8}(2\alpha)$ | — |

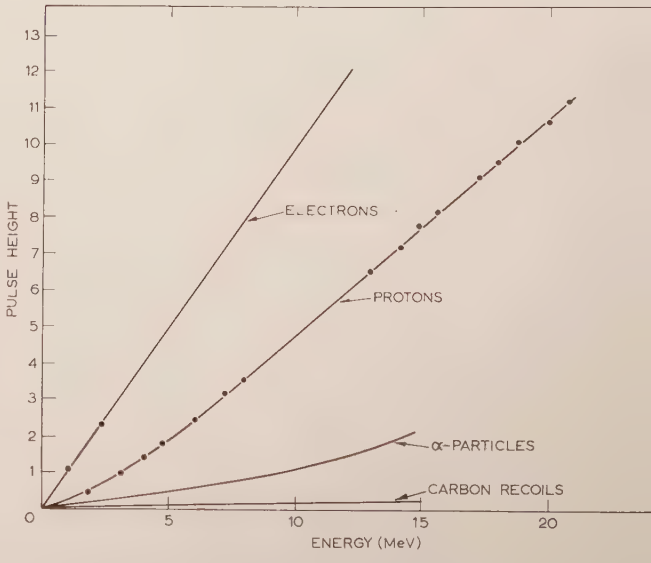


Fig. 2. Relationships between light output and energy for electrons, protons, $\alpha$-particles and carbon recoils, used in the Monte Carlo calculations. The dots are experimental points.

[11]) K. Parker and J. B. Parker, A.W.R.E. (Aldermaston) Report No. 0–20/60 (1960).

[12]) D. J. Hughes and R. S. Carter, B.N.L. Report No. 400 (1956).

For ease of computation the following simple simple relationships between light output (L) and energy of the particle have been used and are plotted in fig. 2.

Protons

$$L_p = 0.215E_p + 0.028E_p^2 \ (0 < E_p < 8 \text{ MeV}) \quad (5a)$$

$$= 0.60E_p - 1.28 \qquad (8 < E_p < 14 \text{ MeV}). \quad (5b)$$

α-particles

$$L_\alpha = 0.046\,E_\alpha + 0.007E_\alpha^2\,. \quad (6)$$

Carbon recoils

$$L_C = 0.017\,E_C. \quad (7)$$

Prior to this investigation, there was no experimental information on the response of the NE213 liquid scintillator to the various particles. The response for protons (eqs. (5a) and (5b)) was obtained experimentally by the method described in section 4.2.

To obtain eqs. (6) and (7), a calculation of the response to α-particles and carbon ions was first performed using the formula due to Birks[13]).

$$\frac{dL}{dE} = \left(1 + kB\frac{dE}{dx}\right)^{-1} \quad (8)$$

where $dE/dx$ is the energy lost by the particle per unit distance travelled in the scintillator. A value of 0.01 g cm$^{-2}$ MeV$^{-1}$ was used for $kB$, which is that found by Evans and Bellamy[14]) for the plastic phosphor NE102. It was found that these curves could be fitted quite well with the expressions (6) and (7). It is obvious that the dominant contribution to the light output arises from the effect of protons and hence the use of the approximate expressions (6) and (7) is not likely to lead to large final errors.

Edge effects, due to the finite ranges of the charged particles, are negligible in the scintillators of sizes considered here, even for neutrons up to 14 MeV.

## 3. Results of the Calculations

Histograms of the various light output distributions are shown in figs. 3–7. Table 2 gives the data from which these curves are drawn. The number of

[13]) J. B. Birks, Proc. Phys. Soc. A **164** (1951) 10.

[14]) H. C. Evans and R. H. Bellamy, Proc. Phys. Soc. **74** (1959) 483.

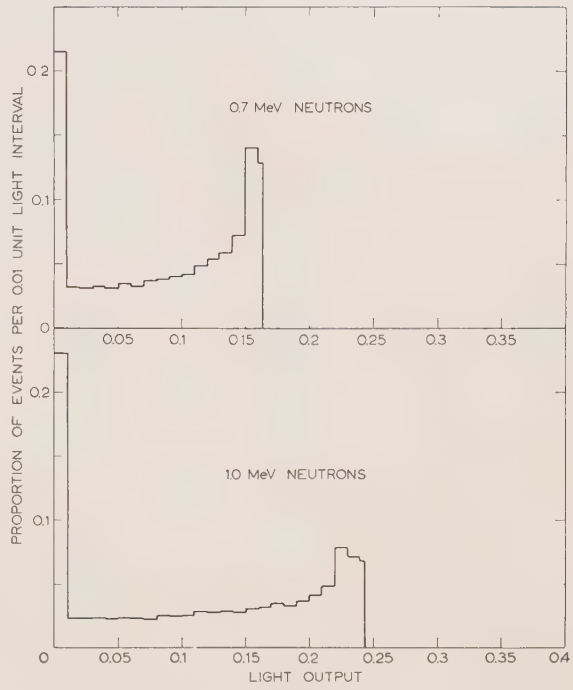


Fig. 3. Theoretical pulse height distributions for 0.7 MeV and 1.0 MeV neutrons, 2″ × 2½é scintillator.

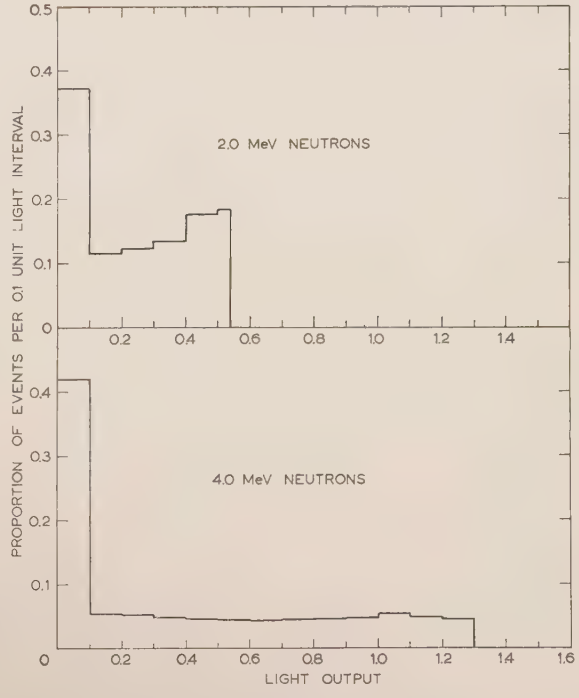


Fig. 4. Theoretical pulse height distributions for 2.0 MeV and 4 MeV neutrons, 2″ × 2½″ scintillator.

TABLE 2

Light output distributions for neutrons of various energies interacting in the scintillators

| Light output interval | Proportion of events | | | Light output interval | Proportion of events | | | Light output interval | Proportion of events | |
|---|---|---|---|---|---|---|---|---|---|---|
| | $2'' \times 2\frac{1}{2}''$, 0.7 MeV | $2'' \times 2\frac{1}{2}''$, 1.0 MeV | $2'' \times 2\frac{1}{2}''$, 2 MeV | | $2'' \times 2\frac{1}{2}''$, 4 MeV | $3'' \times 4''$, 4 MeV | $2'' \times 2\frac{1}{2}''$, 8 MeV | | $2'' \times 2\frac{1}{2}''$, 14 MeV | $3'' \times 4''$, 14 MeV |
| 0 –0.01 | 0.2147 | 0.2298 | 0.2528 | 0 0.1 | 0.4202 | 0.3489 | 0.3917 | 0 –0.1 | 0.4335 | 0.4052 |
| 0.01 0.02 | 0.0310 | 0.0228 | 0.0225 | 0.1 0.2 | 0.0553 | 0.0559 | 0.0486 | 0.1–0.2 | 0.0261 | 0.0336 |
| 0.02 0.03 | 0.0312 | 0.0228 | 0.0123 | 0.2 0.3 | 0.0518 | 0.0531 | 0.0324 | 0.2–0.3 | 0.0234 | 0.0324 |
| 0.03–0.04 | 0.0335 | 0.0230 | 0.0128 | 0.3 0.4 | 0.0484 | 0.0505 | 0.0247 | 0.3–0.4 | 0.0147 | 0.0170 |
| 0.04–0.05 | 0.0318 | 0.0216 | 0.0119 | 0.4 0.5 | 0.0468 | 0.0496 | 0.0243 | 0.4–0.5 | 0.0144 | 0.0191 |
| 0.05–0.06 | 0.0344 | 0.0235 | 0.0123 | 0.5 0.6 | 0.0458 | 0.0510 | 0.0224 | 0.5 0.6 | 0.0570 | 0.0602 |
| 0.06–0.07 | 0.0339 | 0.0231 | 0.0129 | 0.6 0.7 | 0.0448 | 0.0512 | 0.0207 | 0.6–0.7 | 0.0101 | 0.0101 |
| 0.07–0.08 | 0.0374 | 0.0225 | 0.0118 | 0.7 0.8 | 0.0440 | 0.0533 | 0.0204 | 0.7–0.8 | 0.0115 | 0.0118 |
| 0.08 0.09 | 0.0382 | 0.0248 | 0.0117 | 0.8–0.9 | 0.0473 | 0.0554 | 0.0203 | 0.8–0.9 | 0.0100 | 0.0117 |
| 0.09–0.10 | 0.0402 | 0.0242 | 0.0120 | 0.9 1.0 | 0.0487 | 0.0546 | 0.0191 | 0.9–1.0 | 0.0091 | 0.0093 |
| 0.10 0.11 | 0.0432 | 0.0262 | 0.0124 | 1.0 1.1 | 0.0537 | 0.0656 | 0.0188 | 1.0–1.1 | 0.0095 | 0.0103 |
| 0.11–0.12 | 0.0492 | 0.0276 | 0.0110 | 1.1 1.2 | 0.0460 | 0.0538 | 0.0166 | 1.1–1.2 | 0.0090 | 0.0098 |
| 0.12 0.13 | 0.0549 | 0.0268 | 0.0124 | 1.2 1.3 | 0.0438 | 0.0526 | 0.0169 | 1.2 1.6 | 0.0292 | 0.0328 |
| 0.13–0.14 | 0.0590 | 0.0276 | 0.0117 | 1.3 1.4 | 0.0034 | 0.0045 | 0.0152 | 1.6 2.0 | 0.0270 | 0.0280 |
| 0.14 0.15 | 0.0734 | 0.0278 | 0.0126 | 1.4 1.5 | | | 0.0159 | 2.0–2.4 | 0.0274 | 0.0255 |
| 0.15 0.16 | 0.1402 | 0.0307 | 0.0116 | 1.5 1.6 | | | 0.0163 | 2.4–2.8 | 0.0246 | 0.0225 |
| 0.16–0.17 | 0.0538 | 0.0313 | 0.0107 | 1.6–1.7 | | | 0.0154 | 2.8–3.2 | 0.0208 | 0.0220 |
| 0.17–0.18 | | 0.0349 | 0.0116 | 1.7–1.8 | | | 0.0155 | 3.2–3.6 | 0.0211 | 0.0213 |
| 0.18–0.19 | | 0.0333 | 0.0114 | 1.8–1.9 | | | 0.0153 | 3.6–4.0 | 0.0237 | 0.0216 |
| 0.19–0.20 | | 0.0361 | 0.0120 | 1.9–2.0 | | | 0.0146 | 4.0–4.4 | 0.0249 | 0.0236 |
| 0.20–0.21 | | 0.0407 | 0.0117 | 2.0–2.1 | | | 0.0155 | 4.4–4.8 | 0.0253 | 0.0252 |
| 0.21 0.22 | | 0.0482 | 0.0121 | 2.1–2.2 | | | 0.0156 | 4.8–5.2 | 0.0245 | 0.0232 |
| 0.22–0.23 | | 0.0794 | 0.0117 | 2.2–2.3 | | | 0.0149 | 5.2–5.6 | 0.0262 | 0.0256 |
| 0.23–0.24 | | 0.0707 | 0.0122 | 2.3–2.4 | | | 0.0141 | 5.6–6.0 | 0.0247 | 0.0280 |
| 0.24–0.25 | | 0.0206 | 0.0112 | 2.4–2.5 | | | 0.0161 | 6.0 6.4 | 0.0254 | 0.0249 |
| 0.25–0.26 | | | 0.0122 | 2.5–2.6 | | | 0.0163 | 6.4–6.8 | 0.0257 | 0.0246 |
| 0.26–0.27 | | | 0.0124 | 2.6–2.7 | | | 0.0155 | 6.8 7.12 | 0.0211 | 0.0203 |
| 0.27 0.28 | | | 00.120 | 2.7–2.8 | | | 0.0143 | | | |
| 0.28 0.29 | | | 0.0129 | 2.8–2.9 | | | 0.0133 | | | |
| 0.29 0.30 | | | 0.0120 | 2.9–3.0 | | | 0.0144 | | | |
| 0.30 0.31 | | | 0.0120 | 3.0–3.1 | | | 0.0135 | | | |
| 0.31 0.32 | | | 0.0123 | 3.1–3.2 | | | 0.0125 | | | |
| 0.32 0.33 | | | 0.0122 | 3.2–3.3 | | | 0.0122 | | | |
| 0.33 0.34 | | | 0.0143 | 3.3–3.4 | | | 0.0127 | | | |
| 0.34–0.35 | | | 0.0132 | 3.4 3.5 | | | 0.0124 | | | |
| 0.35 0.36 | | | 0.0128 | 3.5 3.6 | | | 0.0016 | | | |
| 0.36–0.37 | | | 0.0137 | | | | | | | |
| 0.37 0.38 | | | 0.0139 | | | | | | | |
| 0.38 0.39 | | | 0.0130 | | | | | | | |
| 0.39 0.40 | | | 0.0125 | | | | | | | |
| 0.40 0.41 | | | 0.0140 | | | | | | | |
| 0.41 0.42 | | | 0.0152 | | | | | | | |
| 0.42 0.43 | | | 0.0155 | | | | | | | |
| 0.43 0.44 | | | 0.0163 | | | | | | | |
| 0.44–0.45 | | | 0.0161 | | | | | | | |
| 0.45–0.46 | | | 0.0170 | | | | | | | |
| 0.46 0.47 | | | 0.0203 | | | | | | | |
| 0.47 0.48 | | | 0.0219 | | | | | | | |
| 0.48–0.49 | | | 0.0245 | | | | | | | |
| 0.49–0.50 | | | 0.0205 | | | | | | | |
| 0.50–0.51 | | | 0.0180 | | | | | | | |
| 0.51 0.52 | | | 0.0181 | | | | | | | |
| 0.52 0.53 | | | 0.0182 | | | | | | | |
| 0.53–0.54 | | | 0.0196 | | | | | | | |
| 0.54–0.55 | | | 0.0036 | | | | | | | |

neutrons tracked was 50000 per run, except for the 8 and 14 MeV runs on the $2'' \times 2\frac{1}{2}''$ scintillator; 100000 neutrons were tracked in these cases. On the average each run took about $\frac{3}{4}$ hour. The statistical errors on the ordinates are less than 10 %.

An interesting feature of these histograms is that as the incident neutron energy increases, there is a shift of pulses from high to low light output. This can be understood in the following way. Multiple neutron scattering in the scintillator tends to give large output pulses whereas the non-linear response of the scintillator to protons concentrates the pulses in the region of low output. For incident neutrons of low energy the proportion of multiple scattered events is relatively high and is sufficient to dominate the pulse output distribution. On the other hand, at high energies multiple scattering is not so important and the non-linear pulse height response is the dominant factor affecting the distribution. All the histograms show a large number of very low light pulses and these are due to the recoiling carbon nuclei. Another point of interest is the narrow peak in the light interval 0.5 to 0.6 in the 14 MeV distributions (figs. 5 and 6). This peak is due to the $\alpha$-particles emitted in the reaction $C^{12}(n, \alpha)Be^{9}$.

Table 3 gives the percentage of neutrons which pass through the scintillator without interacting, the percentage which though interacting, fail to contribute to the light output (due e.g. to $C^{12}(n, n')$) and the total theoretical efficiency. The standard deviations of these results are less than 0.2 %. From the theoretical distributions for the $2'' \times 2\frac{1}{2}''$ scintillator, the counting efficiencies for various bias levels have been calculated, and are plotted as a function of neutron energy in fig. 8. The bias levels quoted refer to proton energy deposited in the scintillator and hence can be regarded as the minimum neutron energy to which the detector is sensitive. The lines drawn in fig. 8 are smooth curves through the points. If the calculations were to be performed at closely spaced neutron energies, then the curve for zero bias is not expected to be smooth, due to the effect of resonances in the carbon cross-section. Also shown in fig. 8 is a curve for zero bias calculated from the simple formula.

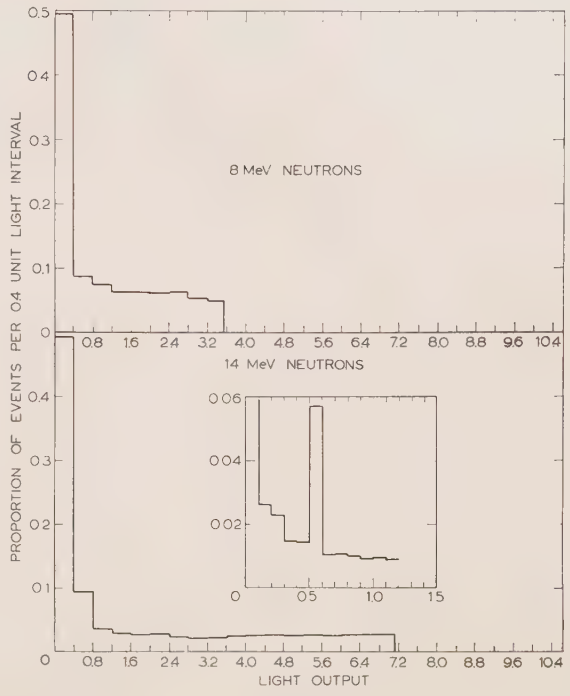


Fig. 5. Theoretical pulse height distributions for 8.0 MeV and 14 MeV neutrons, $2'' \times 2\frac{1}{2}''$ scintillator.

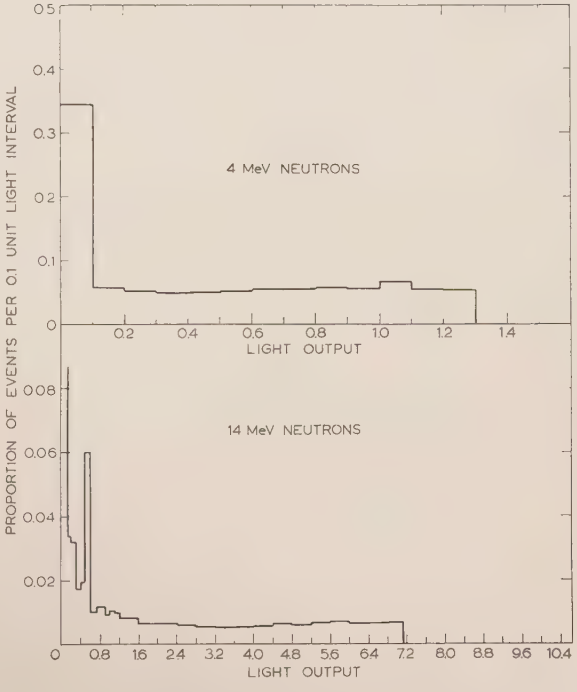


Fig. 6. Theoretical pulse height distributions for 4.0 MeV and 14.0 MeV neutrons, $3'' \times 4''$ scintillator.

TABLE 3
Details of the numbers of neutrons which interact with the scintillators

| Neutron energy (MeV) | $2'' \times 2\frac{1}{2}''$ scintillator | | | $3'' \times 4''$ scintillator | | |
|---|---|---|---|---|---|---|
| | % uncollided neutrons | % absorbed neutrons† | Efficiency (%) | % uncollided neutrons | % absorbed neutrons† | Efficiency (%) |
| 0.7 | 26.4 | 0 | 73.6 | | | |
| 1.0 | 31.8 | 0 | 68.2 | 19.5 | 0 | 80.5 |
| 2.0 | 44.5 | 0 | 55.5 | | | |
| 4.0 | 53.4 | 0 | 46.6 | 41.2 | 0 | 58.8 |
| 8.0 | 63.8 | 4.5 | 31.7 | | | |
| 14.0 | 71.3 | 4.1 | 24.6 | 61.9 | 4.0 | 34.1 |
| Fission spectrum | 37.9 | 0.1 | 62.0 | 26.2 | 0.1 | 73.7 |

† More precisely: percentage of neutrons which interact but do not contribute to the light output.

$$\text{Efficiency} = (1 - e^{-n_H \sigma_H d}) \qquad (9)$$

where

$n_H$ = number of H atoms per cc of scintillator

$\sigma_H$ = (n, p) cross-section

$d = \frac{1}{2}\pi a$ = mean thickness of scintillator.

This formula is based on the following assumptions.

(a) carbon is not present in the scintillator

(b) the radius of the scintillator is small compared with $1/n_H\sigma_H$.

Swartz and Owen[3]) point out that, in some cases, the efficiency calculated using this formula is approximately equal to that calculated if single hydrogen collisions, single carbon collisions and carbon collisions, followed by hydrogen collisions, are allowed to occur.

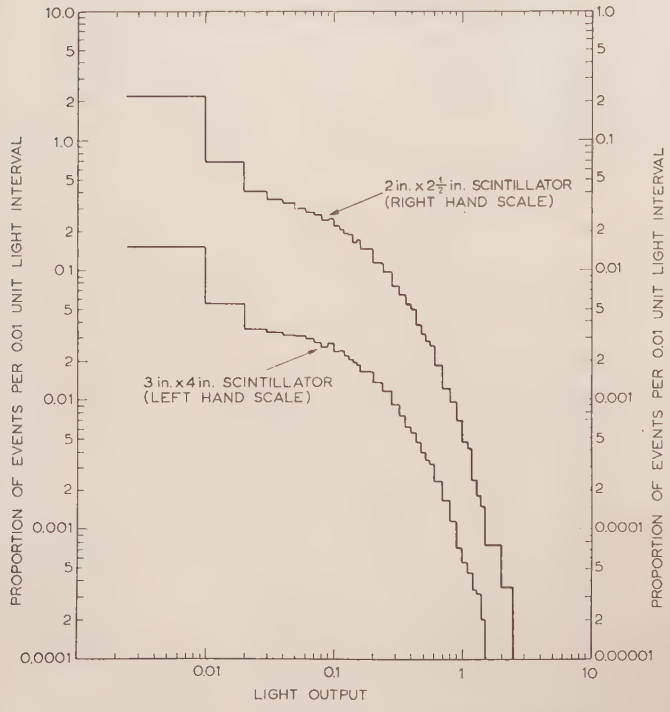
PROPORTION OF EVENTS PER 0.01 UNIT LIGHT INTERVAL
PROPORTION OF EVENTS PER 0.01 UNIT LIGHT INTERVAL
2 in. x 2½ in. SCINTILLATOR (RIGHT HAND SCALE)
3 in. x 4 in. SCINTILLATOR (LEFT HAND SCALE)
LIGHT OUTPUT

Fig. 7. Theoretical pulse height distribution for fission neutrons.

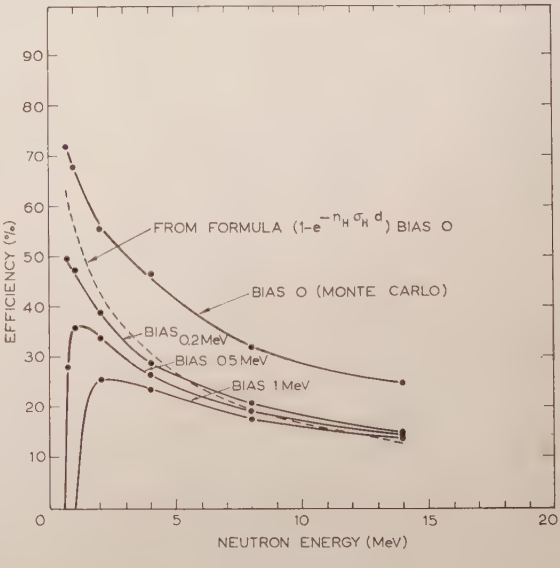


Fig. 8. Theoretical efficiency curves for the $2'' \times 2\frac{1}{2}''$ scintillator biassed at various levels. The broken curve represents the efficiency calculated from eq. (9).

## 4. Experimental Measurements

### 4.1. DETECTOR AND EQUIPMENT

The experiments to be described have been carried out with a 2″ diam. × 2½″ long scintillator which is the detector normally used in the time of flight spectrometer for fast neutron studies using the 6 MV Van de Graaff accelerator at Aldermaston. The time of flight apparatus was used in these experiments and since the details have been published elsewhere[15,16]) only a brief description will be given here.

The NE213 liquid is contained in a right cylindrical glass container of wall thickness approximately $\frac{1}{16}$″, and is viewed by two photomultipliers, type 6810A, one optically coupled to each flat end of the cylinder. The outside of the curved surface of the cylinder is coated with white reflecting paint. The complete detector is housed in a brass tube, of wall thickness $\frac{1}{16}$″, and is placed at the centre of a cylindrical shield of water and lead of diameter 4 ft and height 4 ft. Neutrons are incident on the curved surface of the scintillator through a collimating hole of diameter 2½″ in the shield. This means that the sensitive area of the scintillator is not fully exposed to the incident beam, and hence the experimental arrangement does not accurately reproduce the conditions under which the theoretical calculations have been made. This, however, was considered to be relatively unimportant except in the comparison between theoretical and experimental efficiencies. In this case a suitable correction for the loss in sensitive area has been applied. From time of flight spectrum measurements, neutron energy degradation by the collimator is known to be negligible.

The method of applying pulse shape discrimination to the detector is an extension of the method proposed by Owen[2]) and has been previously described in detail[7]). The voltage between the collector and last dynode of one of the photomultipliers (for convenience this will be called the "left" photomultiplier) is restricted to a few volts. The positive swing of the pulse from the last dynode is used to indicate the type of particle which initiated the event. A proton usually gives a larger positive output than an electron and the proton pulse swings positive at a slightly earlier time. This pulse and two linear pulses, one from each photomultiplier, are amplified (differentiating time 3 $\mu$sec), passed through voltage discriminators and then applied to a threefold coincidence circuit. Adjustment of the various bias levels and also the coincidence resolving time ensures that the coincidence output signifies the incidence of a neutron. The pulse height distribution appropriate to neutrons is then obtained by gating the linear output of the "right" photomultiplier with this coincidence output. The pulses are analysed on a 100 channel pulse height analyser. If the gating pulse is taken from a twofold coincidence between the two linear outputs, then the resulting pulse distribution is that pertaining to the incidence of both neutrons and $\gamma$-rays.

To obtain the pulse distributions by the time of flight method, a pulsed beam is used, the pulse repetition frequency being 5 Mc/sec and the pulse width approximately 2 nanosec. A fast pulse is taken from the "right" photomultiplier and is fed as a start pulse into a time sorter; the stop pulse being obtained from the R.F. which deflects the beam. A twofold coincidence between the two linear pulses from the photomultiplier gates the time sorter output which is observed on a 100-channel pulse height analyser.

The time spectrum exhibits two peaks due to neutrons and two due to $\gamma$-rays, superimposed on a small background. To obtain the pulse height distribution appropriate to neutrons, voltage windows are placed across the neutron peaks by means of two single channel analysers. The outputs of the analysers are mixed and arranged to gate the linear output from the "right" photomultiplier and the spectrum is recorded on a second 100 channel pulse height analyser. If the background of the time spectrum is not negligible, a further measurement with the windows set to pass appropriate sections of the background is made. Provided the background is flat, this measurement gives a suitable correction for the background under the neutron peaks.

[15]) R. Batchelor and J. H. Towle, A.W.R.E. (Aldermaston) Report No. NR/P-12/58 (1958).

[16]) B. E. F. Macefield and J. H. Towle, Proc. Soc. A **76** (1960) 56.

### 4.2. MEASUREMENT OF PULSE HEIGHT RESPONSE FOR PROTONS

A necessary preliminary to this work was to establish that the linear output from the "right" photomultiplier was in fact linear, and also to measure the variation of proton pulse height with proton energy for the liquid scintillator. The method adopted was to make some preliminary observations of the pulse height distributions by the pulse shape discrimination method for monokinetic incident neutrons of various energies. In order to extract the required information it was anticipated that the observed distributions would be similar to those predicted by theory but modified at the high energy cut off by resolution. For neutrons in excess of about 2 MeV it was noted that the high energy half of each spectrum is fairly flat and consequently the average pulse height for a proton of energy equal to the incident neutron energy can be taken as the mid point of the fall off of the observed curve. As can be seen from figs. 10 and 12, in the case of 3.99 MeV, this method gives the same result as that obtained by extrapolating the straight line portion of the integral curve to the bias axis.

For these experiments, neutrons in the energy range 13 to 21 MeV were obtained from the T(d, n)$He^4$ reaction, those in the range 4 to 8 MeV from the d(d, n)$He^3$ reaction and those in the range 2 to 4 MeV from the T(p, n)$He^3$ reaction. Gaseous targets were used and the incident particle energy and angle of observation were adjusted to give the desired neutron energy.

The electron response was also measured by observing the Compton edges for the 2.62 MeV thorium $\gamma$-rays and the 1.28 $Na^{22}$ $\gamma$-rays. Periodic measurements with these sources also served to check on the stability of the apparatus.

The results are shown in fig. 2 in which the ordinate scale is chosen to conform with the convention that the electron pulse height is equal to the electron energy. These curves were obtained with an overall H.T. voltage of 1600 applied to the "right" photomultiplier. When this voltage was increased to about 1900 the proton curve showed definite signs of saturation. Reducing the voltage to 1400 produced no change in the shape of the curve, thus indicating that at 1600 V no saturation was occurring. This suggests that the output is linear. It should be noted that no convenient $\gamma$-ray sources exist for a direct check on the linearity in the energy range required.

It is of interest to note that the shape of the measured curve is close to that obtained by Evans and Bellamy[14]) for the plastic phosphor NE102. The slight difference between the two curves can be understood in terms of the different ionisation losses due to the different C:H ratios in the two materials.

### 4.3. MEASUREMENT OF PULSE HEIGHT DISTRIBUTIONS

Measurements have been made by the two methods for incident neutron energies of 3.99 MeV and 13.95 MeV and by the time of flight method only at 0.96 MeV. Details of the neutron sources used and relevant geometrical details are given in table 4.

The results are shown in figs. 9, 10 and 11. In figs. 10 and 11 the results obtained by the two methods are normalised, for illustrative purposes

TABLE 4

Details of the neutron sources and geometry used in the experiment

| | | | |
|---|---|---|---|
| Incident neutron energy | 3.99 MeV | 13.95 MeV | 0.96 MeV |
| Reaction | $H^3$(p,n)$He^3$ | $H^3$(d,n)$He^4$ | $H^3$(p,n)$He^3$ |
| Type of target | Tritium gas | Tritium gas | Tritium gas |
| Energy of bombarding particles | 5.33 MeV | 1.96 MeV | 2.18 MeV |
| Angle of observation relative to incident charged particle beam direction | 30° | 105° | 30° |
| Distance between source and detector | 171 cm | 171 cm | 171 cm |
| Estimated neutron energy spread | 50 keV | 80 keV | 90 keV |

only, so that the areas under the curves are the same. In section 4.4 (see fig. 13) it is shown that the overall detection efficiency is reduced when pulse shape discrimination is applied and consequently the areas under the corresponding curves should be less than the curves obtained by the time of flight method. From fig. 13 we deduce that the rejection rate of proton pulses by the pulse indicator circuit varies with proton energy. This effect is also noticeable in the 13.95 MeV pulse distribution curves (fig. 11) but does not show up at 3.95 MeV (fig. 10). Figs. 10 and 11 are reasonably consistent, however, if the pulse shape discrimination curve of fig. 10 is reduced by about 5% to allow for the reduced efficiency.

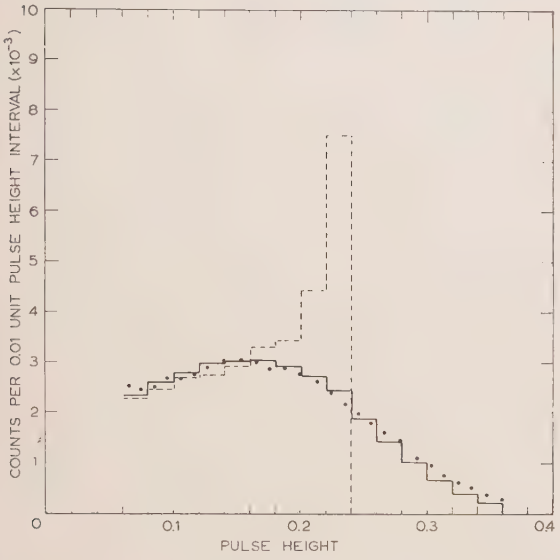


Fig. 9. Pulse height distribution obtained in the 0.96 MeV neutron experiment using the time of flight technique. The dotted line is the theoretical fit without resolution correction; the solid line is the fit with resolution correction.

### 4.4. EFFICIENCY MEASUREMENTS

Measurements of the efficiency of the scintillator with an effective bias of about 200 keV were made in the neutron energy range 0.3 to 3.5 MeV. The $H^3(p, n)He^3$ source, with a gaseous tritium target, was used and the energy of the neutrons incident on the detector was varied by varying the proton energy and the angle of observation relative to the incident proton beam. Angles of 30° and 90° were used, covering the energy ranges 1 to 3.5 MeV and 0.3 to 1.5 MeV respectively. The incident neutron

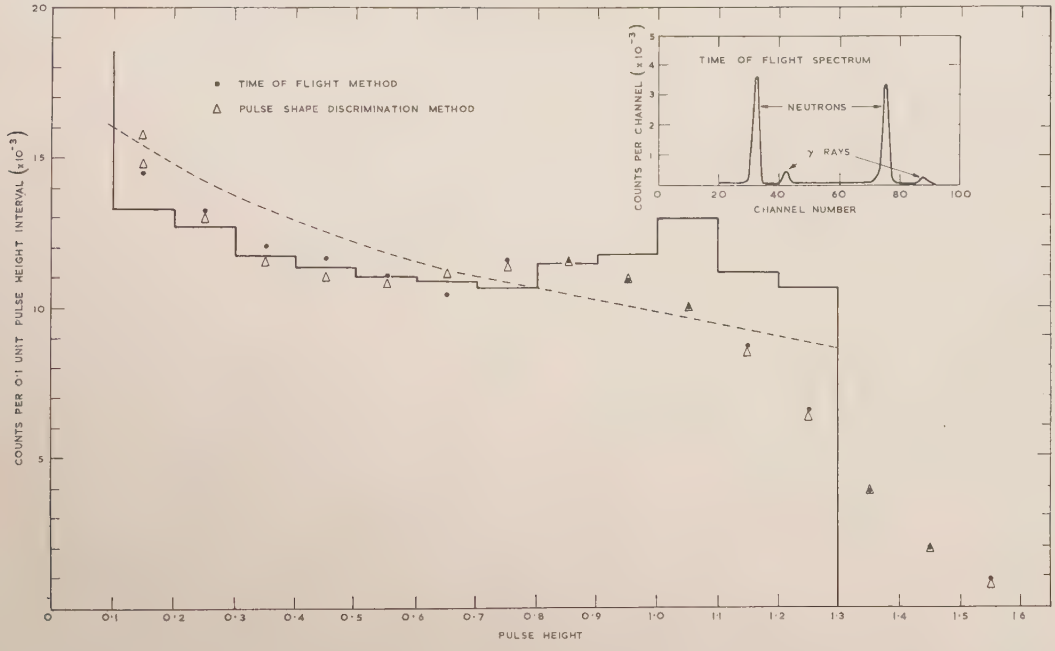


Fig. 10. Pulse height distributions obtained in the 3.99 MeV neutron experiment. The solid line is the fit appropriate to the theory developed in this paper; the dotted line is the theoretical curve based on single collisions with hydrogen. The inset shows the time spectrum of the radiation incident on the scintillator.

flux was measured with a long counter[17]), calibrated with standard neutron sources, placed at the same angle as the scintillator but on the opposite side of the beam piping. The background of the long counter from neutrons not directly emitted from the gas cell was measured by placing a shadow cone of paraffin wax approximately midway between the source and counter. A second long counter served to monitor the neutron output.

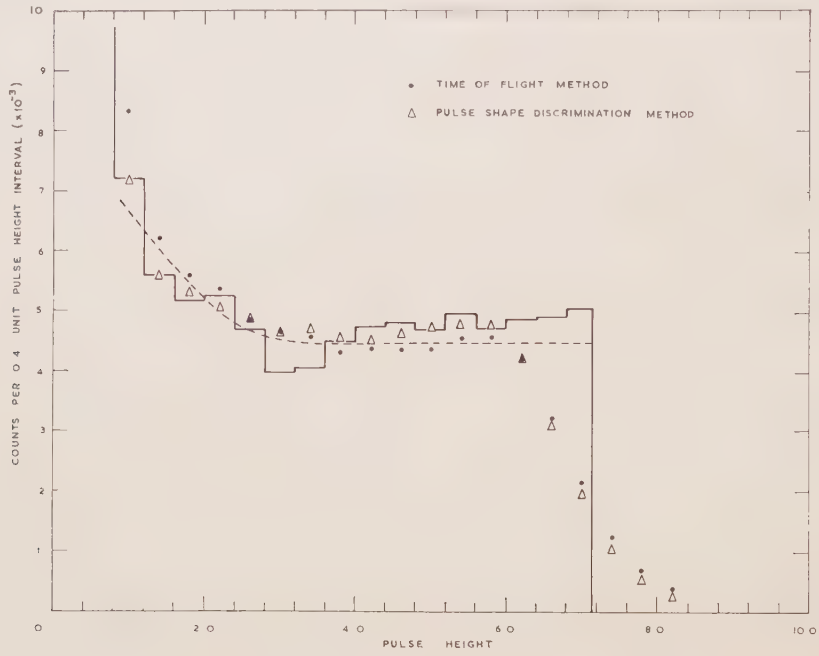


Fig. 11. Pulse height distributions obtained in the 13.95 MeV neutron experiment. The solid line is the fit appropriate to the theory developed in this paper; the dotted line is the theoretical curve based on single collisions with hydrogen.

In this experiment a pulsed beam was used so that at each energy the time spectrum could be observed and the neutron counting rate in the scintillator found by summing the counts in the neutron peaks. Measurements were made with the time sorter output gated by the twofold coincidence between the linear outputs of the photomultipliers and also by the threefold coincidence which introduces the influence of the pulse discriminator circuit.

Apart from the neutron peaks, each time spectrum contains a small fairly flat background which was still present when tritium was removed from the cell. This background reduces by about a factor 2 when pulse shape discrimination is applied. Under these conditions, a large fraction of the background represents neutrons originating directly

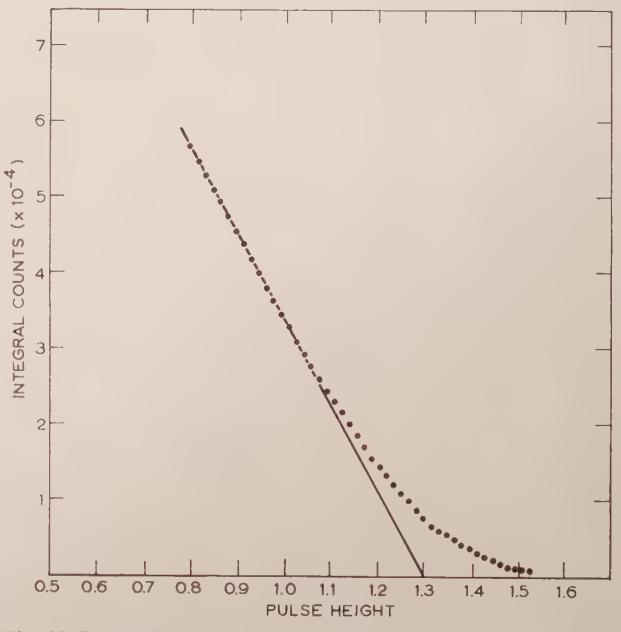


Fig. 12. Integral pulse height curve for 4 MeV neutrons showing the method of extrapolation used to determine the upper cut-off.

[17]) A. O. Hansen and J. L. McKibben, Phys. Rev. **72** (1947) 673.

from interactions between the incident protons and the component parts of the gas cell. Consequently a correction was applied to the long counter rate for the effect of these neutrons since the background

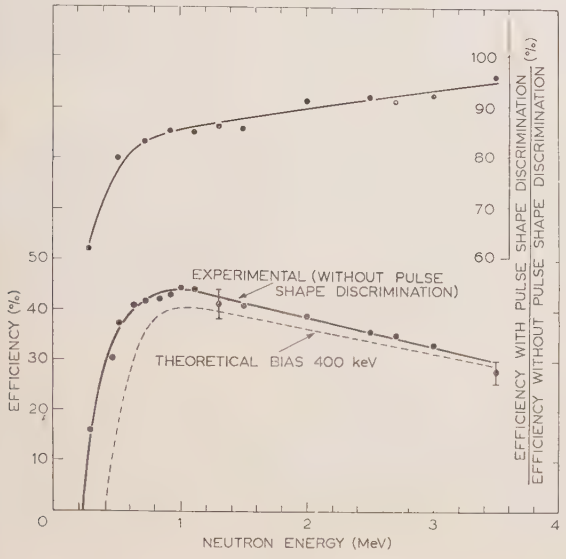
EFFICIENCY (%)
NEUTRON ENERGY (MeV)
EXPERIMENTAL (WITHOUT PULSE SHAPE DISCRIMINATION)
THEORETICAL BIAS 400 keV
EFFICIENCY WITH PULSE SHAPE DISCRIMINATION
EFFICIENCY WITHOUT PULSE SHAPE DISCRIMINATION (%)

Fig. 13. Results of efficiency measurements and comparison with theory. Upper curve shows the ratio of efficiency obtained with pulse shape discrimination applied to that obtained when this technique is not applied.

measurement with the shadow cone does not include them. The correction factor was taken to be the ratio of the total counts in the time spectra to the counts under the neutron peaks observed with pulse shape discrimination applied. Its magnitude varied from about 2% at 0.5 MeV to 5% at 3 MeV neutron energy. In view of the uncertainties involved in applying the correction and also the accuracy of the long counter calibration, the overall uncertainty in the measured efficiency is about $\pm$ 7%. The final results are shown in fig. 13.

Also plotted in fig. 13 is a curve of the ratio of the efficiency with pulse shape discrimination to that obtained when the technique is not applied.

## 5. Comparison between Theory and Experiment

Theoretical pulse distributions for 1, 4 and 14 MeV are fitted to the experimental curves shown in figs. 9, 10 and 11, respectively. In each case the curves are normalised to the same area. At 4 and 14 MeV the high cut off points of the theoretical curves are made to coincide with the points at which the extrapolated straight lines of the experimental integral curves cut the bias axis. In these cases the agreement between theory and experiment is good provided due allowance is made for the resolution of the detector. (Resolution here is taken to mean the spread in output pulse height for monoenergetic charged particles produced uniformly throughout the scintillator.) For comparison, theoretical curves based on the assumption that only single scatterings with hydrogen can take place are also shown. At 4 MeV there is a marked difference between the two theoretical curves, and experiment gives definite support to the sophisticated theory. This difference is not apparent at 14 MeV presumably because multiple scattering effects are much less important at this energy.

At 1 MeV, resolution is expected to modify considerably the predicted curve. To illustrate this a triangular resolution function has been folded into the theoretical curve. From an inspection of the 4 and 14 MeV results it was estimated that the half width of the resolution function was given approximately by the expression $0.29\,L^{\frac{1}{2}}$. It can be seen in fig. 9 that the modified theoretical curve fits the experimental result extremely well. A curve corresponding to single hydrogen collisions would not show a peak.

A direct comparison between the measured efficiency curve and one of the theoretical curves shown in fig. 8 cannot be made since instrumental resolution is expected to have a large effect, particularly at low energy. Since the efficiency is predicted to be a sensitive function of the bias it is obvious that an accurate resolution correction would be required in order to make a quantitative comparison between theory and experiment. This cannot be done because the necessary detailed information on the resolution at low energies is not known. In view of this the discussion will be restricted to a few qualitative remarks.

Resolution will affect the theoretical curves shown in fig. 8 in the following way. The effective bias will be lowered and the efficiency will be increased at all energies. However, as the energy is increased, the percentage increase in efficiency will become smaller. In fig. 13 a theoretical curve for

bias 400 keV is shown along with the experimental results. It can be seen that resolution will modify this curve to produce one which is qualitatively consistent with the experimental curve.

## 6. Conclusions

This study has shown that the line shapes from organic scintillators, having dimensions of a few inches, are well understood and can be calculated by the Monte Carlo programme described. The programme does not include a correction for resolution. The programme also permits the calculation of detector efficiency, but because of uncertainties in applying a resolution correction, and because the efficiency is critically dependent on bias at low energies, and with low bias applied, the calculations can be in serious error at low energy. At high energies and with a bias exceeding say 1 MeV the efficiency changes only slowly with bias and hence the theoretical efficiency, as calculated from table 2 is considered to be quite accurate. In passing, it is worth mentioning that the measurement of efficiency becomes progressively more difficult with increasing neutron energy (apart from 14 MeV). As a general rule, therefore, it is advisable to measure the efficiency at low energies and calculate it at high energies, say above 3 MeV.

Care should be taken in applying the results to a detector which has a technique of pulse shape discrimination applied since this usually eliminates some proton pulses as well as electron pulses. In this connection, a study of the rejection rate of the proton pulses by the circuit used would be of considerable interest.

## Acknowledgement

The assistance of Mr. A. D. Purnell in this work is gratefully acknowledged.

NUCLEAR INSTRUMENTS AND METHODS 13 (1961) 83–91; NORTH-HOLLAND PUBLISHING CO.

# A TWENTY-Mc/s TRANSISTOR DECADE SCALER

T. K. ALEXANDER and D. R. HEYWOOD

*Atomic Energy of Canada Ltd., Chalk River, Canada*

Received 12 December 1960

A transistor decade scaler that operates reliably at 20 Mc/s is described. The scaler has binary-coded decimal outputs isolated from its feed-back path. The circuit does not require close-tolerance components and it operates on negative pulses 0.7 to 3.5 V in amplitude. The carry delay through the decade is approximately 25 ns.

A simple transistor pulse generator has been built and operates at repetition rates from 1 Mc/s to 40 Mc/s; either a continuous train of pulses or bursts of pulses may be produced. The pulse width may be varied from 20 ns to one half the period of the oscillation. The generator produces both positive and negative pulses with a maximum amplitude of 2.5 V into 100 Ω.

## 1. Introduction

The problem of designing a high-speed scale-of-two circuit using transistors has been well investigated with considerable success[1–4]). In this report solutions are given to the problems of coupling the scales-of-two, converting to decade scaling, and providing outputs that can be loaded without affecting the scaler's performance. Usually indication is not required in the first decades of a fast scaler. But some applications, such as life-time measurements or high-speed data processing, require complete digital indication; when this can be produced easily, it is a useful improvement that enhances the versatility of the scaler.

To obtain fast switching the scale-of-two stages and the coupling amplifiers use transistors in the current-switching mode described by Yourke[5]). In this mode of operation the emitter-to-base voltage swing is kept to a minimum and the transistors are prevented from saturating by defining a constant emitter current. A relatively high collector-to-base

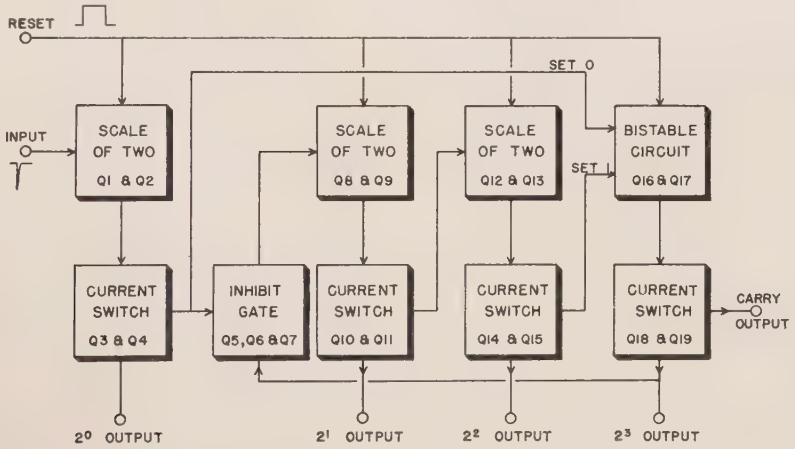


Fig. 1. Block diagram of the decade scaler. The output is a 1–2–4–8 code.

[1]) M. Gettner and W. Selove, Rev. Sci. Instr. **30** (1959) 942.
[2]) R. M. Sugarman, IRE Trans. on Nucl. Sc., Vol. NS–7, No. 1 (1960) 23.
[3]) E. Baldinger, P. Santschi and P. Wehrli, Nucl. Instr. and Meth. **4** (1959) 117.
[4]) C. G. Thornton and J. B. Angell, Proc. I.R.E. **46**, No. 6 (1958) 1166.
[5]) H. S. Yourke, Millimicrosecond Transistor Current Switching Circuits (I.B.M. Technical Publication) Presented at February, 1957 IRE–AIEE Conference on Transistor and Solid State Circuits at the University of Pennsylvania.

voltage is maintained by Zener diode dc-shifting circuits thus operating the transistors in the optimum region for high-speed switching. An analysis of the switching speed obtainable with transistors in this configuration has been made by Salvador[6]).

The coupling circuit between each binary stage is relatively simple and has been designed to provide isolated outputs from each stage. The buffered outputs are suitable for operating automatic readout systems.

A block diagram of the decade scaler is shown in fig. 1. Each binary stage consists of a scale-of-two circuit with a current switch that provides the buffered output and generates a standard carry pulse to the following stage. As shown in the diagram, the logic to convert four binary stages into a scale-of-ten consists of feed-back from the $2^3$ stage to inhibit the fifth carry pulse to the $2^1$ stage and a connection to allow the carry pulse to reset the $2^3$ stage. Thus the circuit is a scale-of-two followed by a scale-of-five which counts as a binary scaler until the eighth pulse causes the 8-bit binary to set and close the gate. The ninth pulse induces a "0" to "1" transition in the first stage and the tenth pulse, in complementing the first stage, produces a carry pulse that cannot reach the $2^1$ stage but resets the $2^3$ stage. Thus all stages are left in the "0" state.

The scale-of-two, its switch, and the inhibit gate will be described before discussing the whole circuit and its performance.

## 2. Scale-of-Two

The circuit diagram of the binary stage is shown in fig. 2. Using the transistors in the current-switching mode offers ideal conditions for a high-speed binary scale-of-two as the transistors are virtually emitter-driven and the impedances within the feedback loop are small and ideally suited for incorporating and inductive or a shorted-cable memory element. In addition, if one may impose pulse-width restrictions, then simple emitter-triggering can be used when scale-of-two operation is desired.

To reset the circuit to the "0" state (Q1 off) a positive pulse is applied to the base of Q1 through the reverse-biased diode CR3. Similarly, a negative pulse into the base of Q1 or Q2 sets a "1" state or a "0" state respectively in the bistable circuit. The $2^3$ stage in the decade unit is operated in this manner with negative pulses.

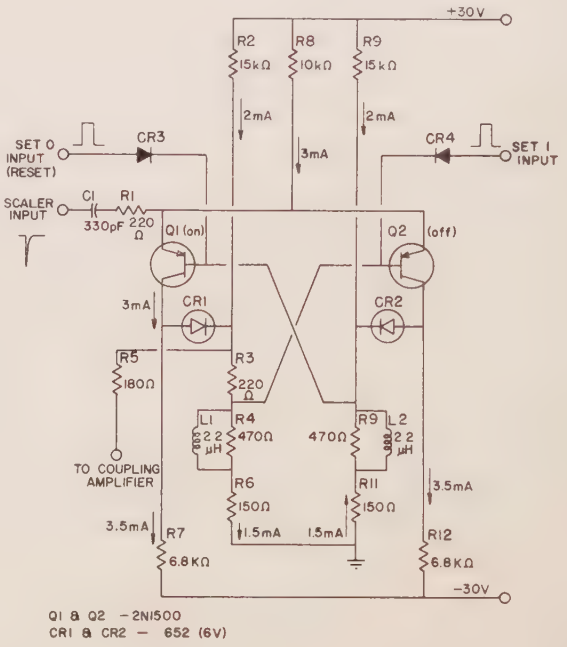


Fig. 2. Schematic of the scale-of-two circuit.

The collector voltages of the transistors are maintained by the Zener diodes CR1 and CR2. A common constant emitter current of 3 mA is supplied by R8. The dc stability of the bistable circuit is maintained by the currents flowing in R6 and R11 as shown in the figure in which Q1 is assumed to be conducting. If Q1 turns off, the changing current in L1 produces a memory pulse ensuring that, at the end of the transient, Q1 is off and Q2 on. The inductive memory was chosen since a memory pulse well defined in time can be achieved in this manner. To interrupt the current in Q1, the current in R8 is momentarily routed out of the circuit by the input pulse. The pulse width of the input pulse must therefore be less than the width of the memory pulse generated in the collector circuit of Q1.

To isolate the binary output and generate a standardized carry pulse to the next stage, another current switch is operated by the bistable circuit. This coupling amplifier is shown in fig. 3. Again a constant current flows into the emitter of either

[6]) J. G. Salvador, UCRL–9035 (Jan. 11, 1960).

Q3 or Q4. The base of Q4 is grounded and the base of Q3 is either + 0.4 V or — 0.4 V as determined by the output of the scale-of-two (see R5 fig. 2). The resistor R3 in fig. 2 is necessary in the binary

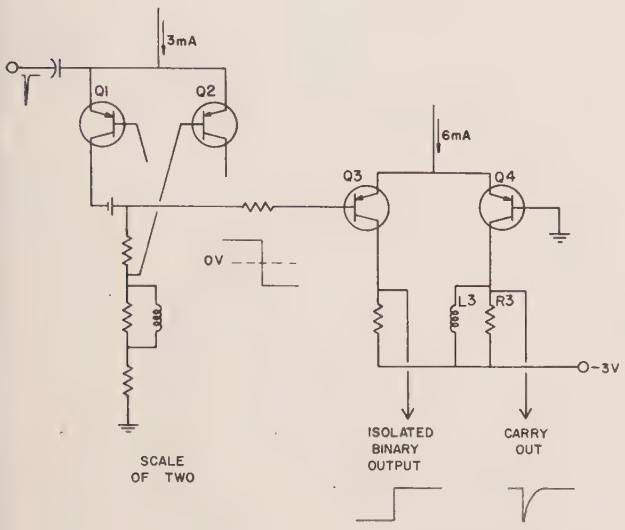


Fig. 3. The coupling amplifier.

circuit to ensure proper operation of the switch. When the binary circuit switches from the "1" state to the "0" state Q4 turns off producing a negative pulse in its collector circuit. The amplitude of the carry pulse is fixed by the constant emitter current of 6 mA and its width by the inductance L3 and the collector load resistance, R3. The impedances in the complete decade scaler circuit have been chosen to maintain approximately equal loading for positive and negative current changes so that each excursion will recover in approximately the same time. The width of the carry pulse is approximately 30 ns at the base, while the amplitude is about 2 V.

The collector of Q3 provides the isolated binary output. A current of 6 mA defines a "0" state while, ideally, zero current defines a "1" state. The only restriction on this output is that Q3 should not be saturated or over-rated.

By connecting the base of Q4 similarly to that of Q3 but from the symmetrical point in the binary circuit, the switching of the coupling stage would not depend on the base of Q3 swinging symmetrically about earth. However a large carry delay is generated by this method since the binary-pair transistor that is about to turn on, cannot do so until the input pulse is over. Hence a carry delay of the switching time plus the input pulse width would be accumulated in each stage. Since the transistor that is *on* in the binary pair *turns off immediately* when an input pulse is applied, we have defined the "1" state as that state when Q1 is conducting and the "0" state when Q1 is cut-off. The collector waveform of Q1 is used only to operate the coupling amplifier (see fig. 3). Hence the "1" to "0" carry pulse is not delayed by the width of the input pulse. The measured carry delay per stage is 10 ns.

### 3. The Inhibit Gate

The inhibit gate is a diode gate consisting of CR3, CR4 and R4 as shown in fig. 4. The carry pulses from the $2^0$ stage are fed to the base of Q5 while the isolated output of the $2^3$ stage is fed to the gate input at the base of Q6. Since the logic requires the gate to be closed when the $2^3$ stage is in its "1" state, the inverter Q6 is necessary. The emitter-follower Q5 is required since the 1-to-0 carry pulse from the $2^0$ stage not only feeds the inhibit gate but also provides the set-0 pulse to the $2^3$ stage.

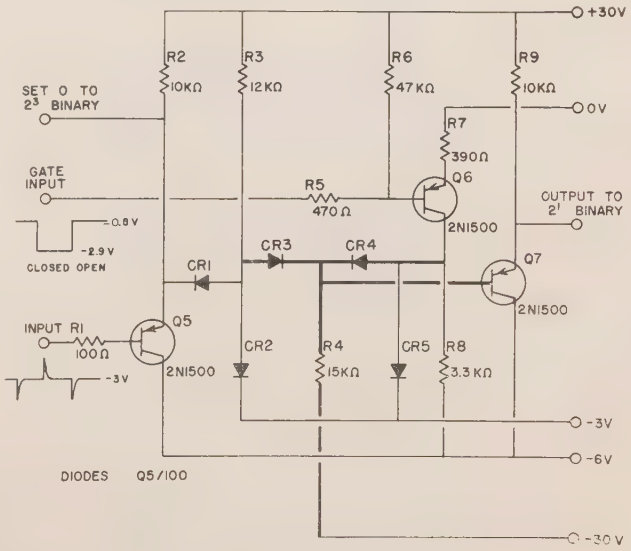


Fig. 4. The inhibit gate. The diode gate is shown in heavy lines.

### 4. Resolving Time and Delay Considerations

The delay and switching times in the scales-of-two and in the inhibit gate are important when considering decade scaling.

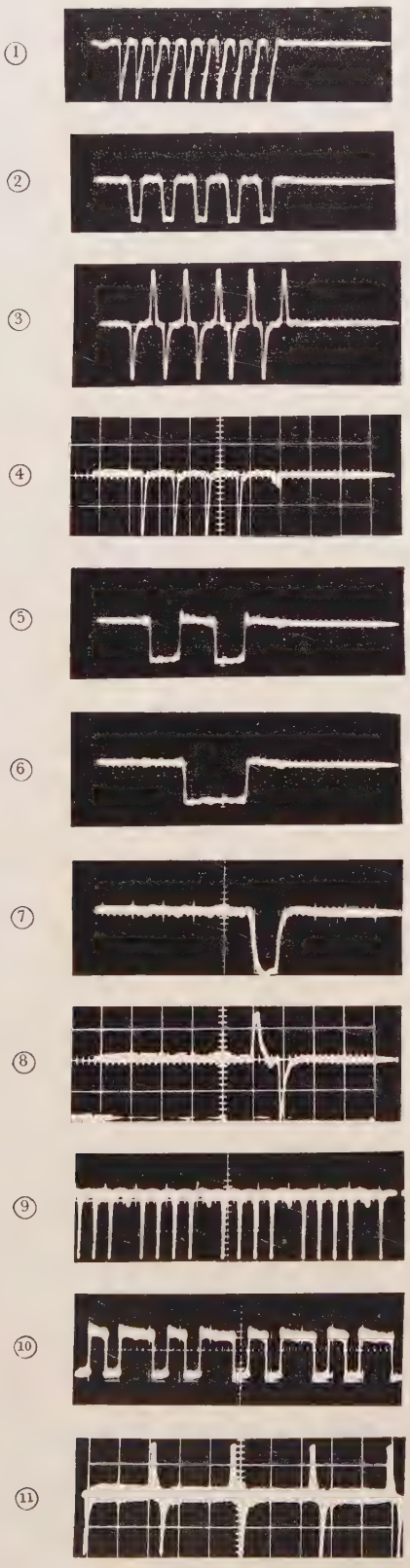


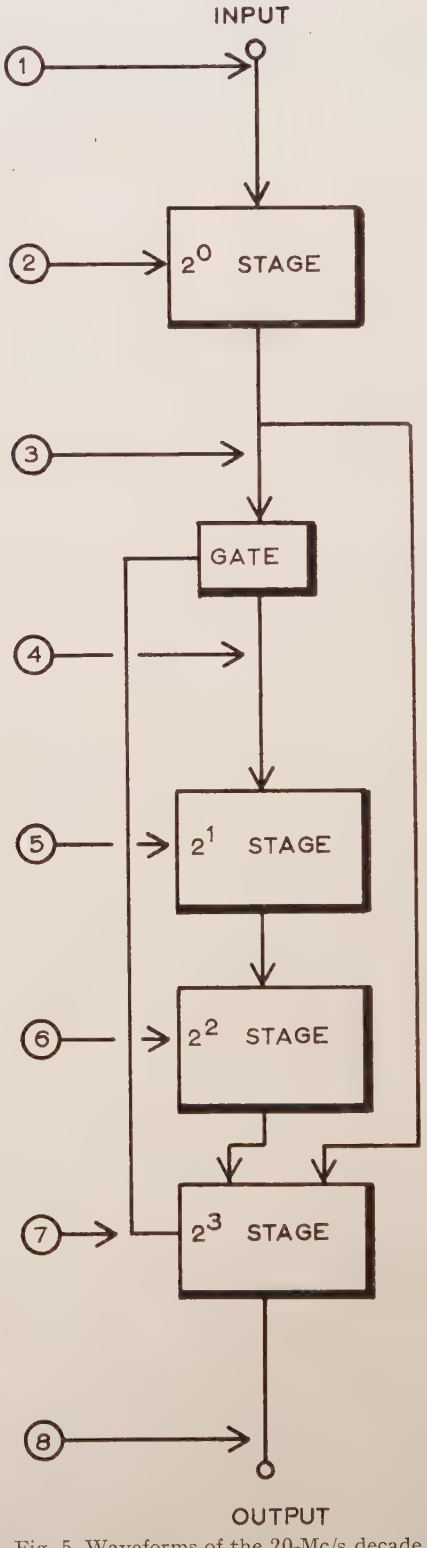


Fig. 5. Waveforms of the 20-Mc/s decade. The series of pictures show the waveforms at various points in the circuit.

To ensure that predictable losses occur with randomly occurring inputs, the following delay and resolving-time relations must be satisfied if dead-time is to be determined by the scaler:

$$T_4 < 2T_1 - 2t_c \quad (1)$$

$$2T_1 > 2t_c + t_{cg} + T_{gc} \quad (2)$$

$$2T_1 > T_{go} > W \quad (3)$$

where $T_1$ = resolving time of first stage $= T_2 = T_3 = T_4$
$T_{go}$ = time for inhibit gate to open
$t_c$ = carry pulse delay through one stage
$t_{cg}$ = pulse delay through inhibit gate
$T_{gc}$ = time for inhibit gate to close
$W$ = width of carry pulse
$T_4$ = resolving time of fourth stage.

All stages are assumed to have equal resolving time $T_1$, which is sufficient but not necessary. Since the $2^3$ stage is operated as a bistable circuit with separate set 0 and set 1 inputs, the delay in the isolated output for the 0-to-1 transition due to the input pulse width to the $2^3$ stage is not involved. The switching delay of the bistable circuit and coupling amplifier is the same as the carry-pulse delay per stage, i.e. 10 ns. The measured delay for a pulse passing through the inhibit gate is approximately 5 ns. With this information and the inequalities (1), (2) and (3), a value of $T_1$ can be chosen such that improper scaling cannot occur with random input pulses. That is, the resolving time of the input scale-of-two defines the upper frequency limit of the whole decade. To satisfy the requirement $T_{go} > W$, the gate waveform is delayed purposely by integrating the output of the $2^3$ stage. The measured value of $T_{go}$ is 25 ns which is the same as $T_{gc}$.

Inequality (1) requires $T_1 > 2t_c > 20$ ns since $T_1 = T_4$;

Inequality (2) requires $2T_1 > 50$ ns;

Inequality (3) requires $2T_1 > 25$ ns'

Hence $T_1$ must be made greater than 25 ns and the highest frequency that can be scaled properly is 40 Mc/s. The measured resolving time of the first stage is 25 ns. For random pulse counting, it would be safer to make $T_1$ even larger or, to precede the scaler with a shaper whose resolving time is greater than 25 ns.

## 5. The Decade Unit and its Performance

The performance of the decade scaler was measured with a pulse generator designed by the authors and described in appendix 1. Photographs of the waveforms displayed on a Tektronix 585 oscilloscope are shown in fig. 5. Pictures (1) to (8) show the waveforms on the isolated outputs, the carry pulses into and out of the inhibit gate, and the carry-ten pulse produced when a burst of ten pulses is fed to the input. The separation between input pulses is approximately 50 ns. Pictures (9) to (11) are waveforms taken with a continuous 20-Mc/s train of pulses feeding the input. As can be seen from the waveforms, the scaler has good tolerances at 20 Mc/s. The circuit is not marginal for frequencies below approximately 40 Mc/s. The measured carry dealy for the unit is approximately 25 ns.

A complete schematic diagram of the decade unit is shown in fig. 6. The logic follows that shown in fig. 1 and in the simplified diagram of fig. 5.

Diodes CR24 to CR27, which form the reset-to-zero facility, are normally reverse-biased by R79 so that the reset input point is normally isolated from the scaler. A positive 5-V pulse applied to the reset input overcomes the bias and turns off the first transistor in each of the binary stages, thereby setting a "0" state into each stage.

It should be noted that the $2^3$-indication output is not the coupling amplifier output, but the emitter of Q6, because of the delay consideration discussed previously.

The circuit operated normally from room temperature to 55°C. This was the only environmental test performed. From the marginal tests (see appendix 1), it can be concluded that reliable performance can be obtained from this decade scaler without the use of close-tolerance components.

### Acknowledgements

This work was carried out as part of the research programme of the Physics Division of Atomic Energy of Canada Limited. The authors thank Mr. R. Abbott for his work in producing the diagrams for this report.

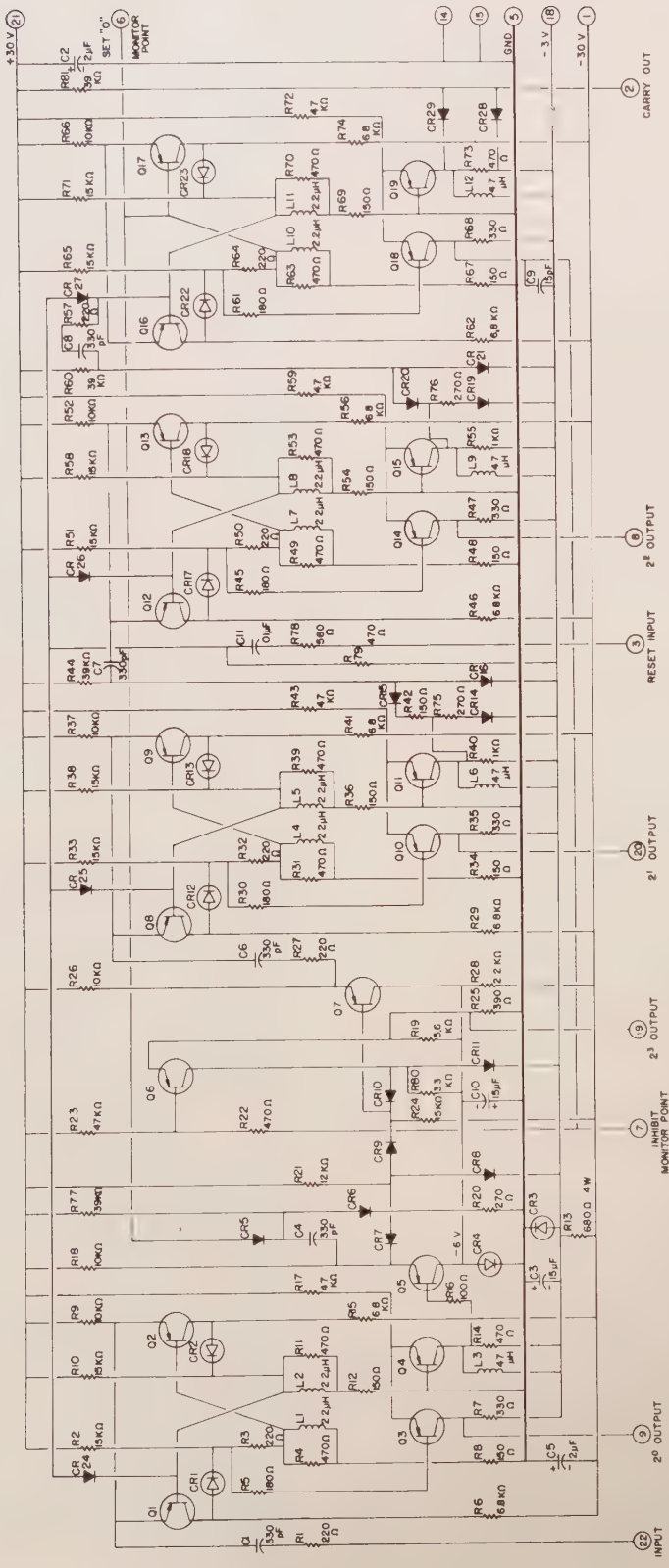


Fig. 6. Schematic of the decade scaler.

## Appendix I

To check empirically that the component and supply voltage tolerances had been adequately accounted for in the design, the decade circuit was tested for margins of performance by varying the positive and negative supply voltages separately at different input-pulse amplitudes. The results of one of the tests taken at 20 Mc/s is shown in fig. 7. If the supplies are fixed at 30 V, input pulses from 0.7 to 3.7 V operate the circuit. The lower limit is just the amplitude required to produce a 3 mA change of current in the input impedance of approximately 220$\Omega$, i.e. the current supplied to the common emitter circuit of the scale-of-two. Failure at large pulse amplitudes is believed to be due to the increase in width at the base of the input pulses. Complete failure of the decade at 24 V and 36 V occurs because proper switching in the coupling amplifiers cannot occur due to the change in dc levels at the input to the amplifier. Since the base of the other transistor in the current switch is grounded, this failure is unavoidable. As described before, this effect could be eliminated by operating the coupling stage with two complementary inputs, however the inherent delays prohibit such a scheme. For a binary scaler the symmetrical drive method would be preferred in applications where carry delays were unimportant.

The input pulses must conform to the specification for the scale-of-two circuit, i.e. they must be negative pulses with a minimum amplitude of 1 V and a maximum width of 30 ns. The carry-out pulses from the unit conform to the input specification so that one decade unit can drive another without requiring buffering or shaping between units.

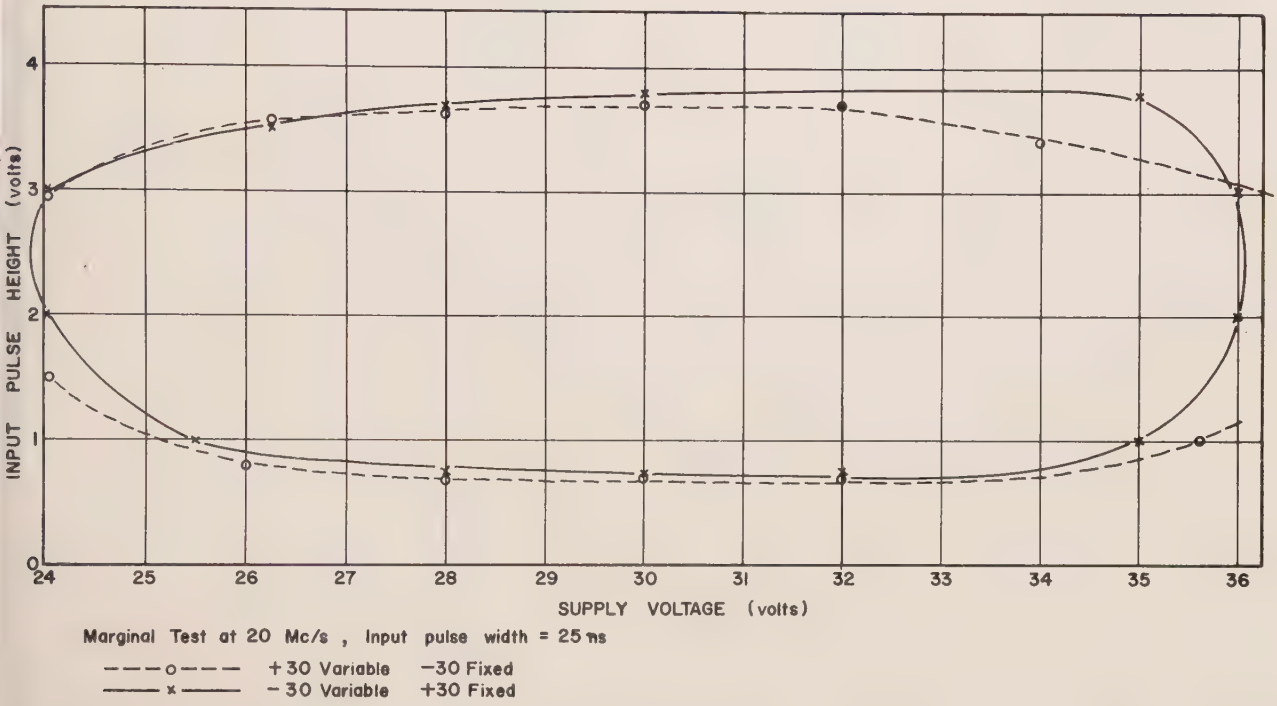


Fig. 7. Marginal performance. In the region enclosed by the curves, the circuit scales properly.

## Appendix II

### A 40-Mc/s PULSE GENERATOR

The pulse generator was developed in order that the high-speed decade could be tested with continuous and bursted trains of variable-amplitude pulses. Further development is required to make this circuit a general-purpose test instrument; however, the simplicity of the generator makes it worth discussing.

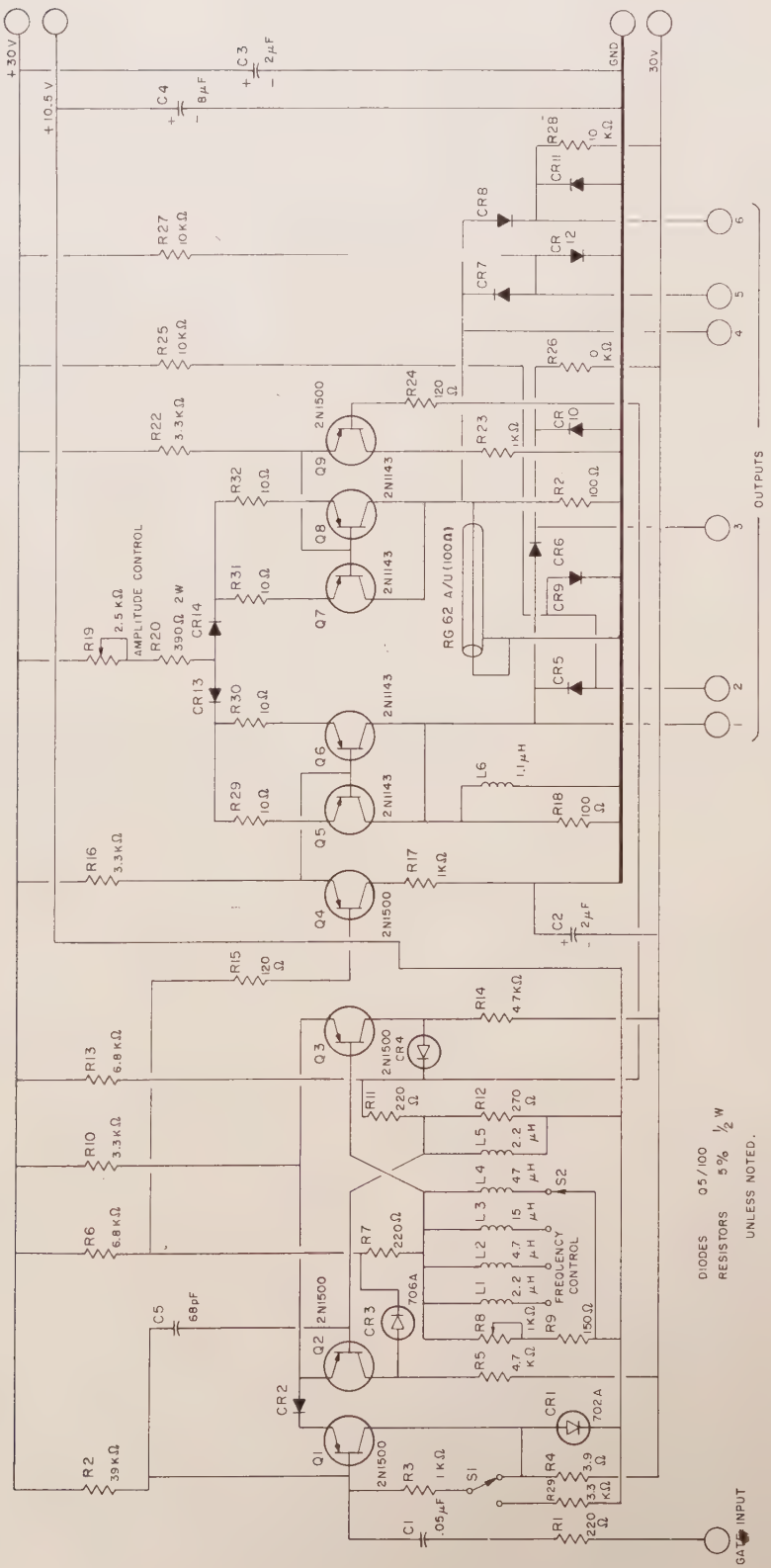


Fig. 8. Schematic diagram of the pulse generator.

The schematic diagram of the pulse generator is shown in fig. 8. The oscillator is Q2 and Q3 in the same configuration as the scale-of-two circuit used in the scaler, but the dc feedback has been removed so that the circuit is astable. Also, the circuit is referenced to 10.5 V instead of to ground so that the final output can be at ground potential. The period of oscillation is determined by the $L/R$ time constant in the collector circuit of Q2. The frequency is varied discontinuously by switching the inductance and continuously by varying the resistance R8.

The output amplifier consists of a current switch similar to the coupling amplifier in the scaler. Here both inputs to the switch are controlled by complementary waveforms from the symmetrical oscillator circuit. The emitter-followers Q4 and Q9 are required since a full output of 50 mA is switched into the output load. The amplitude of the output pulse is varied by varying the potentiometer R19 thereby changing the common emitter current to the output switch. Thus with a pure resistive load in the output collectors of the amplifier, a square wave 50 mA in amplitude is obtained. An 11 V collector-to-emitter voltage is on the output transistors when the output load is short circuited. But the maximum voltage amplitude that can be obtained at the output is 5 V, because the poor bottoming characteristics of the 2N1143 transistors would degrade the rise time. The rise time of the current pulse is $\sim$ 10 ns measured with a Tektronix 585 oscilloscope.

To obtain pulses of short, variable duration, the square waveform is differentiated with a shorted cable ($Z_0 = 91\ \Omega$) on one of the outputs. The complementary output is differentiated with a 1.1 $\mu$H inductor to give short exponentially decaying pulses. Thus one obtains both positive and negative trigger pulses and rectangular pulses. The minimum width without loss in amplitude is limited to 20 ns by the rise-time of the current in the output amplifier.

To inhibit the oscillation, Q1 is brought into conduction by throwing the switch S1. With S1 in the inhibiting position, the oscillator can be gated on by a positive pulse into the base of Q1. Hence a burst of pulses whose frequency is determined by the setting of S2 and R8 and number by the width of the gate pulse can be obtained using an external pulse generator. To ensure that Q3 turns on first when the oscillator starts, the leading edge of the gate pulse is differentiated and fed to the base of Q2. Hence no uncertainty in the phase of oscillation is encountered.

The range of frequency chosen is 1 Mc/s to 40 Mc/s. To obtain frequencies lower than this, an external 1 $\mu$s gate pulse is used and the frequency switch is set near 1 Mc/s. Then the circuit performs as a shaping unit and the frequency is determined by the external pulse generator. Most laboratories have pulse generators as standard test equipment similar to the external generator required.

The power dissipated in the output stage presented a problem and, for this reason, each half of the switch has two 2N1143 transistors in parallel. During oscillation the average power dissipated in one transistor is approximately 140 mW at full output assuming the output is shorted to earth. To ensure that the transistors share the current, 10 $\Omega$ resistors are inserted in the emitters of the transistors. When the oscillator is inhibited, the complementary inputs to the output circuit are (approximately) at the same voltage so that all four output transistors share the common emitter-current and the maximum dissipation is again only 140 mW per transistor.

The pulse generator has two undesirable features. Firstly, the first pulse produced on one output of the generator is approximately one half the amplitude of following pulses in the burst. This is due to the sharing of current in the output transistors when the oscillator is inhibited. However the other output will always have a full-amplitude output pulse. Secondly, since the back-edge of the gate waveform is not locked to the oscillator frequency, the last pulse in a burst may be smaller. This requires the operator to adjust the width of the gate pulse carefully to obtain a uniform burst of pulses. Neither of these limitations was found serious in the actual use of the generator to test the fast decade scaler.

NUCLEAR INSTRUMENTS AND METHODS 13 (1961) 92-94; NORTH-HOLLAND PUBLISHING CO.

LETTERS TO THE EDITOR

# A LOW PRICED AUTOMATIC PRINTOUT SYSTEM FOR THE HUTCHINSON-SCARROTT ANALYZER

RICHARD C. McCALL† and E. INGEMAR LARSSON

*Radiation Physics Department University of Lund, Lund, Sweden*

Received 25 May 1961

Although multi-channel pulse height analyzers now being built are mostly of the magnetic memory type, Hutchinson-Scarrott analyzers are still being built[1]) and there are many in service. The Hutchinson-Scarrott analyzers are at a disadvantage in speed, versatility and ease of readout but they are still good analyzers and are perhaps more reliable than other vacuum tube type pulse height analyzers. In an effort to overcome at least the disadvantage in ease of readout we have developed the automatic printout system described below.

There have been several readout systems designed for the Hutchinson-Scarrott analyzer[2–6]). The system designed by Hansén[6]) has been modified to an automatic printout system in this laboratory.

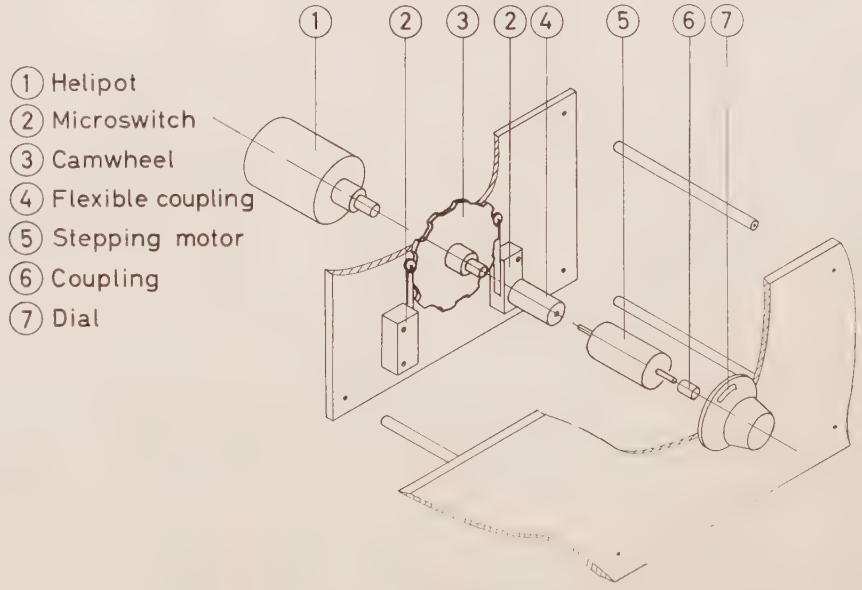


Fig. 1. Mechanical arrangement of readout system.

Hansén developed a readout system by utilizing the possibility of subtracting pulses from the memory. Each channel in turn is read out by subtracting pulses from it until it is empty. A scaler counts the number of pulses required to empty the

† This investigation was carried out during the tenure of a Postdoctoral Fellowship from the National Cancer Institute, United States Public Health Service.

[1]) Frieseke Hoepfner GMBH, Erlangenbruch, Germany.

[2]) G. W. Hutchinson and G. G. Scarrott, Phil. Mag. **42** (1951) 792.

[3]) D. Maeder, Helv. Phys. Acta **29** (1956) 459; Nucl. Instr. **2** (1958) 121.

[4]) J. D. Gallagher *et al.*, LA-1917 (1955).

[5]) H. L. Schultz *et al.*, RSI 27 (1956) 437.

[6]) J. Hansén, Nuclear Instruments **3** (1958) 271.

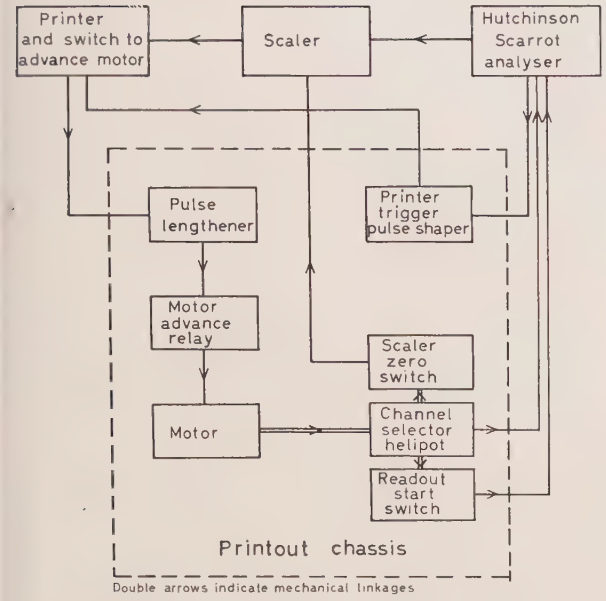


Fig. 2. Block diagram of printout system.

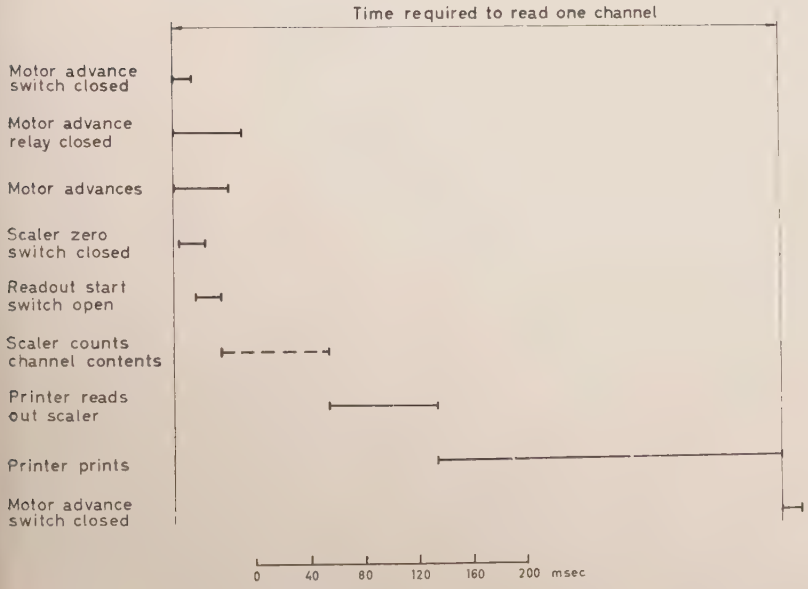


Fig. 3. Sequence of events in printout process.

| | | |
|---|---|---|
| 0001 | 70 | 323 |
| 0002 | | 1 |
| 0003 | | 186 |
| 0004 | 1 | 700 |
| 0005 | 2 | 065 |
| 0006 | 2 | 242 |
| 0007 | 2 | 618 |
| 0008 | 3 | 490 |
| 0009 | 3 | 416 |
| 0010 | 3 | 009 |
| 0011 | 2 | 236 |
| 0012 | 1 | 803 |
| 0013 | 1 | 553 |
| 0014 | 1 | 411 |
| 0015 | 1 | 206 |
| 0016 | 1 | 194 |
| 0017 | 1 | 355 |
| 0018 | 1 | 663 |
| 0019 | 2 | 048 |
| 0020 | 3 | 164 |
| 0021 | 4 | 717 |
| 0022 | 3 | 810 |
| 0023 | 1 | 490 |
| 0024 | | 722 |
| 0025 | | 568 |
| 0026 | | 586 |
| 0027 | | 609 |
| 0028 | | 562 |
| 0029 | | 568 |
| 0030 | | 555 |
| 0031 | | 590 |
| 0032 | | 608 |
| 0033 | | 578 |
| 0034 | | 595 |
| 0035 | | 562 |
| 0036 | | 572 |
| 0037 | | 582 |
| 0038 | | 545 |
| 0039 | | 601 |
| 0040 | | 547 |
| 0041 | | 518 |
| 0042 | | 525 |
| 0043 | | 508 |
| 0044 | | 490 |
| 0045 | | 441 |
| 0046 | | 430 |
| 0047 | | 553 |
| 0048 | | 693 |
| 0049 | 1 | 063 |
| 0050 | 1 | 532 |
| 0051 | 2 | 015 |
| 0052 | 2 | 067 |
| 0053 | 1 | 592 |
| 0054 | | 876 |
| 0055 | | 333 |
| 0056 | | 108 |
| 0057 | | 55 |
| 0058 | | 41 |
| 0059 | | 29 |
| 0060 | | 24 |
| 0061 | | 30 |
| 0062 | | 20 |
| 0063 | | 19 |
| 0064 | | 14 |
| 0065 | | 12 |

Fig. 4. $Na^{22}$ spectrum.

channel. The channel to be read out isselected by adjusting a helipot, which must be advanced $\frac{1}{10}$ turn per channel.

We began by building the one hand arrangement mentioned by Hansén[6]). In this arrangement two microswitchs are actuated by a notched wheel on the helipot shaft to zero the scaler and turn on the readout. A stepping motor[7]) was then added to advance the helipot (fig. 1, 2). This was not only a simplification but was a system lending itself easily to automation.

For a printer we used the Kienzle D1E[8]). This is a low priced transitorized printer designed to print the number registered on almost any type of decade scaler (EIT, Dekatron, conventional hard tube decade etc.). It utilizes parallel entry of information up to 14 digits. The construction is simple and sturdy and it is capable of printing at a maximum speed of three lines per second. A built in feature is a mechanism which prints consecutive numbers on the left side of the tape. This is ideal for numbering the channels.

[7]) Ledex inc. Dayton 2, Ohio.

[8]) Kienzle Apparate GMBH, Villingen im Schwarzwald, Germany.

It is unnecessary to provide a special arrangement to stop the printout system after the last channel. Since there is no channel to be emptied when the helipot is advanced beyond the last channel, the scaler counts continuously and the motor does not advance further. It only remained to incorporate the printer into the readout system as shown in the block diagram (fig. 2). The motor advance switch is also a built in feature of the printer. The sequence of events is shown in fig. 3. The actual printout speed depends upon the number of counts stored in the channels. With all channels empty, the printout proceeds at 2.5 channels per second. A $Na^{22}$ spectrum is illustrated in fig. 4.

The cost of building such a printout system is estimated at about 1000 U.S. dollars.

The authors wish to express their gratitude to Dr. K. Lidén for his constant interest and support.

*Note added in proof:* An improved version of this readout system uses a single relay with three contacts to replace the motor advance relay, the scaler zero switch and the read out start switch and to eliminate the notched wheel.

NUCLEAR INSTRUMENTS AND METHODS **13** (1961) 95–96; NORTH-HOLLAND PUBLISHING CO.

# A FAST FLIP-FLOP CIRCUIT UTILIZING TUNNEL-DIODES

Y. HAZONI

*Atomic Energy Commission, Tel-Aviv, Israel*

Received 6 April 1961

The characteristics of the Tunnel-Diode (T.D.) permit a remarkable simplification in the design of fast bistable Multivibrator (Flip-Flop) circuits. The ultimate speed of the circuit described below is the switching time of the Tunnel-Diode, which could be better than one nanosecond. In the actual circuit, a Double Pulse Resolution of $10^{-8}$ seconds was achieved.

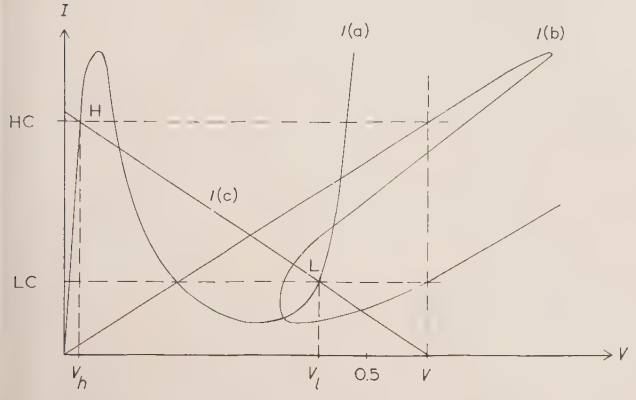


Fig. 1. 1(a): A characteristic $I$–$V$ curve of a Tunnel-Diode; 1(b): A characteristic $I$–$V$ curve of a Tunnel-Diode in series with an ohmic load; 1(c): Load line.

The Tunnel-Diode can be biased to operate as a bistable element. It can then be triggered to change its state by a positive pulse and to switch back by a negative one. Such a circuit has the disadvantage, that one must know the state of the circuit before choosing the polarity of the next switching pulse.

The Flip-Flop described below is triggered symmetrically to switch in both directions by pulses of the same polarity; instead of changing the polarity of the pulses there is a change of Input Channels. This change is performed automatically by the T.D. itself while changing its state.

The circuit is based on the well known $I/V$ characteristic of the T.D. as shown in fig. 1(a). Fig. 2 shows the basic unit of the circuit. The T.D. is mounted between two equal resistors $R$. The dynamic $I/V$ curve (fig. 1(b)) taken across the terminals E and N demonstrates the possibility of having two stable current states at certain values of the voltage $V$.

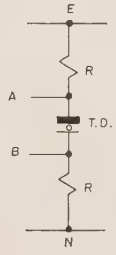


Fig. 2. The basic unit of the flip-flop circuit: The bi-stable unit.

These two stable operating points, H and L, are obtained from the intersection of the load-line and the characteristic curve of the T.D. The potentials at points A and B will therefore depend on the state of the circuit. A change of state will cause the potentials at A and B to change in opposite directions. These changes are utilized in the circuit shown in fig. 3 to block and unblock the Diodes D(A) and D(B) which are connected to points A and B and serve as the two input channels mentioned above. V(A) and V(B) are so chosen that Diode D(A) conducts when the circuit is in its High Current (HC) state and is cut-off when it is in the Low Current (LC) state, while D(B) will be cut-off when the circuit is the HC state and conducting when it is in the LC state. A positive pulse passing through channel A will force the circuit to switch from the HC to the LC state, while a similar pulse

passing through channel B will force it to switch back to the HC state.

Since the bias shift available for the interchanging of the two input channels is equal to $V_1 - V_h$, the bias change on each diode is $\frac{1}{2}(V_1 - V_h)$. In order to achieve symmetry of the two input channels $V(A) - V(B)$ must be equal to $\frac{1}{2}(V_1 - V_h)$.

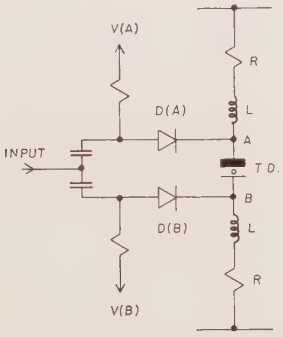


Fig. 3. The flip-flop circuit.

After the trigger pulse has been removed, the circuit is left at an unstable operating point on the negative-resistance part of the $I/V$ curve. If the $I/V$ curve were completely symmetric to switching in both directions, it would be impossible to predict, in which direction the operating point would move. In practice, the T.D. would always switch in the same direction, which is equally unsatisfactory. In order to overcome these difficulties, some inertia must be introduced into the circuit, this is effected by means of the inductance of the two small coils shown in fig. 3. The inductance of the circuit wiring is almost sufficient for this purpose. For proper operation of the circuit it is essential that the duration of the trigger pulse be shorter that the switching time of the system.

Two types of Tunnel Diode (G.E. 2939 and an experimental type) were tried successfully and a Double-Pulse Resolution of about $10^{-8}$ seconds was achieved. The two input diodes used were conventional fast-recovery Germanium diodes (S 570 G and Q 6 100 T) which are biased in the bottom region of their characteristic curve to operate in the forward direction. These diodes have a knee in their forward charactertistic at about 0.25 V and a major disadvantage in that their forward resistance is still quite high above the knee. For this reason the trigger amplitude had to be 1.5 V instead of about 0.25 V with an ideal diode.

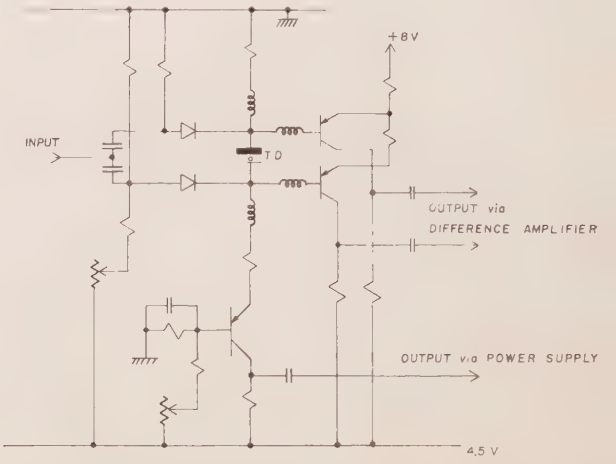


Fig. 4. A simultanuous demonstration of two alternative ways of taking the output of the circuit: a. Via a transistor serving as a current supply; b. Via difference amplifier.

Published characteristics of the Uni-Tunnel-Diode[1]) promise a performance more suitable for this purpose.

Two alternative methods were tried in order to view the operation of the circuit. The first was to observe the change of the current supplied to the circuit. For this purpose the Tunnel-Diode circuit was connected to the emitter of a Common-Base PNP Transistor (2N 501) and the output was taken from its collector. The second method was to look at points A and B through a Difference Amplifier.

The two methods are shown simultaneously in fig. 4. It appears that the second method is preferable for very fast operation.

[1]) I. A. Lesk *et al.*, Germanium and Silicon T.D., Design, operation and Application, 1959 IRE Wescon Convention Record, Part 3 ECG-441, fig. 9 (d).

NUCLEAR INSTRUMENTS AND METHODS **13** (1961) 97–98; NORTH-HOLLAND PUBLISHING CO.

# ELIMINATION OF THE DEAD SPACE BETWEEN CHANNELS IN A HUTCHINSON-SCARROTT PULSE HEIGHT ANALYSER

R. E. JENNINGS and R. E. RAND

*Physics Department, University College London*

Received 30 May 1961

We have found that the Hutchinson-Scarrott[1]) pulse height analyser is liable to "lose" some pulses whose heights lie close to channel boundaries. This loss of counts, which can be as large as a few per cent when a uniform distribution of pulses is being measured, may not be serious if only the relative shape of a spectrum is required but will be serious for absolute measurements. However, a very simple means of overcoming this defect has been found.

The relevant part of the sorting action of the analyser is explained in fig. 1. The input pulse is lengthened to give the (negative) pulse (b) which is compared with the linear sweep (a). The resulting comparison pulse (c) is fed to a coincidence valve which is also supplied with the channel pips (d), the coincidence pulse being shown at (e). This pulse then cancels the pulses (b) and (c) and also records a count in the appropriate channel at the adding gate.

The count will only be recorded if the pulse (e) overlaps a digit current pulse (f), (representing the first digit in the channel concerned). Normally this must occur since the oscillators providing (d) and (f) are locked together. However, the channel pips (d) are usually wider than the digit pulses (f), so that if (b) is of such a height that the leading edge of (c) coincides with the trailing edge of the channel pip (d), a shortened coincidence pulse may be produced which will arrive too late to coincide with the appropriate digit pulse, but will nevertheless be able to reset (b) and (c). Thus pulses whose heights lie within the "dead space" of fig. 1 may be lost.

This anomalous behaviour could be prevented by careful adjustment of the widths and heights of the pulses involved, but this would be tedious and errors could result from any instability of the

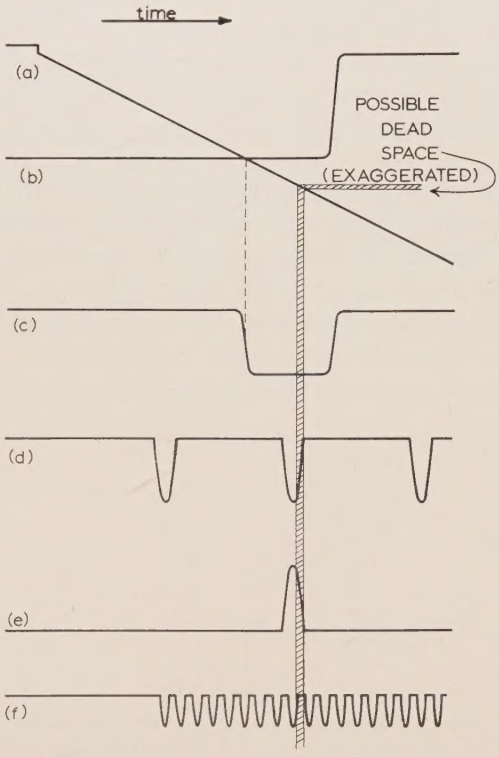


Fig. 1.

circuits. A much simpler solution is to prevent a coincidence occurring when a channel pip is due, the input pulse being held and recorded in the following channel. This has been achieved by connecting a small capacitor (10–15 pF) between the channel oscillator and the linear sweep so that this

[1]) G. W. Hutchinson and G. G. Scarrott, Phil. Mag. **42** (1951) 792.

sweep now has positive channel pips superimposed on it as shown in fig. 2. The sorting action is now normal as far as each new channel boundary. However, a pulse may not be counted in the next channel until the sweep again passes this level so that a time interval is created during which comparison is prohibited. This interval covers the dead time completely, due to the inherent delay of the circuits, and counts are no longer lost. The small displacement of the channel boundaries can be corrected.

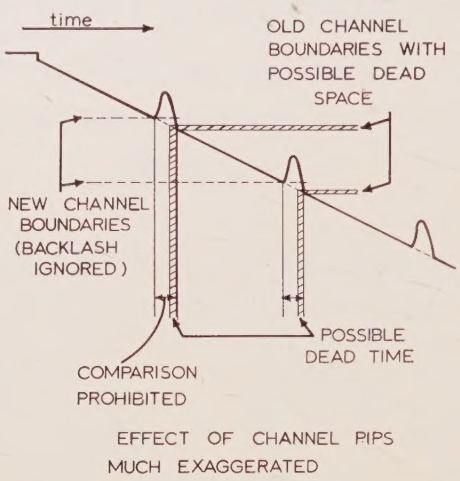
time
OLD CHANNEL BOUNDARIES WITH POSSIBLE DEAD SPACE
NEW CHANNEL BOUNDARIES (BACKLASH IGNORED)
POSSIBLE DEAD TIME
COMPARISON PROHIBITED
EFFECT OF CHANNEL PIPS MUCH EXAGGERATED

Fig. 2.

For two analysers which have been modified here, the loss of counts when measuring a uniform distribution of pulses has been reduced from 3% to 0.03% and 0.6% to less than $10^{-4}$% respectively. (Circuit details account for the difference in behaviour.) The modification is very simple to make, the capacitor being connected between adjacent parts of the circuit (in the original layout). To obtain the best results it may be necessary to modify the shape of the channel pips at the linear sweep output by adjusting the stray capacitance, etc.

NUCLEAR INSTRUMENTS AND METHODS **13** (1961) 99–100; NORTH-HOLLAND PUBLISHING CO.

# A POSSIBLE METHOD FOR DISTINGUISHING CHARGED PARTICLES WITH SEMICONDUCTOR DETECTORS

N. CINDRO

*Institute "Ruđer Bošković" Zagreb, Yugoslavia*

Received 4 July 1961

Semiconductor detectors[1]) have found an ever more increasing use in nuclear physics. High resolution, versatility and simple electronics present the main advantages of these detectors. The energy needed for the creation of an ion pair in Si and Ge crystals so far has been found to be independent of the kind and energy of the bombarding particle. The pulse obtained from semiconductor detectors depends therefore only on the energy loss in the crystal. Hence it is not possible, using a single semiconductor detector, to distinguish between different particles having the same energy. For this purpose semiconductor telescope $dE/dx$ -- $E$ counters have been reported lately. A method based on both the energy and specific ionization of a particle in a scintillation crystal has been developed earlier[2]) and tested by several authors[3]). Following the same ideas, a similar method could be suggested to distinguish between charged particles in a semiconductor detector.

If two particles of different kind (e.g. a proton and a deuteron) but with the same energy are stopped in the space charge region (depletion region) of a p-n junction or a surface barrier detector, they will produce the same voltage pulse. However, due to its higher specific ionization, the deuteron will have a shorter range in the crystal than the proton. If now the width of the depletion region was adjusted so as to have the exact thickness necessary to stop deuterons of a given energy, protons of the same energy will not be stopped completely in traversing the depletion region. Consequently, the proton voltage pulse will be smaller than the deuteron one. Protons (and deuterons) of higher energy will lose still less energy and give a correspondingly smaller pulse, while lower energy protons (and deuterons) although perhaps totally stopped will be ruled out by their smaller charge output. In this way we can always discriminate particles of the highest specific ionization from other particles present in the reaction, e.g. alpha particles from deuterons and protons or deuterons from protons when alpha particles are scarce in number [e.g. in (d,d) reactions on medium heavy nuclei]. The spectrum of two beams of protons and deuterons of the same energy ideally looks like on fig. 1, while a typical spectrum from a reaction giving both protons and deuterons should look like on fig. 2d. Figs. 2a and b present separate proton and deuteron spectra, and fig. 2c the total spectrum

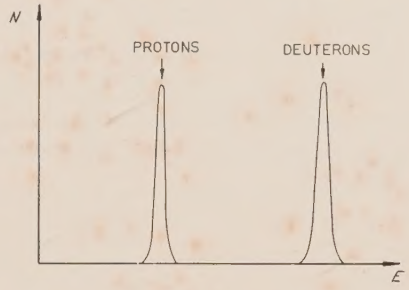


Fig. 1.
Hypothetical spectrum of two monoenergetic proton and deuteron beams stopped in a "thin" semiconductor detector.

[1]) K. G. McKay, Phys. Rev. **76** (1949) 1573.

[2]) N. Cindro and N. S. Wall, Phys. Rev. **119** (1960) 1340.

[3]) P. R. Klein, N. Cindro, W. Swenson and N. S. Wall, Nucl. Phys. **16** (1960) 374;
N. Cindro, I. Šlaus, P. Tomaš and B. Eman, Nucl. Phys. **22** (1961) 96;
I. Šlaus, P. Tomaš and N. Stipčić, Nucl. Phys. **22** (1961) 692;
N. Cindro, M. Cerineo and A. Strzalkowski, Nucl. Phys. **24** (1961) 107.

in a thick detector. On the composite "thin detector" proton + deuteron spectrum, displayed on fig. 2d protons start with an edge, while the high energy peak is far on the left.

$$w \sim [\varrho\,(V_0 + V]^{\frac{1}{2}} .$$

$V_0$ is the intrinsic inverse voltage present between the donor and acceptor regions of the crystal. Since $V_0$ is of the order of 1 V or less, and the applied bias

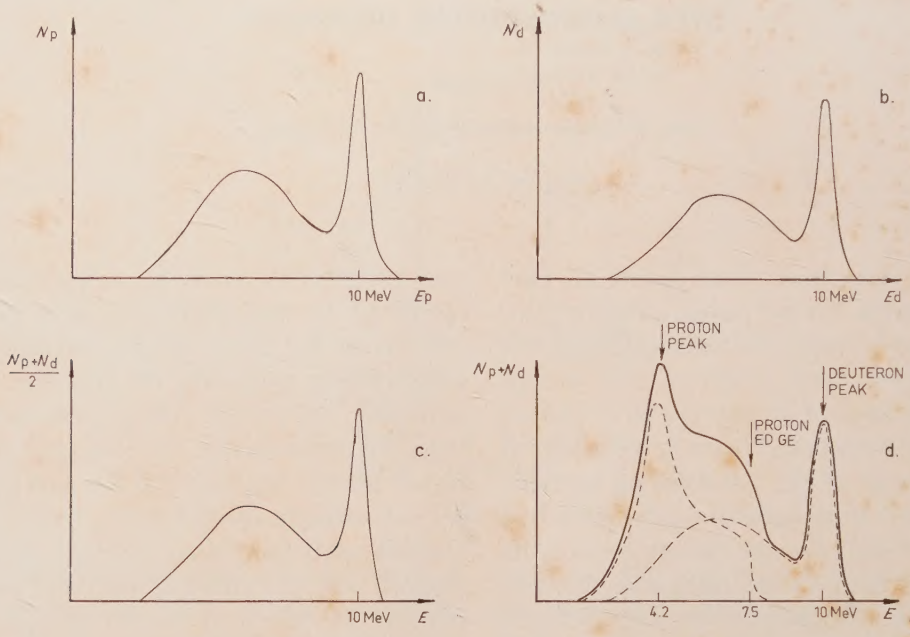


Fig. 2. Hypothetical spectrum of protons and deuterons from a nuclear reaction: a. proton spectrum; b. deuteron spectrum; c. composite proton + deuteron spectrum in a "thick" semi-conductor; d. composite proton + deuteron spectrum in a "thin" semiconductor.

In the "thin crystal" method[2]) the appropriate thickness of the crystal was obtained either by grinding or cutting the crystal. In the semiconductor detectors, the width $w$ of the depletion region depends on the resistivity and the applied bias $V$ in the following way

$V$ can be varied up to several hundred volts, there exists a large possibility of adjusting the width of the depletion region to any given thickness. The thickness of the depletion region can be determined either experimentally or by knowing exactly the resistivity $\rho$ of the semiconductor used.